University of Crete

Department of Materials Science and Technology

Metastability transitions in colloidal supramolecular systems of varying softness and shape

Doctoral Dissertation

IOANNIS M. MARAKIS

Heraklion 2016

ΠΑΝΕΠΙΣΤΗΜΙΟ ΚΡΗΤΗΣ
ΣΧΟΛΗ ΘΕΤΙΚΩΝ ΚΑΙ ΤΕΧΝΟΛΟΓΙΚΩΝ ΕΠΙΣΤΗΜΩΝ
ΤΜΗΜΑ ΕΠΙΣΤΗΜΗΣ ΚΑΙ ΤΕΧΝΟΛΟΓΙΑΣ ΥΛΙΚΩΝ

ΠΡΑΚΤΙΚΟ ΔΗΜΟΣΙΑΣ ΠΑΡΟΥΣΙΑΣΗΣ ΚΑΙ ΕΞΕΤΑΣΗΣ
ΤΗΣ ΔΙΔΑΚΤΟΡΙΚΗΣ ΔΙΑΤΡΙΒΗΣ ΤΟΥ
κ. Μαράκη Ιωάννη
ΥΠΟΨΗΦΙΟΥ ΔΙΔΑΚΤΟΡΑ ΤΟΥ ΤΜΗΜΑΤΟΣ
ΕΠΙΣΤΗΜΗΣ ΚΑΙ ΤΕΧΝΟΛΟΓΙΑΣ ΥΛΙΚΩΝ

Η Επταμελής Επιτροπή της Διδακτορικής Διατριβής του κ. Μαράκη Ιωάννη η οποία ορίσθηκε στην 69η Γ.Σ.Ε.Σ. στις 04/12/2015, εκλήθη την Τρίτη 19 Ιανουαρίου 2016 να εξετάσει την σύμφωνα με το Νόμο υποστήριξη της διατριβής του υποψηφίου με τίτλο:

«Metastability Transitions in Colloidal Supramolecular Systems of Varying Softness and Shape»

Τα παρόντα μέλη της επταμελούς Επιτροπής εκφράζουν ομόφωνα την πλήρη ικανοποίησή τους για την υψηλή ποιότητα του περιεχομένου και της υποστήριξης της διατριβής.
Τα ερευνητικά αποτελέσματα της εργασίας του **κ. Μαράκη Ιωάννη** είναι σημαντικά, πρωτότυπα και διευρύνουν το πεδίο της έρευνας στην Επιστήμη και Τεχνολογία Υλικών.
Ως εκ τούτου η Εξεταστική Επιτροπή προτείνει ομόφωνα την απονομή του Διδακτορικού Διπλώματος στον κ. Μαράκη Ιωάννη.

Τα μέλη της επταμελούς επιτροπής για την αξιολόγηση της Διδακτορικής Διατριβής του κ. Μαράκη Ιωάννη.

Η Επταμελής Επιτροπή:

Βλασσόπουλος Δημήτριος, (Επιβλέπων)
Καθηγητής, ΤΕΤΥ, Παν/μιο Κρήτης

Φυτάς Γεώργιος,
Καθηγητής ΤΕΤΥ, Παν/μιο Κρήτης

Πετεκίδης Γεώργιος,
Αναπληρωτής καθηγητής ΤΕΤΥ, Παν/μιο Κρήτης

Domenico Truzzollilo
CNRS researcher (CR2), Laboratoire Coulomb, University of Montpellier, France

Pavlik Lettinga
Professor, Forschungszentrum Jülich, Germany

Benoit Loppinet
Ερευνητής Β, ΙΤΕ, Ηράκλειο, Κρήτης

Φλούδας Γεώργιος
Καθηγητής, Τμήμα Φυσικής, Πανεπιστήμιο Ιωαννίνων

Contents

Summary

In this research we explored the effects of softness on the metastability transitions and in particular during gel or glass formation. More specifically, we studied the effects of varying the molecular characteristics of a star polymer on the structural rearrangements of the solution upon the appliance of an external flow field. We defined a 'softness parameter', (SP), and highlighted its effect on the structural order of the system. We investigated the effect of shearing parameters on the nucleation process and explained the variations with the modifications of the particle rearrangements. The stability of the structures was associated with softness and concentration, denoting the sensitive dynamics deviations upon changing the molecular characteristics. Flexible shapes of particles allow the systems to reform and accommodate better the external stimuli. We pinpointed the differences of our soft systems with the hard spheres and highlighted the complexity yielded by 'softness'. In general, softness and metastability are two terms, which seem to be inextricably bonded, generating amazing properties.

We also, investigated the properties of two different self-assembled block copolymers. The amphiphilicity of the molecules drive the systems to self-organize and form hydrogels. Depending on the molecular characteristics, the hydrogel structures exhibit varying properties showing solid structures in high concentrations. The elasticity of the networks increase rapidly with concentration demonstrating different types of interactions between the self-assembled structures. The hydrogels studied in this work, showed fast reformation after the cessation of large shear rates, depicting strong interactions among the large self assembled structures. By careful tuning hydrophobic and hydrophilic interactions we can control the kinetic properties of such systems and mimic the natural way of creating supramolecular systems.

Furthermore, we investigated the rheology of two hydrogels which were especially synthesized for targeted drug delivery in pancreatic cancer tissues. The rheological behavior of the hydrogels is highly dependent on pH and temperature since the gel flows upon decreasing pH or increasing temperature. The thixotropy of the gel was studied by applying high shear rates and then capturing the time needed for the gel to reform. Both hydrogels manifested weak thixotropic behavior by instant reformation after the shear cessation. The sensitivity in temperature and pH variations, makes these hydrogels excellent candidate systems for drug delivery applications, offering discovery opportunities in this important field.

Finally, we examined metastability effects in more complicated systems consisted of two different sizes and types of particles. The initial soft colloidal system was perturbed by adding depletion and displayed several phase transitions. The kinetic properties along with mixture's elasticity, change as a function of depletion revealing a way to control the behavior of such systems. Again, metastability was associated with softness and proved to affect the mechanical properties of the mixtures. All, the experimental results were supported by theoretical analysis and simulations, denoting the validity of our outcomes. Also, simulations were performed for different size ratios and functionalities. The combined results demonstrate that by tuning the physical parameters, like star functionality and size ratio, we can steer the rheology of the mixtures.

Περίληψη

Οι μετασταθείς καταστάσεις και μεταπτώσεις της χαλαρής ύλης ήταν το επίκεντρο αυτής της διδακτορικής διατριβής. Με τη χρήση της ρεολογίας και της τεχνικής σκέδασης φωτός μελετήθηκαν διάφορα κολλοειδή υπερμοριακά συστήματα υπό το πρίσμα των μεταπτώσεων σε διαφορετικές καταστάσεις, ιδιαίτερα κατά τη δημιουργία πηκτωμάτων ή υαλωδών δομών. Μελετήθηκαν οι επιπτώσεις της μεταβολής των μοριακών χαρακτηριστικών πολύκλωνων αστεροειδών πολυμερών όσον αφορά τις διαρθρωτικές αναδιατάξεις στη δομή των διαλυμάτων υπό διάτμηση. Για αυτό το σκοπό, ορίσαμε μια παράμετρο χαλαρότητας και διερευνήσαμε την επίδρασή της στην δομή των συστημάτων. Ερευνήσαμε την επίδραση των παραμέτρων του διατμητικού πεδίου κατά τη διαδικασία της κρυστάλλωσης και προσπαθήσαμε να συσχετίσουμε τη σταθερότητα των δομών με την χαλαρότητα των μορίων. Η ικανότητα των μορίων να παραμορφώνονται επιτρέπει στα συστήματα να αναδιαρθρώνονται έτσι ώστε να αντιμετωπίζουν αποτελεσματικότερα τα εξωτερικά ερεθίσματα. Αναδείξαμε τις διαφορές μεταξύ χαλαρών συστημάτων και σκληρών σφαιρών και τονίσαμε την πολυπλοκότητα που παράγεται από την χαλαρότητα των συστημάτων.

Στη συνέχεια διερευνήσαμε την αυτό-οργάνωση δυο συμπολυμερών σε πολυμοριακές δομές, ως αποτέλεσμα της ταυτόχρονης ύπαρξης υδροφιλίας και υδροφοβίας εντός της δομής του μορίου. Η μεταβολή του σχήματος του υδρόφιλου τμήματος των μορίων δημιουργεί σημαντικές διαφορές στις υπερμοριακές αυτό-οργανωμένες δομές. Σε μεγάλες συγκεντρώσεις αυτά τα συστήματα σχηματίζουν πηκτώματα. Η ελαστικότητα αυτών των πηκτωμάτων αυξάνει ραγδαία ως συνάρτηση της συγκέντρωσης υποδεικνύοντας την ύπαρξη αλληλεπιδράσεων μεταξύ των υπερμοριακών δομών. Ακόμα καταγράψαμε το μικρό χρόνο που χρειάζεται το πήκτωμα να επανέλθει στην αρχική του κατάσταση μετά την επιβολή μεγάλων καταπονήσεων και αποδώσαμε το γεγονός αυτό στην ακεραιότητα

των υπερμοριακών δομών ακόμα και σε μεγάλες καταπονήσεις. Με προσεκτική ρύθμιση των υδρόφοβων και υδρόφιλων αλληλεπιδράσεων μπορούμε να ελέγξουμε τις κινητικές ιδιότητες των αυτών των συστημάτων και να μιμηθούμε τη φύση στη δημιουργία υπερμοριακών δομών.

Έπειτα μελετήσαμε τη ρεολογία δύο υδρο-πηκτωμάτων τα οποία συντέθηκαν με απώτερο σκοπό τη στοχευόμενη φαρμακευτική αγωγή σε καρκινικούς παγκρεατικούς ιστούς. Η ρεολογική εξέταση των πηκτωμάτων έδειξε μεγάλη εξάρτηση σε pH και θερμοκρασία, καθώς ότι τα πηκτώματα υγροποιούνται και ρέουν με την μείωση του pH ή την αύξηση της θερμοκρασίας. Ερευνήσαμε τη θιξοτροπία των πηκτωμάτων μέσω της καταγραφής του χρόνου που απαιτείται ώστε το πήκτωμα να επανέλθει στην αρχική του κατάσταση μετά από επιβολή ισχυρής διατμητικής ροής. Η επανάκτηση της αρχικής τους δομής ήταν άμεση και για τα δύο συστήματα. Η ευαισθησία στην θερμοκρασία και το pH, αναγάγει αυτά τα πηκτώματα σε εξαιρετικούς υποψήφιους για ιατρικές εφαρμογές προσφέροντας ευκαιρίες για σημαντικές ανακαλύψεις σε αυτόν τον σημαντικό τομέα.

Επιπλέον, εξετάσαμε τις μετασταθείς καταστάσεις σε μείγματα που αποτελούνται από δύο διαφορετικά είδη σωματιδίων. Το πρώτο είναι ένα πολύκλωνο αστεροειδές πολυμερές ενώ το δεύτερο είναι μία σκληρή κολλοειδή σφαίρα με τέσσερις φορές μικρότερο μέγεθος. Το σύστημα παρουσίασε πολλές διαφορετικές δομές και μεταπτώσεις ως αποτέλεσμα της ωσμωτικής πίεσης που δημιουργείται με την αυξανόμενη συγκέντρωση των μικρών κολλοειδών σφαιρών. Καταγράφηκαν και μελετήθηκαν οι διαφοροποιήσεις της ρεολογικής συμπεριφοράς των διαφορετικών δομών. Στα πειραματικά αποτελέσματα προστέθηκαν θεωρητικές αναλύσεις και αποτελέσματα προσομοιώσεων ώστε να αναδειχθεί η αξιοπιστία των συμπερασμάτων μας.

Συμπερασματικά, η χαλαρότητα είναι άμεσα συνδεδεμένη με ύπαρξη μετασταθών καταστάσεων. Η επιβολή διατμητικής τάσης μπορεί να οδηγήσει τα χαλαρά συστήματα σε αναδιάρθρωση των δομών τους. Η αναδιάρθρωση αυτή εξαρτάται άμεσα από τα

μοριακά χαρακτηριστικά του εκάστοτε συστήματος. Έτσι, με προσεκτική ρύθμιση των φυσικών παραμέτρων των συστημάτων μπορούμε να προσδιορίσουμε τη ρεολογική συμπεριφορά τους.

1. Introduction

1.1. Basic properties of soft matter

In the last few decades, the broad topic of Soft Matter has drawn huge attention, mostly due to the industrial applications. The need for intelligent and effective materials to respond to new, challenging questions raised from social, economical and global changes have multiplied the research on this field. Developments in technological instruments along with progress in experimental methodologies have led to deeper understanding of the theoretical background of soft matter as well as improvements on it. The really unique properties of this kind of materials merge knowledge of various scientific fields, such as physics, chemistry, biology or engineering, therefore, a combination of many specialties are needed for a deeper investigation of these systems.

There are many reasons for this; firstly, soft-matter systems are essential in many technical applications ranging from paints to lubricants and drilling fluids [1, 2]. Moreover, the importance of deformative behavior of soft particles has been recognized in many research areas, such as drug delivery and colloidal dispersion [3], rendering such systems omnipresent in medical and pharmaceutical applications [4]. Furthermore, soft-matter systems play a key role in biological problems such as DNA recognition [5, 6] transport through cell membranes [7] and protein crystallization [8, 9]. In conjunction with all the above, soft materials are finding applications in areas ranging from microfluidic device technology to nanofabrication [10].

Progress in material science stimulates the economy and greatly influences the living standards of the society. Intelligent materials are based on a new concept where the information science is introduced to the material. Using new preparation methods, by a combination of supramolecular constituents one is able to compose ‘intelligent’ materials with novel properties [11, 12]. The use of strong and directional interactions among

molecular subunits can achieve not only rich dynamic behavior but also high degrees of internal order that are not known in ordinary polymers [13]. Such materials respond in an remarkable way to external stimuli, such as external fields, pH changes, pulses of light or temperature jumps, and owe their multi-functionality to their unique structure [14]. The wide applications of these materials are attractive in a range of fields, including sensing [15, 16], drug delivery [17], electronics [18, 19] and vibration control [20].

Besides the '*soft'* materials with applications in advanced areas, similar materials dominate different aspects of our daily life; glues, paints, inks, shampoos, toothpastes, soaps along with many polymer melts which are molded and extruded to form plastics. The term used to define this kind of materials was introduced by Pierre-Gilles de Gennes in the 1970s, and is referred as *Soft Matter*. Another term, widely used in the literature, for addressing such materials is the term Complex fluids. Also, other terms, such as colloidal suspensions or colloidal dispersions, have been used to describe soft matter materials [21].

Soft matter includes a large range of materials such as polymers, colloids, emulsions, foams, liquid crystals, surfactants and various solutions of macromolecules. All these systems can be viewed as physicochemical which have large response functions [22]. Soft matter systems can exhibit a drastic change in their mechanical, optical and electrical properties resulting from the mild chemical or conformational changes in their structures [23]. Their complexity has raised a novel variety of physical problems which makes extremely difficult the task to define them with precision [24]. The key characteristics, that these materials share, are: a) the effect of the small length scales between the atomic sizes, b) fluctuations and Brownian motion, and c) the ability to self-assemble [25]. Starting with the length scales of the particles, the key parameter to understand soft systems is their mesoscopic size [21, 22]. Soft systems exhibit higher sensitivity to mechanical deformations compared to pure molecular materials [26]. The reason for this

phenomenon is that many procedures involving soft particles react on dynamics and structural arrangements on mesoscopic scales [27]. The small size of the structures enhances the importance of the particle fluctuations (Brownian motion) due to the comparable energy from the bonds of structures with the thermal energies [25]. Moreover, self assemble is a process driven by the principles of thermodynamics [28], which leads to lower energy structures or patterns. There are three basic principles for exploring different length-scales in self-assembling structures: a) the competing interactions and sequences, b) entropic frustration and topological dereliction, c) the spontaneous selection of primary length scales [29]. The definition of the term (self-assemble) highlights the absence of human intervention [30] and denotes that this is the way of nature to form large structures [31]. The sophisticated use of self-organizing materials, which include liquid crystals, block copolymers, hydrogen- and π-bonded complexes, and many natural polymers, may hold the key to developing new structures and devices for many technologically advanced industries [29].

For deeper studying of soft matter, we have to draw our attention in the *intermolecular forces*. The strength and the range of such forces, control the basic properties of matter [25]. The origin of these forces is the balance of repulsive interactions at short distances and attractive interactions which are present on larger length scales [32]. The nature of the attractive interactions is dependent on the system. The main categorization of such forces comes from their comparison to the thermal energy k_BT. When the bonds energy is much higher than the thermal energy then these bonds can be thought as permanent or chemical. On the other hand, when then bond energy is comparable to thermal, then these bonds are called temporary or physical. Physical bonds can be separated in different categories depending on their nature. These categories are:

- **Van der Waals bonds**, which energies are in the same order as the thermal energy (k_BT) at room temperature. The potential U_W between two molecules is

given by $U_W \sim \frac{\alpha^2}{r^6}$ where α is the polarisability of each molecule and r is the distance between them.

- **Ionic bonds**, which energies are two orders of magnitude larger than the thermal energy. This bonding occurs from exchanging electrons between the molecules. The Coulomb potential between the ions is given by $U_C = \frac{q_1 q_2}{4\pi\epsilon_0 r}$, where q_1, q_2 are the ions charges, ϵ_0 is the permittivity of free space and r is the distance between the molecules.
- **Covalent bonds**, which energies are, also, a couple of orders larger than the thermal energy. This bonding occurs due to the electron transfer from one atom to another.
- **Metallic bonds**, which energies are similar to covalent bonds but their origins differ. While in covalent bonds the electron dislocation takes place between two or small number of atoms, the same dislocation in metallic bonds take place in a much larger volume in the material.
- **Hydrogen bonds**, which energies vary in orders between the Van der Waals and the covalent bonds. This bond is formed when a hydrogen atom is covalently bonded with an electronegative atom.
- **Hydrophobic interactions**, which are about one order larger than the thermal energy. Such interactions are the result of the decrease of entropy, as nonpolar molecules, which cannot participate in the hydrogen bonding, are "caged" by water molecules.
- **Other noncovalent bonds**, such as π-π, anion-π or cation-π interactions. In general π stacking refers to attractive, noncovalent interactions between aromatic rings, since they obtain pi bonds.

By varying temperature, pH, ionic strength etc, the ratio between the intermolecular forces and thermal energy changes, thus phase transitions occur from glass to liquid or from liquid to gas and vice versa. While for condensed matter is easier to classify the phase of the material between glass and liquid, we cannot argue the same for the soft matter. In contrast to normal condensed matter, which shows two distinct phases, solid (crystalline ordered) and liquid (disordered), in soft matter such a classification is not so straightforward. Soft matter exhibits characteristics of both states. In a simple fluid state the molecules may freely exchange positions, so that their new positions are permutations of their old ones. In a solid state, the positions are fixed, so the position exchange is blocked. However, soft matter is a fluid in which large group of molecules have been constrained so that the permutation freedom within the group is lost [33]. For example, a large number of elementary molecules can be fastened together to create a flexible chain or a rigid rod.

Physical matter might exist in different forms or phases that differ by the type of order, mass density, etc. Materials components can be ordered in a complicated way, exhibiting features at length scales intermediate between the atomic and macroscopic. Disordered, solid-like materials are ubiquitous in soft condensed matter [34]. Such materials are often acquired from a fluid-to-solid transition which drives the system in a non-equilibrium configuration. For these systems that share features of structural disorder and metastability [35], a continuous evolution of mechanical and dynamical properties is observed [36]. It would not be extravagant to state that the most striking feature of soft matter is its ability to create new forms of matter with properties we could only dream of a few decades ago. Softness offers an incredibly large range of flexibility for tuning the properties of the system by manipulating interactions and controlling chemical and physical parameters of the system [37]. A profound theoretical understanding is needed more than ever to provide an insight into the basic principles and mechanisms of phase

transformations. Although bulk phase transitions of soft matter have become well understood, important questions in confining geometries and additional external fields are still open [26]. The motivation to study the influence of external fields has two main sources. Firstly, by definition, soft matter reacts sensitively to external perturbations and manipulations. While this particular behavior has been exploited empirically in many different technical applications, there is still a wide unclarified area to be discovered. Secondly, by controlling and tailoring the external perturbation, qualitatively novel effects can be induced. The final goal is to systematically control properties of colloidal matter by using external fields.

Examples of such external fields are Laser-optical fields [38, 39], magnetic fields [40, 41], electric fields [42, 43] and flow fields [44]. In particular, soft systems, driven far from equilibrium by application of shear, have received widespread attention. The reason for this is the high difficulty in connecting the rheology with the structure and dynamics in soft materials. The main roots of these problems come from the fact that frequently the flows are heterogeneous along with the abscess of a steady state under perturbation [45]. While one would expect that shear would favor disordered states [46-48], there are many studies which claim the inverse effect i.e. shear-induced ordering even though the system displays a disordered state at equilibrium [49-51]. The structural phases depend on the strength of flow in a way that microstructure re-arrangements take place in order to accommodate the applied hydrodynamic forces [52]. At high volume fractions the interactions between the particles become comparable to hydrodynamic forces leading to anisotropic microstructural organizations. A detailed explanation of that process is still unclear, but shear rate has been added as a control parameter to the already known ones, such as temperature, pressure or chemical potential [46, 49, 50].

A lot of theoretical and experimental research on complex fluids (ranging from polymers to surfactants and from colloids to granular materials) has been conducted to

investigate the way in which a system transforms from ergodic to non-ergodic and vice versa [53, 54]. There are many terms for describing this phase transition like jamming, freezing, coagulation, glass formation, gelation kinetic frustration or structural arrest [55-57]. However, the differences of these types of non-ergodic states are rather significant from many aspects [58, 59]. The mechanisms that each time drive the systems to arrested structures are completely different, despite the similarities in the dynamic responses of such systems [60]. The relationship between the kinetic slowing down and growing dynamic heterogeneity is a key problem of the liquid–glass transition [61].

Unfortunately, a wide experimental exploration of these phenomena is not feasible due to the limited range of length and timescales that can be probed [44]. A number of experimental techniques have been employed to investigate the structure and the performance of soft matter systems.

- For structures larger than 1μm, ***microscopy and surface*** probes have proved to be useful techniques for identification and characterization of nano-/mesoscale structures. On the other hand, such techniques face serious resolution limitations as structural analysis methods.
- For structures smaller than 1μm, ***light scattering methods*** have been employed to determine particle size and investigate structures and crystallinity of soft matter systems.
- Different ***spectroscopic techniques*** have utilized in characterizing soft matter. Such methods provide information about the local microstructure, orientational orderings, chain branching, tacticity and dynamic mechanical properties when the materials are probed at very high frequency range.
- ***Rheology*** is the method for investigating the mechanical deformation and flow characteristics of soft matter under stress.

1.2. Examples and applications of soft matter

A deeper look in soft materials is necessary to highlight their characteristics and the advantages comparing to common materials.

- ***Liquid crystals*** are, as the name reveals, individual crystals in a liquid matrix. They constitute a fascinating class of soft condensed matter characterized by the counterintuitive combination of fluidity and long-range order [62]. The unique subtle balance between order and fluidity that characterizes liquid crystals is not only deeply intriguing from a scientific point of view, but, also, it gives rise to a broad range of spectacular phenomena that are yet fully explored. Liquid crystals contain an in-between state of order with various forms of arrangement. These arrangements are called *smetic* or *nematic* or *chiral*. The nematic crystals are only arranged along a similar axis while the crystals are randomly oriented. The chiral, (or cholesteric) orientation is made up of layered nematic crystal levels. This orientation does not have any symmetry and can only form with molecules that are chiral in structure. Finally, smetic crystals are loosely ordered in columns and rows. Smetic crystals can take two orientations, one with a linear arrangement and one with the structural row being tilted at an angle theta from the normal axis [25].

  Today they are best known for their exceptionally successful application in flat panel displays, but they actually exhibit a plethora of unique and attractive properties that offer tremendous potential for fundamental science as well as innovative applications well beyond the realm of displays [63]. One of the more common applications of liquid crystals is a liquid crystal display, or LCD. LCDs are an integral to today's technology based society, as they are present in most electronics including cell phones, computers, calculators and televisions.

- ***Polymers*** are the sequence of monomers, covalently bonded, composing large macromolecules. They can be divided in two categories, homopolymers and copolymers. Homopolymers are consisted of the same repeating unit while copolymers can have two or more different repeating units. Polymer chains can be structurally bonded in different ways resulting in linear, branched, crosslinked and network polymers. When the amount of crosslinking or network forming is high, then we have a structure called ***gel***.

  Specifically, microgel particle dispersions have many applications in surface coatings industry [64]. Such dispersions are shear thinning and provide good rheological control for automotive surface coatings [65]. Due to these characteristics, microgel systems are also widely used in the printing and pharmaceutical industries. Gels dispersed in water are called hydrogels and constitute a special category that plays a huge role in specific drug delivery. Their high water content makes them highly biocompatible [66] and their high flexibility makes them similar to natural tissues.

- ***Colloids*** are systems of particles with size less than 10 microns, dispersed in a liquid matrix. Depending on density, colloidal particles vary from nanometers to microns in size large enough to exhibit random Brownian motion, perpetuated by collisions with solvent molecules, and yet small enough to remain indefinitely suspended against sedimentation [67]. Comparing colloids to other soft matter systems, they play a particular role as they can be prepared and characterized in a controlled way [26]. The intricate multiscale structures of colloids result from the extremely complex interplay of different competing enthalpic and entropic intermolecular forces, some short range such as van der Waals and steric forces operating on the length scale of angstroms (A˚), and others long range including electrostatic interactions and entropic effective forces which operate over much

longer length scales [68]. The effective interaction between the colloidal particles can be tailored by changing system parameters, like macro-ion properties (size, charge, composition), and solvent properties (salt concentration, pH, dielectric constant, temperature) [21, 67]. The basic understanding of these mesoscopic interactions derives the control of an enormously rich equilibrium and dynamical properties displayed by such systems.

Colloidal particles have been extensively used as the major components of industrial products, such as foods, inks, paints, coatings, papers, cosmetics, photographic films, and rheological fluids [69]. Monodispersed systems have emerged as the material of choice for a wide variety of nice applications that range from nanopatterning to fabrication of photonic devices [70]. Moreover, when anisotropy is introduced in the system, its physical properties start to differ from the symmetrical ones [71]. This makes them highly desirable for controlling light scattering and fluid properties [72-74] and for engineering biomaterials [75, 76] and colloid structures [77, 78].

- ***Emulsions*** are heterogeneous dispersions of two immiscible liquids which are susceptible to rapid destabilization by aggregation, coalescence, or flocculation, leading to phase segregation [79]. The stability of these emulsions can be improved by adding surfactants that are able to coat the droplets of the dispersed liquid and prevent them from joining together due to the decrease of the interfacial tension between the immiscible liquids and the increased repulsion between the droplets. Their characteristics can be easily tuned by adjusting parameters such as volume fraction of the dispersed phase, droplet size, or osmotic gradient [80]. Moreover, emulsions can be produced in very large quantities by means of suitable methods [81].

Emulsions are flexible drug formulation systems [79]. Many applications of emulsions and microemulsions involve their interactions with surfaces. The adsorbed surface layer may be no more than a surfactant monolayer, but this may already be enough to change the wettability properties of the surface [82]. Emulsions have many applications in industries with the more pronounced ones to be in milk and dairy, food, pharmacy, chemotherapy, cosmetics and agriculture industry [83].

- ***Foams*** are systems of disordered gaseous bubbles of varying size in a liquid or solid matrix. The single gas inclusions are separated from each other by portions of liquid or solid [84]. Liquid foams can be seen in everyday life, from frothy bubbles in a morning coffee to soap used to clean one's hands. Solid foams can be classified as open cell, when their pores are interconnected and closed cells when the cells are entirely enclosed by liquid or solid and are not interconnected. Both structures have good insulative properties which can be manipulated by filling the pores. They are frequently stabilized by surfactants, polymers or by particles. If the particles have a moderate hydrophobicity, the foams can be extremely stable (lifetimes of the order of years) [85]. Aqueous foams have the capacity to adjust dynamically their channel size over several orders of magnitude, in response to changes in interstitial liquid flow conditions [86].

  Foams are of great practical interest because of their extensive occurrence in food, pharmaceutical and cosmetic industry. The main reason for their wide application is their ability to combine physical and mechanical properties, such as high stiffness in conjunction with very low specific weight or high gas permeability combined with high thermal conductivity. Among man-made cellular materials, polymeric foams are currently the most important ones with widespread applications in nearly every sector of technology. Less known is that even metals

and alloys can be produced as cellular materials or foams and that these materials have such interesting properties that new exciting applications are expected in the near future. Example of metallic foams applications is the utilization of oxide particles as stabilizers [87]. Worth to note is that foams have already been extensively used in applications such as flotation of mineral particles in which the bubble surfaces are covered by particles [88].

1.3.Softness

The soft material's adaptive nature is directly connected with the metastabilty which is often seen in these systems. Figure 1.1 shows the influence of softness on the state transitions at different volume fractions. Comparing hard spheres (Fig. 1.1a) with softer systems (Fig. 1.1b-d), we observe the shift of the metastable states towards higher volume fractions. For example, jamming occurs in much higher concentrations in soft star systems where the compressibility of the particles allows them to accommodate better the increased osmotic pressure by adjusting their volume and shape [89]. Fluid phase expands along with softness, highlighting the polymer coil behavior which remains ergodic throughout the whole window of volume fractions. Moreover, the crystal region seems to decrease and finally, disappear, along with the softness increase. This fact is attributed to the arm interpenetration, for the hairy particles, and their fluctuations beyond the limit set by the Lindeman criterion [21, 37, 90]. However, it has been reported that star glasses can crystallize due to the damping of their large cores fluctuations [91, 92]. Also, external perturbation can promote local rearrangements and eventually lead the system to crystallization [91-93]. In general, the effective volume fractions, where the transitions are observed, depend heavily on softness and become less distinguishable as we diverge from the hard sphere behavior.

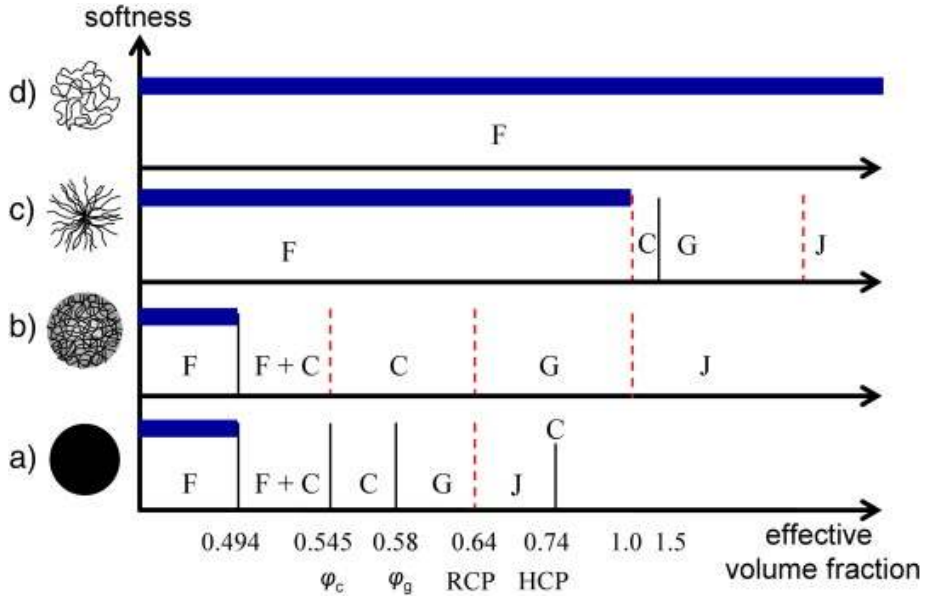

Figure 1.1. *Schematic one-dimensional state diagrams of nearly-monodisperse athermal soft colloidal suspensions, as function of their effective volume fraction. The numbers are values for volume fractions of hard spheres; values above 0.74 are relevant only for soft systems. From bottom to top the diagrams of a): hard spheres, b): microgels, c): star polymers and d): polymeric coils are shown. Letters refer to different regions: fluid (F, the blue-shaded regions), crystal (C, at* $\phi_C = 0.545$ *for hard spheres), coexistence (F + C, above volume fraction 0.494 for hard spheres), glass (G, at* $\phi_g = 0.58$ *for hard spheres), and jammed (J). RCP and HCP are the random close packing and hexagonal close packing volume fractions, which for hard spheres are determined to be 0.64 and 0.74, respectively. The solid black vertical lines represent established transitions (even if occurring at different volume fractions for different systems) whereas red dashed lines represent transitions whose universality is still debatable. The values of the volume fraction in the horizontal scale are indicative and do not respect the actual scale. Taken from Ref. [89].*

Apart from softness, metastability is characterized by factors such as phase sizes and kinetics, which require further consideration. First, we need to understand both the thermodynamic and kinetic limits of metastable polymer systems in which the classical, sharp conceptual boundary between thermodynamics and kinetics may not apply. This requires fundamental theoretical development along with experimental work to support theory and simulations. There is a strong demand to describe quantitatively the metastable states and metastability in polymer systems based on macroscopic experiments. Perhaps, this is not difficult for determining crystal sizes and glass structures, but it might be more complicated in other systems, such as gels. Furthermore, it will be harder to study

systems, which approach single molecular sizes by using conventional experimental methods. Novel developments are necessary for this purpose. Mixing different types of molecules makes the problem even more complicated but offers, also, the great opportunity for tailoring systems properties.

1.4. Metastability

The free energy landscape of a complex system, i.e. soft, presents an intricate aspect consisting of multiple local minima, separated by energy barriers. The concept of metastability is intimately linked with the existence of energy barriers in thermodynamics. These metastable states are the result of local minima in the free energy landscape which, although they do not fully minimize the free energy of the system (and therefore do not appear in the equilibrium phase diagram), may be encountered as an intermediate stage (Fig. 1.2). They may be long-lived, especially if the system must overcome high energy barriers in order to reach its global minimum [94].

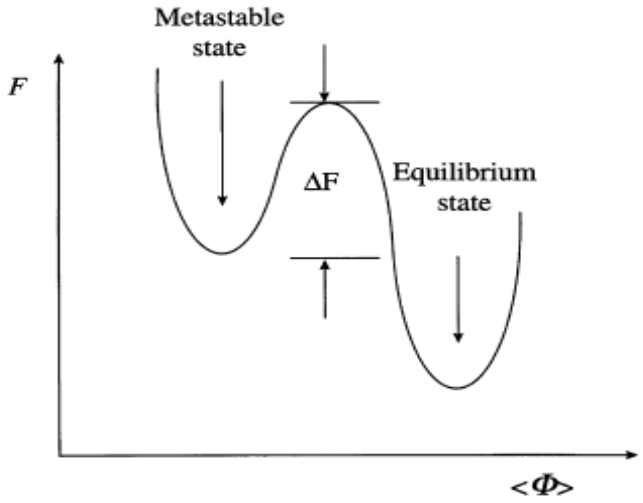

Figure 1.2. *An illustration of a metastable state in a plot between free energy (F) and order parameter (<Φ>). The ΔF is an activation barrier. Redrawn from Ref. [95].*

Many materials can be found in metastable states upon sudden change of temperature as for example during phase transitions. From a thermodynamic approach, the basic

parameter responsible for phase transitions is the free energy and its variations. Landau [96], was the first one to express free energy as a function of temperature (T), pressure (P) and the degree of order (ξ), $G = G\,(T, P, \xi)$:

$$G = G_0 + a\xi + \beta\xi^2 + \frac{1}{3}\gamma\xi^3 + 0(\xi^4) \qquad 1.1$$

where P, T, and ξ are the independent variables that determine the free energy and a, β and γ are functions of pressure and temperature. Some examples of phase transitions are given in Figure 1.3. The thermodynamically stable and metastable states show minimums ($\partial G/\partial\xi = 0$), while the isotropic phases (or in general the lack of order) is defined as: $\xi = 0$.

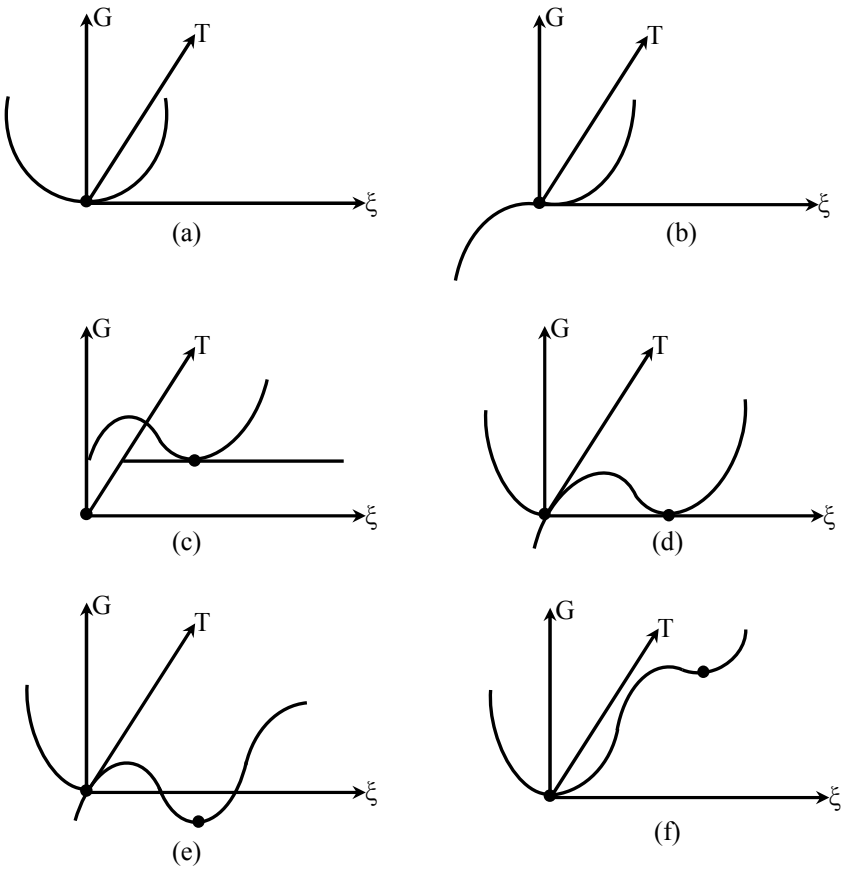

Figure 1.3. *The temperature (T) and ordering (**ξ**) dependence of free energy (G) for some examples of ordering-disordering transitions: (a) thermodynamically stable isotropic phase* $\partial G/\partial\xi = 0$, $\xi = 0$*), (b) critical point (*$\xi = 0$, $\partial G/\partial\xi = 0$, $\partial\,\partial^2 G/\partial^2\xi = 0$, $\partial^3 G/\partial^3\xi = 0$*), (c) stable ordered phase* $\partial G/\partial\xi = 0$ *and* $\xi \neq 0$*), (d) order-disorder transition in equilibrium (*$\xi = 0$ *and* $\xi \neq 0$*), (e) thermodynamically stable ordered phase (*$\xi \neq 0$*) and metastable isotropic phase (*$\xi = 0$*),(f) thermodynamically stable isotropic phase (*$\xi = 0$*) and organized metastable phase (*$\xi \neq 0$*).*

The co-existence of more than one phases is not forbidden as Figure 1.3d shows. Different structures may have the same free energy for the same values of temperature and pressure and this allows the system to display properties of both phases. Furthermore, by small perturbations, metastable structures change towards lower free energy orders, thus a qualitative changes of structure take place responding to quantitative changes yielded from external fields.

The nature of the barriers depends on which thermodynamic potential varies when passing from one well to the other, and their presence plays an important role in the dynamics of the system [97]. Whereas energy barriers are more frequent in problems of solid state physics, entropic barriers, attributed to kinetic limitations, are often encountered in soft condensed matter. In soft materials, thermal motion alone is not enough to achieve complete structural relaxation. The system has to cross energy barriers which are very large compared to typical thermal energies [98].. In many cases, many interesting structures rise during that process which are not at the equilibrium but can be effectively frozen. For attaining the optimum energy state, atoms and molecules have to rearrange themselves, a process that might be very long. In terms of statistical mechanics, the atoms or molecules of the system have a larger probability (due to the limited average fluctuation amplitude) to choose a pathway which possesses a lower energy barrier regardless the thermodynamic stability after the barrier is overcome. In other words, these atoms and molecules are 'blind' and cannot predict the thermodynamic outcome behind the energy barrier [95].

In fact, many "ordering"-transitions that are usually considered to be energy-driven, may be entropy driven. Indeed many transitions may seem to decrease the entropy because the density is no longer uniform in orientation or position, but the total entropy increases because the free-volume per particle is larger [99]. While first- and second-order transitions are typically reversible by changing the temperature, transitions

from a metastable to a more stable phase are not [100]. The rich morphology is the main characteristic of soft matter which often exhibits complex and interesting transitions between equilibrium phases. As a result, there is always a delicate balance between the entropic and enthalpic contributions to the free energy, both contributions playing an important role in the properties of soft materials [101].

1.5. Goals of the thesis and organization

From the above it is evident that linking metastability transitions and softness is an emerging topic of great scientific value and technological significance. Several open and hard questions make it challenging to address those issues. Firstly, we need to enlighten our knowledge on parameters that affect softness. For example, how is system's softness changing by varying concentration, temperature and geometrical characteristics of the molecules? Secondly, a crucial area to be investigated is how softness hinders ordering and ways to overtake its effects. Ordering in hard systems has been widely studied and proved to be a quite simple process [102]. However, crystallization of soft systems proves to be much more challenging. Kinetic boundaries and molecular characteristics reveal high barriers towards equilibrium states. The results of this investigation may illuminate the narrow boundaries between thermodynamics and kinetic limits in soft metastable systems.

Moreover, the questions are extended to the roots of metastability in more complex structures, such as gels. Attraction may be the driving force in these systems, but the origin of it, is still a wide area for investigation. Understanding the roots of attraction will enable us to control responsiveness of such systems to external field perturbations.

There is still a lot of work to be done by linking metastability with system's complexity. The richness of phases in mixtures has been studied in the past, but it still

remains not fully understood. Size ratio, softness, molecular characteristics are variable parameters which adjust responsiveness and properties of these systems.

The main scope of this work is to elucidate the rheological and the structural state transitions of soft systems with respect to softness, shape and size of colloids. This study, also, focuses on the effects of external fields on the structural and mechanical properties of soft systems. There is a wide range of rheological states explored, extending from liquid-like to gel, glass, double glass structures. We focus on kinetic transitions, induced by shear and thermodynamic (depletion) forces, and discuss properties of star glasses and gels. All the systems investigated in this thesis are metastable and exhibit structural rearrangements upon the variation of systematic parameter such as concentration, temperature, depletion, etc.

A large part of this work is based on the development of appropriate experimental protocols for addressing specific problems associated with the properties of model soft systems such as star polymers. The properties which make such systems ideal for research are described in the following chapters. Chapter 3 focuses on the effects of an external shear field on pure star system. Metastable transitions between kinetically arrested and ordered-disordered states were observed and studied in order to illuminate the course of a soft system towards the final equilibrium state. Chapter 4, 5 try to enlighten the natural way of creating large supramolecular structures. Based on the hydro-preference and molecular partial ordering, the system can become pH, thermo and shear responsive. Such systems display strong concentration dependence forming stable networks mostly due to the chemical nature of crosslinks. Chapter 6 describes more complicated systems composed of two different polymers. The shape, size and concentration of each polymer affect the rhelogical state of the system, driving it to many metastable states, just by varying these parameters.

2. Systems-Methods

The following chapters describe different projects, which include similar systems, but have different scopes. In the following lines of this chapter, we will give some short descriptions of the particles properties formatting different systems and methods as applied in the experiments.

2.1. Star polymers

Soft star polymers were utilized to accomplish about 50% of the work presented in this thesis. One of their main features is their ability to combine both polymeric and colloidal characteristics. The high number of linear homopolymer arms joined covalently to a central core give polymeric characteristics to the molecule, while the core itself stands for the colloidal part [103]. Hence, star polymers can actually be viewed as hybrids within polymer-like entities and colloidal particles establishing an important link between these different domains of physics [104]. This unique feature of star polymers results in novel structural and dynamical properties which have been seen in neither the single-chain polymers nor in colloidal spheres [105]. Such properties are attributed to their softness, which can be tuned either at the synthesis level (number of arms, arm degree of polymerization) [21, 106] or by varying solvent and temperature [104, 107].

Due to their topology, star polymers exhibit a nonuniform monomer density distribution [108, 109] and as such, they can be considered as effective core-corona particles with core radius $r_c \sim f^{1/2}$ and overall particle radius in good solvent $R \sim f^{1/5} N_a^{3/5}$. According to the classic Daoud–Cotton model [108], the blob size of a star in a good solvent increases with the radial distance r and three monomer density regimes are distinguished: a) the inner melt-like core regime, b) the intermediate theta-like regime, where the blobs are ideal and only solvent can penetrate in a dense suspension (c > c*),

and c) the outer excluded volume regime, where the blobs are swollen and star–star interpenetration can take place in dense suspensions. Figure 2.1.1 illustrates these regimes for a star in a good solvent along with the monomer density profile$\Phi(r)$.

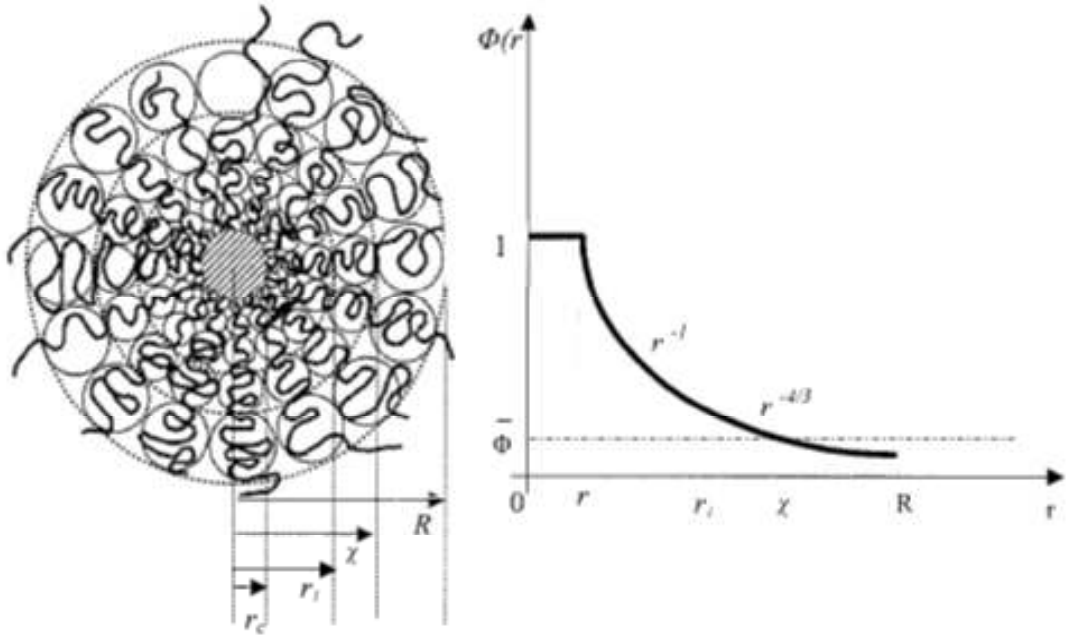

Figure 2.1.1*. Schematic representation of the internal structure of a single colloidal star polymer in a good solvent and its nonuniform monomer density profile. Taken from [60].*

By varying the number of the arms (f) and the degree of polymerization (N_a), the particle softness varies from hard particle limit at large f and small N_a, to polymer coil limit at small f and large N_a. In dense suspensions, these systems exhibit some very intriguing features which are universal for similar systems with soft interaction pair potentials [60]. These unique molecular characteristics constituted the stars a first choice candidate to explore the softness effects on metastability. A rich variety of rheological states will be presented in the following chapters.

2.2. Gels-Hydrogels

The need of studying metastability in attractive systems led us to employ hydrogel systems. A gel can be defined as an intermediate state between a liquid-like and a solid-like rheological behavior [110]. It consists of a dispersed phase (polymers or colloids) together with a dispersing medium (water or other solvents), and can be very close to a liquid or to a solid. The liquid-like properties come from its major constituent, water or other solvents. The solid-like behaviors are own to the network which prevents the system from flowing. In solutions, the particles can easily diffuse, while in gel structures their motion is restricted. However, this definition can be applied only to chemical gels because in physical gels parts of polymer networks can interchange among them [111, 112].

The most widely accepted gel classification is the one based on the nature of the bonds. For chemical gels, the crosslinking region is formed by covalent bonds while for physical gels, this region is formed by hydrogen or ionic bonds and hydrophobic interactions [110]. According to Tanaka [113], the gels could be classified in six categories depending on the structure of crosslinks: 1) simple gelation where one single component of a polymer forms a gel by pairwise crosslinking in a solvent, 2) gelation by multiple crosslinking where more than 3 chains are connected in the junction point, 3) gelation from two different polymers, which include interpenetrating networks, alternately crosslinked networks, randomly mixed networks, 4) gelation competing with hydration (solvation), and coexisting with hydration (solvation), where gelation is either blocked or accelerated by hydration, 5) gelation induced by polymer conformational transition such as coil-helix transition, coil-globule transition, coil-rod transition, 6) gelation coupled with liquid-crystallization, where hydrogen bonded mesogens form crosslinks.

From another point of view, the definition of a gel is highly affected by the environment in which the gel is placed. Physical environments, i.e. force fields, gravity,

electromagnetic fields, pressure, temperature, or biochemical environments i.e. pH, ionic strength, as well as coexistence of various small and large molecules, including enzymes, influence structure and properties of gels. Therefore the material can be a gel in an environment but it may turn into a liquid or a solid in another environment. The gel-solution transition has attracted much attention with respect to properties' and dynamic response's variations that the systems exhibit by varying parameters such as concentration, temperature, degree of crosslinking etc [114-117]. The definition of gels is closely related with understanding these phenomena and consequently crucial for applying gel technology in biomedical science. In particular, hydrogels are widely used in drug delivery applications thanks to their adaptability in different environments. However, producing hydrogels with specific properties and characteristics is still a very difficult task which and expectations are not always warranted.

2.3.Rheology

The dynamical properties of our systems were studied using stress and strain controlled rheology. Shear rheometry experiments included dynamic oscillatory measurements: a) Frequency sweep following an oscillatory strain $\gamma = \gamma_0 \sin \omega t$ in order to probe the viscoelastic relaxation spectrum, i.e., the frequency dependent storage (G') and loss (G'') moduli in the range 0.01 – 100 rad/s. The stress response is $\sigma = \sigma_0 \sin(\omega t + \delta) = \gamma_0(G' \sin \omega t + G'' \cos \omega t)$ with σ_0 being the stress amplitude and δ the phase angle ($\delta = G''/G'$); b) Strain sweep with a duration of about 8 min to determine the linear viscoelastic regime. It involves oscillations at constant frequency ω (usually 1 rad/s) and continuously increasing strain amplitude γ_0 from 10^{-3} to 3 strain units; c) Time sweep at low frequency (usually 1rad/s) and a linear strain amplitude, with duration long enough to ensure that steady state is reached.

For having reproducible and comparable measurements, these tests were proceeded by a time sweep at large strain amplitude in the nonlinear regime (usually at strain amplitude of 2 strain units) or steady shear measurements at different rates (from $1s^{-1}$ to $100s^{-1}$) in order to shear-melt the structure (rejuvenation process), and a subsequent linear time sweep in order to reach steady state (aging). This protocol allowed erasing the sample's history (possible residual stresses during sample preparation and loading) and ensuring reproducible initial conditions for the measurements. For viscous samples at low concentrations, where the dynamic signal was too weak, the zero-shear viscosity was determined from steady shear measurements (rate sweeps).

More specifically, a full sample characterization requires well defined non-linear measurements. Consequently, large amplitude oscillatory shear (LAOS) tests are used to investigate and quantify the nonlinear viscoelastic response of the samples. LAOS characterization is a rigorous test for rheological models and advanced quality control [118]. Therefore, LAOS tests were performed at given frequency and nonlinear γ_0 over long times in order to determine the response of the solutions in nonlinear deformations. The stress-strain amplitude representations (known as Lissajous-Bowditch plots) provide the acquired rheological information.

2.4. Dynamic Light Scattering

Dynamic light scattering experiments were conducted utilizing the photon correlation spectroscopy (PCS) technique [119] with the necessary spatiotemporal resolution. The PCS technique recorded the scattering intensity autocorrelation function $G(Q,t) = \langle I(Q,t)I(Q)\rangle/|I(Q)|^2$ over a broad time range (10^{-7}-10^{3}s) at different scattering wave vectors Q with an ALV-5000 goniometer/correlator setup (ALV, Germany) using an Nd:YAG laser at a wavelength λ = 532nm (Adlas, Germany). The magnitude of the

scattering wave is $Q = (4\pi n/\lambda)\sin(\theta/2)$ where n and θ are the refractive index of the solvent and the scattering angle, respectively. The measurements, both polarized (VV) and depolarized (VH) were performed by using polarized vertically (V) incident laser beam and selection of the scattered light either polarized vertically (VV-configuration) or normal (VH-configuration) to the scattered plane. Under homodyne beating conditions, the desired concentration relaxation function $C(Q,t)$ probing is computed from the experimental $G(Q,t)$:

$$C(Q,t) = \left[\frac{G(Q,t)-1}{f_{ins}^{*}}\right]^{1/2} \qquad (2.4.1)$$

where $f_{ins}^{*} \leq 1$ is an instrumental coherence factor. The analysis of $C(Q,t)$ was performed using the CONTIN software [120] and proceeded by its inverse Laplace transformation (ILT):

$$C(Q,t) = \int_{-\infty}^{\infty} L_Q(\ln\tau)\exp(-t/\tau)\, d\ln\tau \qquad (2.4.2)$$

with $L_Q(\ln\tau)$ being the distribution of relaxation times for a given wave vector Q or by the stretched exponential

$$C(Q,t) = exp[-t/\tau(Q)]^{\beta} \qquad (2.4.3)$$

where τ is the relaxation time and $\beta \leq 1$ is a measure of the width of the single distribution of relaxation times [121].

3. Shear-induced crystallization of colloidal stars with varying softness

It is well known that concentrated Brownian particles will either undergo a transition to an ordered phase or become dynamically arrested into a disordered state. Indeed, the classic example of colloidal spheres shows that they can form crystals or glasses depending on their size polydispersity and interaction potential. Beyond thermal motion in the quiescent state, the action of an external stimulus, such as shear flow, can aid the formation of ordered states or melt them, depending on its strength [26, 52]. In general, understanding the delicate interplay between interparticle forces and hydrodynamic interactions in Brownian spheres allows determining the conditions for achieving and tuning colloidal crystallization [49, 50, 52, 53, 122-127]. For example, shear flow can *enhance* crystallization of hard spheres at low fractions (by creating nuclei due to induced ordering [50]), as well as very high volume fractions (by breaking the jamming cages thus facilitating rearrangements [128]). On the other hand, shear flow can also *frustrate* crystallization either by eroding crystal nuclei during crystal growth or by deforming fully crystalline systems, which can be destroyed and yield to flow [46, 102, 129]. Such observations are often summarized in the form of non-equilibrium phase diagrams indicating the regions where crystals form in the particle volume fraction – imposed stimulus parameter space [49, 130].

Subsequently, it is evident that a powerful framework exists for investigating crystallization phenomena in colloidal dispersions. Whereas the majority of the experimental and simulation work has been performed with hard spheres, several recent results with soft colloids have been reported. Crystallization in soft colloidal systems is in general more complicated. It is known that microgel particles, or hard particles with microgel-like coats can crystallize at roughly the same volume fraction as hard spheres [105, 131-143]. In these systems, particle softness is manifested with shape adjustment at

contact and beyond (microgels) and/or weak interpenetration for hairy particles (however, with large core). Regarding micelles, often the arms can exchange and, for a rather short length of the solvophobic polymer block, these systems resemble crew-cut particles and crystallize easily [144]. When the core is glassy, e.g. styrene-isoprene block copolymers in isoprene-selective solvents, micelles with larger cores form face centered cubic arrays whereas more star-like structures order into body centered cubic crystals [105, 131, 133].

On the other hand, particles with small cores and long hairs, such as star polymers, would not crystallize easily, as polymeric hair interpenetration inhibits or delays this process. Recent simulations suggest that particles overlap, creating longer effective length scales for the inter-particle potentials, which slow-down the nucleation process [145] in contrast to HS where hydrodynamic interactions speed-up the crystallization process [146, 147]. The slowdown of the nucleation process can be also attributed to clustering, which can be regarded as effective polydispersity that suppresses the crystallization in soft micelle systems [148]. In these situations, soft colloids are often trapped kinetically in metastable states [55]. Colloidal glasses may crystallize over time, i.e. reach thermodynamic equilibrium, irrespectively of softness [92, 149].

Similar to the case of hard spheres discussed above, external stimuli, such as flow or temperature, can also induce crystal formation in soft colloidal systems [150-152]. Depending on the rates of applied oscillatory or steady shear, a rich variety of crystal phases, in such systems, are reported [153-157]. Recent studies in two dimensions indicate that shear can provide spatial modulation for particles in a supercooled state, leading to an acceleration of the nucleation process and an eventual ordering [158]. Crystals from block copolymer micelles with large cores are stable in the sense that they can sustain large deformations without melting [154, 157]. However, it is questionable to what extent this is due to the micellar character of these systems. In other words, if the architecture of the micelles and their ability to self-assemble are the key parameters that

drive the systems to ordered structures. For completeness we note that attractive microgels may crystallize due to a delicate balance between repulsive and attractive interactions [159].

From the above, it is evident that crystallization of soft colloids remains a challenging topic with several open questions. In particular, an important missing element is the ability to tune the properties of colloidal crystals (conditions for their formation and stability) by appropriately adjusting the pair interaction potential. This becomes a formidable task for material design where ideally one could synthesize systems and tune their structure. To this end, colloids with tunable interaction potential from soft to hard, are ideal candidates. In fact, star polymers represent a model soft colloidal system with behavior ranging between hard spheres and polymers, depending on their functionality f, i.e., the number of arms, and the arm degree of polymerization N [21, 60]. From the above discussion one can conclude that these ultrasoft colloids do not crystallize easily. In fact, mean-field predictions and molecular dynamics (MD) simulation results suggest that multiarm star polymers form crystals only in a narrow concentration window in athermal solvents [55, 90, 160]. Experimental confirmation of star crystallization under quiescent conditions has proven difficult, in part due to the fluctuations of the outer blobs of the arms [60, 107, 161]. Hence, crystallization was masked by glass transition at high star volume fractions [16]. This in turns meant that a long rest time is needed in order to potentially observe crystal formation, and true enough, MD simulations indicated that star glasses (and hard sphere glasses as well) eventually crystallize if aged for long time [92, 149, 162]. Experimental evidence by multispeckle dynamic light scattering (MSDLS) and small-angle neutron scattering (SANS) experiments supported this scenario and has opened the route for investigating the crystallization of star polymers [163].

Generally, shearing jammed *soft* systems is a complicated process since their original microstructures are non-equilibrium states and may undergo many phase transitions [27].

For hard sphere glasses, the applied shear flow provides the necessary energy for escaping from the kinetic traps [164]. However, softness yields a much richer viscoelasticity response, as seen for example in colloidal star glasses [165]. Here, the size and number of arms determine the interactions between particles, hence their viscoelasticity [160, 166, 167]. On the level of particle microstructure, it is primarily the interpenetration of the arms that is responsible for the complex rheological behavior of the stars [103, 168, 169], implying that shear could promote crystal formation of very soft stars via arm disengagement.

In this chapter we attempt to address the consequences of the softness interplay with the imposition of shear flow on the crystallization of star polymer solutions. By changing star softness via functionality and molar mass of arms, we specifically address the following questions: (i) Does shear flow enhance crystallization or not? (ii) To what extent can these soft systems support shear flow without losing ordering?

To achieve our goals, we employ star solutions of varying softness, i.e. relatively soft and hard star, as quantified by a softness parameter $SP = {R_{cor}}/{R_{sw}} = f^{3/10}N^{-3/5}$, where R_{sw} and R_{cor} are the radii of the swollen regime and the core in the Daoud-Cotton model, respectively [108]. We prepare star solutions at concentrations around the predicted crystallization phase boundary and apply an oscillatory shear field (with varying the amplitude and frequency of oscillations) or to steady shear flow, while detecting the structure of the dispersions *in-situ* by Small Angle Neutron Scattering (SANS). After introducing the systems and experimental technique, we present the results in two parts. In the first part we discuss the softer spheres with $SP = {R_{cor}}/{R_{sw}}$=0.11, where shear-induced crystallization will be described. In the second part, we report the crystal stability of hard stars with $SP = 0.31$.

Materials

We employed two different multiarm 1,4-polybutadiene (PBD) stars, whose synthesis is described elsewhere [106, 170]. Their molecular characteristics are listed in the table 1. We characterize the compactness, or inverse softness of the stars by means of the Daoud Cotton model [108]. Both stars meet the criterion for the swollen region, N≫ $f^{1/2}v^{-2}$, where v is the excluded volume of the monomer. At the level of the particle microstructure, the softness of a star can be quantified by the softness parameter $SP = {R_{cor}}/{R_{sw}}$, where $R_{sw} = N^{3/5}v^{1/5}f^{1/5}l$ is the radius of the swollen regime and $R_{cor} = f^{1/2}l$ is the radius of the core. This yields $SP = f^{3/10}N^{-3/5}$= 0.31 and 0.11 for H-Star and S-Star, respectively. Based on this, hereafter we term the two samples S-Star and H-Star as soft star and hard star, respectively; we emphasize the hard star is clearly apart from a hard-sphere colloid, it is however 3 times less soft than the soft star. Two solvents were used, deuterated toluene, which is nearly athermal and tetradecane, which is of intermediate quality.

The measurements in d-toluene were performed with the soft star at room temperature over a range of concentrations in the liquid-like regime, as determined rheologically, close to the liquid-to-solid transition (see Results section below). The hard star has almost five times lower arm molar mass and a much smaller hydrodynamic radius, as confirmed by the hydrodynamic radii which were measured by dynamic light scattering (DLS) at T=20 °C in athermal solvent cyclohexane.

TABLE 3.1. *Molecular characteristics of the star polymers*

sample	f	M_{arm} (g/mol)	R_h (nm)[a]	c* (mg/ml)[b]	c	t_B (10^{-3}s)	η	SP	solvent
H-Star	304	6500,00	20	97,92	1.82c*-2.08c*	0.0368	0.221 - 0.257	0.31	tetradecane
S-Star	203	30541,87	45	26,97	2.05c*-2.18c*	5.485	0.152 - 0.167	0.11	d-toluene

[a]Measured in cyclohexane.

[b]Estimated (in cyclohexane) from the hydrodynamic radius at 20°C, $c^*=[(4\pi/3)R_h^3]^{-1}$ (fM_a/N_A).

The samples investigated in this work are marked in the predicted phase diagram [55, 160, 166], which depicts different states in the two-dimensional parameter space of functionality f and packing fraction η (FIG. 3.1). Both stars appear to be at the border where face-center cubic crystal order is expected.

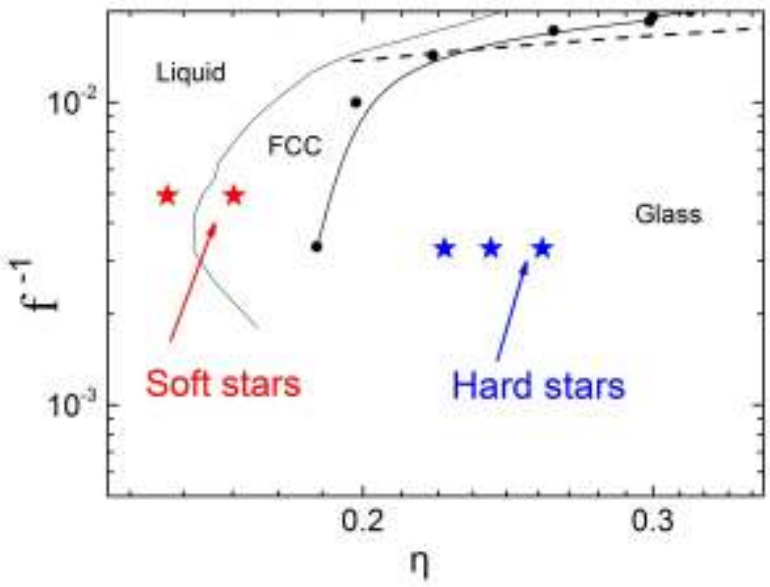

Figure 3.1. *The equilibrium phase diagram of star polymer solutions (broken lines) on the concentration-functionality plane obtained from simulations [160]. The solid black circles represent the experimental isodiffusivity curve for MD-diffusion coefficient* $D = 0.017$ *[55]. The solid black line is guide to the eye. The red and blue stars depict the concentrations of S-Stars and H-Stars, respectively, studied in this research.*

Rheo-SANS

These measurements were carried out at the Swiss spallation neutron source (SINQ) of the Paul Sherrer Institut in Villigen, Switzerland. The rheo-SANS setup was built on the basis of the combination of SANS and a stress-controlled rheometer (Physica MCR 501, Anton Paar, Austira) equipped with a Couette geometry of 50mm diameter. The inside rotating stainless steel cylinder had diameter of 49mm leaving a gap of 0.5mm from the outer glass cap. The experiments were carried out with the incident beam propagating along the gradient velocity or velocity direction, hitting into the vorticity-velocity or vorticity-gradient velocity plane, respectively (Figure 3.2). The experimental test protocol is described in Chapter 2.3.

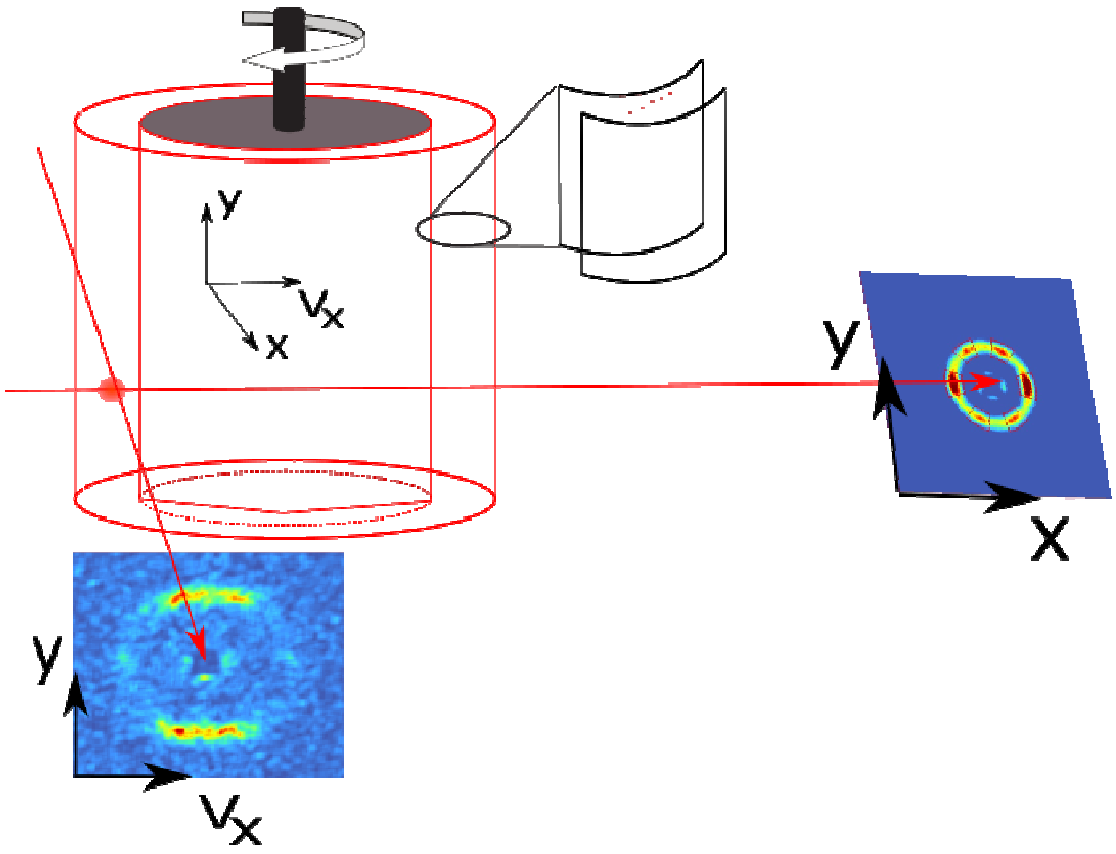

Figure 3.2. *Schematic diagram of the rheo-SANS. The system is composed by a Couette flow geometry with rotating inner cylinder. The beam is directed both in the radial and tangential directions, hitting into vorticity-velocity and vorticity-gradient velocity planes, respectively.*

Linear viscoelasticity and yielding

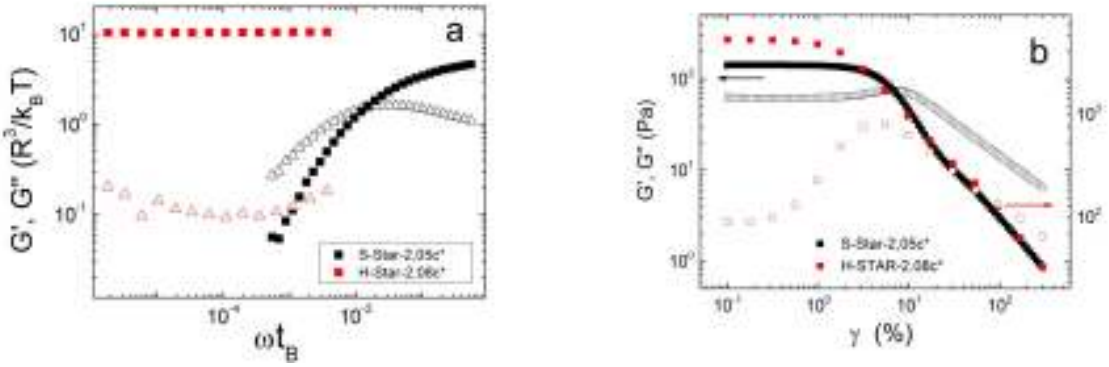

Figure 3.3*. a) Dynamic storage (G′, solid squares) and loss (G″, open triangles) moduli of two different stars samples. The red points represent the data from the H-Star at a concentration of almost twice its overlap concentration and the black points from the S-Star in a similar concentration (2.05c*). b) The strain dependence of the storage and loss modulus of the two different stars samples at 10rad/s. The arrows point the axis for each star samples.*

Figure 3.3a depicts the linear viscoelastic (LVE) response of both stars at virtually identical effective volume fraction $\varphi_{eff} = c/c^* \approx 2$. To properly compare the two different stars, the moduli are normalized with the individual particle modulus k_BT/R^3 whereas the frequency is normalized with the respective Brownian time. For both systems, Brownian time is extracted from the ratio of the square of hydrodynamic radius to diffusion in the dilute regime. We observe that the soft star exhibits liquid-like behavior, with a characteristic time of about 0.4s, extracted from the frequency at the crossover of storage and loss moduli. On the other hand, the hard star exhibits a signature of a soft colloidal glass, as judged from the frequency-independent G' with a value of about $10\,R^3/k_B\,T$, and the weak minimum of G'' [169]. It appears that G' of the soft star increases with increasing frequency and it is tempting to think that it will reach the same plateau as the hard star. In the rheo-SANS experiments we applied frequencies in the solid-like regime so as to prevent the sample from relaxation during an oscillatory period. Specifically, the imposed frequency for the increasing strain oscillations was 10 rad/s. The linear regime of the S-Star at 10rad/s can be seen in Fig.3.3b, where the system

begins to flow as soon as it reaches the 6.6% strain amplitude. The frequency of 10rad/s applied in our experiments, along with the Brownian time of the S-Stars produce Pe=0.05. However, the estimation of the Pe numbers is based on the single star diffusion which holds for dilute systems. Our systems are well above their overlap concentrations, where the viscosity has been proved to increase from 10 to 100 times [103]. Taking into account this, we argue that the shear rates we applied in the S-Star system were very close to Pe=1.

On the other hand, FIG. 3.3b shows that the H-Star melts at higher strain amplitudes depicting a wider elastic regime. For this system, the highest rate applied was $40s^{-1}$, corresponding to $Pe \approx 0.1$, taking into account the increase of the viscosity in the glassy regime.

Soft star in steady oscillatory shear

Figure 3.4 shows data acquired from rheo-SANS experiments with the S-Star and the incident beam passing through the vorticity-velocity plane. The data points display the evolution of the crystal order (DOO), with increasing shear strain at fixed frequency. The shear-induced order is quantified as:

$$DOO = \frac{\sum_1^6 Ip_i - \sum_1^6 Iv_i}{\sum_1^6 Ip_i}$$

where I_p and I_v represent the intensity of the peaks and valleys, respectively, shown with boxes in the inset SANS image of Fig. 3.4.

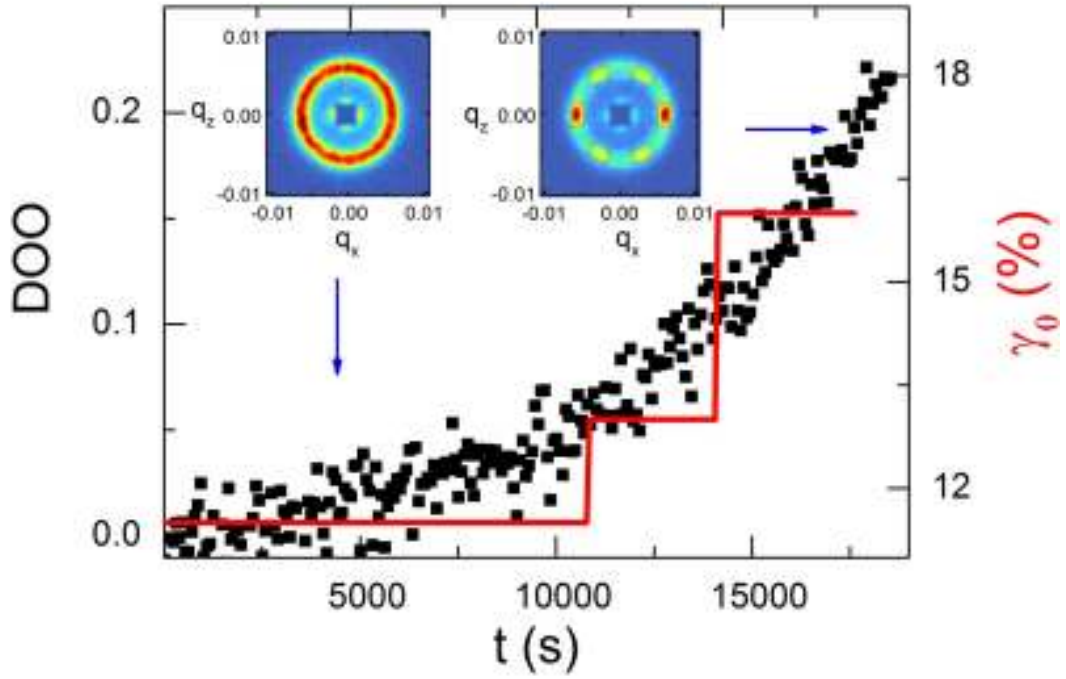

Figure 3.4. *The degree of ordering (DOO) as a function of time and strain for the S-Star in a 2.0c* concentration. Insets in this graph are two SANS images showing the evolution of Bragg peaks in the ring after the increase of the ordering. The two arrows show the degree of ordering when the SANS images were extracted. The indicated annular sections in the right insets show the area used to measure the intensities, which are used to calculate DOO.*

The upper left inset in this figure depicts the amorphous ring of the scattered intensity from the sample, indicating the absence of any structural order at the beginning of shearing. It is easily observed from the first 3 hours that shearing at strain amplitudes close to twice the value of the yield strain (6.6%) induces ordering in the system. Further increase of the shear strain speeds-up the crystallization process [171], increasing the intensity of the Bragg peaks seen in the top right inset of the figure. Note that, whereas rheology plays a role in crystallization, the opposite is true as well: indeed, crystallization influences the rheological signature of the solution. FIG.3.5 depicts the increase of G' and simultaneous decrease of G'' of the sample undergone crystallization compared to the pristine samples before shearing (Fig.3.3). The resulting relaxation times (at moduli crossover) are longer. The same transition from liquid-like structures to solid-like upon

applying oscillatory shear has been observed in the past for hard sphere systems [50]. However, in these systems the cessation of shear led the system to the initial fluid-like structure. In our system, the cessation of shear does not affect the crystal structure, which seems to be the new equilibrium state. Furthermore, the change in the LVE response justifies the argument that increasing the imposed shear rate enhances crystal formation [157] and decreases the nucleation times [52].

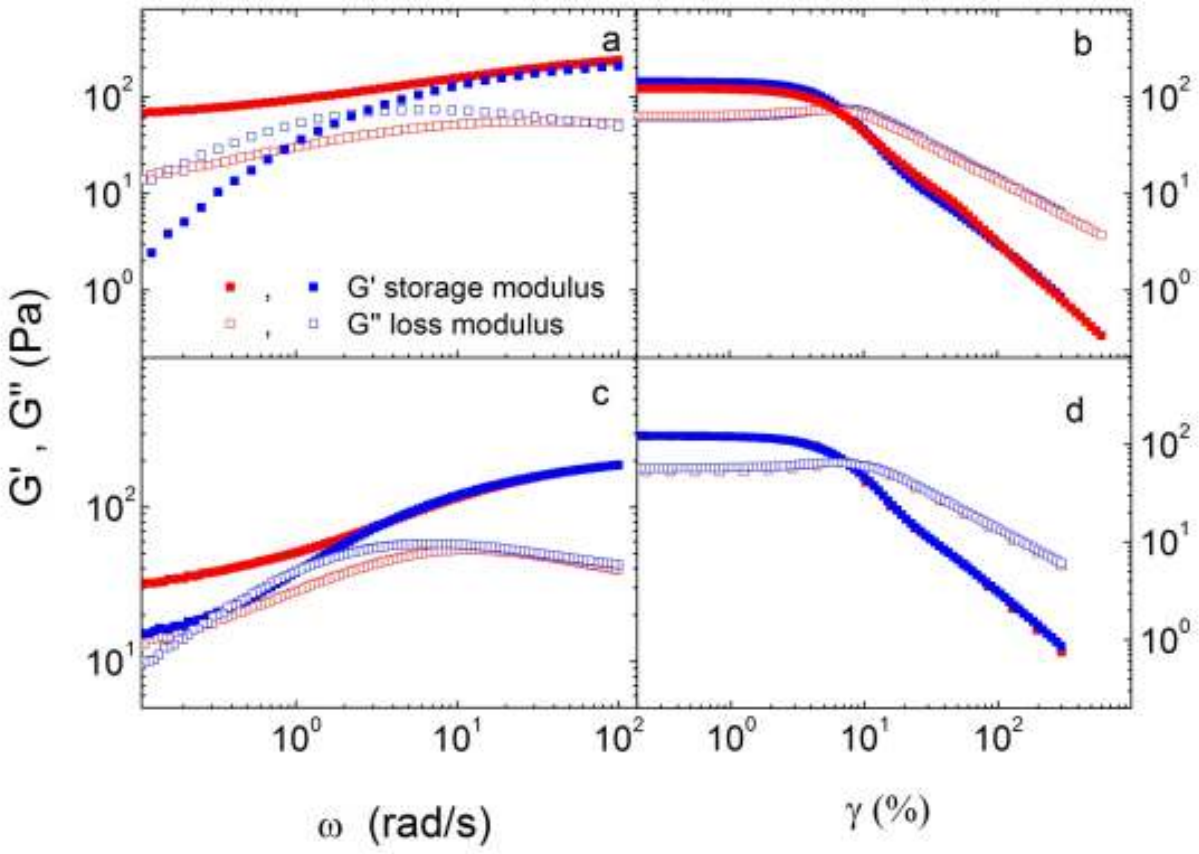

Figure 3.5. *The rheological response of the S-Star under steady low strain amplitude (a, c) and steady frequency (b, d). The top panels (a, b) show data from the 2.0c* while the bottom panels (c, d) show data from 2.2c*. Different colors depict the phase; blue squares stand for non-crystalline structures and red squares show ordered structures.*

An interesting outcome from Figure 3.5 (3.5a, 3.5c) is that at high frequencies the crystal ordering does not seem to affect the rheological response of the system. This feature is also unaffected by concentration and reflect the local scale of the system's response with different degrees of order. Figures 3.5b and 3.5d manifest the virtual

independence of linear and nonlinear viscoelastic properties of the S-Star on concentration and order.

The role of frequency when increasing the effective shear rate is shown in Figure 3.6. Faster oscillations drive the system to higher G'' overshoot close to the yield strain. At the same time, G' increases with increasing frequency, in agreement with the LVE data of Fig. 3.5c.

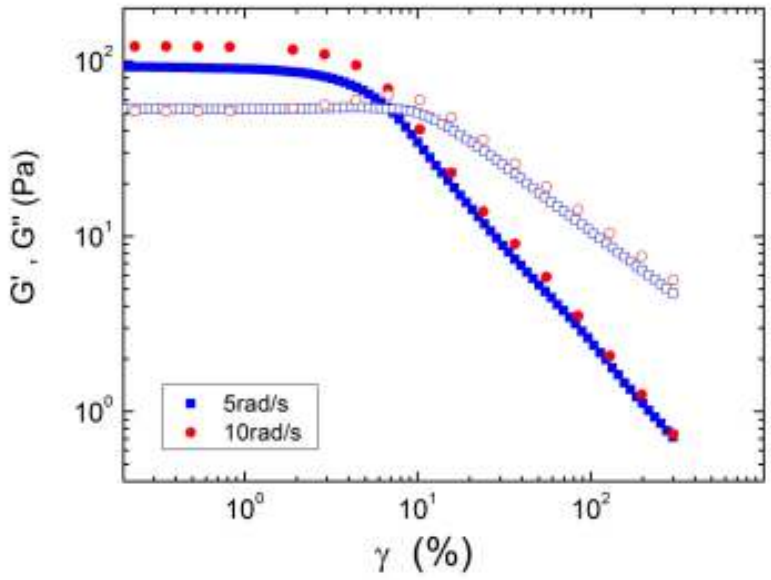

Figure 3.6. *The strain dependence of the storage and loss modulus for two frequencies for 2.2c*concentration.*

The combined effects of the applied strain amplitude and frequency, as well as concentration are highlighted in Fig. 3.7. We observe that the slowest nucleation process reflects the evolution of the DOO for oscillations at 15% strain amplitude and 5rad/s frequency. The nucleation time, extracted from the center of the circle as the inset in Fig. 3.7 shows, is $(7.5 \pm 0.2) \cdot 10^3$s and is the highest of the four data sets shown here. Increasing the frequency, while keeping the other parameters constant (strain amplitude, concentration), results in lower nucleation time, $(5.0 \pm 0.2) \cdot 10^3$s, and higher ordering rates.

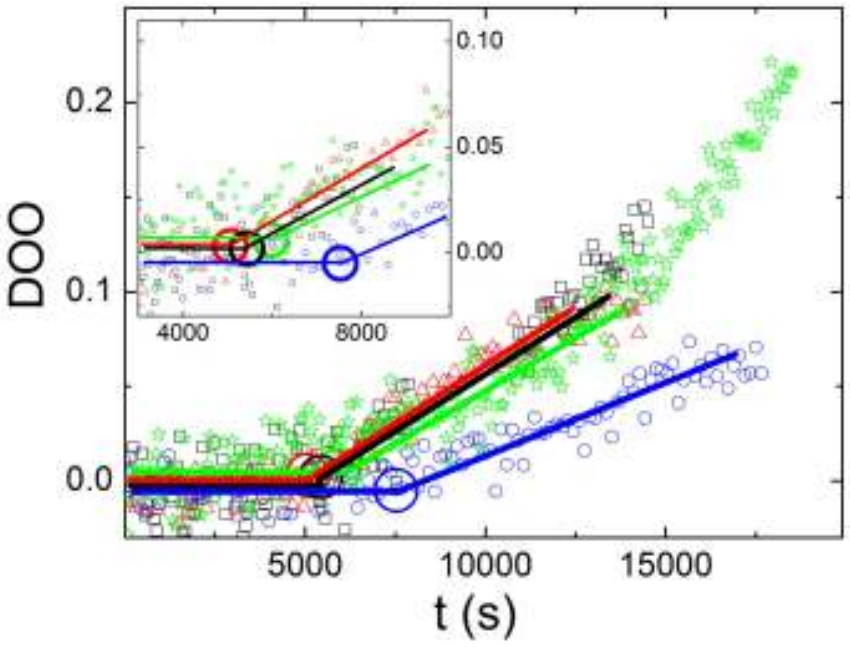

Figure 3.7*. The degree of ordering (DOO) as a function of time, strain, frequency and concentration for the S-Star. The green stars represent the data from oscillations at 11.5% strain and 10rad/s for 2c*, the blue circles come from oscillations at 15% strain and 5rad/s for 2.2c*, the red triangles stand for oscillations at 15% strain and 10rad/s for 2.2c* and black squares represent oscillations at 11.5% strain and 10rad/s for 2.2c*. The colored lines are linear fits demonstrating the ordering growth rate and the nucleation times for the different experiments.*

On the other hand, the applied strain amplitude does not seem to significantly influence the nucleation times and rates. Decreasing the strain amplitude from 15% to 11.5% leads to a small increase of the nucleation time, $(5.4 \pm 0.2) \cdot 10^3$s, but unchanged ordering rates. Same conclusions hold for the effects of concentration. When it decreases by 10%, the nucleation time increases, $(5.9 \pm 0.3) \cdot 10^3$s, with similar rate (10%). The effect of frequency has also been reported for other systems, such as hard spheres, where for inducing crystallization, the fluctuations caused by shear have to be larger than these caused by Brownian motion [102, 172]. Finally, as the strain diverges further from the yield strain, its effect on the evolution rate of the ordered structures is decreased. Hence, we conclude that increasing the shear rate and concentration speeds-up the crystallization process [154, 157, 173], a feature that depends strongly on the frequency of the oscillations.

Soft star crystal changes on Increasing shear strain

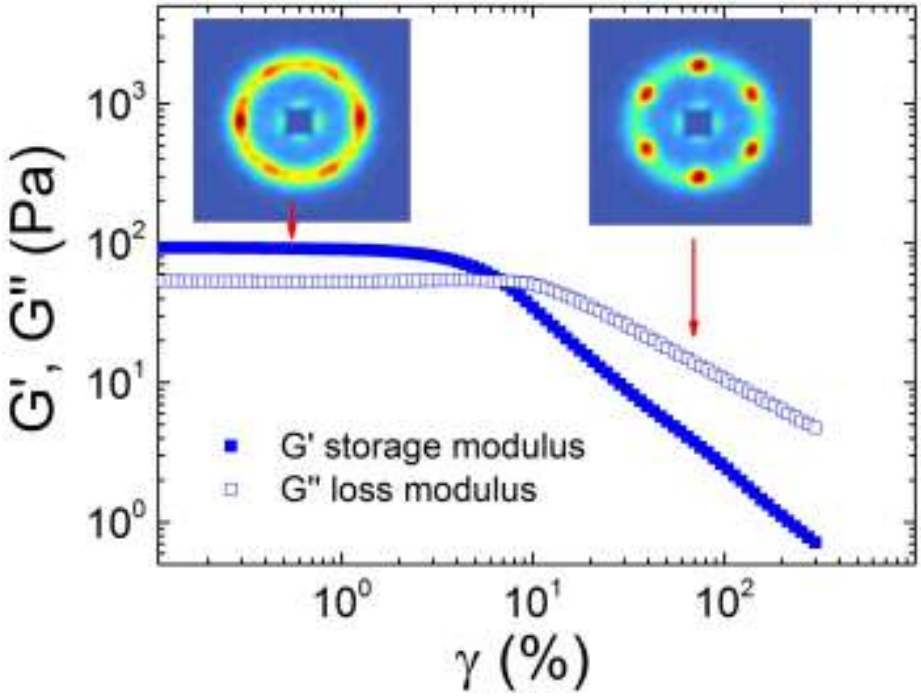

Figure 3.8*. The strain dependence of the storage and loss modulus of the S-Star. The inset images show the 2D ring of the sample at different strains. The arrows depict the strains, at which the images were extracted.*

An intriguing experimental finding is the existence of two crystal orientations found upon application of fast increasing shear strain. As seen in Fig. 3.8, a transition takes place from hexagonal order oriented with a close-packed direction perpendicular to the velocity axis at strain amplitude of 0.5% to another hexagonal order with a close-packed direction parallel to the flow direction at 80%. Such transitions have been observed in the past [151, 154, 157, 173-175] and were rationalized by the tendency of the dense close-packed layers to minimize their resistance against the flow [151, 175]. We note that this flipping of ordered structure took place when the applied frequency was 5rad/s, whereas it was not observed at higher frequencies. We can speculate that although higher frequencies induce crystalline order faster, the frequency should be sufficiently low in order to reach more stable structures, so as the system has the necessary time to be rearranged.

Increasing the applied shear rates to values $\dot{\gamma} > 6s^{-1}$ destroyed the crystal lattice in the solution, as expected [46, 51, 156, 157, 176, 177]. Shear-melting is manifested by the loss of the six-fold scattering peaks in the SANS images (Fig. 3.9) denoting the transformation of the hexagonal pattern structure into the amorphous ring [178]. Thus, it appears that, the softer the system, the more its structure depends on the applied shear.

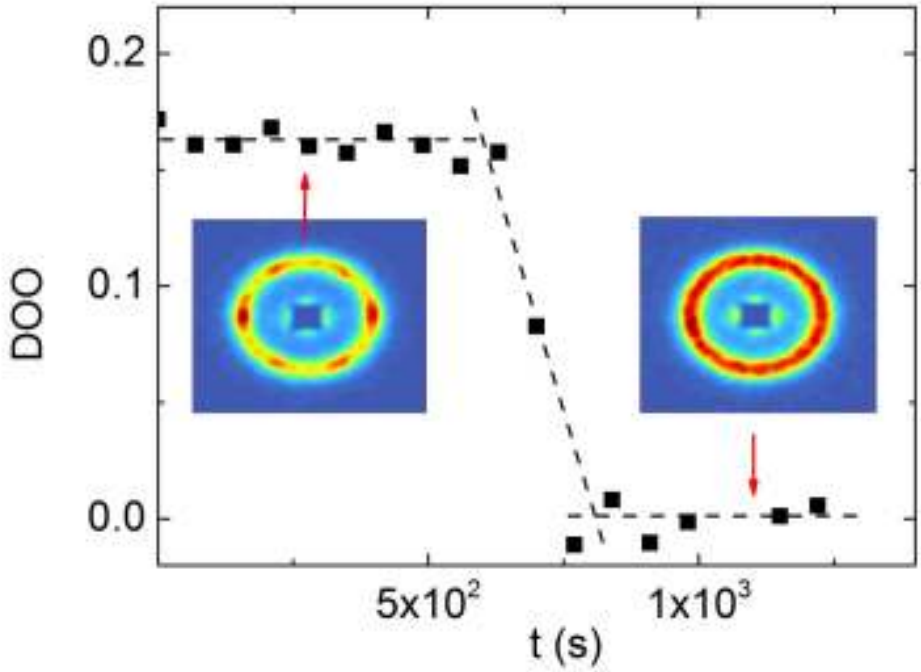

Figure 3.9*. The degree of ordering (DOO) as a function of time during a shear rate of $10s^{-1}$ for the S-Star. The two inset images show the transformation of the Bragg peaks into an amorphous ring as a result from the rejuvenation process.*

Hard star crystallization and stability

The H-Star was crystalline at rest throughout the whole concentration range investigated, as revealed by SANS measurements (see Fig. 3.11 below). As already mentioned, its rheology differs from that of the S-Star (Fig. 3.3). The relative ease of crystallization compared to the S-Star is attributed to the compactness of the former, or else its larger SP. This should relate to reduced arm fluctuations and eventually a stronger tendency for order.

To address the role or shear in altering the crystal order or melting it, the H-Star was examined by the same means and experiments as the S-Star. The highest concentration of this star solution (2.08c*) was found to exhibit an ordered structure only a few seconds after the beginning of the shearing. SANS images showed a hexagonal pattern with six clear Bragg peaks around the ring but the positions of the peaks indicate a different structure compared to the S-Star case (Fig. 3.11). This system showed a hexagonal pattern with a close-packed direction parallel to the flow direction similar to the flipped structure of the S-Star. Note that the formation of HCP-layered structure is rather common in sheared colloidal crystals irrespectively of softness [151, 155, 173, 177, 179].

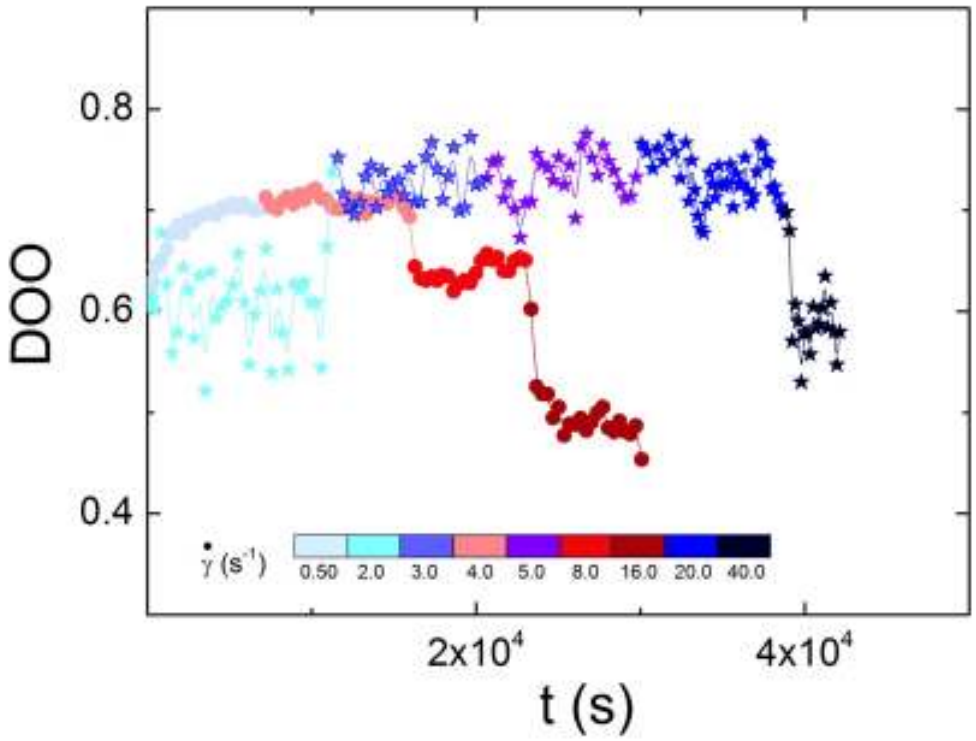

Figure 3.10. *The degree of ordering (DOO) as a function of time and oscillatory rate for the H-Star at 2.08c*(stars) and 1.92c* (circles) concentrations. The shear rates for the 2.08c* vary from 0 to 40.0s^{-1}, while the rates for 1.92c* vary from 0 to 16s^{-1} and are showed with different colors.*

A remarkable finding here, is that the DOO for this star is more than three times higher than that of the S-Star. This suggests a stable system, an argument supported by the absence of melting despite the increasing applied shear (Figure 3.10). Note that the DOO

remains high even at the highest shear rates imposed ($40s^{-1}$), demonstrating indeed a very stable, hard-to-break crystal [128, 180]. This sets the present hard-star crystal apart from other colloidal crystals such as hard sphere ones [46, 129, 130]. Similar behavior is evidenced at a slightly lower concentration (1.92c*), although in that case there is a larger sensitivity to shear rate variations (Fig. 3.10). In particular, in Fig. 3.10 we see that shear rates higher than $20s^{-1}$ seem to have a weak influence on the 2.08c* system, while the lower concentration system exhibits signs of decreasing DOO.

The stability of the H-Star crystal was further tested by means of altering the concentration. Indeed, a loss of ordering was found when the solution was diluted to 1.82c*. Actually, at this concentration an amorphous ring was observed in SANS, denoting a glassy state of the star.

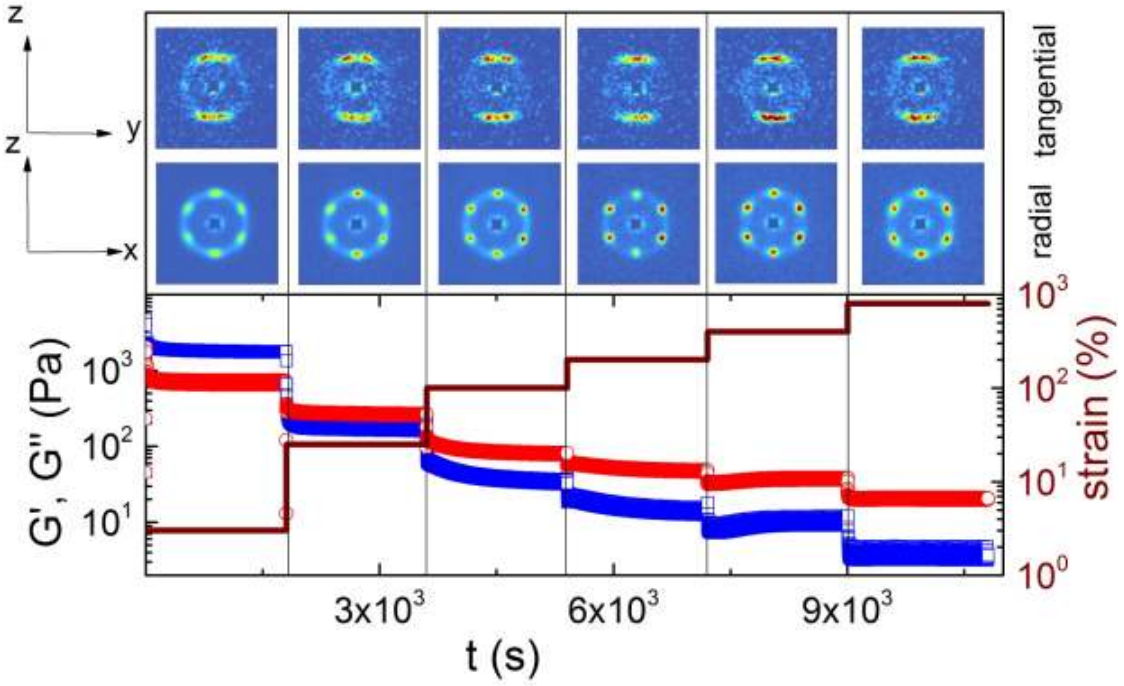

***Figure 3.11**. The storage and loss modulus dependence of the time and strain for the H-Star. The SANS images show the 2D ring from two different beam positions. The top row show images from the beam hitting in tangential direction while the second row shows images from the beam hitting in radial direction.*

Apart from radial, tangential measurements were also performed in order to acquire more information about formed 3D structures. Fig. 3.11 depicts a summary of SANS

images from both types of measurements upon increasing shear strain. Comparing the results from vorticity-velocity and vorticity-gradient velocity planes, the side peaks of the former disappear in the latter, while at the same time the two broad peaks on the top and bottom of the ring remain.

Increasing strain amplitude alters the broadness of the two crystal peaks shown in the tangential measurements, which are originally (lower strains) very close to each other on the top and bottom of the SANS scattering ring. These two peaks seem to merge as the strain increases and then split again when the strain reaches very high values ($\gamma_0 =$ 800%). Comparing tangential with radial measurements, we observe that when the two peaks merge in the tangential experiments, the top and bottom peaks of the radial direction ring fade out. The sequential splitting of the peaks from the tangential images, results in increasing the intensity of the peaks in the radial direction.

Concluding remarks

In conclusion, using rheo-SANS measurements in vorticity-velocity and vorticity-gradient velocity planes, we reported the microstructural transitions of two multiarm polybutadiene stars. The measurements showed that oriented structures were induced by shear and two different crystal formations were observed. The softer star displayed three structural transitions: 1) formation of a FCC lattice structure, 2) formation of random AB stacking (HCP) and 3) shear melting at high rates. In addition, the effect of the shear rate on the nucleation process was investigated and correlated with the different crystal structures. The harder star demonstrated an instant crystallization and a significant resistance to shear-melting. Moreover, while it showed a slight dependence on the shear rate, the concentration proved to have a much higher influence in its structural formation.

This work has highlighted the effect of softness in the structural arrangements of soft particles and explored the influence of shearing in soft systems. We recorded strong differences between our systems and hard spheres. The most pronounced of them were the lack of the decrease of the moduli along with the difficulty of melting the crystal structures. These remarks suggest that soft systems display higher energy barriers in their path towards equilibrium state. Moreover, the concentration of the systems plays a key role regarding the mechanical properties of the material. The softness, which can be translated in deformability and interpenetration between the particles, is highly affected by the density. Jammed soft systems exhibit behaviors similar to hard spheres but still display discrepancies due to their soft nature, thus different particle interaction potential.

Softer systems seem to be more sensitive to external field perturbations. In our case, the rate of oscillations led the softer star system to rearrange between two different crystal formations. This observation points out the complexity of the system which shows high sensitivity to the type and amount of shearing. Additionally, the harder star solution displayed, also, responsive behavior to the variations of shearing. Thus, we can assume that shearing influences strongly the orientation of the soft systems structures.

An interesting question, yielded from this work, is whether a model can be built up to correlate the softness of the particles with concentration and shearing parameters. The softness should be related with the particle architecture along with the shifting of the interparticle potential as function of concentration. This model could be, later, extended to other similar systems like hard spheres.

4. Controlled formation and physical gelation of hydrogel fibers [31, 181]

Supramolecular polymer networks represent an emerging new class of responsive soft materials with significant technological implications [182-188]. The technology evolution of the last decades has increased rapidly the need for design tunable networks which can adapt to different environments. In particular, the ability to selectively tailor their rheology from liquid-like to solid-like has recently received a great deal of attention [186, 189-195]. In particular, the structure-dynamics interplay of such systems is highly important for being able to facilitate their processing and handling [182, 183, 190-194]. The key for understanding these systems is the synergy of chemistry, metrology and modeling. Furthermore, the new advances in synthesis offer an unprecedented versatility of supramolecular assemblies which serve as building blocks for the formation of physical networks [183-185, 196]. Metrology involves mainly structrural as dynamic techniques such as microscopy, X-ray and neutron scattering, dynamic light scattering, rheometry and rheo-physics. On the other hand, modeling (or simulations) is based on the concept of a given strength, activation energy and finite lifetime of bonds and their coupling to the viscoelasticity of chain elements.

Hydrogels and supramolecular hydrogels are particularly appealing as they combine the above versatility with their biocompatibility that makes them in biomaterials applications, such as tissue engineering and regenerative medicine [197-202]. Good example of such supramolecular systems are the hydrogel fibers, which can be produced naturally or synthetically. In nature, the relation between water and macromolecules is responsible for the mechanical properties of the materials. For example, water is an important component of both the collagen fibers and the polysaccharide gel matrix which comprises the highly organized composite structure (structural, bound and free water)

[203]. This example shows that nature is able to activate weak intermolecular interactions (hydrogen bonds, Van der Waals forces) to control fiber formation [204].

On the other hand, chemists utilize either physical methods such as extruding [205], microfluidic processes [206], electrospinning [207] or also molecular self-assembly, i.e., formation of discrete architectures from molecules via intermolecular forces, for fiber preparation thereby competing with nature [13, 208-211]. The strength of such forces, should be high enough to form stable structures under physiological (aqueous) conditions but also sufficiently low to yield defined thermodynamic equilibrium structures. The self-assembly and phase behaviour of amphiphiles have attracted chemists, physicists and material scientists for a long time [30, 208, 212-214]. Principles known from nature, inspired researchers to use self-assembly as a tool for structuring materials on nanometre scale. In spite of the major step forward which was made in the understanding of the self-assembly it still remains a big challenge to understand or even predict the principles of the self-assembly and to control the properties. Hydrogel fibers can be formed by synthetic methods as well, however, they require a chemical crosslinking. For example, extruded fibers of poly(vinyl alcohol) and poly(acrylic acid) can be converted to bundles of hydrogel fibers after a crosslinking by ester formation upon heating [215, 216].

In this chapter, we will demonstrate an attempt to mimic the concepts of nature with adjusting carefully the molecular interactions of different amphiphiles in order to achieve hydrogel fibers via self-assembly. Hexaphenylbenzene (HPB) was chosen as large hydrophobic carbon source and PEG as hydrophilic part of the amphiphile on the account of their large antagonistic forces [29]. The shape of the molecule and the chain length of the solubilizing group were varied keeping the fraction of the solubilizing PEG units constant (Figure 4.1). In this way, the propeller-like HPB self-assembled in fiber formations via π-π interactions, even in very dilute aqueous solutions [217]. Depending on the molecular shape and the length of the PEG chains (i.e., density of the hydrophilic

group in the periphery of HPB, Figure 4.1), space filling will control water uptake by the formed hydrogel fibers.

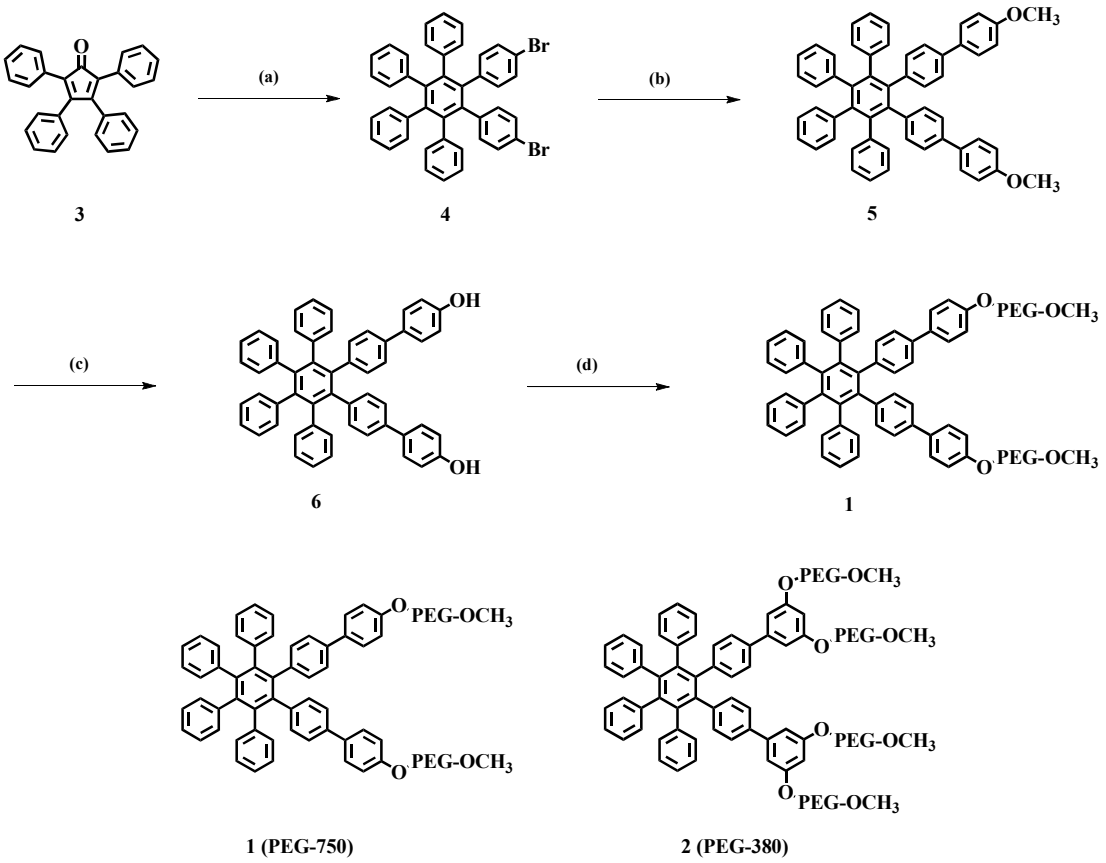

Figure 4.1. *Synthetic scheme for* ***1*** *.(a) 1,2-bis(4-bromophenyl)ethyne, diphenyl ether, microwave: 220 °C, 300 W, 12 h (45%); (b) (4-methoxyphenyl) boronic acid, Pd(OAc) 2 , Cs 2 CO 3 , DABCO, DMF, 80 °C, 3d (65%); (c) BBr 3 , DCM, 0 °C to rt (84%); (d) CH 3 O-PEG-Br, KOH, THF, refl ux, 18 h. Molecular structure and the schematic representation of* ***1*** *(PEG-750) and* ***2*** *(PEG-380).*

We performed dynamic polarized and depolarized light scattering measurements to assess both the form factor and the two transport (translation, rotation) coefficients of the assemblies necessary to uniquely reveal the complex supramolecular structures. Based on the characteristic parameters, number of molecules within the fibers N_S, length L, diameter d, length density M/L, the supramolecular structure is represented by bundles of fibers whose size and water content relates to the shape and amphiphilicity of the molecular precursor; **1** and **2** in Figure 4.1 possess both different shape (two and four PEG) and amphiphilicity ($M_n = 750$ gmol^{-1} and M_n = 380 gmol^{-1}, respectively). In fact, the molecule **2** with the shorter PEG chains led to longer self-assembled structures

containing less water than for molecule **1** with the longer PEG chains. The self-assembly behavior of hexaphenylbenzene containing PEG molecules with different architecture (**1** and **2**) was explored in aqueous solution by cryo-TEM. For cryofixation, the aqueous solution of sample **1** (PEG-750) was dropped onto a TEM grid and the excess of amount of liquid was blotted off with filter paper. Subsequently, the samples were frozen in liquid ethane (-89°C) and transferred to the TEM. For electron microscopical analysis, a Tecnai F20 transmission electron microscope of FEI Co. operated was used.

For the aqueous solution of **1** at 30.7gL^{-1}, long self-assembled structures are observed with a worm-like structure (Figure 4.2). The length of worm-like micelles of sample **1** displays in the range of ~5 and ~350 nm with a diameter of ~3 nm.

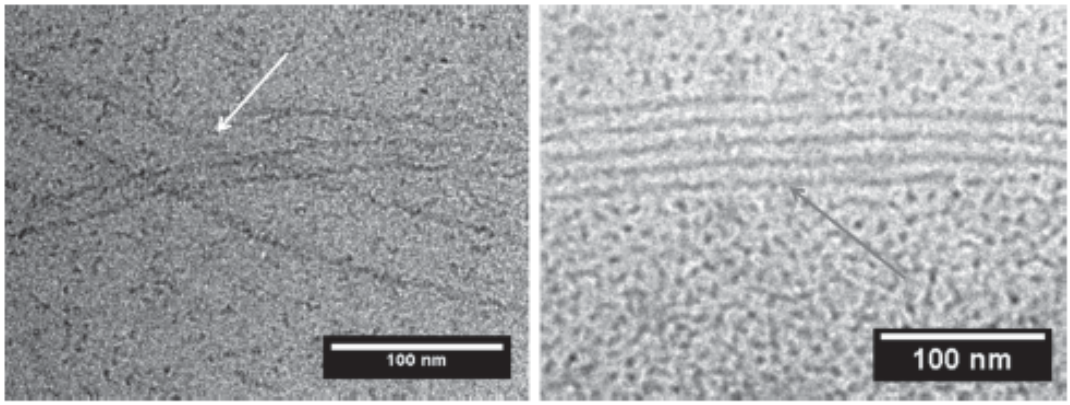

Figure 4.2. *Cryo-TEM micrograph of **1** in aqueous solution at 30.7 gL^{-1}. The white arrow shows worm-like structures and the black arrow shows a bundle of fibers.*

The cmc values of these samples as estimated from the change of the surface tension with increasing concentration are indeed very low. Sample **2** possesses a cmc value of 0.002 gL^{-1} which is even lower than for sample **1** (Figure 4.3). The latter seems to display two crossover concentrations between 0.003 and 0.01 gL^{-1}. Therefore, the cryo-TEM image (Figure 4.2), obtained at concentrations (~30 gL^{-1}) several orders of magnitude above cmc, might render any prediction of the structures at much lower concentrations (near cmc) ambiguous. The surface tension profile of **2** is similar to the surface tension profile of conventional ionic surfactant such as sodium dodecyl sulfate (SDS) [218]. The

measured cmc values are clearly lower than the cmc of ionic surfactants which assume values in the range of gL^{-1} (cmc_{SDS} = 2.65 gL^{-1}) [219]. Very small cmc, comparable to the value of **2**, occur for high molecular weight block copolymers. However, these values are obtained from air/water interface measurements and might deviate for the bulk solution.

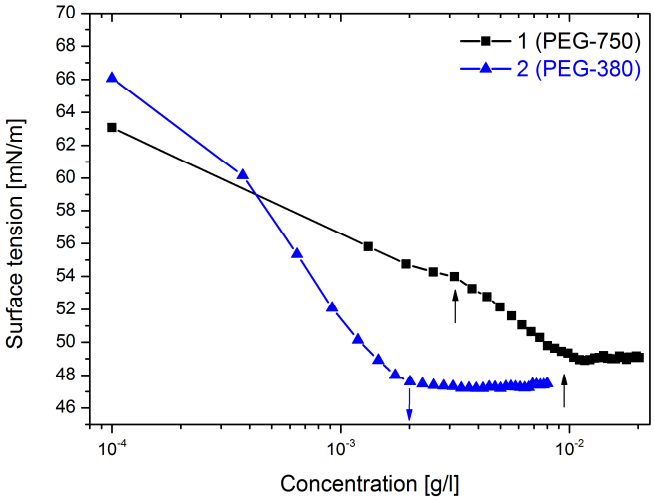

Figure 4.3. *Surface tension versus the concentration of **1** and **2** in water at 25°C. The black arrows show the two kinks of **1**. The blue arrow indicates the kink of **2**.*

The performed dynamic light scattering experiments at different concentrations, described in Chapter 2.4, has reconciled all available structural information of the self-assembly behavior of **1** and **2**. We have initiated the PCS experiments with a concentration of 1.7gL^{-1} that is between cmc and the concentration used for the cryo-TEM images. We, first, examined aqueous solutions of **1** prepared at 20°C and also recorded the experimental relaxation function $C_{VV}(Q,t)$ also at 20°C at a high scattering wave vector $Q = 0.03\,nm^{-1}$ corresponding to a probing length of about 200nm (open squares in Figure 4.4). Dynamics of the order of 100μs cannot be rationalized by the small size of the structures of **1** and **2** and clearly implies formation of supramolecular assemblies. Two populations of assemblies are revealed which unexpectedly change

with annealing at 20°C over a period of about weeks. To speed up this equilibration procedure and warrant time invariant structures, we have annealed the solutions at 50°C for about 3h with subsequent slow cooling to 20°C.

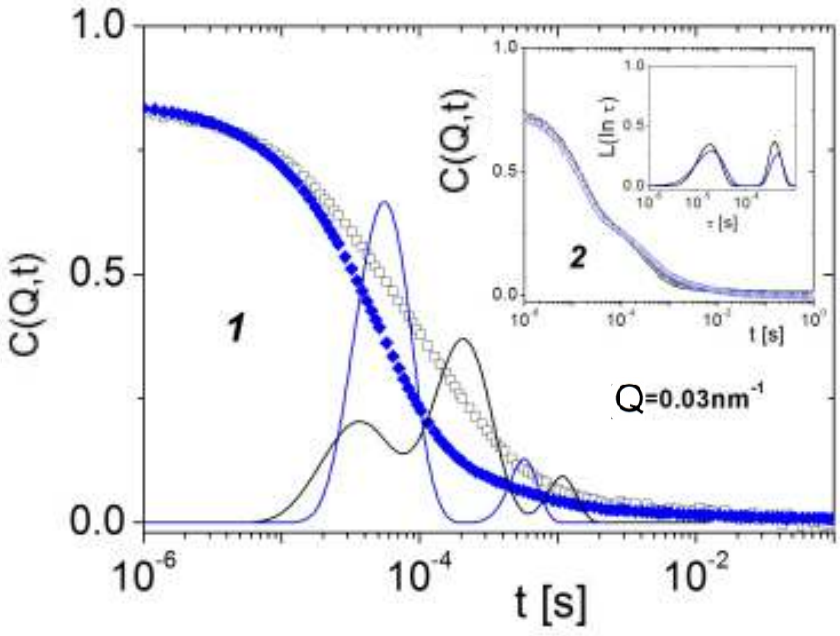

Figure 4.4. *Normalized field correlation functions $C_{VV}(Q,t)$ at 20°C and scattering wave vector $Q = 0.03nm^{-1}$ (diffusion length of ~210nm) for the translational diffusion dynamics in aqueous solution of **1** at 1.7 gL^{-1} recorded after dissolution (white squares) and after annealing (for few hours) at 50°C and subsequent slow cooling to T=20°C (blue solid rhombi). The double shape is indicated by the inverse Laplace transformation (ILT) of the two relaxation functions. Inset: $C_{VV}(Q,t)$ at $Q = 0.03nm^{-1}$ along with the corresponding ILT inverse Laplace for **2** at 1.7 gL^{-1} subject to similar thermal treatment.*

The recorded $C_{VV}(Q,t)$ (blue solid rhombi) is different from the relaxation function before the particular annealing protocol was employed as both peaks of ILT shift to shorter times with heating and the stronger impact is on the amplitude and position of the slow process. This peculiar metastability effect is not observed for the aqueous solutions of **2** at similar concentration (inset of Figure 4.4). The depicted $C_{VV}(Q,t)$ recorded as dissolved (black open squares) and after annealing at 50°C (blue open rhombi) display experimentally the same shape as it is reflected more in the corresponding ILT profiles. The origin of kinetically trapped structures in relatively dilute concentrations of the present amphiphiles due to the formation of thermodynamically unfavorable

configurations is unclear and needs further investigation. For the elucidation of the formed structures, however, it suffices to know the pathway towards equilibrium of self-assembled structures.

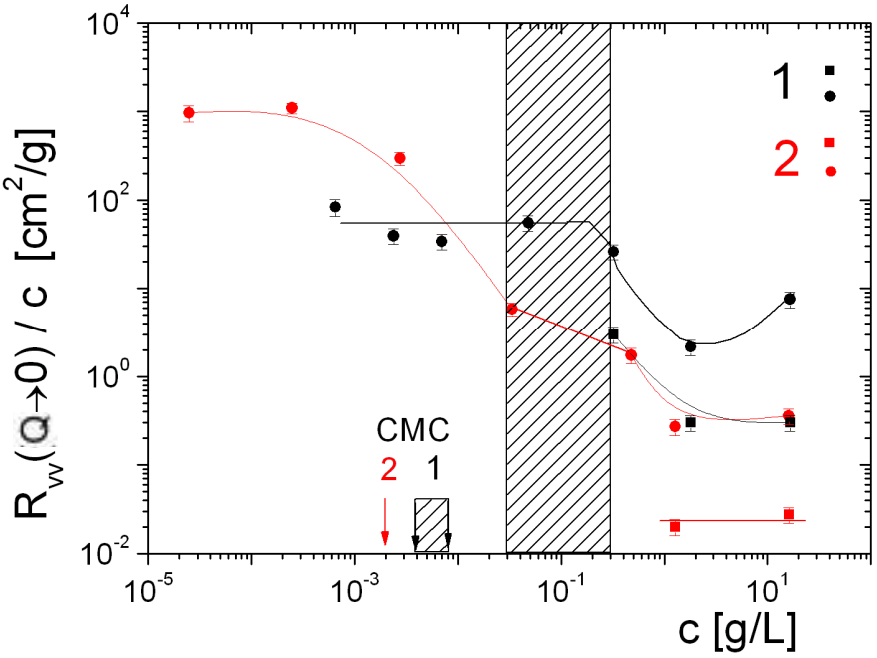

Figure 4.5. *Reduced absolute scattering intensity $R_{VV}(Q \longrightarrow 0)/c$ is shown as function of concentration, c, at 20°C for **1** and **2**. The shaded area indicates a crossover to semidilute regime in which two relaxation processes are resolved in $C_{VV}(Q,t)$. Circles and squares denote the R_{VV} intensities associated with the main and fast processes. The two arrows are for the CMC values from **Figure 4.3.***

The second unexpected observation relates to the very low overlap concentration c* above which interactions between the supramolecular assemblies in the aqueous solutions become important; their structural characterization is meaningful at $c < c^*$. The reduced Rayleigh ratio $R_{VV}(Q \longrightarrow 0)/c$ for the samples **1** and **2** obtained from the extrapolation of the Q-dependent $R_{VV}(Q)$ at $Q = 0$ (Figure 4.5) represents the reciprocal of the osmotic pressure of the solutions and hence its concentration dependence sensitively reflects interactions between solutes [220]. This diagram identifies two regimes with a crossover c* roughly around 0.1gL^{-1} for **1** with the dilute regime, identified by $R_{VV}(Q \longrightarrow 0) \sim c$, below this concentration. Above c* two relaxation processes are present in $C_{VV}(Q,t)$ (Figure 4.4) with intensity contributions (circles and squares) (Figure 4.5); this crossover

concentration is larger than the two values for **1** (Figure 4.3 and arrows in Figure 4.5). Above this c*, two processes are also observed in the $C_{VV}(Q,t)$ for **2** (Figure 4.6) but a c-independent $R_{VV}(Q \longrightarrow 0)/c$ is reached at much lower concentrations (<0.002gL^{-1}) in agreement with its cmc value (red arrow in Figure 4.5). However, the limiting $R_{VV}(Q \longrightarrow 0)/c$ values for both **1** and **2** do not correspond to the molecular species (Figure 4.1) but to much larger structures as indicated by the estimated molecular weight $M_w = R_{VV}(Q \rightarrow 0)/H_C$. Using for the contrast factor $H = [2\pi n(dn/dc)]^2/(N_A\lambda^4) = 5.5.10^{-7} cm^2 g^{-2}$, with N_A being the Avogadro number, M_w amounts to 1.3·10^8 gmol^{-1} and 1.8·10^9 gmol^{-1} respectively, for the assemblies in **1** and **2** aqueous solutions at c ~ 0.001gL^{-1} below cmc. The latter obtained from surface tension measurements (Figure 4.3) do not signalize transition to molecular species and should therefore be considered with caution. Conversely, the variation of $R_{VV}(Q \longrightarrow 0)/c$ with concentration (Figure 4.5) defines the dilute regime in which supramolecular structures free of mutual interactions should be investigated. Consistently, the two different regimes are well documented by the concentration dependence of the translation diffusion coefficient(s) in Figure 4.12.

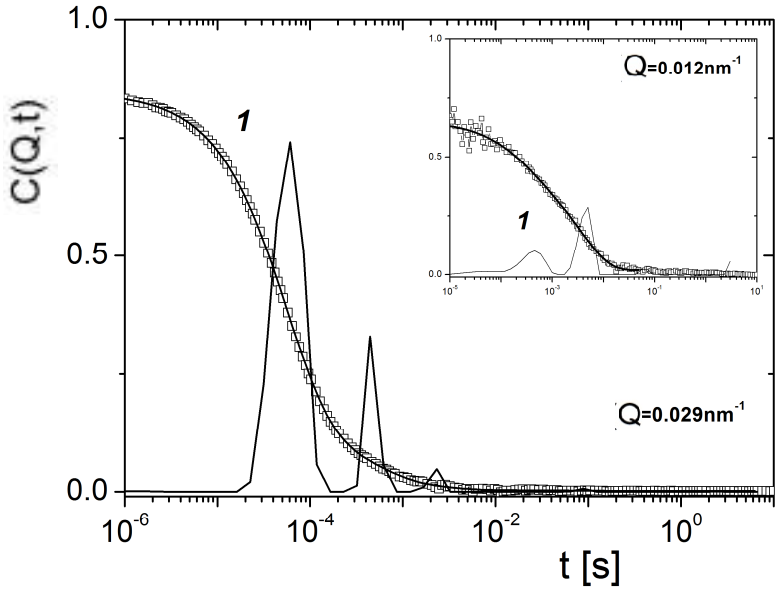

Figure 4.6. *$C_{VV}(Q,t)$ at $Q = 0.029nm^{-1}$ for the aqueous solutions of **1** at 1.7gL^{-1} (black squares) at 1.5gL^{-1} (red circles) at T=20°C recorded after annealing at T=50°C for few hours and subsequent slow cooling to T=20°C. The double shape leads to two relaxation times as indicated*

by the results be the bimodal shape of the ILT. Inset: $Cor(Q,t)$ *at* $Q = 0.012nm^{-1}$ *(θ=45°) for the orientation dynamics in dilute aqueous solution of* ***1*** *(black squares) at 1.7 gL*$^{-1}$ *at T=20°C recorded after annealing at T=50°C.*

To reduce ambiguities in the structural characterization of complex systems, we seek also for information on the dynamic properties. Figure 4.7 is an example of such information source including the form factor (static) and transport coefficients (dynamic) for the association of **1** in a dilute aqueous solution. Both translational $C_{VV}(Q,t)$ and orientation $C_{or}(Q,t)$ relaxation functions are described by a single decay process ascribed to a single population of supramolecular assemblies whose average dimension can be still captured by the longest probing wavelength, as seen by the intensity downturn in the Holtzer presentation, $QR_{VV}(Q)/c$ vs Q (inset to Figure 4.7) [221]. Moreover, the limiting value of orientation relaxation rate Γ_r at $Q = 0$ is nonzero (upper inset) that allows the determination of the rotational diffusion $D_r = \Gamma_r(Q = 0)/6$ in addition to the translation diffusion $D = \Gamma(q)/Q^2$ at $Q = 0$ [222]. We should note that at this extremely low concentration other scattering (X-ray or neutron) techniques are hardly applicable and $C_{or}(Q,t)$ is still measurable owing to the optical anisotropy of the phenyl rings in the parent **1** and **2** structures.

Since the relaxation function $C_{VV}(Q,t)$ is unimodal, there is a single contribution to the static $R_{VV}(Q)$ which at such dilute conditions is safely obtained from the total intensity and the short amplitude of $C_{VV}(Q,t)$. The pattern of $R_{VV}(Q)$ is represented well by a worm-like shape [222-224] using an average contour length L~2 μm and Kuhn segment $l_K \sim 75nm$ (solid line in the Holtzer plot of Figure 4.7); in this model the chain conformation is rather semirigid ($L/l_K = 26$) than a coil assuming shorter Kuhn segment. Further, since the thickness, *d*, of the chain is ignored in the model, its applicability in the light scattering experiment presumes thin enough ($Qd >> 1$) structures; this assumption is justified by the representation of the two diffusion coefficients in Figure 4.8. The large

contour length implies large aggregation number N_S, already suggested by the high molecular weight value ($1.3 \cdot 10^8$gmol^{-1}) of the supramolecular structures suggesting ~$6 \cdot 10^4$ **1**-monomers per assembly. Consistency between this number and the value of the contour length (L) implies a micellar structure of the "repeat" unit.

Complementary information on the internal structure of the supramolecular assembly stems from the length density $M/L = Q\mathrm{R_{VV}(Q)}/(\pi \mathrm{H_C})$ ~$6 \cdot 10^{11}$ gmol^{-1}cm^{-1} obtained from the quasi-plateau $Q\mathrm{R_{VV}(Q)/c}$ value at high Q's (inset to Figure 4.7). For comparison, this quantity for the "monomer" **1** is about $3.8 \cdot 10^{10}$ gmol^{-1}cm^{-1} using 2300 gmol^{-1} for its molecular mass and 0.6 nm for its thickness [225, 226]. Hence its repeat unit should contain approximately 16 monomer units.

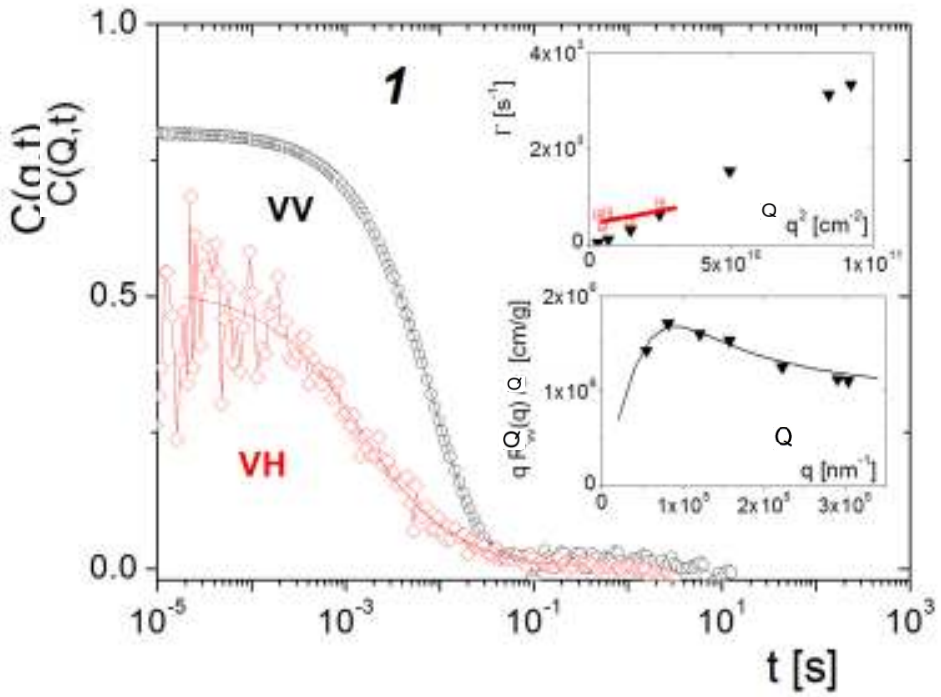

Figure 4.7*. $C_{VV}(Q,t)$ (open circles) and $C_{or}(Q,t)$ (open rhombi) at $Q = 0.0081nm^{-1}$ and 20°C for **1** at 0.007g/L recorded after annealing at T=50°C for few hours and subsequent slow cooling to 20°C. Inset: The single translational and rotational relaxation rate, and the Holtzer plot $QR_{VV}(Q)/c$ vs Q. Solid line denotes the representation by a worm-like model.*

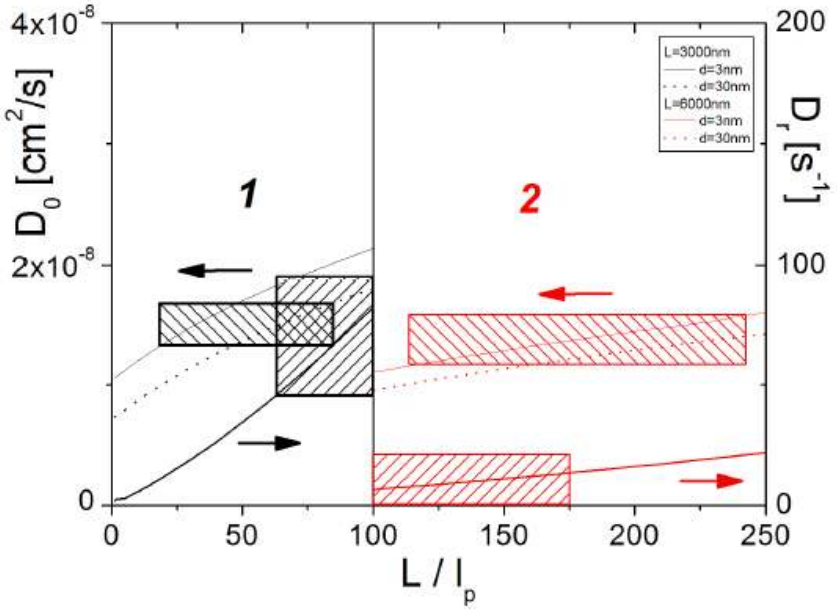

Figure 4.8. *Translation, D_0, and rotation, D_r diffusion coefficients as a function of the ratio L/l_P of the contour to persistence length according to worm-like model. The different lines indicate calculations based on the length parameters (L and thickness d) reported in the plot. The shaded areas indicate overlapping with the experimental values for* ***1*** *and* ***2*** *systems. Considering the effect of the polydispersity [227] between L_Z (for D_0), $L_W L_Z \sim 0.75$ for $M_W/M_n \sim 2$.*

As already mentioned, uncertainties in the determination of self-assembled structures are minimized if a consistent representation of the dynamic parameters is obtained. Both transport coefficients, D_0 and D_r can be represented by a worm-like model [222, 228] with three adjustable parameters, L_W, Kuhn segment, l_K and thickness, d assuming stick hydrodynamic boundary conditions. The speed-up of the two transport coefficients with flexibility L/l_p for constant contour length L and d, and their expected slowdown, though with different rate, with increasing L and d is shown (Figure 4.8). A simultaneous representation of both D_0 and D_r (skew and vertically hatched boxes in Figure 4.8) of the **1** assembly occurs for $L_W \sim 2.2\mu m$, $L/l_p \sim 70$, d~30nm, i.e., $l_p \sim 30nm$ in agreement with the representation of the $R_{VV}(Q)$ pattern in Figure 4.7. Considering the presence of size polydispersity [227, 229] and the different moments of the distribution entering the static and dynamic experiments, the dimensions and conformation of the supramolecular structure in dilute aqueous solutions of **1** can be adequately estimated.

Turning to the structure characterization for **2,** the experimental situation is less convenient due to the lack of access to all previous physical quantities. Figure 4.9, the analogue of Figure 4.7 for **1,** shows that at the concentration of $2.5 \cdot 10^{-4} gL^{-1}$ the assemblies are too large to be captured by the longest light scattering wavelength, i.e., absence of downturn in the Holtzer plot. Consistently, the rotational D_r is too low, i.e., the intercept $\Gamma_r(Q = 0)$ is not finite (insets to Figure 4.9). The information is then limited to the translation coefficient D_0 and the length density $M/L = Q\mathrm{R_{VV}(Q)}/(\pi \mathrm{H_C}) \sim 7 \cdot 10^{12} \mathrm{gmol^{-1}cm^{-1}}$ obtained from the quasi-plateau $(\mathrm{QR_{VV}(Q)})/\mathrm{c}$ value at high Q's in Figure 4.9 which clearly exceeds the corresponding plateau in Figure 4.7. The large M/L along with the shape of the Holtzer plot suggests high molecular mass. A rough estimate of the latter can be obtained from the $\mathrm{R_{VV}(Q \longrightarrow 0)/c}$ obtained from the intercept in the Debye plot which predicts linear dependence of $[\mathrm{R_{VV}(Q \longrightarrow 0)}]^{1/2}$vs Q^2 at low Q's; $M_W = R_{VV}(Q \to 0)/H_C$ is about 10 times higher than for **1**. The description of D_0 and $D_r \sim 0$ (skew and vertically red hatched boxes in Figure 4.8 by the worm-like model suggests larger dimensions: L~6μm, $L/l_p \sim 150$, d ~30nm, i.e., l_p~40nm and implies similar structure as of **1.**

The characteristic lengths summarized in the table of Figure 4.10 support the proposed supramolecular structures of **1** and **2** in dilute aqueous solutions as schematically illustrated in the same figure. As the diameter of the both worm-like structures of **1** and **2** largely exceeds the fully extended molecular size (8.9nm and 5.1nm for **1** and **2** according to Corey-Pauling-Koltun model) a columnar structure with a single molecule per layer, in which PEG protects the hydrophobic core can be excluded. In fact, each layer contains large number of molecules accounting for the high M/L values, which is different for the two structures. According to the hydrophilic/hydrophobic interactions and Percec's

tobacco mosaic virus model the HPB-PEG derivatives can self-assemble to small fibers [208, 209].

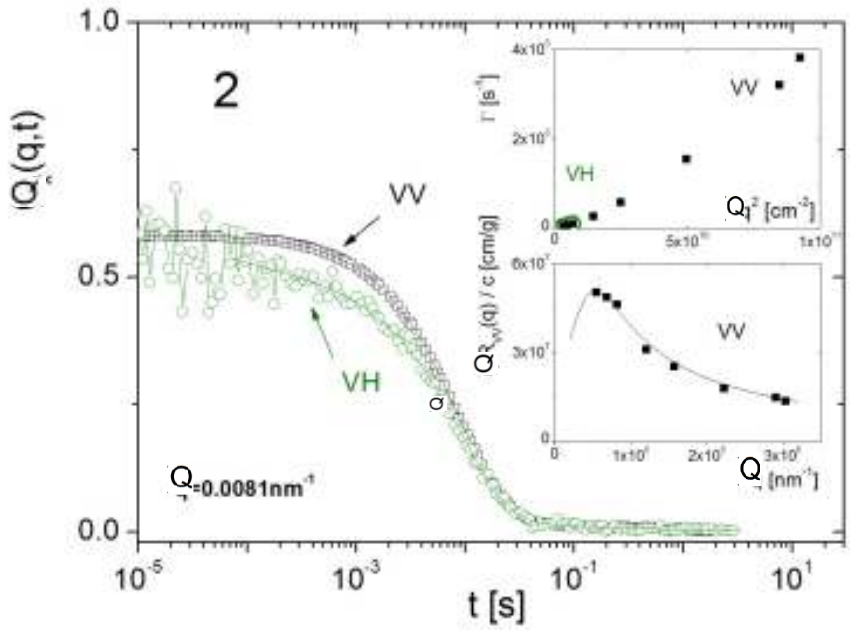

Figure 4.9. *$C_{VV}(Q,t)$ (open squares) and $C_{or}(Q,t)$ (open circles) at $Q = 0.0081nm^{-1}$ and 20°C for **2** at $2.5 \cdot 10^{-4}\ gL^{-1}$ recorded after annealing at T=50°C for few hours and subsequent slow cooling to 20°C. Inset: The single translational and rotational relaxation rate, and the Holtzer plot $QR_{VV}(Q)$ vs Q.*

Structural parameters	1	2	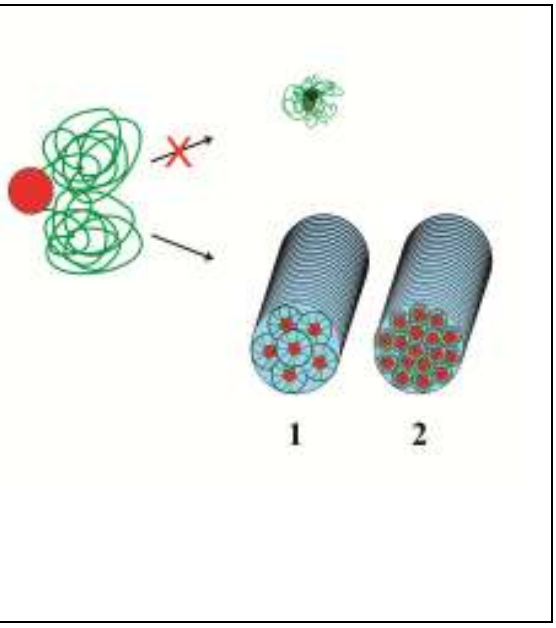
$M_w(gmol^{-1})$	$1.3 \cdot 10^8$	$1.8 \cdot 10^9$	
$M/L(gmol^{-1}cm^{-1})$	$6 \cdot 10^{11}$	$7 \cdot 10^{12}$	
$L_Z(\mu m)$	2.0	6.0	
L_Z/l_p	30	10	

Figure 4.10. *Structural parameters for **1** and **2** self-assembled structures in aqueous solution obtained from dynamic and static experiment. Schematic representation of the proposed self-assembled equilibrium structures of **1** and **2** conforming to the structural parameter.*

Further, we assume that several fibers are bundled to a single large supermolecular object (Figure 4.10) confirmed by cryo-TEM at high concentration (Figure 4.2). Superstructures of bundled fibers were reported for amphiphilic block copolymers of oligo(phenylene vinylene) and poly(propylene oxide) [216]. The assemblies of **2** have a higher density than **1**. In **2,** the shorter PEG chains can accommodate more molecules in the same cross-section. Based on the table in Figure 4.10, the superstructures of **1** and **2** with a volume $V = \pi d^2 L/4$ and mass M_w/N_A (N_A is the Avogadro number) have a density of about 0.2 g·cm^{-3} and 0.7 g·cm^{-3} for **1** and **2,** respectively. This disparity can be rationalized by the different swelling of short and long (degree of polymerization N>12) PEG chains in water [230]. The reported thickness increase of solid-supported lipid monolayers with PEG chains with humidity was ascribed to brush-like behavior of the PEG chains with N ≥ 12; for PEG with N = 3 and 6, the swelling was very low. It is therefore conceivable that the diameter of an isolated fiber is larger for **1** than for **2** due to the different water content. The difference in the persistence length (and hence stiffness) (Figure 4.10) can be also rationalized by the density disparity since the higher the number of molecules per layer is the stiffer the supramolecular structure is expected (for **2**).

In the concentration regimes presented above, $C_{VV}(Q,t)$ are single decay functions representing the translational diffusion of the supramolecular structures probed over distances of the order $2\pi/Q$ (in the range 200-1500nm). This picture is changed as the increase of the concentration leads to a spatial overlapping of the long worm-like structures. As shown in Fig. 4.11a, $C_{VV}(Q,t)$ at c=16.6g/L and 20°C cannot be described by one single decay but two processes become discernible and clearly revealed by ILT at high Q's (solid lines). A two decay $C_{VV}(Q,t)$ is in contrast to the dynamics of semidilute solutions of conventional homopolymers, where the chain translational diffusion D above the overlap concentration c*(~0.5g/L) crossovers to the cooperative diffusion D_C of the transient network above c*.

$$D_C/D \sim (^{c}/_{c^*})^{\nu/(3\nu-1)} \qquad (4.1)$$

where the scaling exponent $\nu = 0.5$ for Gaussian chains and about 0.6 for swollen ones [231]. From the two diffusion coefficients in Fig. 4.11c, it is the slow $D_S(Q = 0)$ that is comparable to D (~1.5x10^{-8}cm^2/s) in the dilute regime [182] and hence it is identified with D_C. The observed Q-dependence is due to the contribution of internal dynamics at high Q's. The new fast D_f is by an order of magnitude faster than D and it should indicate the presence of much small species, e.g., small micelles.

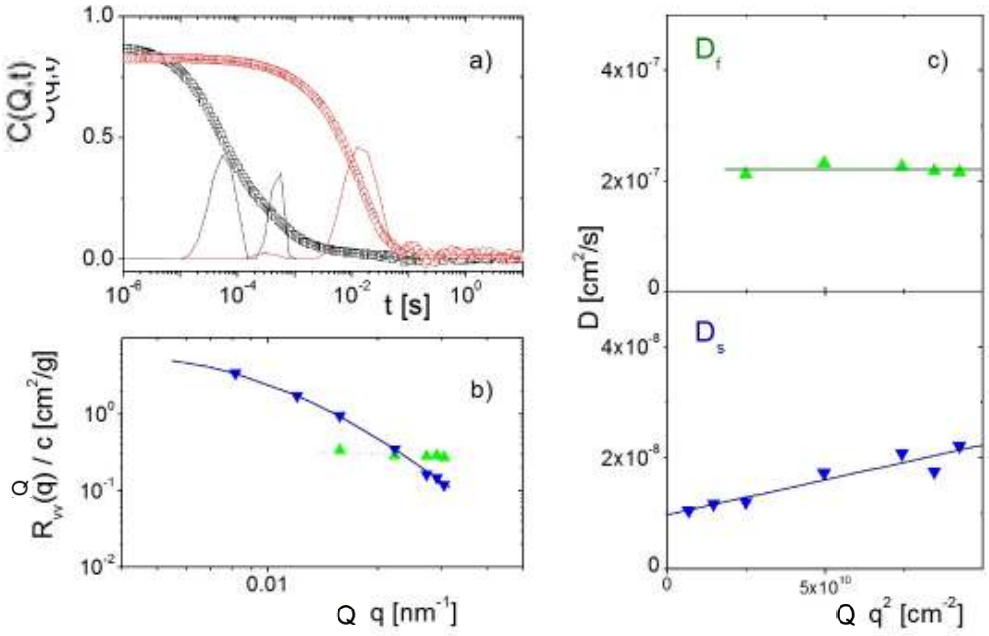

Figure 4.11. *a) Relaxation function $C_{VV}(Q,t)$ describing the diffusion of two species in a 16.6g/L aqueous solution of* ***1*** *at two scattering wave vectors ($Q = 0.0304\,nm^{-1}$, black and Q= $0.00815nm^{-1}$ red symbols) at 20°C as revealed by the inverse Laplace tranformation of $C_{VV}(Q,t)$ (black and red curves). b) The absolute Rayleigh scattering intensities associated with the large (slow) component (blue inverse triangles) and small (fast) component (green triangles) obtained from the average scattering intensity and the amplitudes of the two processes in $C_{VV}(Q,t)$. c) The fast (upper) and slow (lower panel) diffusion coefficients.*

The proposed assignment of the two diffusive processes is further supported by their contribution to the total light scattering intensity of the solution. The absolute intensities $(\mathrm{R_{VV}(Q)})/\mathrm{c}$) associated to the two processes, obtained from their amplitude in $C_{VV}(Q,t)$ and the total light scattering intensity of the solution, display distinctly different Q-

dependence as shown in Fig. 4.11b. The Q-independent contribution of the fast process (solid green triangles in Fig. 4.11b) is in accordance to the small size $R_m = kT/(6\pi\eta_0 D_f) \sim 12nm$ relatively to the wavelength of the probe laser light; η_0 denotes the solvent (water) viscosity. The slow process intensity, $R_{VV}(Q)$, however, exhibits a Q-dependence (Fig. 4.11b, inverse blue triangles) reminiscent of a much larger size, ξ_S. For long objects with characteristic size, R, the static mesh size [231]:

$$\xi_S(c) \sim R(c/c^*)^{-\nu/(3\nu-1)} \qquad (4.2)$$

of the network near and above c* can still be large [232].

For semidilute solutions of homopolymers, ξ_S can be obtained from the Q-dependence of the static scattering intensity, $R_{VV}(Q)$ represented by the Ornstein-Zernicke equation, $(R_{VV}(Q))/c \sim (1 + Q^2\xi_S^2)^{-1}$. The same mesh size is also entered in the hydrodynamic the Stokes-Einstein-Sutherland equation, $\xi(c) = kT/(6\pi\eta_0 D_S)$. This homopolymer semidilute solution behavior was found to apply for long and thin β-sheet tapes formed from the one-dimensional self-assembly of oligomeric peptides. In contrast, the semidilute solutions of the present assemblies deviate from this classical behavior. The slow process intensity contribution cannot be represented by the Ornstein-Zernicke equation but by the Debye-Bueche, $(R_{VV}(Q))/c \sim (1 + Q^2\xi_S^2)^{-2}$ (solid line in Fig. 4.11b) with $\xi_S = 90nm$ at ~17g/L (c/c*~35). The particular form of the $R_{VV}(Q)$ is justified by the thick (d~$30nm$) fiber-like strands of the network, as schematically shown in Fig. 4.13 below. The mesh size ξ computed from D_S at ~17g/L assumes a larger (200nm) value than $\xi_S = 90nm$.

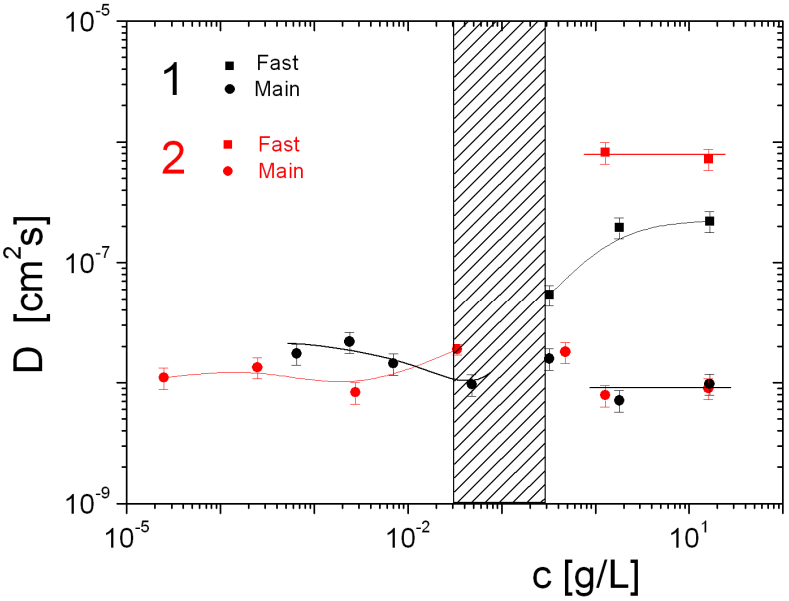

Figure 4.12. *Translational diffusion coefficient D obtained at* $D(Q \to 0)$ *as a function of concentration at 20°C for* ***1*** *and* ***2***. *The shaded area indicates a crossover to semidilute regime in which two relaxation processes in* $C_{VV}(Q,t)$ *are resolved.*

A convenient presentation of the structural changes in polymer solutes in solutions as a function of solute concentration has been described previously in Fig. 4.5. The crossover from dilute to semidilute regime is marked be the drop of intensity due to negative intereference between overlapping worm-like supramolecular objects. However, this transition is hardly seen in the dynamic plot (Fig. 4.12), propably due to size polydispersity and the slight shift to cooperative diiffusion at $\mathbf{c \sim c^*}$.

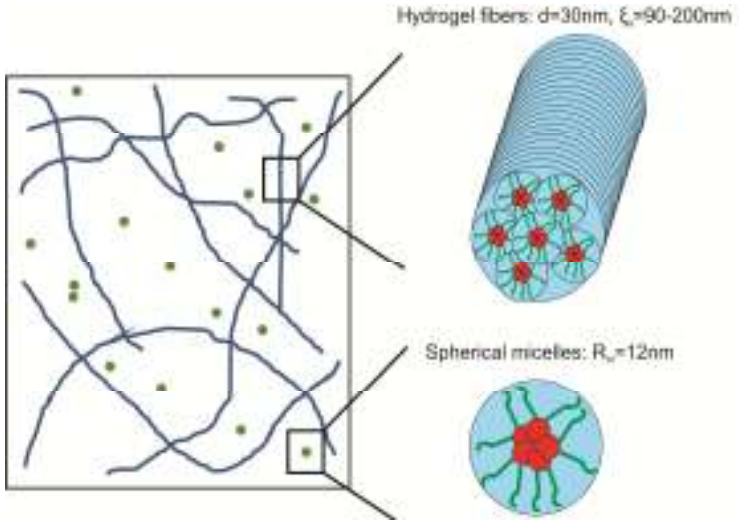

Figure 4.13. *The network structure of long hydrogel fibers coexisting with small micelles of* ***1***.

The Cryo-TEM image for a solution at c~31g/L in Fig. 4.12 reveals the presence of long fibers and micelles. This isotropic structure in semidilute solutions is further supported by the depolarized light intensity $I_{VH}/c \sim <\beta_2>[1+<3cos\theta_{ij}{}^2-1>]$, where $<\beta_2>$ is the segment optical anisotropy and θ_{ij} the angle between adjacent segments. The observed concentration dependence of I_{VH}/c shown in the inset of Fig. 4.14 excludes the formation of liquid-like structure with $<\theta_{ij}>\sim 0$. Instead the unexpected drop of I_{VH}/c near c* indicates a random segmental orientation, which is further supported by the viscoelastic measurements discussed below, which do not show any signature of nematic liquid-crystalline domains [233].

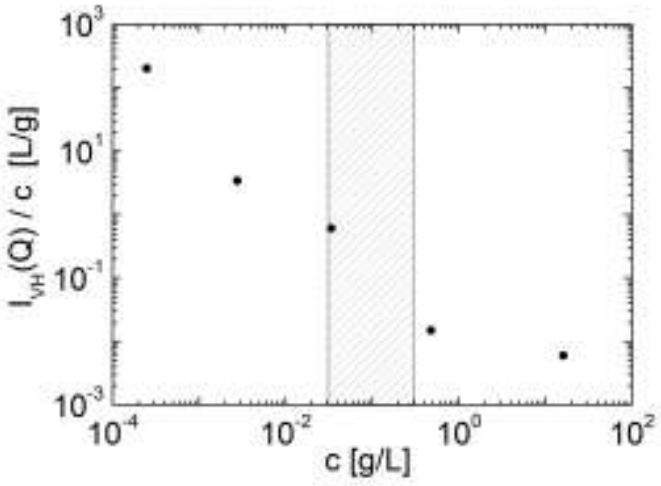

Figure 4.14. *The depolarized scattering intensity normalized with concentration as a function of concentration.*

For concentrations $c > 100g/L \approx 200c^*$, the solutions were found by shear rheometry to exhibit solid-like behavior. Shear rheometry probes the linear and nonlinear viscoelastic response of a sample in rheometric simple shear flows. Rheological measurements of the different aqueous solutions of the hydrogel fibers were performed with a sensitive strain-controlled ARES 100 FRTN1 rheometer (Rheometric Scientific, USA) and a stress-controlled Physica MCR-501 rheometer operating in strain-controlled mode (Anton Paar, Austria). A home-made, stainless steel cone-plate geometry was utilized (4 mm diameter, 0.04 rad cone angle, in order to accommodate the minimal

amounts of sample available, (of the order of 50 mg) along with a Peltier temperature control system (at 20°C). A home made solvent trap that saturates the atmosphere with solvent vapor and thus minimizes the risk of evaporation was used. The solvent trap was shown to be particularly efficient for these aqueous solutions for at least 2 hours. Details of the experimental the protocol applied in these measurements is described extensively in Chapter 2.3.

Typical viscoelastic spectra are shown in Fig. 4.15. It is worth noting that for all concentrations $G' >> G''$ and $G' \sim \omega^0$ throughout the whole frequency range, whereas G'' increases weakly as the frequency is reduced. Such a behavior reflects the formation of entanglement-like network of fibers, which is expected for micrometer long lengths at these relatively low concentrations. We assign this solid network to a physical gel. This is consistent with the reported gel-like network formation in aqueous solutions of long fibrils made from self-assembled peptide beta-sheet tapes [232, 234, 235]. Considering that the effective plateau modulus is kT/ξ_{rheo}^3, with ξ being the correlation length (mesh size), we find that passing from 150 to 311 mg/ml results in a tenfold decrease of the average ξ_{rheo} from 220 to 23 nm, i.e., a decrease much stronger compared to that expected from the semidilute scaling (eq. 3.5). Note that these concentrations are much higher than those of the PCS experiment falling in the low range of the semidilute regime with liquid-like and not solid-like behavior. In fact, for the semidilute solutions, concentrations up to about 100g/L show a viscous liquid-like bahavior, while higher concentrations exhibit gel-like, as shown in Fig. 4.15. The strong decrease of ξ_{rheo} between 150 to 311g/L occurs in the gel regime suggesting that other interactions in addition to the topological entanglement constraints of purely entropic origin contribute to the gel formation well above c*. Hence, whereas a rationalization remains elusive at this point, the experimental evidence calls for the presence of additional interactions (beyond entanglements), as discussed below.

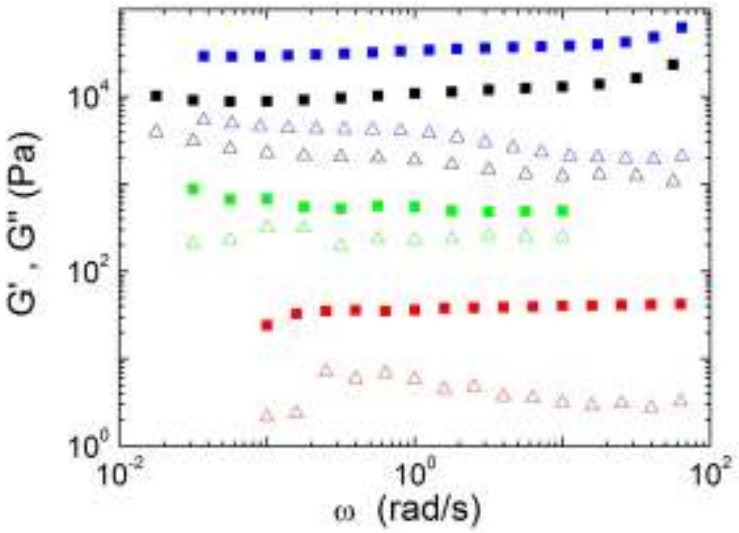

***Figure 4.15**. Dynamic storage (G′, solid squares) and loss (G′′, open triangles) moduli of four solutions of 1 in the gel regime at 20°C. The blue, black, green and red points represent the data extracted from 311 g/L, 255 g/L, 200g/L and 150 g/L concentrations, respectively.*

Fig. 4.16 compiles the results from the rheological measurements. A liquid to gel transition is clearly observed. Such an abrupt change from sol-to-gel is known from other systems e.g. PEG-PLGA-PEG in water [236]. This sudden transition takes place because a certain amount of **1** is necessary until the concentration and the interactions are enough for forming a gel. For concentrations higher than 140 g/L, measuring zero shear viscosity is not feasible anymore and the solution of HPB-PEG derivative **1** develops a plateau modulus (Fig. 4.15) which reflects the formation of entanglements among the hydrogel fibers. Although the available data are not enough, it is tempting to remark that with the viscosity increases as a function of concentration with a power-law slope of about 2.5. This signifies semidilute solution behavior of flexible linear polymers [231] (for unentangled and good solvent $\sim \phi^{1/(3\nu-1)} \sim \phi^{1.2}$ or ϕ^2 in theta solvent ; for entangled and good solvent $\sim \phi^{3/(3\nu-1)} \sim \phi^{3.9}$), and is consistent with the estimated c* from DLS (0.5 g/L).

On the other hand, the plateau modulus G'_p in Fig. 4.16 seems to follow a power-law exponent of about 8 with concentration, which is much larger than the value of 2.25 of linear flexible polymers and semidilute and entangled regimes [235] or the value reported

from hydrogels formed spider silk fibrous proteins [200]. This suggests that, whereas a concentration well above c* is needed for the gel to form, fiber topology (analogous to entangled flexible polymers) is not the only reason for gelation. In addition, there seem to be fiber-fiber attractions, likely van der Waals and hydrogen bonding of the PEO grafts to promote local associations, hence gelation. Similar power-law exponents of non-dilute solutions have been reported for spherical colloidal particles. For example, two oxyethylene/oxybutylene block copolymers ($E_{92}B_{18}$ and $B_{20}E_{510}$) forming spherical micelles in aqueous solution were found to exhibit power-law exponents μ between 3 and 5.3 [237]. For aqueous suspensions of PS/PNIPAM core/shell particles, $\mu = 4$ [238] whereas for PMMA hard spheres suspended in benzyl alcohol, $\mu = 7.7$. In general, increasing softness leads to a lower exponent [169]. Similar behavior has been also observed in associating telechelic polymers. For example, Suzuki et al. [239] reported that urea-functionalized polymers are capable of forming local micellar clusters via inter- and intra-chain association, which resulted in stronger dependence of G'_p on concentration. They invoked the formation of a percolated network connected through micelles in order to explain their findings.

Inspired by this we attempt at explaining the strong concentration dependence of our fiber network by considering fibers connected with each other as well as through spherical micelles. The DLS analysis (above) showed the coexistence of two species in the semi-dilute regime. With the help of the cryo-TEM images, these species were attributed to spherical micelles and bundles of fibers. With increasing concentration the fibers and spherical micelles come closer and the probability of getting into contact is higher. This is statistical, hence, it is promoted at higher concentrations. But once this happens, the micellar "hair" PEG chains penetrate those of the fiber, resulting in strong hydrogen bonding and core-core interaction (existing already in within the fiber). Naturally, interacting fibers (i.e., crossing) exhibit similar bonding, which is much stronger than the

classic topological bond of an entanglement network. This is why the modulus increases so rapidly with increasing concentration. To rationalize this, we argue that at high concentrations of molecule **1**, water is not truly good solvent for PEG, hence there is strong micelle-fiber interpenetration, leading to a smaller surface of PEG which is energetically favored [240]. Such "fusion" of fibers and spheres is known from the rod-sphere transition of block copolymers [241]. Of course in our case, perhaps due to the special shape of molecule **1** ("triangular") a complete rod-sphere transition is not possible.

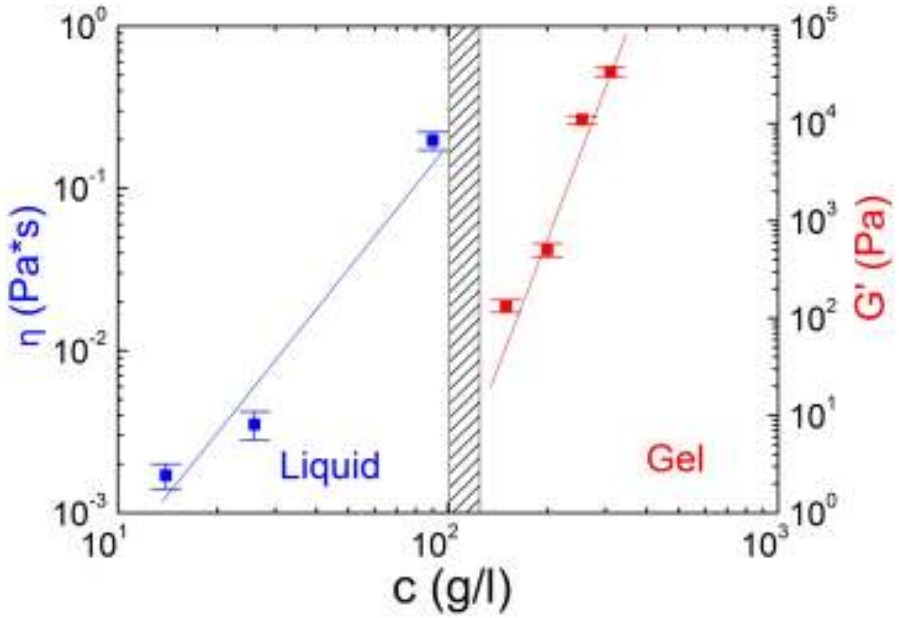

Figure 4.16. *Concentration dependence of the zero-shear viscosity and effective plateau modulus of the HPB-PEG derivatives. Lines are drawn to guide the eye.*

For example, at high concentration, say 311 g/L (see Fig. 4.17, where the space filling is higher than it was drawn in the cartoon), in addition to fiber-fiber contact the spherical micelles can interact with the fibers and bind with them in three different ways. Bonding should be strong based on the above speculative picture.

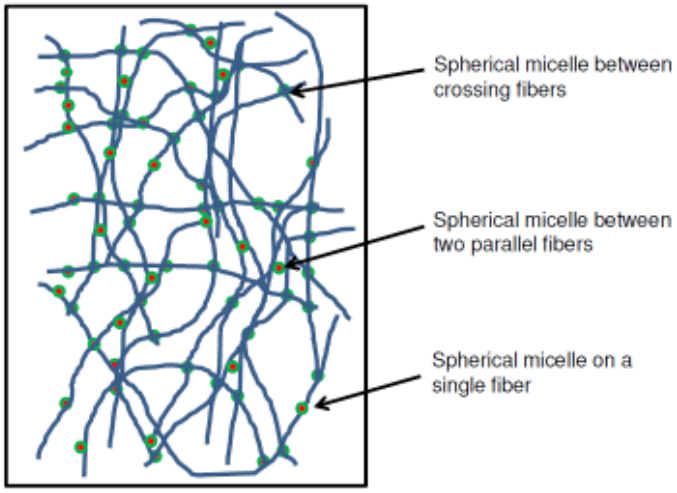

Figure 4.17. *Model of HPB-PEG (c=311 g/L) in water forming a network connected through spherical micelles.*

Another example corroborating our picture is the gelation of poly(2-methoxy-5-(2'-ethylhexyloxy)-1,4-phenylenevinylene) MEH-PPV. The solution of this polymer turned into gel by colloidal bridging after one-day aging [240]. The main difference from the present work is that there is a rod-like packing of MEH-PPV which leads to bridging whereas in our case two different species (bundles of fibers and spherical micelles) exist. We also note that covalently crosslinked PEO-PPO-PEO triblock copolymers were reported to exhibit improved mechanical properties compared to conventional hydrogels [242]. In general, colloidal gels exhibits power-law exponents (above 4) and this depends on their fractal dimension [243, 244]. However, the main difference between these examples and our system is that the colloidal aggregates are much larger (micrometer-sized colloidal aggregates) compared to the spherical micelles of HPB-PEG, whose size is several nanometers.

The present fiber gel behaves as a yield stress material, i.e., it liquidifies under the action of stress [245]. In fact, the study of yield stress is an old topic that remains at the forefront of engineering research, in large due to its vast technological implications. Here, however, we shall only use an established yielding protocol, oscillatory strain-amplitude sweeps at a given frequency [165], in order to compare the mechanical conditions of

yielding for different concentrations (i.e., gels). A typical example is depicted in Fig. 4.18a where the recorded moduli G' and G'' are plotted against the imposed strain amplitude γ_0 at a frequency of 1 rad/s. The crossover of G' and G'' corresponds to the yield strain γ_y and yield stress $\sigma_y = (G'^2 + G''^2)^{1/2}/\gamma_0$ for the given frequency and concentration. At strain amplitudes $\gamma_0$below γ_y, the material exhibits solid-like response ($G' > G''$) and above γ_y, it exhibits liquid-like response ($G'' > G'$). Note that as the yield point is approached, $G'$is reduced whereas G'' increases and in fact reaches a maximum at about the yield point.

The so obtained yield stress and yield strain values are plotted against concentration of the HPB-PEG derivatives in the inset of Fig. 4.18a. The independence of the yield strain at about $\gamma_y = 20\%$, upon the concentration increase is typical of gels with some kind of ductile response [246]. Simultaneously, the yield stress exhibits an increase with the concentration as $\sigma_y \sim c^{7.5}$, in agreement with the increase of the plateau modulus (Fig. 4.16), hence confirming that $\sigma_y = G_p\gamma_y$. The strong concentration dependence reflects the strong H-bonding between the fibers as discussed in the context of our proposed picture (Fig. 4.17).

Moreover, in Fig. 4.18b we see the Lissajous-Bowditch (LB) representation of stress as a function of strain during oscillatory cycles at different values of strain amplitude [247], for a HPB-PEG derivative with concentration 311 g/L in water and an oscillatory frequency of 1 rad/s. For small strain amplitudes the material exhibits a viscoelastic solid response whereas with increasing strain amplitude viscous dissipation becomes more significant. At the highest value of $\gamma_0 = 100\%$ it is clear that the different cycles used for obtaining the LB plots do not superimpose. We note that this effect has been observed for all nonlinear strain amplitudes (for example, it is clearly observed for 30% in Fig. 4.18b), but is more pronounced at larger values. In particular, these plots reflect a sequence of

processes starting from elastic deformation at stresses $\sigma > 0$, with the effective modulus $G_{eff} = d\sigma/d\gamma$ at $\sigma \to 0$ (obtained from the stress-strain slope in the LB plots of Fig. 4.18b, see also Ref. [247]) being identical for all strain amplitudes, continuing with enhanced viscous dissipation and thinning, and closing the cycle back to solid-like response and so on [247]. However, at the highest strains the dissipative part shows clear time dependence (or aging) in the sense that with increasing time the stress decreases and eventually appears to reach a steady state.

This behavior suggests a strong interplay of shear and structural time, or else thixotropy in the system, which can be understood in terms of bonding and debonding. In Fig. 4.18a we also plot G_{eff} against strain amplitude (red closed triangles). We observe that G_{eff} is almost identical to G' at lower strain amplitudes and slightly decreases with increasing strain amplitude. This slight decrease is at odds to what has been observed in dense systems like colloidal glasses [247] and suggests that the HPB-PEG derivative gel is weakly thixotropic, i.e., it takes some time to reform after shear-induced break-up, in contrast to the nearly non-thixotropic glassy systems [247]. The thixotropic response [243] of this gel is better appreciated in Fig. 4.19, where the apparent G' of the 311 g/L aqueous HPB-PEG derivative solution is plotted as function of time during a dynamic strain sweep starting at $\gamma_0 = 0.1\%$ and reaching a maximum strain amplitude of $\gamma_0 = 300\%$, at a frequency of 1 rad/s. This is in fact the same test at Fig. 4.18a but plotted against time. The dramatic decrease of G' by more than one order of magnitude signifies the break-up of the gel and a fluid response (see also Fig. 4.18a).

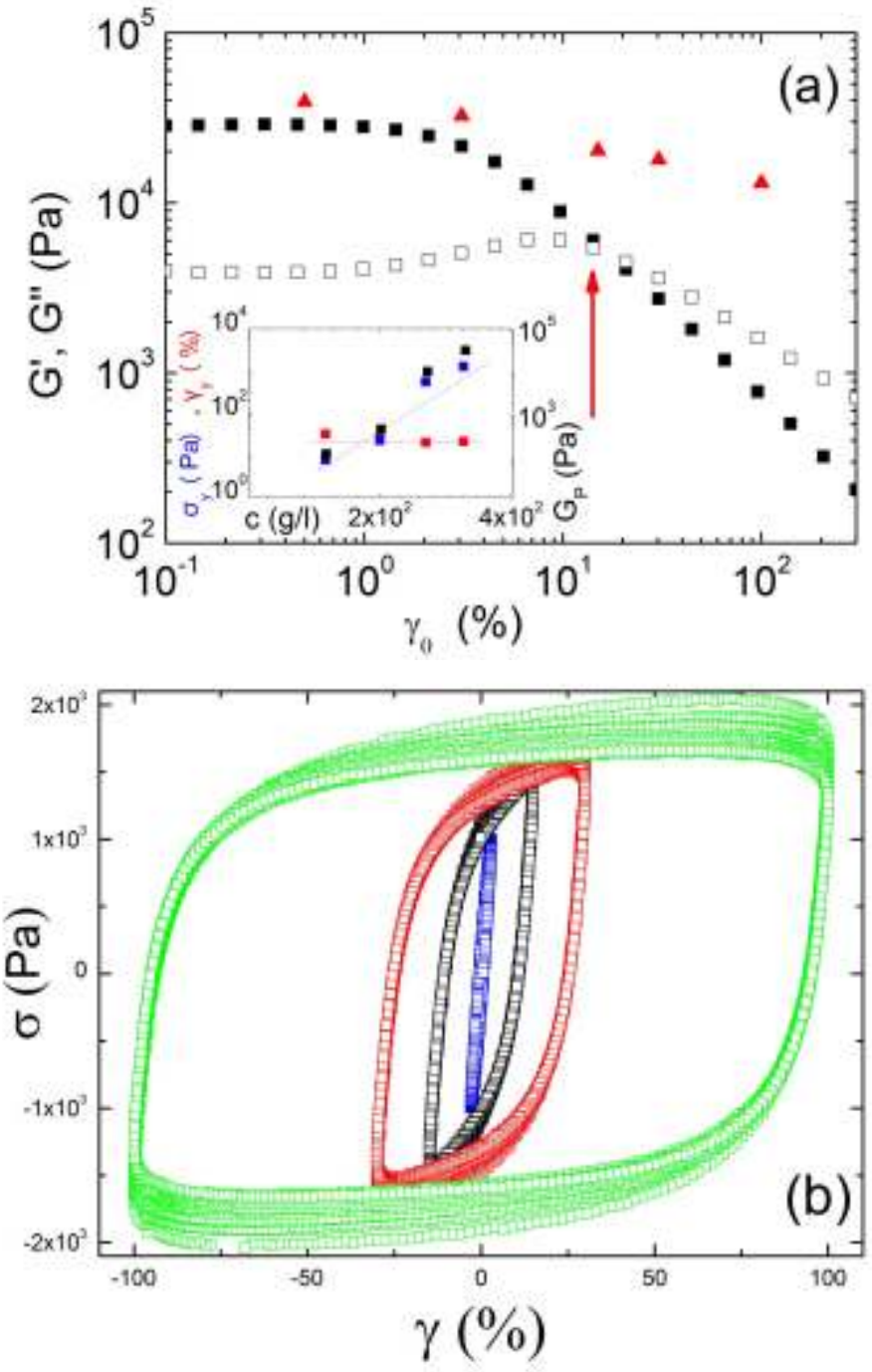

Figure 4.18. *(a) Dynamic strain amplitude sweep for a 311 g/L aqueous HPB-PEG derivative solution at 1 rad/s. Along with the apparent viscoelastic storage (black squares) and loss (red squares) moduli, the values of the effective modulus* $G_{eff} = d\sigma/d\gamma$ *at* $\sigma \to 0$ *are depicted with full triangles (see text for details). The vertical arrow indicates the yield point. Inset: Concentration dependence of the yield stress and yield strain (left axis), determined from the crossover of* G' *and* G'' *in strain amplitude sweeps such as that of (a), and of the plateau modulus extracted from the frequency sweeps (right axis). (b) Typical Lissajous-Bowditch representation of stress vs strain for different strain amplitudes, obtained from oscillatory measurements (see text). Here it is shown for a 311 g/L aqueous solution of HPB-PEG derivative at 1 rad/s. Data obtained at strain amplitudes 100%, 30%, 15% and 3% in the direction inwards.*

Hence, for about 1000s the material is in the linear viscoelastic regime (quasi-equilibrium), for another 1000s it undergoes nonlinear deformation with yielding and modulus decrease and then, upon flow cessation its structure builds-up very fast as evidenced but the increase of G' to steady state, which is nearly identical to the original G'_p value. In fact, it is slightly higher than G'_p, suggesting that the system is weakly metastable, hence corroborating the picture of physical gelation put forth. Indeed, given the specific pre-shear history (which leads to yielding of the gel), it is expected that the reformed (aged) gel will be slightly different from the original. One may even think is terms of the system reaching different local minima in the energy landscape.

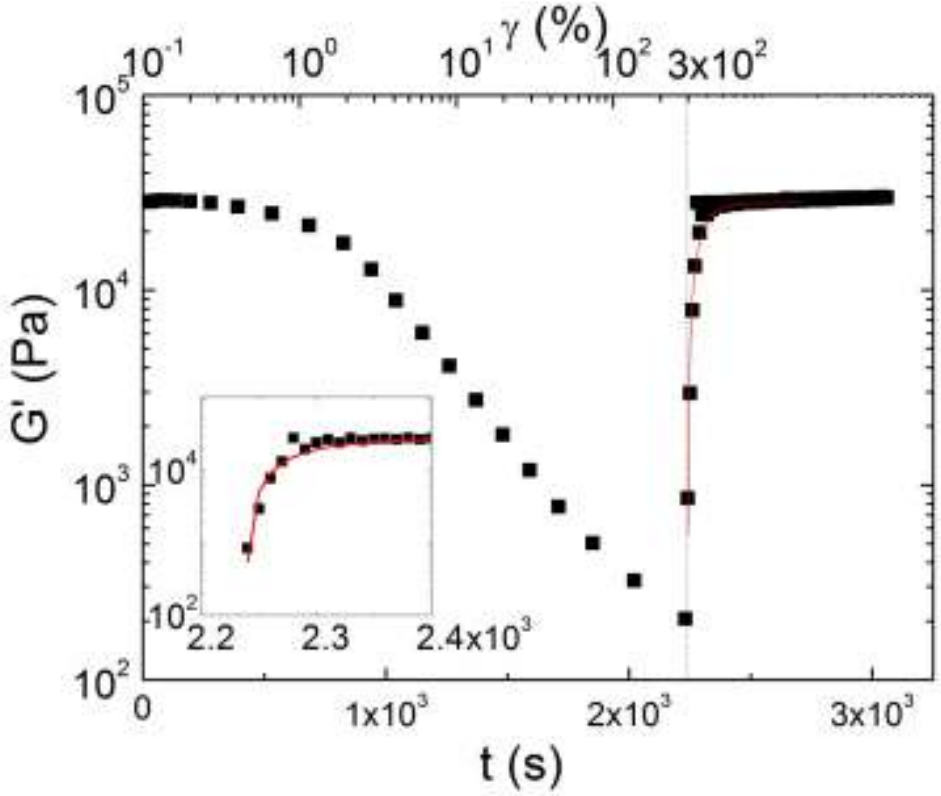

Figure 4.19. *Apparent G' as function of time during a dynamic strain sweep of a 311 g/L HPB-PEG derivative solution in water, starting at $\gamma_0 = 0.1\%$ and reaching a maximum strain amplitude of $\gamma_0 = 300\%$. The data are plotted against time and indicate that the sweep is completed after the measurement at 300% is taken and the whole duration is $2220\,s$. The dramatic decrease of G' signifies break-up of the gel and a fluid response. Upon completion of the strain sweep, a dynamic time sweep is performed at a small linear strain amplitude of 1% and frequency of 1 rad/s, reaching a steady state value. Inset: Characteristic gel reformation time τ_{gel} after shear-induced break-up as function of concentration (see text).*

The structural build-up of the gel after the large strain amplitude has been a very intriguing task. Upon completion of the strain sweep at $2200s$, a dynamic time sweep is performed at a small linear strain amplitude of 1% and frequency of 1 rad/s, in order to probe the structural evolution of the broken gel (aging). It can be observed in Fig. 4.19 that the system reaches a steady state value of G' rather fast as already mentioned, indicating full reversibility of the process in this metastable system with very fast aging kinetics. The gels can be disrupted mechanically and rebuild strength over time. Our understanding of this phenomenon can be imaged in Fig. 4.20. During shearing the spherical micelles are ripped apart from the fiber (Fig. 4.20 right) leading to a viscoelastic behavior. After $2000s$, the spherical micelles stick again to the fibers, the three dimensional network is reformed, large amounts of water can be entrapped and the elastic gel is rebuilt (Fig. 4.20 left).

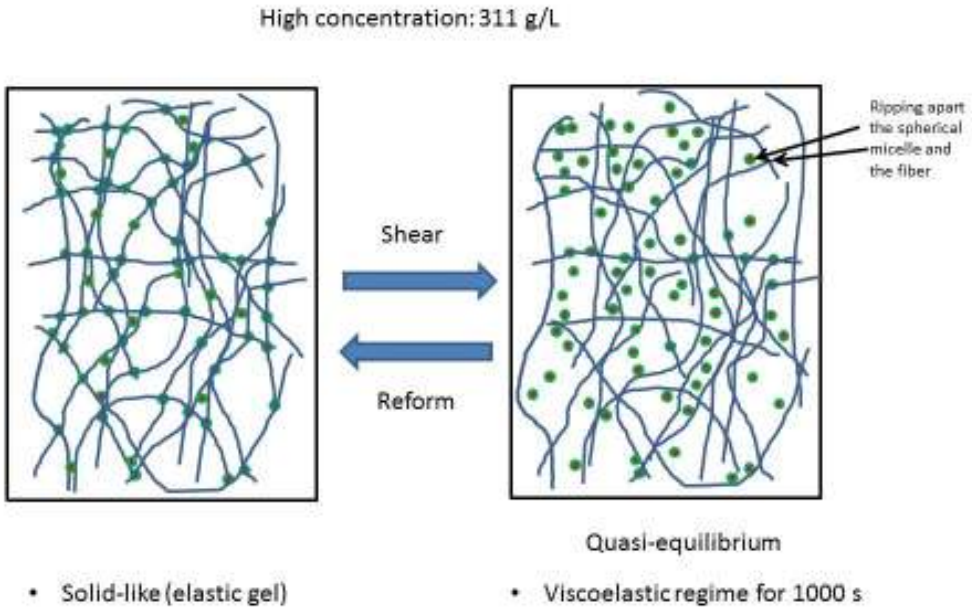

Figure 4.20. *Model for the shearing of the aqueous solution of HPB-PEG.*

Alternatively, the fiber network of Fig. 4.20 can be thought of as a self-healing gel, which breaks-up under shear and reforms in time. The gel reformation time can be estimated by fitting the linear time sweep of Fig. 4.19 with a function of the form $G' = G'_{steady-state}[1 - \exp(-t/\tau_{gel})]$ shown by the solid red line in the inset plot of

Fig. 4.19. The steady state value of G', is found to be identical to the original G'_p value. At the same time, the characteristic gelation time τ_{gel} is found to be rather short, about 50s, and more remarkably, to be virtually independent of concentration in the limited range investigated. This is qualitatively consistent with the weakly decreasing G_{eff} with strain amplitude and suggests, again, that the origin of gelation is not only topological but, more importantly, due to the fiber-fiber interaction. The very fast reformation time complies with the strong bonding energy discussed above and the associated elasticity of the network. Given the nature of the performed experiment (the sample was sheared with continuously increasing strain amplitude from 10% to 300% in the nonlinear regime for about 10^3s, it is not possible to directly compare against other gels (which are typically sheared at constant amplitude exceeding 100% from not more than $600s$. Nevertheless, given the dramatic decrease of G' achieved beyond the yield point, it is instructive to consider that colloidal gels are characterized by reformation times which are orders of magnitude slower [246]. The fast gel reformation time is suggestive of the robustness of the fibers and the fact that yielding relates to the break of fiber-fiber and fiber-micelle contacts (rather than break of fibers into pieces). These contacts reform spontaneously very fast in a dense solution, whereas if the fiber breaks into pieces its overall reformation may be a bit slower as it may involve motion of broken pieces (a more complicated structure would have a clearly different modulus which is not the present case).

In conclusion, for the first time, a detailed study of the self-organization of a two-dimensional, flexible HPB-PEG amphiphiles was performed. HPB-PEG derivatives form bundles of hydrogel fibers in very dilute aqueous solution. It has been shown that, the water amount in the hydrogel fibers does not depend on the number of hydrophilic groups but on the length of the PEG chains and the shape of the precursor molecules. Molecule **2** with the shorter PEG chains led to longer and stiffer self-assembled structures containing less water than the longer PEG chains.

At higher concentrations the fibers form a solid network which is recognised as a physical gel. It has been proven that fiber topology is not the only reason for the gel formation. There seem to be fiber-micelle contacts along with fiber-fiber interactions, which increase rapidly the elasticity of the network as a function of concentration. Large shear rates liquidify the gel structure of the system, which, however, reforms rather fast after the shear cessation. This fact drives us to believe that oscillations at large strain amplitudes lead the system to a debonding state, meaning that the connections between the fiber-fiber and fiber-micelle are lost. The fast gel reformation suggests that, at large strains, the fibers are not broken into pieces because in that case the time needed to reform would be much larger.

Herein, we argue that the hydrogel fibers with the variable water uptake resemble nature systems unlike fiber formation processes e.g. extruding, microfluidic processes and electrospinning. Although a direct comparison to natural systems is presently not possible, similar antagonistic forces (hydrogen bonds, Van der Waals forces) are responsive for the formation of well-defined objects. It has been demonstrated that in water, swellable fibers can be created utilizing hydrophobic and hydrophilic interactions. These interactions have to be carefully tuned to allow thermodynamic control of the systems. We showed that this control is possible by varying the hydrophilic building blocks of the amphiphiles. Due to the strong interaction among the hydrophobic (HBC) units, the yielded self-assembly becomes kinetically controlled. Similar to nature, our case was controlled by different molecular interactions. However, the main difference is that nature achieves such extended hydrogel fibers by the self-assembly of large polymers such as polycarbohydrates or polypeptides, while we focused on “small” two-dimensional amphiphiles.

5. Hydrogels exhibiting self-healing, pH- and temperature-responsiveness for localized targeted drug delivery.

While the overall incidence of cancer mortality has steadily decreased over the last decades thanks to improvements in the effectiveness of new drugs, early detection and delivery of technology advancements are still in high demand. For example, there are some types of cancer, i.e. pancreatic cancer, where the mortality is still increasing. Despite the recent techniques involving nanoparticulate drug delivery through intravenous administration, which deliver drugs to most parts of the body, a more efficient targeted technology is required in order to achieve selective accumulation in cancer cells rather than in the healthy ones. The challenges that current delivery techniques face are the severe barriers that prevent the nanoparticles from reaching the target, such as the pancreatic cancer (*PC*). PC has the unique property among other forms of cancers, of a high stromal-to-epithelial ratio. Tumor stroma increases the interstitial fluid pressure, which impedes drugs from penetrating the tissue interstitium. Unlike other solid tumors, in which cancer-associated fibroblasts promote tumor growth and angiogenesis, the fibrotic stroma in PC inhibits the formation and the function of blood vasculature. As a result drug delivery via perfusing blood is diminishing, leading to poor effectiveness of systemic chemotherapy by using drug nanoparticles as nanocarriers [248, 249]. It is clear that for this tumor it would be desirable to apply local administration technology rather than nanoparticulate drug carriers for effective drug delivery.

The best systems to achieve local drug release involve hydrogels. However, in order to achieve effective and selective drug delivery via hydrogels, the materials carrying the drugs must present specific characteristics to achieve effective and sustained release and must be solely administered to reduce patient morbidity. The drug carrier should present multiple functions so as to implant the formulation into the body without surgical operation, to prolong the drug release kinetics from the hydrogels, and to expand the

nature of deliverable drugs. Today, most of the materials used to deliver drugs through the hydrogel approach function only when injected within the cancer tissue taking advantage of the lower pH and the higher temperature turning into situ-forming hydrogels, followed by unselective drug release [250-252]. However, the injection of such a large amount of a solid material in the cancer tissue results in trauma and metastasis. To our knowledge, there is no "smart" hydrogel In the market to locally deliver chemotherapeutics to treat cancer with the desired properties mentioned above. Advanced synthetic chemical approaches are required to produce a polymer that will have the appropriate functionality to afford a "smart" hydrogel. Golinska M. et al. presented a triblock quarterpolypeptide that was pH-sensitive and formed self-healing hydrogels, but did not use it to deliver drugs at cancer tissues [253].

In this work, we present formulations with macromolecular architecture that gives the desired *in situ*-forming, injectable and rapid self-healing properties. The system consists of a pentablock polymer composed of one middle hydrophilic block, two hydrophobic blocks, followed by two hydrophilic blocks, each one of them connected at the other side of the hydrophobic blocks. In order to achieve the desired properties, we synthesized two different pentablocks, one terpolypeptide and one hybrid quarterpolymer. The chemical structures of the polymers are provided in FIG. 5.1. Details of the two polymers are given in Appendix A.

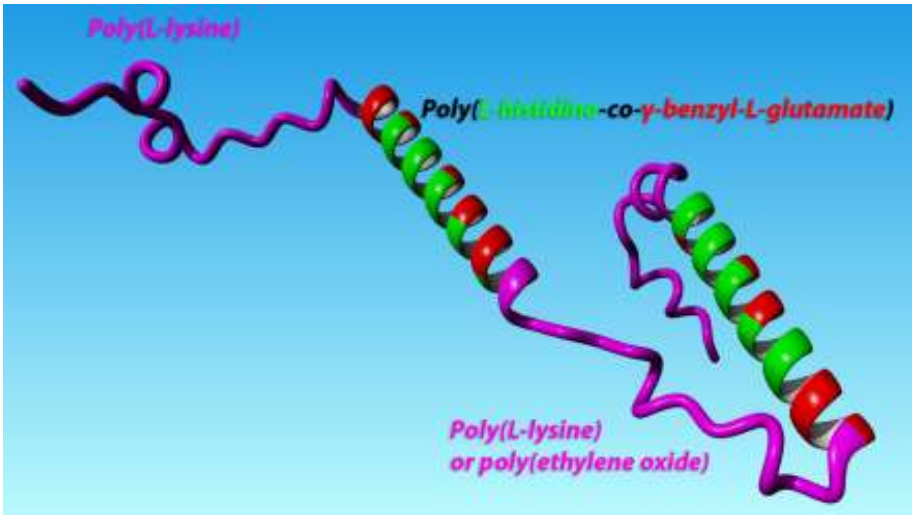

Figure 5.1. *Polymeric structures of the invention used to form hydrogels.*

5.1. Amphiphilic Pentablock Terpolypeptide Hydrogels

The pentablock terpolypeptide was characterized by a combination of methods. The combined characterization methods revealed that the pentablock terpolypeptide was the one expected by the stoichiometry and the design of the synthesis. The SEC chromatograms of the synthesis of the PTH are given in FIG. 5.1.1. As we can see in FIG. 5.1.1 the polymers have low polydispersity and high degree of molecular and compositional homogeneity.

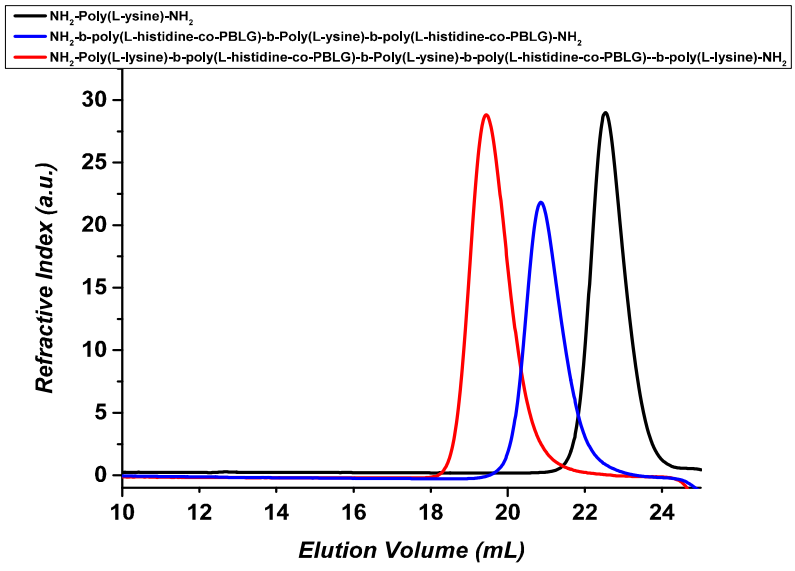

Figure 5.1.1. *Size Exclusion Chromatograms of the synthesis of the PTH polymeric material with a mobile phase of water/acetonitrile/trifluoroacetic acid in a composition of 60/39.9/0.1 (v.v).*

The strength of the hydrogel as a function of water content, drug content, pH and temperature between the values of cancer and healthy tissues has been studied by rheology measurements. The measurements were performed by utilizing a sensitive strain-controlled ARES 100 FRTN1 rheometer (Rheometric Scientific, now TA, USA) with force rebalance transducer 0.004 to 200 gcm torque and a home-made cone-plate stainless steel geometry (25 mm diameter, 0.04 rad cone angle). Temperature control (of ±0.4°C) was achieved via a recirculating ethylene glycol/water mixture temperature control system, whereas the measured sample was separated from the external environment by being covered with PDMS oil with viscosity of 4.7cPa. The experimental protocol is described in Chapter 2.3.

First we examined the rheological properties of the empty hydrogel, i.e. the hydrogel without drug. The parameters that influence the strength of the hydrogel are a) the concentration of the polymer, i.e. the polymer to water content ratio, b) the temperature and c) the pH. Initially, we studied the dependence of the strength of the empty hydrogel as a function of polymer concentration and pH at constant temperature of 37^{o}C, i.e. the temperature of the animal's body. It was found that the concentration of the hydrogel influences significantly the storage modulus G' and the loss modulus G'' of the hydrogel, as shown in Dynamic Frequency Sweep (DFS), as well as Dynamic Strain Sweep (DSS) measurements of the empty hydrogel PTH at pH=7.4 shown in FIG. 5.1.2b and FIG. 5.1.2a, respectively. The concentrations are referred as the ratio of the polymer to the water content. For example, c=1:30 reflects that for every 1 mg of polymer there are 30 mg of water in the solution. In FIG. 5.1.2, we observe the concentration dependence of the hydrogel at body temperature (37°C). The moduli drop with the decrease of concentration and the gel becomes weaker, exhibiting a crossover of the moduli in the lower concentration at low rates. Interestingly, the yield strain (crossover of the moduli from DSS) seems to increase upon dilution depicting a more flexible system [254].

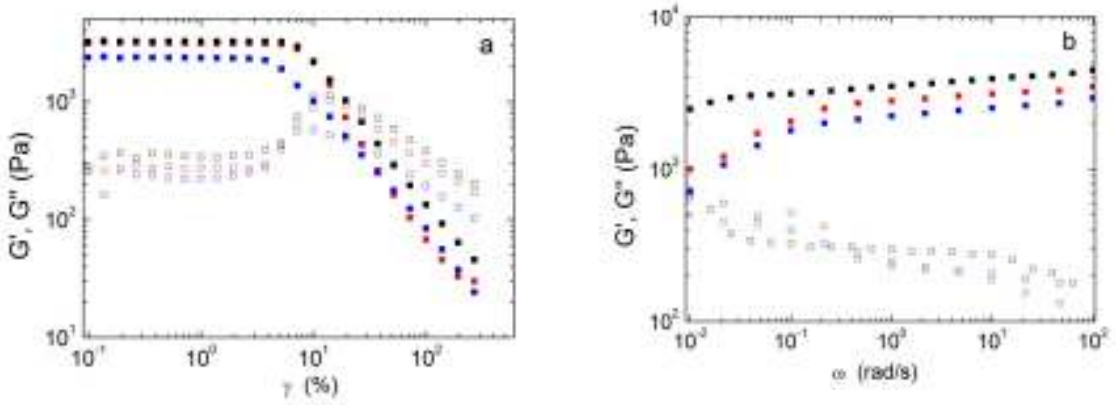

Figure 5.1.2. *a) Dynamic Strain Sweep of 3 different concentrations of the hydrogel PTH at pH7.4 and 37°C. Storage and loss moduli are represented with full and empty symbols, respectively. Concentrations of 1:30, 1:40, 1:60 are represented with black, red and blue colors respectively. b) Linear viscoelastic spectra of the 3 different concentrations of the hydrogel PTH at pH7.4 and 37°C. The moduli are plotted against frequency. The colors represent the same concentrations as (a).*

Subsequently, we studied the influence of the pH and temperature on the empty hydrogel (FIG. 5.1.3). The concentration of the polymer in the figure is c=1:30. The DFS plots of the PTH at 37^{o}C are depicted in FIG. 5.1.3a, each at three different pH values, i.e. at 7.4, 6.5 and 6.0. The results showed that the influence of the pH is very strong. The polymer passes from a strong hydrogel at healthy tissue pH to a very weak hydrogel, almost liquid, at cancer tissue pH. The transition is dramatic and the hydrogel exhibits liquid-like behavior at even lower pH=6.0. In contrast to the strength of the pH dependence of the hydrogel, the temperature did not show the same influence on the polymer (FIG. 5.1.3b) in the temperature range between 37^{o}C (healthy tissue) and 40^{o}C (cancer tissue). PTH hydrogel has a very weak, almost negligible, responsiveness to temperature.

Additionally, we studied the time required for the hydrogel to self-heal, i.e. the time required for the hydrogel to have the initial strength after applying a high shear rate to melt the structure and rejuvenate the sample. Self-healing is based on the transformation of the 3D secondary structure from α-helix or β-sheet to random coil. The secondary structure is the hydrophobic part of the polymer that induces the organization and the

formation of the hydrogel. It is well known that in order to form a strong hydrogel with high storage modulus G' it is necessary to develop hydrogen bonding through β-sheets [255]. At pH=7.4 the strong hydrogel derives from the large amount of β-sheet conformation. At lower pH, up to pH=6.6, where the poly(L-histidine) (PHIS) is partially protonated, the conformation of PHIS changes to a mixture of α-helix and random coil. When the pH lowers more, the conformation becomes random coil. This transition in conformation lowers the modulus of the hydrogel, and therefore the hydrogel relaxes faster, directing the delivery towards the cancer tissue, which has the lower pH.

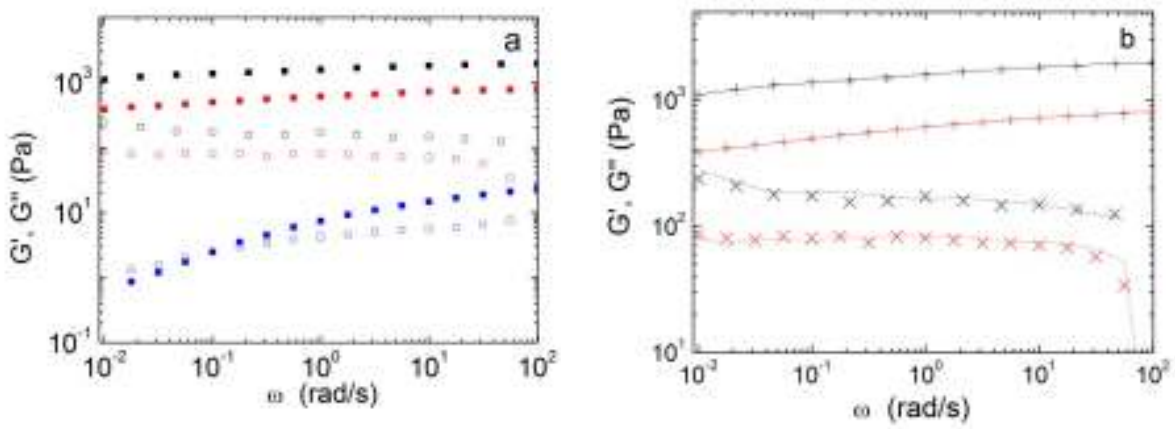

Figure 5.1.3 *a) Linear viscoelastic spectra of the 3 different pH values of the hydrogel PTH at c=1:30 and 37°C. Storage and loss moduli are represented with full and empty symbols, respectively. PH Values of 7.4, 6.5, 6.0 are represented with black, red and blue colors respectively. b) Linear viscoelastic spectra of two different pH values at the same concentration (c=1:30). Black symbols and lines stand for data at pH=7.4 while the red ones stand for pH=6.5. Crosses and solid lines represent data for storage modulus at 37°C and 40°C, respectively. Slanted crosses and dashed lines represent data for loss modulus at 37°C and 40°C, respectively.*

The rate, depending on its duration can make the secondary structure to unfold, resulting in a lower organization of the protein. Since the formation of the hydrogel and its value of the storage modulus increases with the increasing amount of β-sheet, the shear rate results in destruction of the organization, transforming the material to viscous liquid. However, based on the rate cessation, the initial secondary structure is reassumed, and the hydrogel returns surprisingly quickly in its initial equilibrium state. This characteristic gel

behavior is critical from the point that the hydrogel reforms really fast when injected and keeps its structure for longer time without spreading the drug.

We found that the linear pentablock terpolypeptide was the optimum architecture for this property. The presence of the outer poly(L-lysine) chains obliges the hydrophobic chains to become better organized, inducing the formation of a strong hydrogel. In addition, it was necessary to incorporate two hydrophobic parts in the same molecule, which induce the organization and the formation of the strong hydrogel. The two hydrophobic components create bridges between different hydrophobic boundaries, resulting in a well-defined 3D interconnected nanostructure surrounded by large water boundaries that keep the mixture of the polymer-water in hydrogel form. In addition, it was found that the pentablock macromolecular architecture was very critical for the quick self-healing of the hydrogel and recovery from liquid structure. The simple diblock terpolypeptide of the poly(L-lysine)-*b*-poly(L-Histidine-*co*-*γ*-benzyl-L-glutamate) type or the triblock terpolypeptide of the poly(L-lysine)-*b*-poly(L-Histidine-*co*-*γ*-benzyl-L-glutamate)-*b*-poly(L-lysine) resulted in significantly higher self-healing times rather than the pentablock terpolypeptide. When shear rate is applied, it probably causes the unfolding of one of the two hydrophobic parts of the chain, breaks the interconnections and destroys the organization. A probable mechanism is shown is in FIG. 5.1.4. The second hydrophobic part that stays connected with other hydrophobic chains creates a "memory" to the organization, resulting in the very quick formation and self-healing of the hydrogel (Fig. 5.1.5)

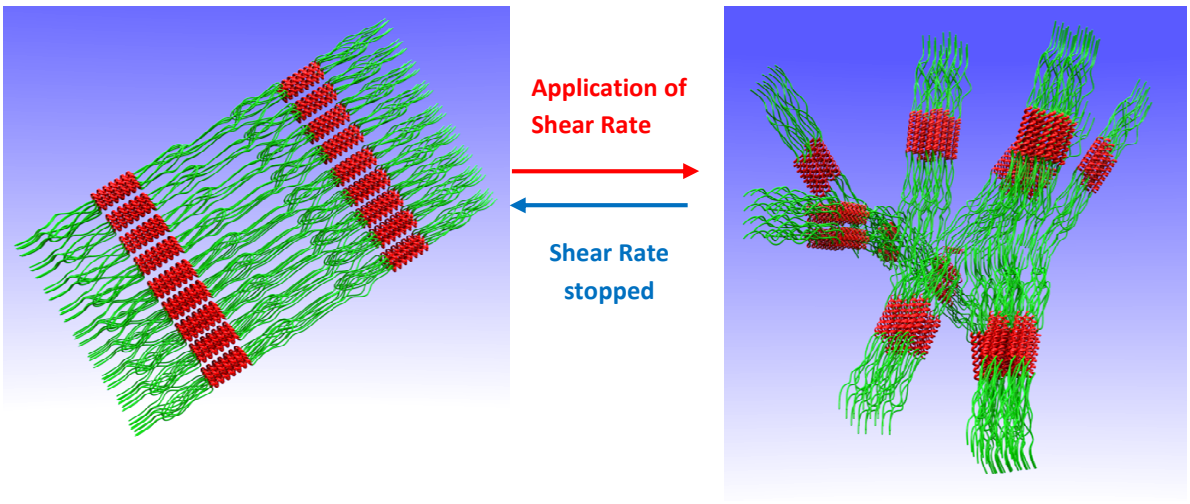

Figure 5.1.4. *Schematic representation of the mechanism that renders the self-healing of the hydrogel almost instantaneous: the pentablock structure and the presence of two hydrophobic blocks in one polymeric chain create a "memory" on the structure of the hydrogel and the formation of the hydrogel after the injection occurs instantly.*

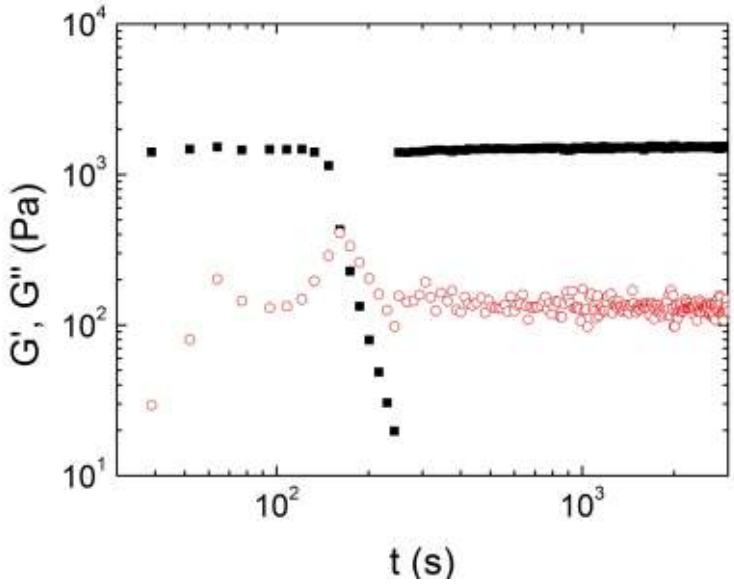

Figure 5.1.5*. Time required for the reformation of the hydrogel after applying a strain sweep (DSS).*

Secondly, we examined the rheological behavior of the hydrogel loaded with gemcitabine (Hydrogem). Gemcitabine is a hydrophilic drug and stays in the aqueous phase, therefore its addition is not expected to alter significantly the rheological behavior of the hydrogel, since its stability depends on the hydrophobic part of the polymer. One of the most important parameters that we have to investigate was the drug delivery of the

hydrogel. Taking into account that the diffusion of drug and water in a hydrogel is very slow, the delivery of the drug depends on the rate of which hydrogel transforms from gel to liquid in order to achieve directed release towards the cancer tissue. We found that the rate of this transformation depends on the initial strength of the hydrogel, which can be fine-tuned by the polymer concentration. In order to relate directly the rheological properties of the hydrogel with the *in vivo* properties of the stability and duration of the hydrogel in the mice body, we performed a "calibration". By injecting subcutaneously different polymer concentrations in healthy mice, we found that the higher polymer concentration (c=1:30) stayed as a gel formation, four times longer than the next lower concentration (c=1:40). Obviously, the polymer storage modulus depicting the numbers of the bonds within the gel, influences dramatically the duration time of the hydrogel in the mice.

A slightly different behavior was observed when the hydrogel was loaded with drug. As mentioned above, we chose the highest concentration as the most appropriate for the drug delivery. The gemcitabine concentration in the water was 1:30, thus the ratio of the drug polymer was 1:1. It was found that the presence of the drug resulted in a slight destabilization of the hydrogel at pH=7.4 and 37^{o}C indicated from the lower storage modulus of hydrogem (hydrogel with gemcitabine) as compared to the empty hydrogel (FIG. 5.1.6a). The loss modulus showed a clear minimum in the case of hydrogem in contrast to pure polymer where the minimum is not so prominent. At pH=6.5 and temperature 37^{o}C, the decrease of the storage modulus is not so high as in the case of the empty hydrogel at same temperature and pH (FIG. 5.1.6b). However, since the decrease of the modulus of the empty polymer at pH=6.5 was very large, it would result in a quick collapse of the hydrogel and we would lose the slow release properties of the hydrogel. Therefore, the smaller decrease of the hydrogem is beneficial for our system since the slower transformation of the hydrogel to liquid delays the release of the drug.

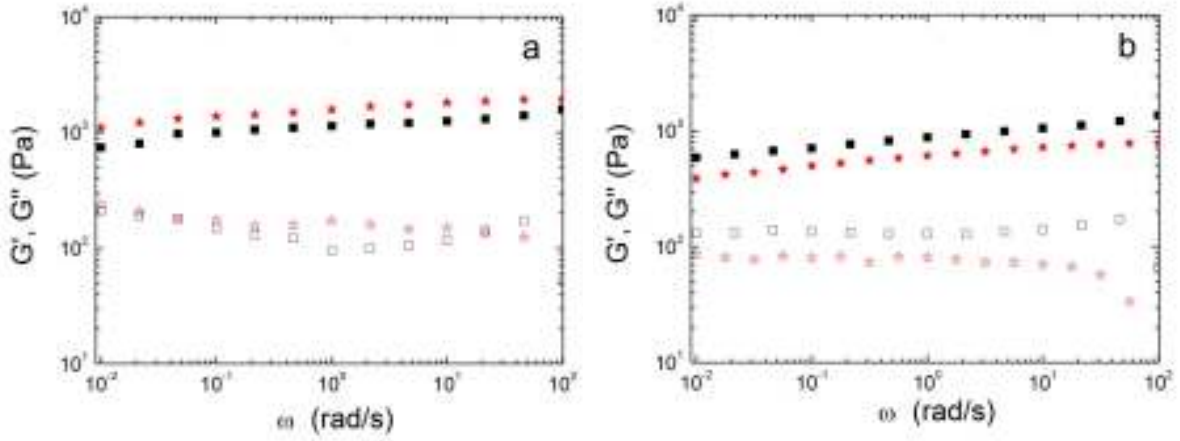

Figure 5.1.6*. a) Linear viscoelastic spectra of the hydrogel with and without the drug. Red stars represent pure polymer at c=1:30, pH=7.4 and 37°C, while black squares stand for polymer with drug at the same conditions. Storage and loss moduli are represented with full and empty symbols, respectively. b) Linear viscoelastic spectra of the hydrogel with and without drug at pH=6.5. The data are represented in the same way as in a.*

At 40°C and pH=7.4, we see a slightly different behavior at low frequencies (FIG. 5.1.7). In the empty hydrogel case, we did not see any significant difference in any of the storage and loss modulus as compared to the values at 37°C. However, the hydrogem showed a stronger decrease of the storage modulus followed by a simultaneous increase of the loss modulus at low frequencies. This suggests that at 40°C (cancer tissue) the hydrogem relaxes faster denoting a weak temperature responsiveness.

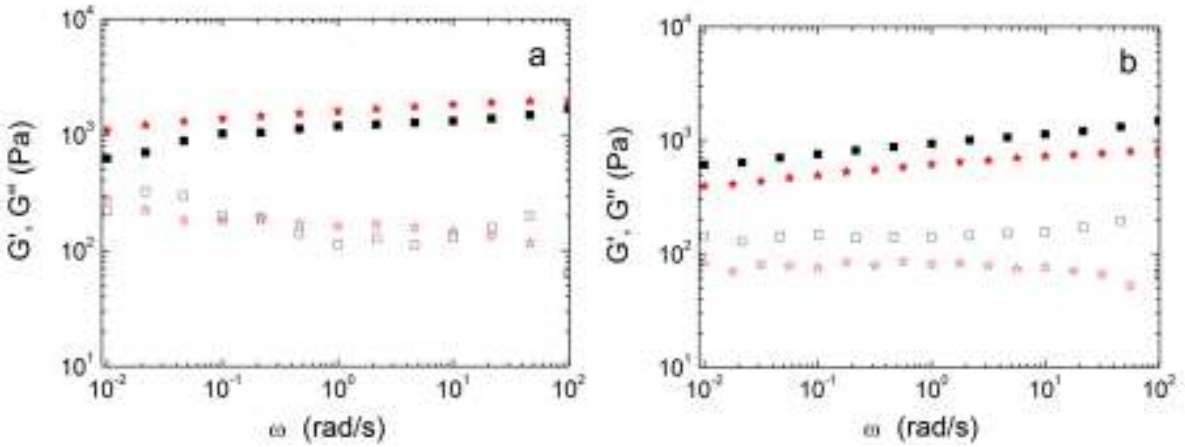

Figure 5.1.7*. a) Linear viscoelastic spectra of the hydrogel with and without the drug. Red stars represent pure polymer at c=1:30, pH=7.4 and 40°C, while black squares stand for polymer with drug at the same conditions. Storage and loss moduli are represented with full and empty symbols, respectively. b) Linear viscoelastic spectra of the hydrogel with and without drug at pH=6.5. The data are represented in the same way as in a.*

The reformation rate of the empty hydrogel and hydrogem (hydrogel loaded with gemcitabine) were carefully exploited since this property is of vital importance for rendering the hydrogel injectable. At first, we studied the self-healing of the empty hydrogel (FIG. 5.1.5) and later we focused on the drug effect of that rate. It was found that neither the concentration nor the pH influenced significantly the time required for the empty hydrogel or hydrogem (FIG. 5.1.5) to re-structure. All the experiments (not shown here) showed that the time required for the hydrogel to self-heal is less than 10 seconds. This means that during the injection of any formulation of the hydrogel (hydrogem) to the mice, even before completion of the injection the hydrogel has recovered and reformed. The application of shear rate unfolds the secondary structure; therefore it destroys partially the self-organization of the gel, resulting in fluid-like behaviors. However, due to the existence of two aggregating parts per single chain, even if one of the two parts unfolds the other possibly keeps aggregating creating a memory on the polymeric chains which results in a quick recovery upon the shear cessation. In other words, the macromolecular architecture creates “memory” on the molecules to recover quickly after the completion of the injection of the liquid-like hydrogel in mice.

The rheological evidence were supported by Scanning Electron Microscopy (SEM) measurements for the hydrogel. Three different vials of the same amount of polymer and water have been pH-adjusted by adding a small amount of dilute HCl, i.e. at pH=7.4, pH=6.5 and pH=6.0. The final mixtures are shown in FIG. 5.1.8 where we can see that the strongest hydrogel is found at pH=7.4, while at pH=6.0 the mixture gives a liquid like outlook, and at pH=6.5 the material is in an intermediate state. Sample of the hydrogel with pH=7.4 and pH=6.5 was frozen quickly with liquid nitrogen and then the water was lyophilized under high vacuum. The SEM of the samples are shown in FIG. 5.1.9. As we can observe at the SEM of pH=7.4, there is a 3D structure of interconnected

nanostructures which holds the mixture in the form of hydrogel, while the structure at 6.5 is collapsed, giving the form of an almost liquid-like one.

Figure 5.1.8. *Vials containing the same amount of polymer and water at different pH values. Left: pH=6.0, middle: pH=7.4, right: pH=6.5*.

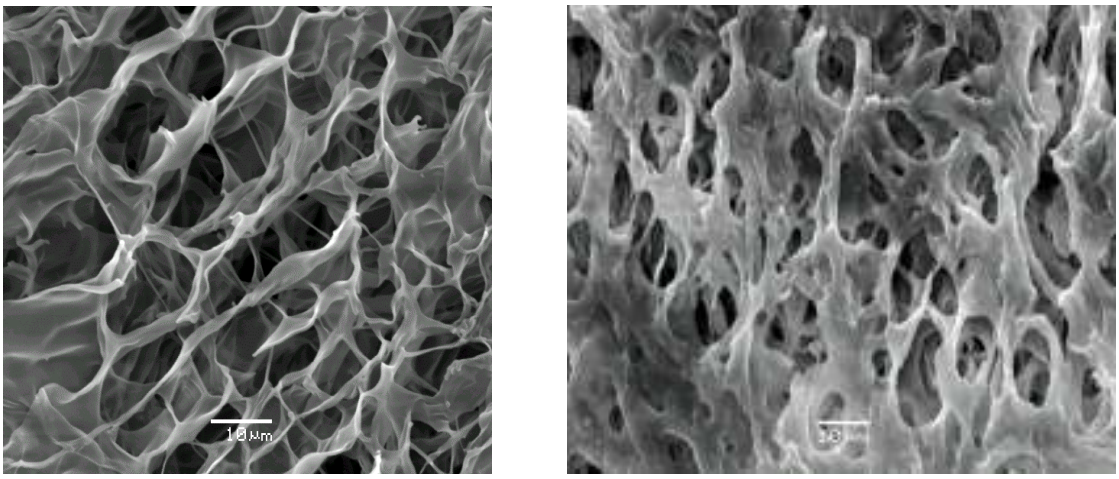

Figure 5.1.9. *SEM micrograph of the hydrogel at pH=7.4 (left image), and at pH=6.5 (right image).*

To summarize, we have found that amphiphilic pentablock terpolypeptide hydrogels (PTH) can be fine tuned by altering the relative PBLG/PHIS molar ratio of the hydrophobic component. Also, size, rigidity and density of the PTH can be finely adjusted by altering PTH concentration, pH and composition. The most important property of the

hydrogel obtained by rheology was the fast recovery of the gel after the shear cessation. The simplest possible administration of the hydrogel in the animal is significant, since the hydrogel easily melts upon a slight shear rate and reforms within a few seconds close to the cancer tissue without spreading around when injected.

5.2.Amphiphilic Pentablock Quarterpolymer Hydrogels

The pentablock quarterpolymer was excessively characterized by a combination of methods including Size Exclusion Chromatography, FTIR and H NMR spectroscopy. The combined characterization methods revealed that the pentablock quarterpolymer was the one expected by stoichiometry and the design of the synthesis. The molecular characteristics of the PQH hybrid quarterpolymer are given in Appendix A.

Rheology measurements were conducted at two different pH values, 7,4 and 6.5, i.e. the pH of healthy and cancer tissue. At these pH values rheology was performed at three different temperatures, i.e. 25, 37 and 40^{o}C. The results are shown in FIG. 5.2.1-5.2.2.

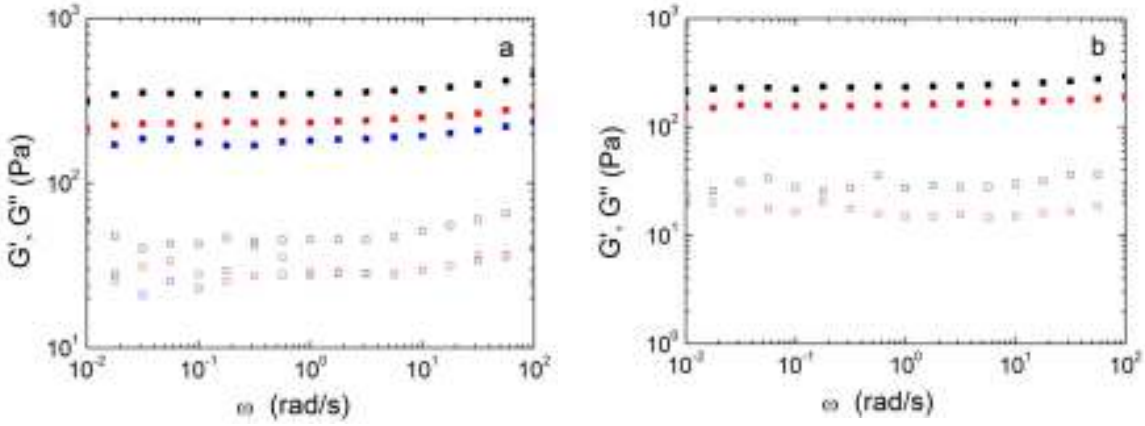

Figure 5.2.1*. a) Linear viscoelastic spectra of the hydrogel PQH at three different temperatures. Storage and loss moduli are represented with full and empty symbols, respectively. Temperatures of 25°C, 37°C, 40°C are represented with black, red and blue colors respectively. b) Linear viscoelastic spectra of the hydrogel PQH at body temperature (37°C) for two pH values. Black and red symbols represent data from pH7.4 and 6.5, respectively.*

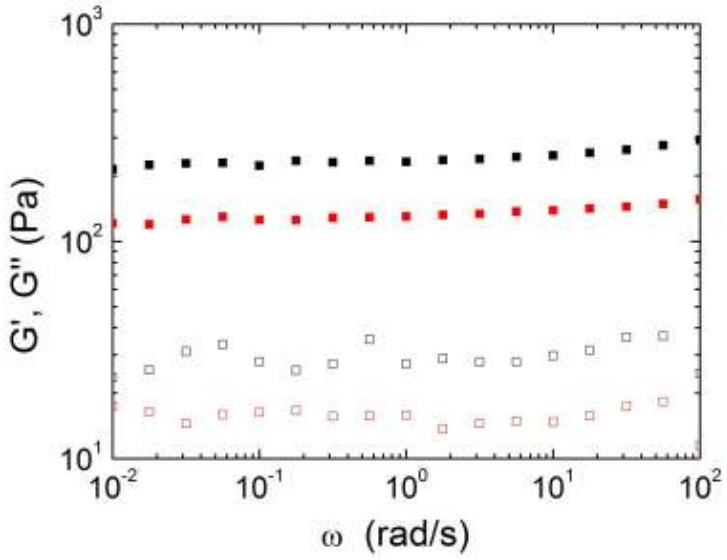

Figure 5.2.2. *Linear viscoelastic spectra of the hydrogel PQH at healthy (37°C, pH7.4) and cancer tissues (40°C, pH6.5) represented with black and red symbols, respectively. Storage and loss moduli are represented with full and empty symbols, respectively.*

From the DFS plots it is obvious that the hydrogel is pH and temperature responsive. The strength of the hydrogel is significantly influenced by the temperature and pH between the healthy and cancer tissue values. Most significantly, the strength of the hydrogel decreases by going from the healthy to cancer tissue values. As a consequence, this material is expected to respond even more targeted to cancer tissues, and melt only towards the cancer tissues rather the healthy ones. Consequently, PTH will release directionally anticancer agents that will be encapsulated in this material selectively to cancer tissues.

Furthermore, in *vivo* studies were conducted on the empty PTH hydrogel as well as on the hydrogem formed by the PTH loaded with gemcitabine. Results of these studies are shown in Appendix A. The in vivo results of the PTH hydrogem showed that the material is very effective in delaying the development of human pancreatic cancer. By using only 40% of the drug, compared to the set of animals that 100% of the drug was delivered subcutaneously close to the cancer tissue, the delay through the hydrogem was

comparable and even better. This shows that the polymeric material directs the delivery of the drug targeted towards the cancer tissue.

In conclusion, we synthesized a material that hierarchically self-assembles from a few angstroms to micrometers to achieve the desired properties. The polymeric material forms an injectable, *in situ*-forming hydrogel through physical interactions. The hydrogel becomes a viscous liquid after applying a slight shear rate by stirring the needle of a syringe within its volume, in order to be drawn into the syringe, and when injected close to the cancer tissue becomes a hydrogel within a few seconds, regardless of the tissue characteristics. The reconstruction originates from the combination of their advanced macromolecular architecture and their unique properties of the polymer's hydrophobic part, whose secondary structure denatures under shear rate and quickly self-heals when the shear rate stops [256, 257]. Once the hydrogels are injected close to cancer tissues, they can selectively deliver gemcitabine to cancer rather than to healthy tissues according to their pH and temperature sensitivity. This material's ability results in its melting at pH values found in the cancer tissue, i.e. pH=6.5 [258] while it remains in the hydrogel form under healthy tissue conditions. The polymeric composition of the hydrogel contains a larger amount of water than that of cancer tissue. Due to osmotic pressure, the material is absorbed along with the drug within the cancer tissue to selectively and efficiently deliver the encapsulated chemotherapeutic. The release of the drug is limited towards the healthy tissue, since it remains in the hydrogel form, and the diffusion of water and drugs through a hydrogel is significantly slower than in a nanoparticle, depending on the system. The hydrogel has the ability to adhere selectively to the cancer tissue through electrostatic interactions during its degradation in order to maintain a constant degradation rate. In addition, it features a buffering capacity in order to stay in the hydrogel form for a significant time and slowly release.

The functionality of the hydrogel is not limited only to the targeted drug delivery in cancer tissues, but also aids in the effective and quantitative delivery within the cytoplasm of the cancer cells. The polymer that is incorporated along with the drug into the cell through endocytosis has the ability to rupture the endosome allowing the drug to be released in the cytoplasm and avoid exocytosis and chemoresistance [259, 260].

By fine tuning of the pH and the polymer concentration of the hydrogels their strength can be increased to the desired levels; therefore it is possible to control the period of time of the targeted drug delivery. The unprecedented versatility and properties of these pentablock polymer hydrogels provide multiple molecule adjustments to tune different properties and achieve the desired functionality, such as the sustained release duration, the amount of the encapsulated drug, the delivery of either hydrophilic or hydrophilic drugs, the co-delivery of hydrophilic and hydrophobic drugs as well as the delivery of nanoparticles in which the drugs are encapsulated.

6. Metastable star-mixtures [261, 262]

Suspensions of spherical colloidal particles are ubiquitous in nature and represent an ever stimulating and technologically challenging field of research [263]. The majority of work relating to the dynamics and rheology of colloids has been performed with the simplest hard sphere systems, both experimentally and theoretically [264, 265]. Colloidal interactions are known to control properties, and can be influenced by a number of means, such as the presence of charges, the stabilizing layers around the particles and the suspending medium. However, the controlled interplay of attractive interactions and their implications on emerging, macroscopic properties have received systematic attention only in the last decade.

Depending on the size of the polymers and colloids, it is possible to distinguish two cases: a) when the polymer is smaller than the colloidal particle, the main equilibrium properties of the system can be rationalized within the depletion picture, since the macromolecules act as depletants for the larger colloidal particles. In this case, the Asakura and Oosawa approach (AO) can be used to describe the equilibrium phase diagram of the mixture along with other features such as a variety of phases and kinetic states, dynamic heterogeneities and gel formation [266-272]. b) when the polymer is larger than the colloid, the size of the polymer plays a crucial role since it interacts with more than one colloidal particles. As a consequence the system becomes more complex and the depletion potential is affected by the polymer correlation length [273-275]. The most widely investigated colloid-polymer mixture is a combination of hard colloids and linear polymers which interact via exclusive volume repulsions.

In recent years, advances in experimental work as well as in theoretical and computational descriptions allowed the consideration of mixtures of star polymers and colloids. The former are branched polymer made of f chains anchored on a common

core; such complex macromolecules were demonstrated to be highly versatile models for soft colloids [21]. When they are brought into contact at large concentrations, they deform but also interpenetrate via their grafted arms. Their tunability at molecular level allows ranging their repulsive pair interaction potential from ultrasoft to hard as their functionality f changes from typically below 30 to typically above 400 [167]. Stars with functionalities $f \geq 50$ are known to form glassy states at large volume fractions [37, 55].

Mixtures involving star polymers and smaller linear polymers have shown great richness in metastable states, which are controlled by the osmotic pressure of the latter, leading to star shrinkage and depletion [37, 107, 163, 166]. Replacing the linear polymers by small stars leads to formation of different glassy states: single glass and double glass depending on whether the larger or both star systems are kinetically frozen, as well as asymmetric stars when the small star fraction increases [276]. Given this wealth of behaviour and related ability to tailor the properties of suspensions at wish, a challenge is to combine soft and hard interactions. In this respect, star polymers with $f \leq 32$ have been mixed with larger hard spheres and their phase separation was examined experimentally and theoretically [277]. The demixing bimodal was found to shift to lower star concentrations with increasing f or decreasing star-to-colloid size ratio, which was kept below 0.5. However, the use of hard spheres as depletants to high-f glass-forming stars has not been addressed to-date.

In this work, we address the formation of multiple glassy states in soft-hard colloidal mixtures composed of large star glasses and small hard-like depletants. To ensure purely entropic interactions we use stars of the same chemistry and drastically different functionalities for the hard-like particles. The latter were stars with very short chains, which were thus fully stretched in the core regime [106], so that they effectively act as hard spheres (HS). Using rheology and Dynamic Light Scattering (DLS), we observe vitrification of the soft star glass, melting upon addition of colloidal spheres and

subsequent arrested phase separation. Our experimental results were validated by Mode-Coupling Theory (MCT) and Molecular Dynamics (MD) simulations.

In the experiments described below, we employed multiarm 1,4-polybutadiene (PBD) stars with a weight-average functionality $f_S = 214$, a weight-average molar mass M_w^S=14500 kg/mol and arm molar mass $M_{arm}^S = 67000$ g/mol of whose synthesis is described elsewhere [106, 170]. The effective hard-sphere systems consisted of PBD stars with $f_H = 1109$, M_w^H=1600 kg/mol and $M_{arm}^H = 1270$ g/mol. The polydispersity indexes (PDI) and the molar fraction of contaminants (MFC) have been measured via size exclusion chromatography (SEC): PDI=1.07 and MFC=0.12 for the soft spheres, whereas PDI=1.11 and MFC=0.036 for the hard spheres (Figure 6.1).

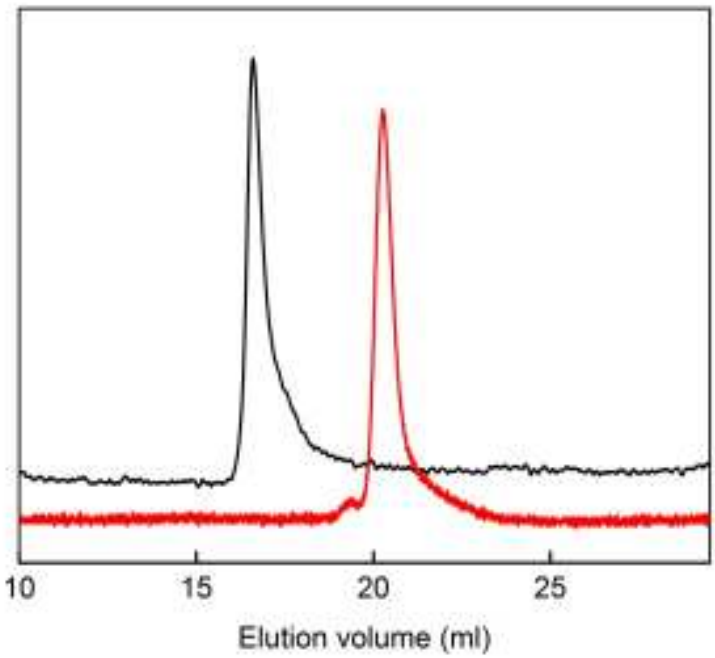

Figure 6.1. *Size exclusion chromatography traces for the HS ($f_H = 1109$ and $M_w^H = 1600\ kg/mol$, red line) and star (f_S = 214 $M_w^S = 14500 kg/mol$, black line) PBD samples.*

The lack of a peak (due to linear side chain contaminant) on the right of the main peak confirms the purity of the samples. The particles were dissolved in squalene, a nearly athermal, non-volatile solvent for PBD. The respective hydrodynamic radii $R_h^S = 45.0\ nm$ and $R_h^H = 11.5\ nm$ were determined from dynamic light scattering

measurements in dilute solution at 20°C, yielding overlap concentrations $c_S^* = 44.5\, mg/ml$ and $c_H^* = 416\, mg/ml$, respectively. We define the ratio of hydrodynamic sizes as $\xi \equiv R_h^S/R_h^H \simeq 4$ in the case at hand. The respective nominal effective volume fraction $\Phi_S^g = \frac{c_S^g}{c_S^*} = 1.6125 \pm 0.0125$ and $\Phi_H^g = \frac{c_S^g}{c_H^*} = 0.75 \pm 0.05$ for rheological glass transitions were determined via small amplitude oscillatory experiments (SAOS), performed with a sensitive strain-controlled ARES 100 FRTN1 rheometer (Rheometric Scientific, now TA, USA) with a home-made cone-plate stainless steel geometry was utilized (7.9 mm diameter, 0.166 rad cone angle), in order to accommodate the minimal amounts of sample available. Temperature control (of ±0.1°C) was achieved by means of a Peltier temperature control system (at 20°C), whereas the measured sample was protected from the external environment (possible slight air currents) by means of a simple teflon cover. The experimental test protocol is described in Chapter 2.3.

The rheology of the mixtures was investigated at different star and HS concentrations. To express the concentrations in terms of the number densities of the star- and colloid-components (ρ_S and ρ_H, respectively), we employ the effective corona diameter of the stars, σ_S, as the unit of length. This allows for a direct comparison with the theoretical results, where this scale appears in the effective star-star interaction. The nominal glass transition concentrations for the stars and HS, translated in number densities, are $\rho_S\sigma_S^3 = 0.339 \pm 0.002$ and $\rho_H\sigma_S^3 = 10.75 \pm 0.7$. Accordingly, the pure star solutions were investigated at number densities $\rho_S\sigma_S^3 = 0.33, 0.342, 0.347,$ 0.368 and 0.421, and colloidal spheres of various concentrations have been added to analyze the ensuing rheology of the mixture.

We will begin with the effects of adding HS to stars at $\rho_S\sigma_S^3 = 0.342$, where more than one glassy state as well as melting of the mixture can be unambiguously distinguished. In the absence of HS ($\rho_H\sigma_S^3 = 0$), the concentrated star solution with

$\rho_S\sigma_S^3 = 0.342$ exhibits a typical glassy behavior: both storage (G') and loss (G'') moduli are weakly frequency dependant, with G'' reaching a broad minimum, $G'(\omega) > G''(\omega)$ over four decades of frequency, while being also time dependent due to aging (Figure 6.2) [37].

Upon addition of HS at increasing concentrations, while maintaining the star fraction fixed at $\rho_S\sigma_S^3$ = 0.342, the moduli become increasingly sensitive to frequency. Initially the addition of hard spheres has a reinforcing effect on the stars, but with further colloid addition, depletion takes place and the modulus decreases while the mixture remains glassy. This softening of the initial glassy suspension, leads eventually to a transition to the ergodic liquid state above a certain HS volume fraction $\rho_H\sigma_S^3 > 0.05$ (Figure 6.2b). This state is also confirmed by the absence of aging, shown in Figure 6.2e [37]. The characteristic time of the liquid (extracted from the terminal cross-over of the moduli) varies over three decades; it first decreases with ρ_H, then goes through a minimum and finally increases as the reentrance is approached. As the colloid concentration is further increased ($\rho_H\sigma_S^3 > 1.0311$) a re-entrant, solid-like regime is found, which, with the help of MCT, can be attributed to arrested phase separation (APS), and which, in turn, is characterized by different regions, marking solid-solid transitions. The first reentrant region is described as APS due to the fact that at the lower colloid fraction ($\rho_H\sigma_S^3 < 4.0$), the plateau modulus is virtually independent of the amount of added hard spheres and has a value nearly identical to that of the repulsive glass, (Fig. 6.4) consistent with a mechanism distinct from attractive vitrification. This suggests a scenario of a purely repulsive glass regime up to the reentrant line, an interpretation supported by the theoretical analysis. Note that if the reentrant state was an attractive glass, its storage modulus would have been much higher as compared to that of the repulsive glass [278].

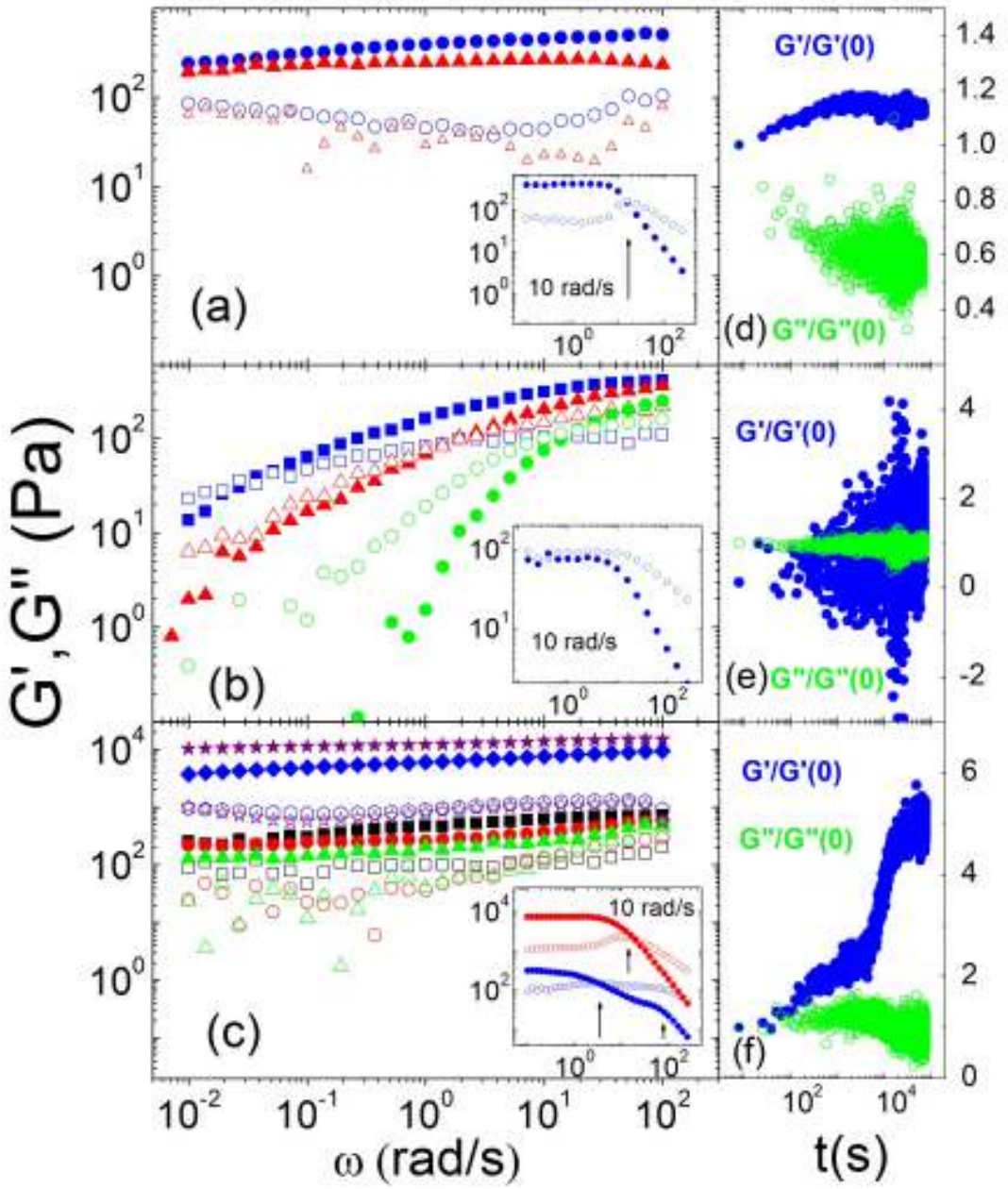

Figure 6.2. *Linear viscoelastic spectra for HS-star mixtures at* $\phi_S = 1.625$ *(*$\rho_S\sigma_S^3 = 0.342$*). G' and G'' are shown with full and empty symbols respectively. (a) Repulsive glass:* $\rho_H\sigma_S^3 = 0$ *(blue circles) and* $\rho_H\sigma_S^3 = 0.0147$ *(red up triangles). Inset: Dynamic strain sweep for* $\rho_H\sigma_S^3 = 0$ *at 10rad/s. The arrow indicates the yield point. (b) Liquid:* $\rho_H\sigma_S^3 = 0.1473$ *(blue squares);* $\rho_H\sigma_S^3 = 0.2946$ *(red up triangles);* $\rho_H\sigma_S^3 = 0.4419$ *(green circles). Inset: Dynamic strain sweep for* $\rho_H\sigma_S^3 = 0.4419$ *at 10rad/s. (c) Reentrant glass:* $\rho_H\sigma_S^3 = 1.1784$ *(black squares);* $\rho_H\sigma_S^3 = 1.7676$ *(red circles);* $\rho_H\sigma_S^3 = 3.5352$ *(green triangles);* $\rho_H\sigma_S^3 = 5.892$ *(blue diamonds);* $\rho_H\sigma_S^3 = 7.070$ *(purple stars). Inset: Dynamic strain sweep for* $\rho_H\sigma_S^3 = 1.7676$ *(blue circles) and* $\rho_H\sigma_S^3 = 5.892$ *(red squares). The arrows show the yield points: the two step yielding occurs in the arrested phase separated mixtures. Normalized moduli as functions of time after rejuvenation (aging) for fixed star density* $\phi_S = 1.625$ *(*$\rho_S\sigma_S^3 = 0.342$*),* ω*=1rad/s,* $\gamma_0 < 1\%$ *and for colloid concentrations: (d)* $\rho_H\sigma_S^3 = 0$*; (e)* $\rho_H\sigma_S^3 = 0.44$*, and (f)* $\rho_H\sigma_S^3 = 1.17$*.*

With further addition of hard spheres, the modulus increases rather dramatically following two distinct power laws (see Fig. 6.4). This behavior sets mixtures based on soft colloids apart from their hard sphere counterparts. We attribute this to the deformability of the soft colloids due to the presence of an increasingly crowded hard spheres environment.

The rheological yielding transition was examined with dynamic strain sweeps at different frequencies (here the 10 rad/s results are projected). While a single yield point could be identified in the initial repulsive glassy phase (Fig. 6.2a, inset) and no yielding was observed in the liquid state [Fig. 6.2b, inset], the re-entrant state exhibited a two-step yield process (Fig. 6.2c, inset) for $\rho_H\sigma_S^3 < 3.53$. Beyond this value the single yielding behavior was recovered along with an increase in the modulus. Double yielding is thought of as reflecting two constraining length scales (say bonds and cages) which occur in attractive glasses [278] or arrested phase separating systems alike.

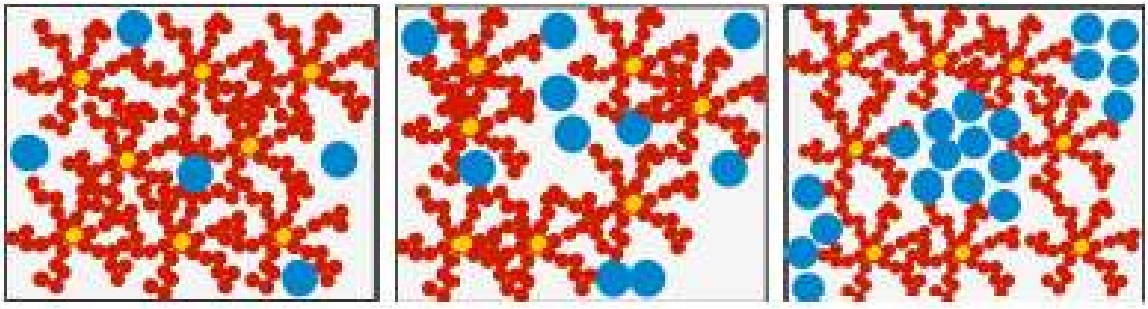

Figure 6.3. *The three cartoons show, from left to right, sketches of the repulsive glass, the liquid and the arrested phase separation-state.*

The remarkable consequences of these transitions are the drastic changes in macroscopic properties of the mixtures, as evidenced in the values of the moduli. This is demonstrated in Fig. 6.4 where upon increasing $\rho_H\sigma_S^3$, the storage modulus G' first increases and then drops in the repulsive glass regime and later, increases again by more than two decades after the arrested re-entrant region. Moreover, the fact that just at the re-entrance ($\rho_H\sigma_S^3 = 1.0$) the value of the G' is nearly identical to that of the original

repulsive glass, corroborates to proposed scenario of a purely repulsive glass regime up to the (binodal) re-entrant line. The two-step yielding in the re-entrant region is attributed to the large compositional heterogeneity in this regime which is dominated by depletion attractions. On the other hand, the characteristic time (extracted from the terminal crossover of the moduli) of the liquid regime varies by several decades: it first decreases with $\rho_H \sigma_S^3$ as we move away from the repulsive glass due to depletion, and then goes through a minimum and increases as the re-entrance is approached.

To elucidate this behavior further, we analyzed the osmotic effects of the small colloids. Our starting point is the osmotic shrinkage of a star of radius R_s due to the addition of a smaller colloidal additive with size R_C and a packing fraction η_H [163]. The free energy balance is given by:

$$\frac{fR_S}{Na^2} - \nu_0 \frac{N^2 f^2}{2R_S^4} + \frac{R_S^2}{R_H^3} \eta_H Z(\eta_H) = 0 \qquad (6.1)$$

where N is the polymerization degree of each arm of the star, α is the monomer size ($\alpha = 0.5$ nm for PBD [104]), v_0 is the excluded volume parameter that can be set equal to α^3, and Z(η) is the compressibility factor of the colloidal bath. For the case of hard colloids, it takes the form [279]:

$$Z(\eta) = \begin{cases} \frac{1+\eta+\eta^2-\eta^3}{(1-\eta)^3} & \eta < \eta^{(g)} \\ \frac{2.67}{1-1.543\eta} & \eta > \eta^{(g)} \end{cases} \qquad (6.2)$$

where $\eta^{(g)} = 0.58$ is the packing fraction at the glass transition for hard spheres. Note that here the volume fraction of hard spheres has been calculated as $\eta_H = V_H/(V_{solv} + V_H)$. The normalized colloid concentration may then be expressed as a function of the known experimental parameters:

$$\rho_H \sigma_S^3 = \frac{3}{4\pi}\left(\frac{R_S}{R_H}\right)^3 \left[1 - \left(\frac{3}{4\pi R_S^3}\frac{M_{w,S}}{N_A \rho_{PBD}}\right)\phi_S\right]\eta_H \qquad (6.3)$$

where $R_S \equiv R_S^{(h)}$ is the hydrodynamic radius of the soft star at infinite dilution, $\phi_S = {c_S}/{c_S^*} = 1.625$, and ρ_{PBD} is the density of polybutadiene.

Equations (6.1)-(6.3) were employed in a fully self-consistent fashion to calculate the star shrinkage factor $\alpha_S = R_S^{(h)}(\rho_H)/R_S^{(h)}$ as function of the colloid density $\rho_H \sigma_S^3$. We expect this to be accurate even if the presence of more stars (overlapping) was not considered in Eq. (6.1). From the above we can also conclude that, initially, the size (and conformation) of the stars is not significantly perturbed for a large addition of colloids because the star osmotic pressure is weakly increased. As can be seen in Fig. 6.4, the modulus G_p increases significantly from a colloid fraction $\rho_H \sigma_S^3 \sim 4$, when the star size starts decreasing (albeit weakly). Moreover, a slope change for G_p occurs at a colloid fraction $\rho_H \sigma_S^3 \sim 8$, when the size of the stars (and hence their osmotic pressure) is reduced appreciably. Note that the star radius can drop continuously up to the limit of star collapse [280], i.e. when a star reaches its hard-like compact shape and $R_S \sim \alpha(fN)^{1/3}$. In the present case the collapsed R_S is about 16 nm, i.e., slightly above the colloid size. At such high colloid concentrations, the soft stars become dramatically squeezed and assume a collapsed configuration akin to that observed under poor solvency conditions. The summary of the star size calculations at the transitions is shown in Table 6.1. The table, also, contains the star size extracted from the molar mass divided with the density of PBD. The sizes predicted from the collapsed R_S and the molar mass are very close, showing the validity of the theoretical analysis. Accordingly, they can also be thought of as hard spheres that are slightly larger than the original colloids. The system, under these conditions is thus very similar to a slightly asymmetric binary hard sphere mixture. The

overall packing fraction can be estimated to lie very close to the glass transition packing fraction of the hard-sphere system, shown with the green full circle in Fig. 6.4.

TABLE 6.1. *Summary Table of Stars size in different regimes*

	Dilute	Reentrant transition	G' increase in APS	G' change of slope	Double Glass	$\alpha(Nf)^{1/3}$	$(\frac{3M_w}{\rho N_A 4\pi})^{1/3}$
$\rho_H \sigma_S^3$	< 1.0	1.0	4.0	8.1	10.7		
$R_S^{(h)}\ (nm)$	45.0	45.0	44.6	42.4	24.6	16.0	18.6

Therefore we interpret this new solid as a glass formed by a binary hard sphere mixture and we call it a double glass, in accordance with the general terminology of multiple glasses for such systems [276, 281, 282]. In contrast to the star polymer glass (repulsive and APS) encountered at lower concentrations of colloidal particles, in which the stars are arrested but the colloids are mobile, in this double-glass both components are mutually caged.

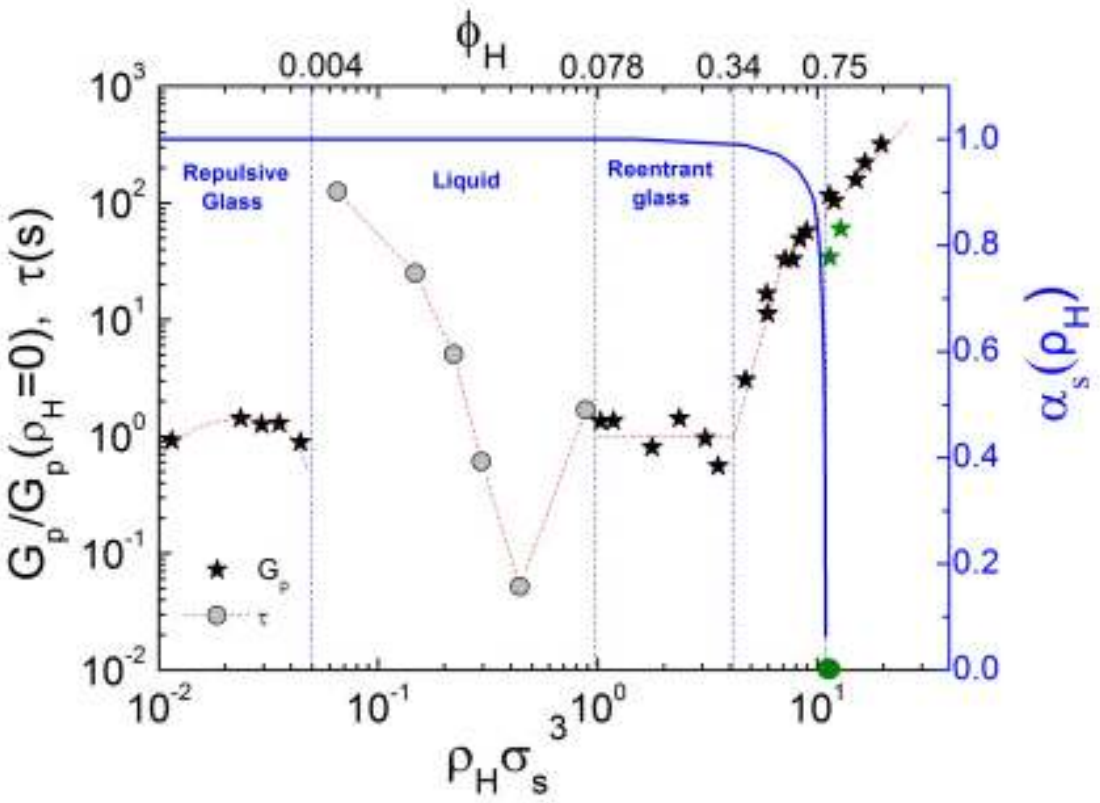

Figure 6.4. *Left vertical axis: Normalized plateau modulus (G_p, stars) of the arrested states and relaxation time (τ, circles) of the ergodic phase of the mixture as a function of the colloid*

concentration at $\phi_S = 1.625$ ($\rho_S\sigma_S^3$=0.343). Vertical dashed lines separate the different rheological states identified and are located at the colloid volume fraction φ_c indicated in the upper horizontal axis. The green circle and stars indicate, respectively, the (rheological) glass transition concentration ($\phi_H^g = 0.75$, $\rho_H\sigma_S^3 = 10.75$) and G_p at $\phi_H = 0.79$ and 0.89 measured for pure solutions of small hard-like particles. Dashed red lines are a guide to the eye. Right vertical axis: Shrinkage factor in squalene for the soft stars (α_S, blue solid line) as a function of colloid density calculated according to Eqs. (6.1)-(6.3).

It is interesting, here, to note that the size (and conformation) of the stars is not significantly perturbed by the addition of a small amount of hard depletants, because the star osmotic pressure is weakly increased. However as ρ_H approaches the hard sphere glass transition, $\rho_H \to \rho_H^{(g)}$, the osmotic pressure abruptly increases and leads to the virtual collapse of the soft stars with a concomitant jump in G_p, which reaches a slightly larger value of the elastic modulus than the one for pure hard sphere-like glasses at the same ϕ_H (without soft stars added), as shown in Fig. 6.4. The additional increase in G_p at higher colloid densities is attributed to the reinforcing effect of the hard spheres, as the stars cannot further shrink and a double-glass of asymmetric hard spheres is formed. The transition to the double glass at a colloid volume fraction $\phi_H \geq 0.75$ is promoted by the action of osmotic forces of colloids which reduced the size of the stars and the reduced available space and large concentrations of both components. As already mentioned the collapsed star size is expected to be about 16 nm, slightly larger than the size of the colloids, leading to a size ratio of 0.72. High size ratios (above 0.6) in hard spheres binary mixtures are expected to stabilize the glass states by both species becoming arrested [283, 284]. From similar works in soft star binary mixtures, the structures, expected in large size ratios and high colloidal densities, are asymmetric glasses since the caging originates from both species [276, 281]. The possible formation of an asymmetric or attractive glass, also, cannot be excluded, since the effective colloid-to-star size ratio is increased proportionally to the shrinkage factor (α_S) from 0.25 ($q = 3$) to 0.72 ($q \simeq 1$), as shown in Fig. 6.4. On the other hand, this is an arrested phase separation regime (Fig. 6.3),

providing the driving force for star attraction (depletion). This cannot be currently further examined, so we leave it as a speculation worth investigating in the future.

Selected nonlinear rheological measurements (LAOS) were performed in the different states of the diagram of Fig. 6.4 in order to provide further phenomenological evidence of their distinct nature. We show some indicative examples in Fig. 6.5 which depicts the so-called elastic representation of the Lissajous-Bowditch plot (stress vs strain amplitude) for the different regimes sheared at the same strain nonlinear amplitude ($\gamma_0 = 100\%$) and frequency ($\omega = 1 rad/s$). LB plots of more strain amplitudes are included in Appendix B. Here all Lissajous plots exhibit two regimes: (a) an elastic regime starting beyond the maximum strain where the strain reversal takes place and the stress increases linearly until the system yields and (b) a viscous regime beyond the yielding point where the stress is independent of the shear rate [285, 286]. The case of repulsive glass and liquid (a and b) is typical for such star glasses, i.e., the plot reflects the sequence of physical processes governing the sample's response [247]: elastic straining; yielding; shear thinning and cage reformation.

Re-entrant solid and the double glass (Fig. 6.5 c and d), exhibit behavior of typical viscoplastic materials, similar to microgel glasses with a rather smooth transition from elastic straining to flow. It is interesting to note that, in the repulsive glass and the liquid regime, the point where yielding starts is signaled by a small overshot of the stress, which is reminiscent of the static yield stress. In general, this stress overshot is not observed in systems close to HS limit and, therefore, attributed to softness [118, 169, 247, 287-291]. The mechanism behind this behavior is not clear yet. One possible explanation could be the strong arm interpenetration due to the star overlapping during the large amplitude oscillatory cycles [169]. A slightly different one could be the deformability of the soft particles along with the cage deformation which allow the system to store more stress

[288]. The stress overshoot might depict the maximum particle's and cage's deformation under shear (Fig 6.6).

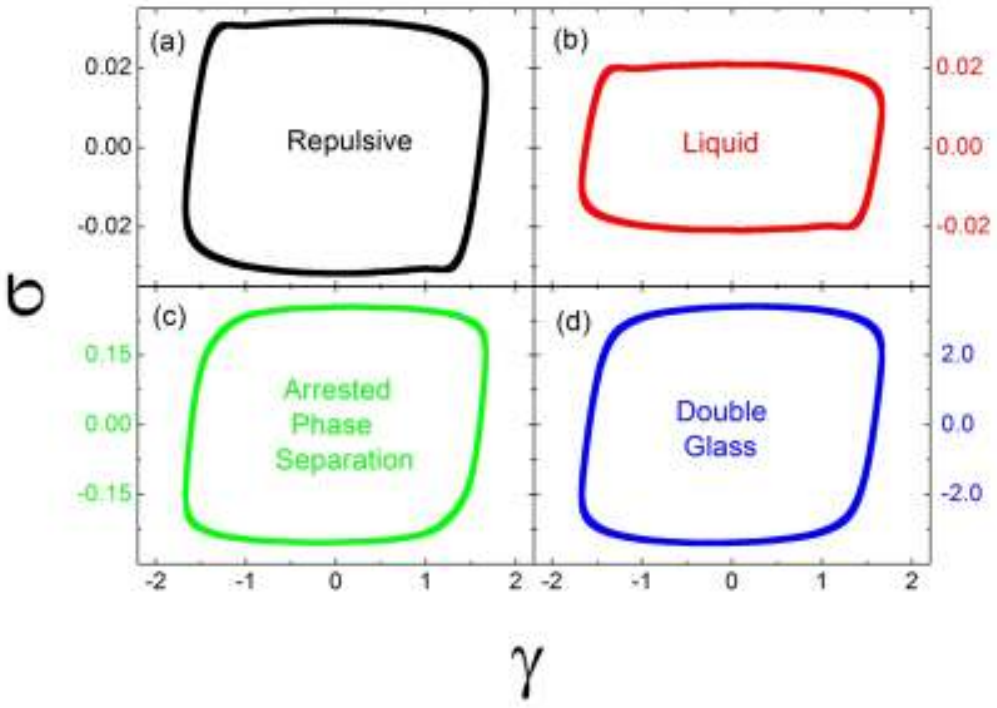

Figure 6.5. *Lissajous plots (Elastic stress vs Strain). (a) repulsive glass ($\rho_H\sigma_S^3 = 0.023$); (b) liquid ($\rho_H\sigma_S^3 = 0.048$) arrested phase separation ($\rho_H\sigma_S^3 = 3.094$), double glass ($\rho_H\sigma_S^3 = 15.013$). The plotted data are extracted from time sweeps at 100% strain and 1 rad/s frequency.*

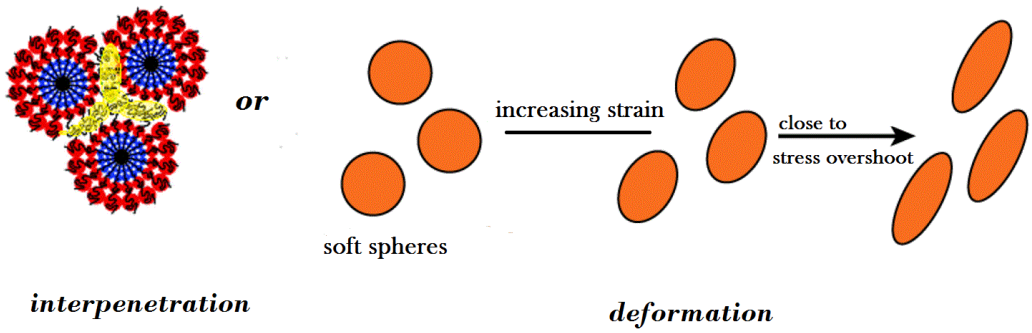

Figure 6.6*. The cartoon show the two possible explanations of the stress overshoot close to the yielding. Left: Star arm interpenetration. Right: Particle and cage deformation.*

However, it is clear that this phenomenon is highly dependent on frequency and strain amplitude of oscillations [169, 288, 289, 292]. At very low Peclet numbers, stress overshoots are lost, while by increasing Peclet numbers the yield stress rises. Hence, there

are qualitative differences between these states, and this corroborates the above discussed assignments, which nevertheless have the same entropic origin: excluded volume interactions mediated by like or different-size particles. We can assume that the initial entangled system is gradually transformed to a less overlapping system as we add hard colloids and at the same time the soft stars are compressed.

The experimental work, described above, was supported by theoretical analysis and simulations. The theoretical study was carried out by employing a recently introduced coarse-grained description of the mixture [280, 293]. In such a representation both star polymers (S) and colloids (H) are represented by spheres separated by a center-to-center distance r and interacting through effective potentials $V_{ij}(r)(i,j = S,H)$. The excellent agreement between the experimental result and this approach will be pinpointed in the following discussion and figures. Moreover, the theoretical analysis, described in Appendix B, has been extended to different star functionalities and size ratios. Remarkable, quantitative and parameter-free agreement between experiment and theory can be seen by comparing Fig. 6.7a with Fig. 6.7b as regards the glass-to-liquid transition for the mixture most closely to the glass transition in the absence of colloids. Figure 6.7b presents a compilation of the MCT-results and shows the ergodic and non-ergodic states that the theory predicts depending on the stars and colloids concentrations.

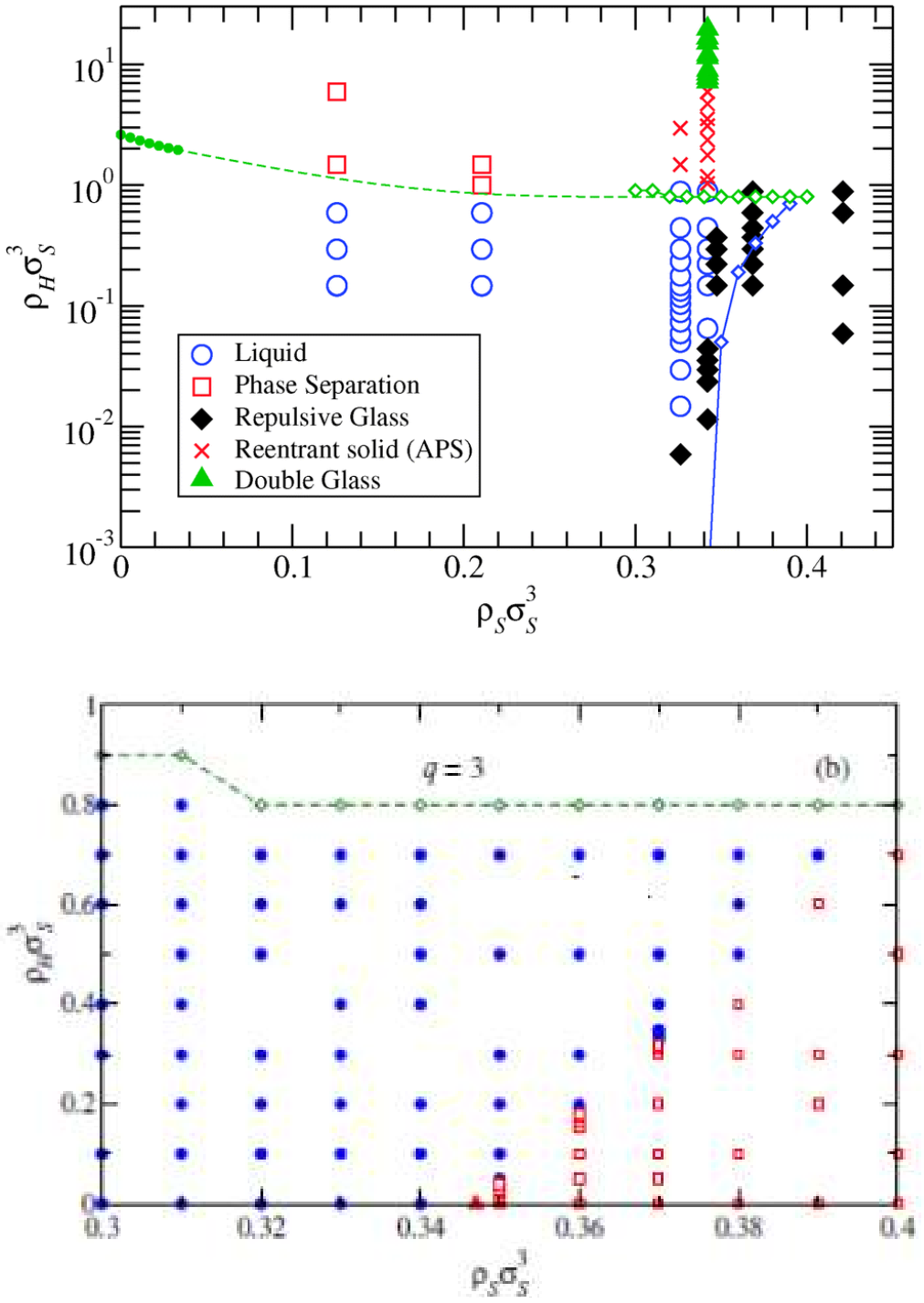

Figure 6.7. *(a) State diagram of star polymer–colloidal mixtures for f = 214 and q = 3 extracted from the linear viscoelastic response and light scattering. Green and blue diamonds indicate, respectively, the theoretically estimated demixing and (MCT) liquid-glass lines in the theoretical phase diagram. Green filled circles at the left correspond to the low-ρ_S branch of the binodal calculated in the reservoir representation, as explained in Appendix B; this branch is the same as the one of the system representation for $\rho_S \to 0$. The dashed line is a guide to the eye. (b) The MCT-phase diagram of the same system. The blue circles mark fluid-like states while the red squares represent glassy states. The filled triangles indicate the liquid to glass transition density ρ_S^g for the pure star system. The dashed line corresponds to the convergence line above which the mixture is considered to undergo an arrested phase separation, as explained in the Appendix B.*

Comparing the theoretical with the experimental work, one can point out only few discrepancies. One of them is an overestimation of the liquid regime from the theory in the higher star densities. The reentrant glass seen in experiments can be seen to arise by the intervention of the demixing binodal, rendering thus the high-ρ_H glass to be the result of an arrested phase separation. The repulsive glass line meets the binodal on the high-density side of the star-polymer glass former. With the addition of the small colloids, increasing attraction leads to a strengthening of the repulsive glass before the binodal is met. When the binodal is crossed, the ensuing phase separation becomes arrested in the continuation of the glass line within the demixed region and the system arrests into a high-star concentration glass. The high star concentration counterbalances for the decreasing repulsion and results in structures which have the same modulus as the original one. However, as the colloidal concentration keeps increasing, the depletion attractions become much more important and lead to shrinkage of the stars, thus the formation of a slightly asymmetric binary hard sphere mixture with much higher modulus values. Accordingly, the high-ρ_S -region above the demixing line in Fig. 6.7b corresponds to a glassy state, consistently with the experimental findings of a reentrant glass. It is, however, not amenable to a MCT-analysis since no structural data are available there, due to the lack of convergence of the integral equations (explained in Appendix B).

We have, also, examined the phase separation by studying the dynamics of star mixtures via DLS, at low star concentrations (liquid region) as function of hard sphere concentration. This corroborates the notion of arrested phase separation at larger star concentrations in the glassy regime. The main experimental challenge was to detect the phase separation of the mixture as a result of the colloidal additions. Dynamic light scattering (DLS) measurements were performed in the same way as already described in Chapter 2.4.

Typical intermediate scattering functions for various hard sphere concentrations are depicted in the Fig. 6.9 inset. We implemented the Debye-Bueche analysis, which is appropriate for circularly symmetric scattering elements [119]. In this case, the angular dependence of the scattering intensities can be described by the Debye-Bueche type scattering function [119]:

$$I(Q) = \left(\frac{A}{1 + (\xi Q)^2}\right)^2 \qquad (6.4)$$

where A is a constant and ξ is the correlation length. The way the A and the ξ are calculated can be seen in Figure 6.8. A is the intercept of the linear regressions, while ξ is extracted from the slope.

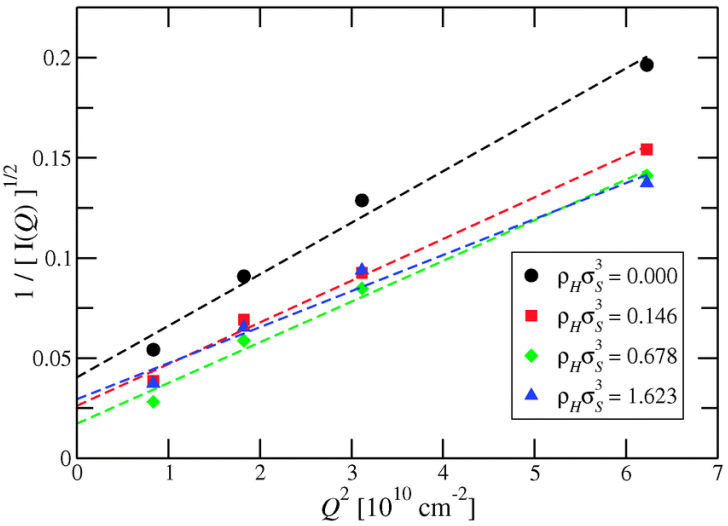

Figure 6.8. *Inverse square root of the slow process intensity vs Q^2 for $\rho_S\sigma_S^3 = 0.126$. Dashed lines represent linear fits.*

Figure 6.9 shows the correlation length ξ determined from the total scattering intensity, normalized to the nominal diameter of the star, as function of the hard sphere concentration. The data correspond to two effective volume fractions of stars $\phi_S = c_S/c_S^*$=0.6 and 1.0 ($\rho_S\sigma_S^3$ = 0.126 and 0.210, respectively) and indicate that with the addition of hard spheres, the star correlation length increases, thus conforming to an incipient phase separation. In fact, at the phase separation line the correlation length should diverge. Here this transition region is also characterized by a (weak) increase in turbidity,

in addition to that of ξ. At higher colloid fractions beyond phase separation, a correlation length is still measurable (the sample is turbid albeit not substantially) and it is indeed expected to decrease with increasing colloid fraction. Although the limited range of Q values considered in DLS gives rise to uncertainty in the estimation of the correlation length, the results are unambiguous for the purpose of the present study, i.e., they confirm the presence of phase separation through the non-monotonic behavior of the $\xi(\rho_H)$.

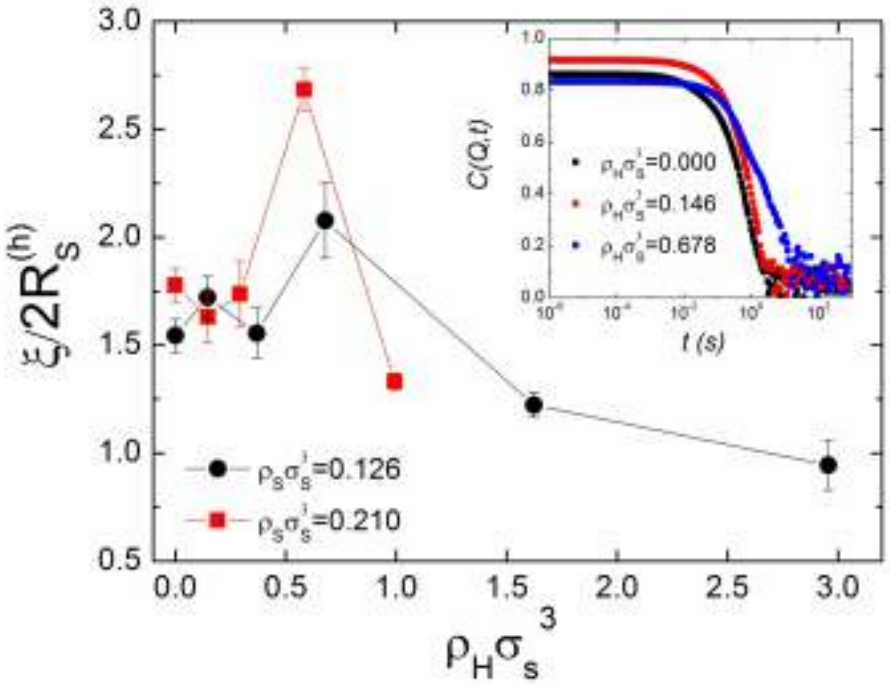

Figure 6.9. *Experimental correlation length for two different star concentrations, as indicated in the legend, as function of colloid density for* $f = 214$ *and* $q = 3$. *Inset: Typical DLS intermediate scattering functions for* $\phi_S = 0.6$ ($\rho_S\sigma_S^3 = 0.126$) *at scattering angle* $\vartheta = 30^\circ$ ($Q\sigma_S = 1.12$) *and at increasing colloidal concentrations.*

The same non-monotonic behavior is also confirmed from the scattering intensity (Fig. 6.10) far from the first peak of the structure factor ($Q \ll Q_{peak}$). The reason for the loss of the monotonicity is the presence of the phase separation. The result of the extrapolation of the scattering intensity at $Q = 0$, where the scattering intensity I(Q) of both DLS relaxation processes exhibit a local maximum, supports the argument of the phase separation. The intensity peaks clearly suggest critical fluctuations and a pass to a phase

separation regime in agreement with the Debye-Bueche analysis and the theoretical predictions shown below/Appendix B.

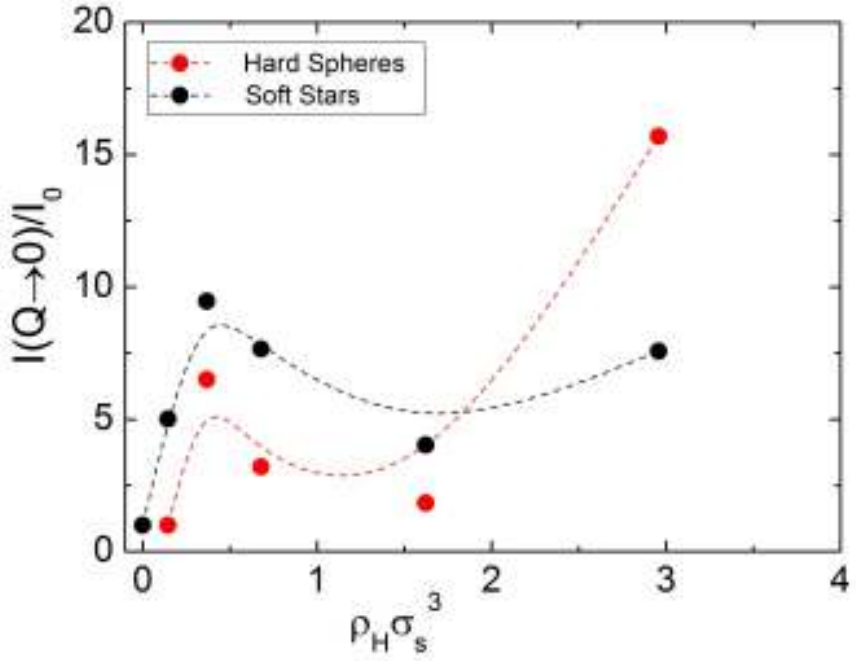

***Figure 6.10**. Normalized scattered intensity extrapolated at Q=0 for the slow and fast processes in HS-star mixtures at $\rho_S\sigma_S^3 = 0.126$. Here I_0 is the intensity measured in absence of HS.*

Further analysis of the DLS data provides more evidence of the phase separation process. Representative results are provided in Fig. 6.11, showing scaled rate constants for the relaxation processes extracted from the $C(Q,t)$ curves. Two such processes can be observed plotted in the form of an apparent diffusion coefficient (relaxation rate Γ over Q^2). The fast process is attributed to the hard spheres since at low colloid fractions, the extracted diffusion coefficient yields the hydrodynamic radius of the hard-like particles from the Stokes-Einstein-Sutherland equation. Up to the phase separation region, this diffusion coefficient is practically independent of colloid concentration. It then slows down rather dramatically in the phase separated region. At the same time, the diffusion coefficient of the slow mode, which is attributed to star-related motions, slows down for increasing colloid fractions (see Fig. 6.10). However the slow-down is sharper in the pre-

transitional homogeneous region, conforming to the respective increase in correlation length.

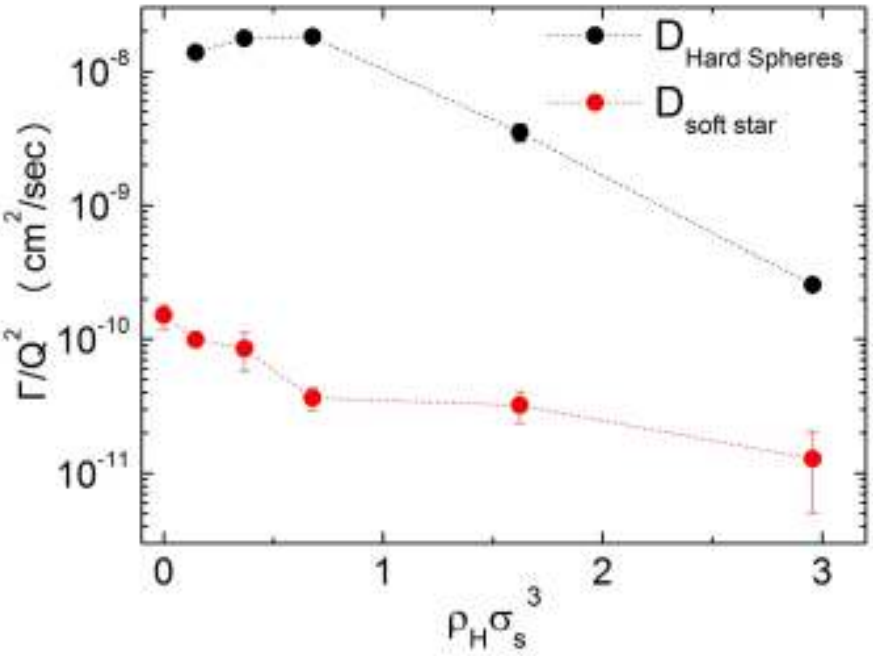

Figure 6.11. *The apparent diffusion coefficient at ϕ_S = 0.6 ($\rho_S\sigma_S^3$ = 0.126) as function of colloid density. Diffusion of the fast and slow processes are attributed to hard and soft colloids, respectively.*

The physical mechanism which is responsible for the glass state melting and the subsequent demixing transition can be attributed to the fact that the small colloids act like depletants for the large stars. A moderate colloid additive concentration causes the reduction in the star-star repulsion, leading to melting of the glass [107, 276]. Further increase in the colloidal density leads to the rise of the net attractive potential between the stars, which results in phase separation, as corroborated by rheology measurements at high ρ_S (Fig. 6.2).

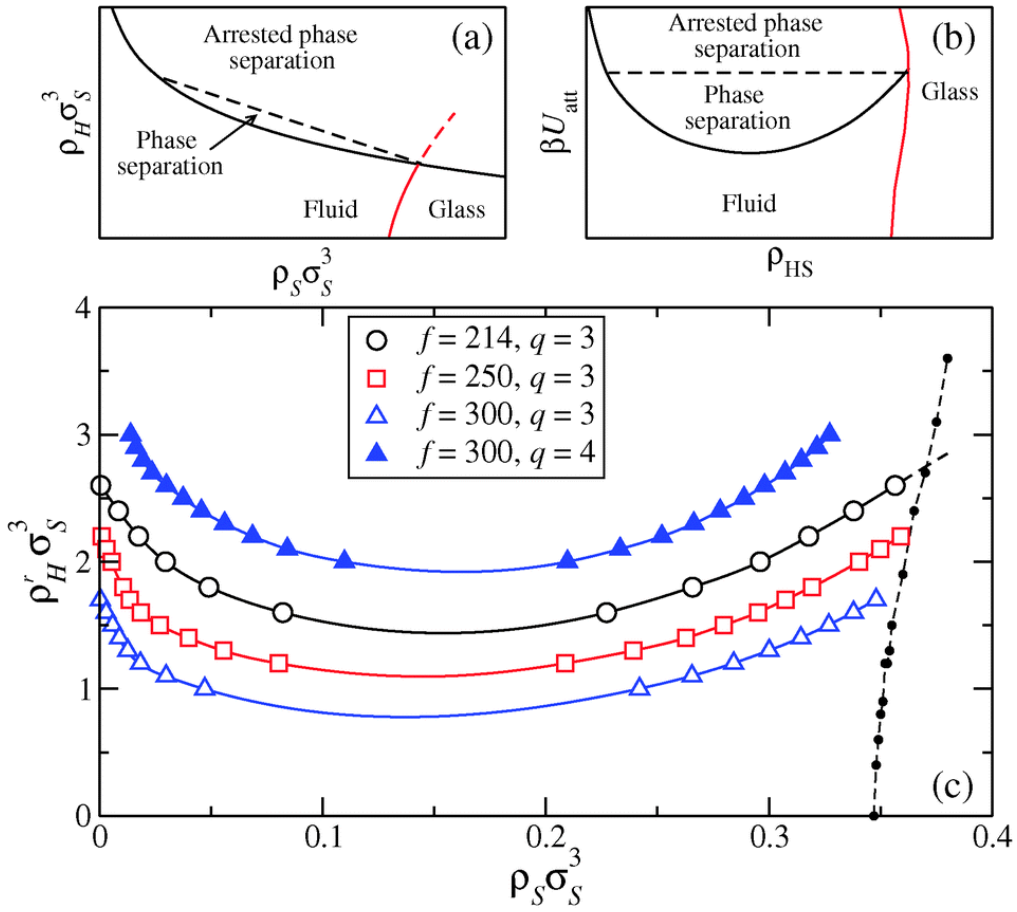

Figure 6.12. *Top: Schematic phase diagram for star-colloid mixtures in the system representation (a) and for hard-sphere systems with long-range attractive interaction [294, 295] (b). Bottom, (c): Demixing binodal lines in the reservoir representation for different functionalities and size ratios, as indicated in the legend. Small filled circles indicate the MCT liquid-glass line calculated using the modified, effective potential* $V_{SS}^{(mod)}(r;\rho_H^r)$ *for* $f = 214$ *and* $q = 3$ *(More details in Appendix B).*

Figure 6.12 displays the binodal lines for different values of f and q. In agreement with estimates based on the non-additivity parameter [280], phase separation is observed at higher colloid reservoir densities for smaller colloid particles, as well as for softer stars. For the experimentally relevant system $f = 214$ and $q = 3$, we employed the modified effective potential $V_{SS}^{(mod)}(r;\rho_H^r)$ to evaluate both $S(Q)$ and $\phi(Q)$ (Appendix B). The resulting (MCT) liquid-glass line crosses the binodal driving the phase separation to an arrested state, as plotted in Fig. 6.12. This scenario is reminiscent of the one found in hard spheres suspensions with (long-range) attractive interactions, which phase diagram is sketched in Fig. 6.12b, at intermediate volume fraction and intermediate strength of the

attraction [294, 295]. A similar behavior is expected for larger functionalities and size ratios with the glass line shifted to lower star density. Note that these trends are in complete agreement with the predictions made in the state diagram (Fig. 6.6b) based on the convergence limit of the OZ-RY approach to study the structure of the mixture, and also with the assumption of an arrested phase separation above this convergence line. In this way, the generic behavior of the mixture can be schematically represented as in Fig. 6.12a.

In conclusion, we have shown by combining experiments, theory and simulation that the addition of small, hard colloidal additives to a structural glass formed by big, soft colloids brings forward a wealth of novel, tunable rheological states. These rheological states include phase separation (demixing) of a fluid-like suspension (at low star densities) and the melting of a repulsive glassy state (at high star densities). We made use of DLS/SLS to detect phase separation in liquid-like samples and rheology to detect repulsive glass melting, as well as reentrant solid-like states above the glass line of the colloid-free system. In the latter case, as the depletant concentration is further increased, interplay between structural arrest and demixing takes place, leading to an arrested phase separation and therefore to a new re-entrant glassy state, as shown in Fig. 6.6 and 6.12. The theoretical results were corroborated by experimental studies of the dynamics of stars *via* DLS along with the linear viscoelastic response of the mixtures for different hard sphere concentrations.

Our findings should be generic for soft- hard mixtures for which the former component is significantly larger than the latter. The star functionality and the size ratio are the natural, physical parameters to adjust in order to steer the rheology of the mixture. Similar transitions have been observed, also, in other star mixtures where the role of the depletant was played by linear chains [296]. The melting of the initial repulsive glass was followed by the formation of a reentrant gel revealing different states depending on the softness of

the depletion. The effect of the size ratio and the concentration of the stars on the dynamics of such mixtures is highlighted in the figures of Appendix C. Thus, we can argue that we are able to tune the rheological behavior of such systems along with the interparticle potential by adjusting the softness, concentration and the size ratio.

Controlling these physical parameters can transform our system, providing it with features similar to other deformable systems. Examples of such systems are hyperbranched polymers including microgels, copolymer micelles, polymer-grafted nanoparticles and dendrimers, all of which can be well-described through a core–shell structure and whose interactions can be easily tuned through several physical and chemical factors. Since the theoretical description is independent of adjustable fitting parameters, we expect our results to hold for more generic systems, which offer interesting insight into the design and precise tunability of new soft composites that are of great interest in materials science and industrial applications.

7. Conclusions and Recommendations

The scope of this work was to explore and enlighten the metastable states of different systems belonging in the wide world of soft materials. Metastability is a property of these materials and one of the key reasons why we consider them as "*the materials of the future"*. By manipulating internal interactions and transitions between different states, someone can control the dynamics and the response of the systems to external forces. The microstructural changes, which take place upon the appliance of external fields, like flow or electric, make this study promising and attractive for various scientific areas. The current technological applications of these materials are countless, highlighting the importance of working with them and discovering the possibilities not yet captured.

In this research we explored the effects of metastability on three different systems. In chapter 2, we studied how molecular structural characteristics lead the system to several transitions upon the appliance of an external flow field. We defined a 'softness parameter', (SP), and highlighted its effect on the structural arrangements of the particles. We investigated the effect of shearing parameters on the rheological response of the systems and explained the variations with the modifications of the particle rearrangements. The stability of the structures was associated with softness and concentration, denoting the sensitive dynamics deviations upon changing the molecular characteristics. Flexible shapes of particles allow the systems to reform and accommodate better the external stimuli. We pinpointed the differences of our soft systems with the hard spheres and highlighted the complexity yielded by 'softness'. In general, softness and metastability are two terms, which seem to be inextricably bonded, generating amazing properties.

In chapter 3, we investigated the self assembly of two different block copolymers. The amphiphilicity of the molecules drive the systems to self-organize and form hydrogels. Depending on the molecular characteristics, the hydrogel structures exhibit varying

properties showing solid structures at high concentrations. The elasticity of the networks increase rapidly with concentrations demonstrating different types of interactions between the self-assembled structures. Both hydrogels studied in this work, showed fast reformation after the cessation of large shear rates, meaning that the attraction of the system is very high due to the particle amphiphilicity. By tuning hydrophobic and hydrophilic interactions we can control the kinetic properties of such systems and mimic the natural way of creating supramolecular systems. The sensitivity in temperature and in pH variations, makes these hydrogels excellent candidate systems for drug delivery applications, offering discovery opportunities in this important field.

Furthermore, we examined metastability effects in more complicated systems consisted of two different size and type of particles. The initial soft colloidal system was perturbed by adding depletion and displayed several phase transitions. The kinetic properties, along with mixture elasticity, change as a function of depletion type revealing a way to control the behavior of such systems. Again, metastability was associated with softness and proved to adjust the mechanical properties of the mixtures. All, the experimental results were supported by theoretical analysis and simulations, denoting the validity of our outcomes. Also, simulations were performed for different size ratios and functionalities than those tested experimentally. The combined results demonstrate that by tuning the physical parameters, like star functionality and size ratio, we can steer the rheology of the mixtures.

The work presented in this thesis highlights the connection between softness and metastability. Softness has been manifested molecularly in many different ways, from varying the particle's geometrical characteristics to controlling through amphiphilicity their self assembly. Understanding this thermodynamic network is of crucial importance for controlling properties and responses of these systems. The rich variety of metastable states like glass, gel, arrested state, phase separation etc, and their transitions are results

from this complicated thermodynamic equilibrium. Another highly important factor which influences the outcomes of the equilibrium equation is the external field. External forces can lead to various transitions until the system reaches its favorable state. The connection between external fields and microstructure is capable of opening new routes in designing systems with desired properties and tunable rheology. Materials that can vary their response depending on external perturbations are extremely promising and very strong candidates for various applications.

Unavoidable effects of every scientific research are the open questions left to be addressed in future works. Building a model correlating system's softness with external fields parameters will allow us to construct a phase diagram on the axes of softness, concentration and imposed shear. Going deeper in molecular structures, it would be interesting to investigate further the key properties of softness i.e. deformability, interpenetration etc., that lead the systems to ordered structures.

Moving to self-assembly, the next step is to examine extended structures created by large polymers in three-dimensional space. The roots of the gel properties are not clear, requesting deeper investigation to explain the evolution of the structures depending either on concentration or external parameters such as temperature or pH. Since current demands require abrupt transitions and well-controlled properties, the connection between synthesis and rheological properties attracts great attention.

Furthermore, having predicted the ergodicity of a complex system, such as star-hard sphere or star-linear mixture, there is still work to be done on the characterization of the structures. It is difficult to distinguish, rheologically, states like attractive, double or asymmetric glass. Therefore, further theoretical and experimental analysis is needed to enlighten this dark area. Also, the different states that have been seen depending on the softness of depletion raise new questions regarding more complicated ways of inducing depletion. For example, with the utilization of linear polymers as depletants we found gel

structures while using hard spheres or stars, we discovered double and asymmetric kinetically arrested states. What will happen if we combine hard and soft depletants and how can we build a phase diagram of mixtures depending on the softness and concentration of the particles.

Our expectation is that this work has shed some light on unaddressed metastable effects and added a small part of knowledge in this extremely wide field. Hopefully, we offered pioneering initiatives for new perspectives on the soft systems research..

8. Acknowledgements

I would like to begin with highlighting the role of my supervisor Professor Dimitris Vlassopoulos who gave me the opportunity to work in such an advanced laboratory and provided me with his supportiveness, mentorship, guidance and patience. It has been an honor for me to work with Professor Vlassopoulos and share views not restricted inside the scientific borders. Furthermore, I am more than thankful to Professor George Fytas, whose endless energy has been an inspiration and motivation for my work. I would also like to thank Professor George Petekidis and Benoit Loppinet for participating in many fruitful discussions which have broadened my knowledge and way of thinking.

Working in this lab for the past 4 years, it would be a remiss of me not to thank every member of this lab for sharing my problems and thoughts. Special thanks to Esmaeel Moghimi, Maria Merola, Alan Jacob, Panagiota Bogri and Andreas Pamvouxoglou, for the interesting scientific discussions and more.

There are a lot of people whose part in this work was of significant importance. A large part of this work has been carried out with the help of Domenico Truzzolillo who was the first person to introduce me to the experimental techniques. Domenico's patience, support and guidance was a great help to me from the beginning and throughout this work.

Moreover, it was a great opportunity for me to meet and work with Professor Pavlik Leittinga who provided me with a different view of science. I will always remember his passion and energy which have been a constant motivation for me. I would also like to thank Joachim Koelbrecher from the bottom of my heart for providing all the necessary equipment used for the experiments in Paul Schurrer Institute. I will never forget Joachim's and Agnieszka's warm hospitality during my stay there.

I would also like to thank the different groups with which I have worked for the different projects described in this thesis. I would like to thank Professor Likos' group in Vienna who provided all the theoretical analysis which supported the experimental results shown. Moreover, I am also very thankful to Professor Iatrou and his group in Athens who have given me the chance to participate in his very interesting projects. We hope that the outcomes of this particular work will be a small step towards the solution of a very sensitive and large problem affecting our society.

Finally, I need to thank my parents, family, friends who stood by me all this time and supported my efforts. As a final note, I would like to thank Professor Floudas and the Greek General Secretariat for Research and Technology (ESPA, Thalis META-ASSEMBLY project) for their financial support.

9. References

1. Smith, R.G. and G.C. Maitland, *The Road Ahead to Real-Time Oil and Gas Reservoir Management.* Chemical Engineering Research and Design, 1998. 76(5): p. 539-552.
2. Fordham, E.J., et al., *Depth Filtration of Clay in Rock Cores Observed by One-Dimensional 1H NMR Imaging.* Journal of Colloid and Interface Science, 1993. 156(1): p. 253-255.
3. Kuo-Kang, L., *Deformation behaviour of soft particles: a review.* Journal of Physics D: Applied Physics, 2006. 39(11): p. R189.
4. Kaneda, Y., *Virosomes: evolution of the liposome as a targeted drug delivery system.* Advanced Drug Delivery Reviews, 2000. 43(2–3): p. 197-205.
5. Bloomfield, V.A., *DNA condensation.* Current Opinion in Structural Biology, 1996. 6(3): p. 334-341.
6. Gelbart, W.M., et al., *DNA-Inspired Electrostatics.* Print edition, 2000. 53(9): p. 38-44.
7. Andrews, D.W., *Transport across Membranes.* Cell. 102(2): p. 139-144.
8. Roberto, P. and P. Matteo, *Protein interactions near crystallization: a microscopic approach to the Hofmeister series.* Journal of Physics: Condensed Matter, 2000. 12(8A): p. A443.
9. Poon, W.C.K., et al., *Protein crystallization: scaling of charge and salt concentration in lysozyme solutions.* Journal of Physics: Condensed Matter, 2000. 12(35): p. L569.
10. Quake, S.R. and A. Scherer, *From Micro- to Nanofabrication with Soft Materials.* Science, 2000. 290(5496): p. 1536-1540.
11. Antonietti, M. and C. Göltner, *Superstructures of Functional Colloids: Chemistry on the Nanometer Scale.* Angewandte Chemie International Edition in English, 1997. 36(9): p. 910-928.
12. Zrínyi, M., *Intelligent polymer gels controlled by magnetic fields.* Colloid and Polymer Science, 2000. 278(2): p. 98-103.
13. Aida, T., E.W. Meijer, and S.I. Stupp, *Functional Supramolecular Polymers().* Science (New York, N.y.), 2012. 335(6070): p. 813-817.
14. Shahinpoor, M. and H.-J. Schneider, *Intelligent materials*. 2008: Royal Society of Chemistry.
15. Niu, X., et al., *Generation and manipulation of "smart" droplets.* Soft Matter, 2009. 5(3): p. 576-581.
16. Yarimaga, O., et al., *Polydiacetylenes: supramolecular smart materials with a structural hierarchy for sensing, imaging and display applications.* Chemical Communications, 2012. 48(19): p. 2469-2485.
17. Tsitsilianis, C., *Responsive reversible hydrogels from associative "smart" macromolecules.* Soft Matter, 2010. 6(11): p. 2372-2388.
18. Liu, Y.D. and H.J. Choi, *Electrorheological fluids: smart soft matter and characteristics.* Soft Matter, 2012. 8(48): p. 11961-11978.
19. Ohko, Y., et al., *Multicolour photochromism of TiO2 films loaded with silver nanoparticles.* Nat Mater, 2003. 2(1): p. 29-31.
20. Kexiang, W., et al., *Vibration characteristics of electrorheological elastomer sandwich beams.* Smart Materials and Structures, 2011. 20(5): p. 055012.
21. Likos, C.N., *Effective interactions in soft condensed matter physics.* Physics Reports, 2001. 348(4–5): p. 267-439.
22. *Soft matter: more than words.* Soft Matter, 2005. 1(1): p. 16-16.
23. de Gennes, P.G., *Soft matter.* Reviews of Modern Physics, 1992. 64(3): p. 645-648.
24. Kleman, M. and O.D. Lavrentovich, *Soft Matter Physics: An Introduction.* Partially Ordered Systems, 2004.
25. Jones, R.A., *Soft condensed matter*. Vol. 6. 2002: Oxford University Press.

26. Löwen, H., *Colloidal soft matter under external control.* Journal of Physics: Condensed Matter, 2001. 13(24): p. R415.
27. Stokes, J.R. and W.J. Frith, *Rheology of gelling and yielding soft matter systems.* Soft Matter, 2008. 4(6): p. 1133-1140.
28. Jiang, X.C., et al., *Self-assembly of particles: some thoughts and comments.* Journal of Materials Chemistry, 2011. 21(42): p. 16797-16805.
29. Muthukumar, M., C.K. Ober, and E.L. Thomas, *Competing Interactions and Levels of Ordering in Self-Organizing Polymeric Materials.* Science, 1997. 277(5330): p. 1225-1232.
30. Whitesides, G.M. and B. Grzybowski, *Self-Assembly at All Scales.* Science, 2002. 295(5564): p. 2418-2421.
31. Wunderlich, K., et al., *Controlled Hydrogel Fiber Formation: The Unique Case of Hexaphenylbenzene-Poly(ethylene glycol) Amphiphiles.* Small, 2014. 10(10): p. 1914-1919.
32. Hamley, I.W., *Introduction to soft matter: synthetic and biological self-assembling materials*. 2013: John Wiley & Sons.
33. Witten, T., *Insights from Soft Condensed Matter*, in *More Things in Heaven and Earth*, B. Bederson, Editor. 1999, Springer New York. p. 617-628.
34. Cipelletti, L., et al., *Universal non-diffusive slow dynamics in aging soft matter.* Faraday Discussions, 2003. 123(0): p. 237-251.
35. Sollich, P., *Rheological constitutive equation for a model of soft glassy materials.* Physical Review E, 1998. 58(1): p. 738-759.
36. Cipelletti, L. and L. Ramos, *Slow dynamics in glassy soft matter.* Journal of Physics: Condensed Matter, 2005. 17(6): p. R253.
37. Vlassopoulos, D. and G. Fytas, *From Polymers to Colloids: Engineering the Dynamic Properties of Hairy Particles*, in *High Solid Dispersions*, M. Cloitre, Editor. 2010, Springer Berlin Heidelberg. p. 1-54.
38. Block, S.M., *Making light work with optical tweezers.* Nature, 1992. 360(6403): p. 493-495.
39. Wright, W.H., G.J. Sonek, and M.W. Berns, *Radiation trapping forces on microspheres with optical tweezers.* Applied Physics Letters, 1993. 63(6): p. 715-717.
40. Zahn, K., J.M. Méndez-Alcaraz, and G. Maret, *Hydrodynamic Interactions May Enhance the Self-Diffusion of Colloidal Particles.* Physical Review Letters, 1997. 79(1): p. 175-178.
41. Zahn, K. and G. Maret, *Two-dimensional colloidal structures responsive to external fields.* Current Opinion in Colloid & Interface Science, 1999. 4(1): p. 60-65.
42. Hansen, J.-P. and H. Löwen, *EFFECTIVE INTERACTIONS BETWEEN ELECTRIC DOUBLE LAYERS.* Annual Review of Physical Chemistry, 2000. 51(1): p. 209-242.
43. Lyklema, J., *Fundamentals of interface and colloid science 2, 2*. 1995, London: Academic Press.
44. Borówko, M., *Computational methods in surface and colloid science*. 2000: CRC Press.
45. Cates, M.E. and M.R. Evans, *Soft and Fragile Matter: Nonequilibrium Dynamics, Metastability and Flow (PBK)*. 2000: CRC Press.
46. Ackerson, B.J. and N.A. Clark, *Shear-Induced Melting.* Physical Review Letters, 1981. 46(2): p. 123-126.
47. Ackerson, B.J. and N.A. Clark, *Shear-induced partial translational ordering of a colloidal solid.* Physical Review A, 1984. 30(2): p. 906-918.
48. Lindsay, H., M. and P. Chaikin, M., *SHEAR ELASTICITY AND VISCOSITY IN COLLOIDAL CRYSTALS AND LIQUIDS.* J. Phys. Colloques, 1985. 46(C3): p. C3-269-C3-280.
49. Ackerson, B.J., *Shear induced order and shear processing of model hard sphere suspensions.* Journal of Rheology, 1990. 34(4): p. 553-590.
50. Ackerson, B.J. and P.N. Pusey, *Shear-Induced Order in Suspensions of Hard Spheres.* Physical Review Letters, 1988. 61(8): p. 1033-1036.

51. Yan, Y.D. and J.K.G. Dhont, *Shear-induced structure distortion in nonaqueous dispersions of charged colloidal spheres via light scattering.* Physica A: Statistical Mechanics and its Applications, 1993. 198(1–2): p. 78-107.
52. Vermant, J. and M.J. Solomon, *Flow-induced structure in colloidal suspensions.* Journal of Physics: Condensed Matter, 2005. 17(4): p. R187.
53. Liu, A.J. and S.R. Nagel, *Nonlinear dynamics: Jamming is not just cool any more.* Nature, 1998. 396(6706): p. 21-22.
54. Trappe, V., et al., *Jamming phase diagram for attractive particles.* Nature, 2001. 411(6839): p. 772-775.
55. Foffi, G., et al., *Structural Arrest in Dense Star-Polymer Solutions.* Physical Review Letters, 2003. 90(23): p. 238301.
56. Prasad, V., et al., *Rideal Lecture Universal features of the fluid to solid transition for attractive colloidal particles.* Faraday Discussions, 2003. 123(0): p. 1-12.
57. Dawson, K.A., *The glass paradigm for colloidal glasses, gels, and other arrested states driven by attractive interactions.* Current Opinion in Colloid & Interface Science, 2002. 7(3–4): p. 218-227.
58. Tanaka, H., et al., *Kinetics of ergodic-to-nonergodic transitions in charged colloidal suspensions: Aging and gelation.* Physical Review E, 2005. 71(2): p. 021402.
59. Tanaka, H., J. Meunier, and D. Bonn, *Nonergodic states of charged colloidal suspensions: Repulsive and attractive glasses and gels.* Physical Review E, 2004. 69(3): p. 031404.
60. Vlassopoulos, D., *Colloidal star polymers: Models for studying dynamically arrested states in soft matter.* Journal of Polymer Science Part B: Polymer Physics, 2004. 42(16): p. 2931-2941.
61. Shintani, H. and H. Tanaka, *Frustration on the way to crystallization in glass.* Nat Phys, 2006. 2(3): p. 200-206.
62. Prost, J., *The physics of liquid crystals*. 1995: Oxford university press.
63. Lagerwall, J.P.F. and G. Scalia, *A new era for liquid crystal research: Applications of liquid crystals in soft matter nano-, bio- and microtechnology.* Current Applied Physics, 2012. 12(6): p. 1387-1412.
64. Saunders, B.R. and B. Vincent, *Microgel particles as model colloids: theory, properties and applications.* Advances in Colloid and Interface Science, 1999. 80(1): p. 1-25.
65. Bradna, P., et al., *Thickening effect of dispersions of ethyl acrylate-methacrylic acid copolymer prepared by different polymerization routes.* Colloid and Polymer Science, 1995. 273(4): p. 324-330.
66. Bae, Y.H. and S.W. Kim, *Modern Hydrogel Delivery Systems Hydrogel delivery systems based on polymer blends, block co-polymers or interpenetrating networks.* Advanced Drug Delivery Reviews, 1993. 11(1): p. 109-135.
67. Denton, A., *Effective Interactions in Soft Materials*, in *Nanostructured Soft Matter*, A. Zvelindovsky, Editor. 2007, Springer Netherlands. p. 395-433.
68. Murtola, T., et al., *Multiscale modeling of emergent materials: biological and soft matter.* Physical Chemistry Chemical Physics, 2009. 11(12): p. 1869-1892.
69. Klingler, J., *RJ Hunter: Introduction to Modern Colloid Science, Oxford University Press, Oxford, New York, Melbourne, 1993. ISBN 0–19–855386–2, 338 Seiten, Preis: $14.95.* Berichte der Bunsengesellschaft für physikalische Chemie, 1995. 99(3): p. 591-592.
70. Xia, Y., et al., *Monodispersed colloidal spheres: old materials with new applications.* Advanced Materials, 2000. 12(10): p. 693-713.
71. Kim, J.-W., R.J. Larsen, and D.A. Weitz, *Synthesis of Nonspherical Colloidal Particles with Anisotropic Properties.* Journal of the American Chemical Society, 2006. 128(44): p. 14374-14377.
72. Mishchenko, M.I., L.D. Travis, and A.A. Lacis, *Scattering, absorption, and emission of light by small particles*. 2002: Cambridge university press.
73. Larson, R.G., *The structure and rheology of complex fluids*. Vol. 33.

74. Jogun, S.M. and C.F. Zukoski, *Rheology and microstructure of dense suspensions of plate-shaped colloidal particles.* Journal of Rheology, 1999. 43(4): p. 847-871.
75. Peigney, A., *Composite materials: Tougher ceramics with nanotubes.* Nat Mater, 2003. 2(1): p. 15-16.
76. Glotzer, S., M. Solomon, and N.A. Kotov, *Self-assembly: From nanoscale to microscale colloids.* AIChE Journal, 2004. 50(12): p. 2978-2985.
77. Roh, K.-H., D.C. Martin, and J. Lahann, *Biphasic Janus particles with nanoscale anisotropy.* Nat Mater, 2005. 4(10): p. 759-763.
78. Ryadnov, M.G. and D.N. Woolfson, *Engineering the morphology of a self-assembling protein fibre.* Nat Mater, 2003. 2(5): p. 329-332.
79. Soussan, E., et al., *Drug Delivery by Soft Matter: Matrix and Vesicular Carriers.* Angewandte Chemie International Edition, 2009. 48(2): p. 274-288.
80. Bjerregaard, S., et al., *Formulation and evaluation of release and swelling mechanism of a water-in-oil emulsion using factorial design.* International Journal of Pharmaceutics, 1999. 193(1): p. 1-11.
81. Fukushima, S., et al., *Preparation and evaluation of o/w type emulsions containing antitumor prostaglandin.* Advanced Drug Delivery Reviews, 2000. 45(1): p. 65-75.
82. Israelachvili, J., *The science and applications of emulsions — an overview.* Colloids and Surfaces A: Physicochemical and Engineering Aspects, 1994. 91: p. 1-8.
83. Chappat, M., *A selection of papers presented at the First World Congress on EmulsionsSome applications of emulsions.* Colloids and Surfaces A: Physicochemical and Engineering Aspects, 1994. 91: p. 57-77.
84. Banhart, J., *Manufacture, characterisation and application of cellular metals and metal foams.* Progress in Materials Science, 2001. 46(6): p. 559-632.
85. Stocco, A., et al., *Aqueous foams stabilized solely by particles.* Soft Matter, 2011. 7(4): p. 1260-1267.
86. Koehler, S.A., S. Hilgenfeldt, and H.A. Stone, *A Generalized View of Foam Drainage: Experiment and Theory.* Langmuir, 2000. 16(15): p. 6327-6341.
87. Banhart, J., *Metal Foams: Production and Stability.* Advanced Engineering Materials, 2006. 8(9): p. 781-794.
88. Neethling, S.J. and J.J. Cilliers, *Solids motion in flowing froths.* Chemical Engineering Science, 2002. 57(4): p. 607-615.
89. Vlassopoulos, D. and M. Cloitre, *Tunable rheology of dense soft deformable colloids.* Current Opinion in Colloid & Interface Science, 2014. 19(6): p. 561-574.
90. Witten, T.A., P.A. Pincus, and M.E. Cates, *Macrocrystal Ordering in Star Polymer Solutions.* EPL (Europhysics Letters), 1986. 2(2): p. 137.
91. Stiakakis, E., et al., *Slow dynamics, aging, and crystallization of multiarm star glasses.* Physical Review E, 2010. 81(2): p. 020402.
92. Rissanou, A.N., et al., *Temperature-induced crystallization in concentrated suspensions of multiarm star polymers: A molecular dynamics study.* The Journal of Chemical Physics, 2006. 124(4): p. 044905.
93. Panine, P., et al., *Structure and rheology during shear-induced crystallization of a latex suspension.* Physical Review E, 2002. 66(2): p. 022401.
94. Williamson, J.J. and R.M.L. Evans, *The effects of polydispersity and metastability on crystal growth kinetics.* Soft Matter, 2013. 9(13): p. 3600-3612.
95. Keller, A. and S.Z.D. Cheng, *The role of metastability in polymer phase transitions.* Polymer, 1998. 39(19): p. 4461-4487.
96. Landau, L.D. and E.M. Lifshitz, *Quantum mechanics: non-relativistic theory*. Vol. 3. 2013: Elsevier.
97. Reguera, D. and J.M. Rubí, *Kinetic equations for diffusion in the presence of entropic barriers.* Physical Review E, 2001. 64(6): p. 061106.
98. Sollich, P., et al., *Rheology of Soft Glassy Materials.* Physical Review Letters, 1997. 78(10): p. 2020-2023.

99. Frenkel, D., *Soft condensed matter.* Physica A: Statistical Mechanics and its Applications, 2002. 313(1–2): p. 1-31.
100. Cheng, S.Z., *Phase transitions in polymers: the role of metastable states: the role of metastable states*. 2008: Elsevier.
101. Sakai, V.G., C. Alba-Simionesco, and S.H. Chen, *Dynamics of Soft Matter: Neutron Applications*. 2011: Springer Science & Business Media.
102. Koumakis, N., A.B. Schofield, and G. Petekidis, *Effects of shear induced crystallization on the rheology and ageing of hard sphere glasses.* Soft Matter, 2008. 4(10): p. 2008-2018.
103. Vlassopoulos, D., et al., *Multiarm star polymers dynamics.* Journal of Physics: Condensed Matter, 2001. 13(41): p. R855.
104. Likos, C.N., et al., *Ordering phenomena of star polymer solutions approaching the \ensuremath{\Theta} state.* Physical Review E, 1998. 58(5): p. 6299-6307.
105. Gast, A., *Structure and Interactions in Tethered Chains*, in *Solvents and Self-Organization of Polymers*, S. Webber, P. Munk, and Z. Tuzar, Editors. 1996, Springer Netherlands. p. 259-280.
106. Roovers, J., et al., *Regular star polymers with 64 and 128 arms. Models for polymeric micelles.* Macromolecules, 1993. 26(16): p. 4324-4331.
107. Stiakakis, E., et al., *Kinetic arrest of crowded soft spheres in solvents of varying quality.* Physical Review E, 2002. 66(5): p. 051804.
108. Daoud, M. and J.P. Cotton, *Star shaped polymers : a model for the conformation and its concentration dependence.* J. Phys. France, 1982. 43(3): p. 531-538.
109. Pakula, T., et al., *Structure and Dynamics of Melts of Multiarm Polymer Stars.* Macromolecules, 1998. 31(25): p. 8931-8940.
110. Nishinari, K., *Some Thoughts on The Definition of a Gel*, in *Gels: Structures, Properties, and Functions*. 2009, Springer Berlin Heidelberg. p. 87-94.
111. Tanaka, F. and S.F. Edwards, *Viscoelastic properties of physically crosslinked networks.* Journal of Non-Newtonian Fluid Mechanics, 1992. 43(2): p. 289-309.
112. Tanaka, F. and S.F. Edwards, *Viscoelastic properties of physically crosslinked networks. 1. Transient network theory.* Macromolecules, 1992. 25(5): p. 1516-1523.
113. Tanaka, F., *Theory of molecular association and thermoreversible gelation*, in *Molecular Gels*. 2006, Springer. p. 17-77.
114. Winter, H. and M. Mours, *Rheology of Polymers Near Liquid-Solid Transitions*, in *Neutron Spin Echo Spectroscopy Viscoelasticity Rheology*. 1997, Springer Berlin Heidelberg. p. 165-234.
115. Chambon, F. and H.H. Winter, *Stopping of crosslinking reaction in a PDMS polymer at the gel point.* Polymer Bulletin, 1985. 13(6): p. 499-503.
116. Miyoshi, E., T. Takaya, and K. Nishinari, *Rheological and thermal studies of gel-sol transition in gellan gum aqueous solutions.* Carbohydrate Polymers, 1996. 30(2–3): p. 109-119.
117. Matsoukas, T., *Statistical Thermodynamics of Irreversible Aggregation: The Sol-Gel Transition.* Scientific Reports, 2015. 5: p. 8855.
118. Hyun, K., et al., *A review of nonlinear oscillatory shear tests: Analysis and application of large amplitude oscillatory shear (LAOS).* Progress in Polymer Science, 2011. 36(12): p. 1697-1753.
119. Berne, B.J. and R. Pecora, *Dynamic light scattering: with applications to chemistry, biology, and physics*. 2000: Courier Corporation.
120. Provencher, S.W., *CONTIN: A general purpose constrained regularization program for inverting noisy linear algebraic and integral equations.* Computer Physics Communications, 1982. 27(3): p. 229-242.
121. Brown, W., *Dynamic light scattering : the method and some applications*. 1993, Oxford [England]; New York: Clarendon Press ; Oxford University Press.
122. Haw, M.D., W.C.K. Poon, and P.N. Pusey, *Direct observation of oscillatory-shear-induced order in colloidal suspensions.* Physical Review E, 1998. 57(6): p. 6859-6864.

123. Imhof, A., A. van Blaaderen, and J.K.G. Dhont, *Shear Melting of Colloidal Crystals of Charged Spheres Studied with Rheology and Polarizing Microscopy.* Langmuir, 1994. 10(10): p. 3477-3484.
124. Besseling, T.H., et al., *Oscillatory shear-induced 3D crystalline order in colloidal hard-sphere fluids.* Soft Matter, 2012. 8(26): p. 6931-6939.
125. van Megen, W. and S.M. Underwood, *Change in crystallization mechanism at the glass transition of colloidal spheres.* Nature, 1993. 362(6421): p. 616-618.
126. Ackerson, B.J., et al., *Neutron scattering from charge stabilized suspensions undergoing shear.* The Journal of Chemical Physics, 1986. 84(4): p. 2344-2349.
127. Haw, M.D., et al., *Colloidal glasses under shear strain.* Physical Review E, 1998. 58(4): p. 4673-4682.
128. Duff, N. and D.J. Lacks, *Shear-induced crystallization in jammed systems.* Physical Review E, 2007. 75(3): p. 031501.
129. Wu, Y.L., et al., *Melting and crystallization of colloidal hard-sphere suspensions under shear.* Proceedings of the National Academy of Sciences, 2009. 106(26): p. 10564-10569.
130. Holmqvist, P., et al., *Crystallization Kinetics of Colloidal Spheres under Stationary Shear Flow.* Langmuir, 2005. 21(24): p. 10976-10982.
131. Watanabe, H., T. Kanaya, and Y. Takahashi, *Equilibrium Elasticity of Diblock Copolymer Micellar Lattice.* Macromolecules, 2001. 34(3): p. 662-665.
132. McConnell, G.A., et al., *Disorder-order transitions in soft sphere polymer micelles.* Physical Review Letters, 1993. 71(13): p. 2102-2105.
133. Laurati, M., et al., *Starlike Micelles with Starlike Interactions: A Quantitative Evaluation of Structure Factors and Phase Diagram.* Physical Review Letters, 2005. 94(19): p. 195504.
134. Laurati, M., et al., *Asymmetric poly(ethylene-alt-propylene)-poly(ethylene oxide) micelles: A system with starlike morphology and interactions.* Physical Review E, 2007. 76(4): p. 041503.
135. Richter, D., et al., *Polymer Aggregates with Crystalline Cores: The System Polyethylene−Poly(ethylenepropylene).* Macromolecules, 1997. 30(4): p. 1053-1068.
136. Mortensen, K., *Phase Behaviour of Poly(ethylene oxide)-Poly(propylene oxide)-Poly(ethylene oxide) Triblock-Copolymer Dissolved in Water.* EPL (Europhysics Letters), 1992. 19(7): p. 599.
137. Alexandridis, P. and T. Alan Hatton, *Poly(ethylene oxide)・poly(propylene oxide)・poly(ethylene oxide) block copolymer surfactants in aqueous solutions and at interfaces: thermodynamics, structure, dynamics, and modeling.* Colloids and Surfaces A: Physicochemical and Engineering Aspects, 1995. 96(1–2): p. 1-46.
138. Gohy, J.-F., *Block Copolymer Micelles*, in *Block Copolymers II*, V. Abetz, Editor. 2005, Springer Berlin Heidelberg. p. 65-136.
139. Nicolai, T., F. Laflèche, and A. Gibaud, *Jamming and Crystallization of Polymeric Micelles.* Macromolecules, 2004. 37(21): p. 8066-8071.
140. Wagner, N.J., *The High-Frequency Shear Modulus of Colloidal Suspensions and the Effects of Hydrodynamic Interactions.* Journal of Colloid and Interface Science, 1993. 161(1): p. 169-181.
141. Senff, H. and W. Richtering, *Temperature sensitive microgel suspensions: Colloidal phase behavior and rheology of soft spheres.* The Journal of Chemical Physics, 1999. 111(4): p. 1705-1711.
142. Ballauff, M. and C.N. Likos, *Dendrimers in solution: insight from theory and simulation.* Angewandte Chemie International Edition, 2004. 43(23): p. 2998-3020.
143. Alsayed, A.M., Y. Han, and A.G. Yodh, *Melting and Geometric Frustration in Temperature-Sensitive Colloids*, in *Microgel Suspensions*. 2011, Wiley-VCH Verlag GmbH & Co. KGaA. p. 229-281.

144. Puaud, F., et al., *Dynamic Arm Exchange Facilitates Crystallization and Jamming of Starlike Polymers by Spontaneous Fine-Tuning of the Number of Arms.* Physical Review Letters, 2013. 110(2): p. 028302.
145. Sandomirski, K., et al., *Heterogeneous crystallization of hard and soft spheres near flat and curved walls.* The European Physical Journal Special Topics, 2014. 223(3): p. 439-454.
146. Roehm, D., S. Kesselheim, and A. Arnold, *Hydrodynamic interactions slow down crystallization of soft colloids.* Soft matter, 2014. 10(30): p. 5503-5509.
147. Radu, M. and T. Schilling, *Solvent hydrodynamics speed up crystal nucleation in suspensions of hard spheres.* EPL (Europhysics Letters), 2014. 105(2): p. 26001.
148. Gupta, S., et al., *Dynamic phase diagram of soft nanocolloids.* Nanoscale, 2015. 7(33): p. 13924-13934.
149. Zaccarelli, E., et al., *Crystallization of Hard-Sphere Glasses.* Physical Review Letters, 2009. 103(13): p. 135704.
150. Markus, S., L. Peter, and R. Walter, *Structure formation in thermoresponsive microgel suspensions under shear flow.* Journal of Physics: Condensed Matter, 2004. 16(38): p. S3861.
151. Jiang, J., et al., *Shear-Induced Layered Structure of Polymeric Micelles by SANS.* Macromolecules, 2007. 40(11): p. 4016-4022.
152. Hamley, I.W., *Structure and flow behaviour of block copolymers.* Journal of Physics: Condensed Matter, 2001. 13(33): p. R643.
153. Slawecki, T.M., C.J. Glinka, and B. Hammouda, *Shear-induced micellar crystal structures in an aqueous triblock copolymer solution.* Physical Review E, 1998. 58(4): p. R4084-R4087.
154. López-Barrón, C.R., N.J. Wagner, and L. Porcar, *Layering, melting, and recrystallization of a close-packed micellar crystal under steady and large-amplitude oscillatory shear flows.* Journal of Rheology, 2015. 59(3): p. 793-820.
155. Hamley, I.W., et al., *Shear-induced orientation of the body-centered-cubic phase in a diblock copolymer gel.* Physical Review E, 1998. 58(6): p. 7620-7628.
156. Molino, F.R., et al., *Identification of flow mechanisms for a soft crystal.* The European Physical Journal B - Condensed Matter and Complex Systems, 1998. 3(1): p. 59-72.
157. McConnell, G.A., M.Y. Lin, and A.P. Gast, *Long Range Order in Polymeric Micelles under Steady Shear.* Macromolecules, 1995. 28(20): p. 6754-6764.
158. Nikoubashman, A., G. Kahl, and C.N. Likos, *Flow quantization and nonequilibrium nucleation of soft crystals.* Soft Matter, 2012. 8(15): p. 4121-4131.
159. Meng, Z., et al., *Crystallization Behavior of Soft, Attractive Microgels.* The Journal of Physical Chemistry B, 2007. 111(25): p. 6992-6997.
160. Watzlawek, M., C.N. Likos, and H. Löwen, *Phase Diagram of Star Polymer Solutions.* Physical Review Letters, 1999. 82(26): p. 5289-5292.
161. Kapnistos, M., et al., *Reversible Thermal Gelation in Soft Spheres.* Physical Review Letters, 2000. 85(19): p. 4072-4075.
162. Rissanou, A.N., D. Vlassopoulos, and I.A. Bitsanis, *Thermal vitrification in suspensions of soft colloids: Molecular dynamics simulations and comparison with experiments.* Physical Review E, 2005. 71(1): p. 011402.
163. Truzzolillo, D., D. Vlassopoulos, and M. Gauthier, *Osmotic Interactions, Rheology, and Arrested Phase Separation of Star–Linear Polymer Mixtures.* Macromolecules, 2011. 44(12): p. 5043-5052.
164. Rogers, S.A., D. Vlassopoulos, and P.T. Callaghan, *Aging, Yielding, and Shear Banding in Soft Colloidal Glasses.* Physical Review Letters, 2008. 100(12): p. 128304.
165. Helgeson, M.E., N.J. Wagner, and D. Vlassopoulos, *Viscoelasticity and shear melting of colloidal star polymer glasses.* Journal of Rheology, 2007. 51(2): p. 297-316.
166. Likos, C.N., *Soft matter with soft particles.* Soft Matter, 2006. 2(6): p. 478-498.
167. Likos, C.N., et al., *Star Polymers Viewed as Ultrasoft Colloidal Particles.* Physical Review Letters, 1998. 80(20): p. 4450-4453.

168. Kapnistos, M., et al., *Viscoelastic response of hyperstar polymers in the linear regime.* The Journal of Chemical Physics, 1999. 111(4): p. 1753-1759.
169. Koumakis, N., et al., *Direct comparison of the rheology of model hard and soft particle glasses.* Soft Matter, 2012. 8(15): p. 4271-4284.
170. Gauthier, M. and A. Munam, *Synthesis of 1,4-Polybutadiene Dendrimer−Arborescent Polymer Hybrids.* Macromolecules, 2010. 43(8): p. 3672-3681.
171. Tsuchida, A., et al., *Kinetic analyses of colloidal crystallization in shear flow.* Colloid and Polymer Science, 2004. 282(10): p. 1105-1110.
172. Derks, D., et al., *Dynamics of colloidal crystals in shear flow.* Soft Matter, 2009. 5(5): p. 1060-1065.
173. Chen, L.B., B.J. Ackerson, and C.F. Zukoski, *Rheological consequences of microstructural transitions in colloidal crystals.* Journal of Rheology, 1994. 38(2): p. 193-216.
174. Banchio, A.J. and G. Nägele, *Short-time transport properties in dense suspensions: From neutral to charge-stabilized colloidal spheres.* p. -.
175. Eiser, E., et al., *Nonhomogeneous textures and banded flow in a soft cubic phase under shear.* Physical Review E, 2000. 61(6): p. 6759-6764.
176. Hess, S., *Shear-induced melting and reentrant positional ordering in a system of spherical particles.* International Journal of Thermophysics, 1985. 6(6): p. 657-671.
177. Laun, H.M., et al., *Rheological and small angle neutron scattering investigation of shear-induced particle structures of concentrated polymer dispersions submitted to plane Poiseuille and Couette flowa).* Journal of Rheology, 1992. 36(4): p. 743-787.
178. Butler, S. and P. Harrowell, *The shear induced disordering transition in a colloidal crystal: Nonequilibrium Brownian dynamic simulations.* The Journal of Chemical Physics, 1995. 103(11): p. 4653-4671.
179. Loose, W. and B.J. Ackerson, *Model calculations for the analysis of scattering data from layered structures.* The Journal of Chemical Physics, 1994. 101(9): p. 7211-7220.
180. Lacks, D.J. and M.J. Osborne, *Energy Landscape Picture of Overaging and Rejuvenation in a Sheared Glass.* Physical Review Letters, 2004. 93(25): p. 255501.
181. Marakis, J.W., Katrin; Klapper, M; Vlassopoulos, Dimitris; Fytas, George; Müllen, K., *Physical gelation of hydrogel fibers formed by supramolecular assembly of an hexaphenylbenzene-poly(ethyleneglycol) amphiphile. To be published*.
182. Cordier, P., et al., *Self-healing and thermoreversible rubber from supramolecular assembly.* Nature, 2008. 451(7181): p. 977-980.
183. Seiffert, S. and J. Sprakel, *Physical chemistry of supramolecular polymer networks.* Chemical Society Reviews, 2012. 41(2): p. 909-930.
184. Sijbesma, R.P. and E.W. Meijer, *Self-assembly of well-defined structures by hydrogen bonding.* Current Opinion in Colloid & Interface Science, 1999. 4(1): p. 24-32.
185. De Greef, T.F.A., et al., *Supramolecular Polymerization.* Chemical Reviews, 2009. 109(11): p. 5687-5754.
186. Fox, J.D. and S.J. Rowan, *Supramolecular Polymerizations and Main-Chain Supramolecular Polymers.* Macromolecules, 2009. 42(18): p. 6823-6835.
187. Wojtecki, R.J., M.A. Meador, and S.J. Rowan, *Using the dynamic bond to access macroscopically responsive structurally dynamic polymers.* Nat Mater, 2011. 10(1): p. 14-27.
188. Serpe, M.J. and S.L. Craig, *Physical Organic Chemistry of Supramolecular Polymers.* Langmuir, 2007. 23(4): p. 1626-1634.
189. Goldansaz, H., et al., *Controlling the melt rheology of linear entangled metallo-supramolecular polymers.* Soft Matter, 2015. 11(4): p. 762-774.
190. Nguyen, J.Q. and B.L. Iverson, *An Amphiphilic Folding Molecule That Undergoes an Irreversible Conformational Change.* Journal of the American Chemical Society, 1999. 121(11): p. 2639-2640.

191. Xu, D., C.-Y. Liu, and S.L. Craig, *Divergent Shear Thinning and Shear Thickening Behavior of Supramolecular Polymer Networks in Semidilute Entangled Polymer Solutions.* Macromolecules, 2011. 44(7): p. 2343-2353.
192. Xu, D., et al., *Mechanism of Shear Thickening in Reversibly Cross-Linked Supramolecular Polymer Networks.* Macromolecules, 2010. 43(7): p. 3556-3565.
193. Herbst, F., et al., *Self-Healing Polymers via Supramolecular Forces.* Macromolecular Rapid Communications, 2013. 34(3): p. 203-220.
194. Maes, F., et al., *Activation and deactivation of self-healing in supramolecular rubbers.* Soft Matter, 2012. 8(5): p. 1681-1687.
195. Versteegen, R.M., et al., *Dendrimer-Based Transient Supramolecular Networks.* Journal of the American Chemical Society, 2005. 127(40): p. 13862-13868.
196. Xu, D. and S.L. Craig, *Scaling Laws in Supramolecular Polymer Networks.* Macromolecules, 2011. 44(13): p. 5465-5472.
197. Friedrich, T., et al., *Thermoresponsive Copolymer Hydrogels on the Basis of N-Isopropylacrylamide and a Non-Ionic Surfactant Monomer: Swelling Behavior, Transparency and Rheological Properties.* Macromolecules, 2010. 43(23): p. 9964-9971.
198. Stadler, F., et al., *Elongational rheology of NIPAM-based hydrogels.* Rheologica Acta, 2013. 52(5): p. 413-423.
199. Peak, C., J. Wilker, and G. Schmidt, *A review on tough and sticky hydrogels.* Colloid and Polymer Science, 2013. 291(9): p. 2031-2047.
200. Rammensee, S., et al., *Rheological characterization of hydrogels formed by recombinantly produced spider silk.* Applied Physics A, 2006. 82(2): p. 261-264.
201. Breedveld, V., et al., *Rheology of Block Copolypeptide Solutions: Hydrogels with Tunable Properties.* Macromolecules, 2004. 37(10): p. 3943-3953.
202. Pape, A., et al., *Mesoscale Characterization of Supramolecular Transient Networks Using SAXS and Rheology.* International Journal of Molecular Sciences, 2014. 15(1): p. 1096.
203. Nomura, S., et al., *Interaction of water with native collagen.* Biopolymers, 1977. 16(2): p. 231-246.
204. Bakota, E.L., et al., *Self-Assembling Multidomain Peptide Fibers with Aromatic Cores.* Biomacromolecules, 2013. 14(5): p. 1370-1378.
205. Jianqi, F. and G. Lixia, *PVA/PAA thermo-crosslinking hydrogel fiber: preparation and pH-sensitive properties in electrolyte solution.* European Polymer Journal, 2002. 38(8): p. 1653-1658.
206. Onoe, H., et al. *Microfluidic handling of hydrogel microfibers*. in *Micro Electro Mechanical Systems (MEMS), 2012 IEEE 25th International Conference on*. 2012.
207. Hsieh, A., et al., *Hydrogel/electrospun fiber composites influence neural stem/progenitor cell fate.* Soft Matter, 2010. 6(10): p. 2227-2237.
208. Hudson, S.D., et al., *Direct Visualization of Individual Cylindrical and Spherical Supramolecular Dendrimers.* Science, 1997. 278(5337): p. 449-452.
209. Percec, V., et al., *Towards tobacco mosaic virus-like self-assembled supramolecular architectures.* Macromolecular Symposia, 1994. 77(1): p. 237-265.
210. Israelachvili, J.N., *Intermolecular and surface forces*. 1992, London: Academic Press.
211. Dankers, P.Y.W., et al., *Hierarchical Formation of Supramolecular Transient Networks in Water: A Modular Injectable Delivery System.* Advanced Materials, 2012. 24(20): p. 2703-2709.
212. Lehn, J.-M., *Perspectives in Supramolecular Chemistry—From Molecular Recognition towards Molecular Information Processing and Self-Organization.* Angewandte Chemie International Edition in English, 1990. 29(11): p. 1304-1319.
213. Förster, S. and M. Antonietti, *Amphiphilic Block Copolymers in Structure-Controlled Nanomaterial Hybrids.* Advanced Materials, 1998. 10(3): p. 195-217.
214. Riess, G., *Micellization of block copolymers.* Progress in Polymer Science, 2003. 28(7): p. 1107-1170.

215. Fei, J., et al., *PVA/PAA thermo-induced hydrogel fiber: Preparation and pH-sensitive behavior in electrolyte solution.* Journal of Applied Polymer Science, 2002. 85(11): p. 2423-2430.
216. Wang, H., et al., *Supramolecular Self-Assembly of Conjugated Diblock Copolymers.* Chemistry – A European Journal, 2004. 10(4): p. 986-993.
217. Schmidt-Mende, L., et al., *Self-Organized Discotic Liquid Crystals for High-Efficiency Organic Photovoltaics.* Science, 2001. 293(5532): p. 1119-1122.
218. B. Jönsson, B.L., K. Holmberg, B. Kronberg, *Surfactants and Polymers in Aqueous Solution*. 1998, New York: Wiley.
219. Kölbel, H. and P. Kurzendörfer, *Konstitution und Eigenschaften von Tensiden*, in *Angewandte Chemie*. 1969, Springer Berlin Heidelberg. p. 252-348.
220. Bockstaller, M., et al., *Characterization of association colloids of amphiphilic poly (p-phenylene) sulfonates in aqueous solution.* Macromolecules, 2001. 34(18): p. 6353-6358.
221. Holtzer, A., *Interpretation of the angular distribution of the light scattered by a polydisperse system of rods.* Journal of Polymer Science, 1955. 17(85): p. 432-434.
222. Kroeger, A., et al., *Supramolecular Structures in Aqueous Solutions of Rigid Polyelectrolytes with Monovalent and Divalent Counterions.* Macromolecules, 2006. 39(20): p. 7098-7106.
223. Koyama, R., *Light Scattering of Stiff Chain Polymers.* Journal of the Physical Society of Japan, 1973. 34(4): p. 1029-1038.
224. Kroeger, A., et al., *Equilibrium Length and Shape of Rodlike Polyelectrolyte Micelles in Dilute Aqueous Solutions.* Macromolecules, 2007. 40(1): p. 105-115.
225. Jiménez-García, L., et al., *Phosphonated Hexaphenylbenzene: A Crystalline Proton Conductor.* Angewandte Chemie International Edition, 2009. 48(52): p. 9951-9953.
226. Garcia, S.J. and H.R. Fischer, *9 - Self-healing polymer systems: properties, synthesis and applications*, in *Smart Polymers and their Applications*, M.R. Aguilar and J.S. Román, Editors. 2014, Woodhead Publishing. p. 271-298.
227. Aragón, S.R. and R. Pecora, *Theory of dynamic light scattering from polydisperse systems.* The Journal of Chemical Physics, 1976. 64(6): p. 2395-2404.
228. Yamakawa, H. and M. Fujii, *Translational Friction Coefficient of Wormlike Chains.* Macromolecules, 1973. 6(3): p. 407-415.
229. Bantle, S., M. Schmidt, and W. Burchard, *Simultaneous static and dynamic light scattering.* Macromolecules, 1982. 15(6): p. 1604-1609.
230. Mathe, G., et al., *Equilibrium Swelling Behavior of Solid Supported Poly(ethylene glycol) Lipid Monolayers. Effects of Short Chain Lengths.* Langmuir, 2000. 16(8): p. 3835-3845.
231. Rubinstein, M. and R.H. Colby, *Polymer Physics*. 2003, Oxford University Press: NY.
232. Aggeli, A., et al., *Structure and Dynamics of Self-Assembling β-Sheet Peptide Tapes by Dynamic Light Scattering.* Biomacromolecules, 2001. 2(2): p. 378-388.
233. Doi, M., *Molecular dynamics and rheological properties of concentrated solutions of rodlike polymers in isotropic and liquid crystalline phases.* Journal of Polymer Science: Polymer Physics Edition, 1981. 19(2): p. 229-243.
234. Aggeli, A., et al., *Responsive gels formed by the spontaneous self-assembly of peptides into polymeric [beta]-sheet tapes.* Nature, 1997. 386(6622): p. 259-262.
235. Mawer, P.J., et al., *Small-Angle Neutron Scattering from Peptide Nematic Fluids and Hydrogels under Shear.* Langmuir, 2003. 19(12): p. 4940-4949.
236. Jeong, B., Y.H. Bae, and S.W. Kim, *Thermoreversible Gelation of PEG−PLGA−PEG Triblock Copolymer Aqueous Solutions.* Macromolecules, 1999. 32(21): p. 7064-7069.
237. Kelarakis, A., et al., *Micellar Spheres in a High Frequency Oscillatory Field.* Langmuir, 2006. 22(16): p. 6814-6817.
238. Deike, I., et al., *Rheology of thermosensitive latex particles including the high-frequency limit.* Journal of Rheology, 2001. 45(3): p. 709-720.

239. Suzuki, S., T. Uneyama, and H. Watanabe, *Concentration Dependence of Nonlinear Rheological Properties of Hydrophobically Modified Ethoxylated Urethane Aqueous Solutions.* Macromolecules, 2013. 46(9): p. 3497-3504.
240. Guo, R.H., et al., *Colloidal Aggregate and Gel Incubated by Amorphous Conjugated Polymer in Hybrid-Solvent Medium.* The Journal of Physical Chemistry B, 2015. 119(7): p. 3320-3331.
241. Denkova, A.G., E. Mendes, and M.-O. Coppens, *Non-equilibrium dynamics of block copolymer micelles in solution: recent insights and open questions.* Soft Matter, 2010. 6(11): p. 2351-2357.
242. Wu, C.-J., et al., *Mechanically Tough Pluronic F127/Laponite Nanocomposite Hydrogels from Covalently and Physically Cross-Linked Networks.* Macromolecules, 2011. 44(20): p. 8215-8224.
243. Mewis, J. and N.J. Wagner, *Colloidal suspension rheology*. 2012: Cambridge University Press.
244. Rueb, C.J. and C.F. Zukoski, *Viscoelastic properties of colloidal gels.* Journal of Rheology, 1997. 41(2): p. 197-218.
245. Magnin, A. and J.M. Piau, *Cone-and-plate rheometry of yield stress fluids. Study of an aqueous gel.* Journal of Non-Newtonian Fluid Mechanics, 1990. 36(0): p. 85-108.
246. Truzzolillo, D., et al., *Depletion gels from dense soft colloids: Rheology and thermoreversible melting.* Journal of Rheology, 2014. 58(5): p. 1441-1462.
247. Rogers, S.A., et al., *A sequence of physical processes determined and quantified in LAOS: Application to a yield stress fluid.* Journal of Rheology (1978-present), 2011. 55(2): p. 435-458.
248. Trédan, O., et al., *Drug Resistance and the Solid Tumor Microenvironment.* Journal of the National Cancer Institute, 2007.
249. Olive, K.P., et al., *Inhibition of Hedgehog Signaling Enhances Delivery of Chemotherapy in a Mouse Model of Pancreatic Cancer.* Science (New York, N.Y.), 2009. 324(5933): p. 1457-1461.
250. Sanchez-Ferrer, A., et al., *Thermo-responsive peptide-based triblock copolymer hydrogels.* Soft Matter, 2013. 9(16): p. 4304-4311.
251. Singh, N.K. and D.S. Lee, *In situ gelling pH- and temperature-sensitive biodegradable block copolymer hydrogels for drug delivery.* Journal of Controlled Release, 2014. 193: p. 214-227.
252. He, C., S.W. Kim, and D.S. Lee, *In situ gelling stimuli-sensitive block copolymer hydrogels for drug delivery.* Journal of Controlled Release, 2008. 127(3): p. 189-207.
253. Golinska, M.D., et al., *Dilute Self-Healing Hydrogels of Silk-Collagen-Like Block Copolypeptides at Neutral pH.* Biomacromolecules, 2014. 15(3): p. 699-706.
254. Koumakis, N. and G. Petekidis, *Two step yielding in attractive colloids: transition from gels to attractive glasses.* Soft Matter, 2011. 7(6): p. 2456-2470.
255. Abe, A., et al., *Controlled Polymerization and Polymeric Structures*. 2013, Springer.
256. Ashton, L., et al., *Susceptibility of Different Proteins to Flow-Induced Conformational Changes Monitored with Raman Spectroscopy.* Biophysical Journal, 2010. 98(4): p. 707-714.
257. Bekard, I.B., et al., *[small alpha]-Helix unfolding in simple shear flow.* Soft Matter, 2011. 7(1): p. 203-210.
258. Gerweck, L.E. and K. Seetharaman, *Cellular pH gradient in tumor versus normal tissue: potential exploitation for the treatment of cancer.* Cancer research, 1996. 56(6): p. 1194-1198.
259. Amiji, M.M., *Polymeric gene delivery: principles and applications*. 2004: CRC press.
260. Nelson, N., *Structure and pharmacology of the proton-ATPases.* Trends in Pharmacological Sciences, 1991. 12: p. 71-75.
261. Truzzolillo, D., et al., *Glassy States in Asymmetric Mixtures of Soft and Hard Colloids.* Physical Review Letters, 2013. 111(20): p. 208301.

262. Marzi, D., et al., *Depletion, melting and reentrant solidification in mixtures of soft and hard colloids.* Soft Matter, 2015.
263. Russel, W.B., D.A. Saville, and W.R. Schowalter, *Colloidal dispersions*. 1992: Cambridge university press.
264. Mewis, J. and N.J. Wagner., *Colloidal Suspension Rheology*. 2012: Cambridge University Press.
265. Hansen, J.P., D. Levesque, and J. Zinn-Justin, *Liquids, Freezing and the Glass Transition : Part I (Les Houches Summer School Proceedings)*. 1991: North-Holland.
266. Asakura, S. and F. Oosawa, *Interaction between particles suspended in solutions of macromolecules.* Journal of Polymer Science, 1958. 33(126): p. 183-192.
267. Vrij, A., *Polymers at interfaces and the interactions in colloidal dispersions.* Pure and Applied Chemistry, 1976. 48(4): p. 471-483.
268. Dawson, K., et al., *Higher-order glass-transition singularities in colloidal systems with attractive interactions.* Physical Review E, 2000. 63(1): p. 011401.
269. Pham, K.N., et al., *Multiple Glassy States in a Simple Model System.* Science, 2002. 296(5565): p. 104-106.
270. Puertas, A.M., M. Fuchs, and M.E. Cates, *Mode Coupling and Dynamical Heterogeneity in Colloidal Gelation: A Simulation Study†.* The Journal of Physical Chemistry B, 2005. 109(14): p. 6666-6675.
271. Puertas, A.M., M. Fuchs, and M.E. Cates, *Competition between glass transition and liquid–gas separation in attracting colloids.* Journal of Physics: Condensed Matter, 2007. 19(20): p. 205140.
272. Imhof, A. and J.K.G. Dhont, *Experimental Phase Diagram of a Binary Colloidal Hard-Sphere Mixture with a Large Size Ratio.* Physical Review Letters, 1995. 75(8): p. 1662-1665.
273. Bolhuis, P.G., E.J. Meijer, and A.A. Louis, *Colloid-Polymer Mixtures in the Protein Limit.* Physical Review Letters, 2003. 90(6): p. 068304.
274. Mutch, K.J., J.S. van Duijneveldt, and J. Eastoe, *Colloid-polymer mixtures in the protein limit.* Soft Matter, 2007. 3(2): p. 155-167.
275. Mahynski, N.A., T. Lafitte, and A.Z. Panagiotopoulos, *Pressure and density scaling for colloid-polymer systems in the protein limit.* Physical Review E, 2012. 85(5): p. 051402.
276. Mayer, C., et al., *Asymmetric caging in soft colloidal mixtures.* Nat Mater, 2008. 7(10): p. 780-784.
277. Dzubiella, J., et al., *Phase separation in star-polymer\char21{}colloid mixtures.* Physical Review E, 2001. 64(1): p. 010401.
278. Pham, K.N., et al., *Yielding behavior of repulsion- and attraction-dominated colloidal glasses.* Journal of Rheology (1978-present), 2008. 52(2): p. 649-676.
279. Rutgers, M.A., et al., *Measurement of the hard-sphere equation of state using screened charged polystyrene colloids.* Physical Review B, 1996. 53(9): p. 5043-5046.
280. Marzi, D., C.N. Likos, and B. Capone, *Coarse graining of star-polymer – colloid nanocomposites.* The Journal of Chemical Physics, 2012. 137(1): p. 014902.
281. Zaccarelli, E., et al., *Tailoring the Flow of Soft Glasses by Soft Additives.* Physical Review Letters, 2005. 95(26): p. 268301.
282. Th, V., *Multiple glasses in asymmetric binary hard spheres.* EPL (Europhysics Letters), 2011. 96(3): p. 36006.
283. Götze, W. and T. Voigtmann, *Effect of composition changes on the structural relaxation of a binary mixture.* Physical Review E, 2003. 67(2): p. 021502.
284. Cottin, X. and P.A. Monson, *Substitutionally ordered solid solutions of hard spheres.* The Journal of Chemical Physics, 1995. 102(8): p. 3354-3360.
285. Renou, F., J. Stellbrink, and G. Petekidis, *Yielding processes in a colloidal glass of soft star-like micelles under large amplitude oscillatory shear (LAOS).* Journal of Rheology, 2010. 54(6): p. 1219-1242.

286. Poulos, A., J. Stellbrink, and G. Petekidis, *Flow of concentrated solutions of starlike micelles under large-amplitude oscillatory shear.* Rheologica Acta, 2013. 52(8-9): p. 785-800.
287. Siebenburger, M., M. Fuchs, and M. Ballauff, *Core-shell microgels as model colloids for rheological studies.* Soft Matter, 2012. 8(15): p. 4014-4024.
288. van der Vaart, K., et al., *Rheology of concentrated soft and hard-sphere suspensions.* Journal of Rheology, 2013. 57(4): p. 1195-1209.
289. Mohan, L., et al., *Local mobility and microstructure in periodically sheared soft particle glasses and their connection to macroscopic rheology.* Journal of Rheology, 2013. 57(3): p. 1023-1046.
290. Le Grand, A. and G. Petekidis, *Effects of particle softness on the rheology and yielding of colloidal glasses.* Rheologica Acta, 2008. 47(5-6): p. 579-590.
291. Carrier, V. and G. Petekidis, *Nonlinear rheology of colloidal glasses of soft thermosensitive microgel particles.* Journal of Rheology, 2009. 53(2): p. 245-273.
292. Poulos, A., et al., *Large amplitude oscillatory shear (LAOS) in model colloidal suspensions and glasses: frequency dependence.* Rheologica Acta, 2015. 54(8): p. 715-724.
293. Jusufi, A., et al., *Effective interactions between star polymers and colloidal particles.* Journal of Physics: Condensed Matter, 2001. 13(28): p. 6177.
294. Foffi, G., et al., *Scaling of Dynamics with the Range of Interaction in Short-Range Attractive Colloids.* Physical Review Letters, 2005. 94(7): p. 078301.
295. Cardinaux, F., et al., *Interplay between Spinodal Decomposition and Glass Formation in Proteins Exhibiting Short-Range Attractions.* Physical Review Letters, 2007. 99(11): p. 118301.
296. Truzzolillo, D., et al., *Depletion gels from dense soft colloids: rheology and thermoreversible melting.* in preparation, 2014.
297. Hansen, J.-P. and I.R. McDonald, *Theory of Simple Liquids: With Applications to Soft Matter*. 2013: Academic Press.
298. Rogers, F.J. and D.A. Young, *New, thermodynamically consistent, integral equation for simple fluids.* Physical Review A, 1984. 30(2): p. 999-1007.
299. Dzubiella, J., C.N. Likos, and H. Löwen, *Star-polymers as depleting agents of colloidal hard spheres.* Europhys. Lett., 2002. 58(1): p. 133-139.
300. Hansen, J.-P. and I.R. McDonald, *Chapter 3 - Static Properties of Liquids: Thermodynamics and Structure*, in *Theory of Simple Liquids (Third Edition)*, J.-P. Hansen and I.R. McDonald, Editors. 2006, Academic Press: Burlington. p. 46-77.
301. Stiakakis, E., et al., *Depletion and cluster formation in soft colloid - polymer mixtures.* EPL (Europhysics Letters), 2005. 72(4): p. 664.
302. Loppinet, B., et al., *Reversible Thermal Gelation in Star Polymers: An Alternative Route to Jamming of Soft Matter.* Macromolecules, 2001. 34(23): p. 8216-8223.
303. Zaccarelli, E., et al., *Is There a Reentrant Glass in Binary Mixtures?* Physical Review Letters, 2004. 92(22): p. 225703.
304. Hansen, J.P. and I.R. McDonald, in *Theory of Simple Liquids (Third Edition)*, J.-P. Hansen and I.R. McDonald, Editors. 2006, Academic Press: London.
305. Dijkstra, M., R. van Roij, and R. Evans, *Direct Simulation of the Phase Behavior of Binary Hard-Sphere Mixtures: Test of the Depletion Potential Description.* Physical Review Letters, 1999. 82(1): p. 117-120.
306. Testard, V., L. Berthier, and W. Kob, *Influence of the Glass Transition on the Liquid-Gas Spinodal Decomposition.* Physical Review Letters, 2011. 106(12): p. 125702.
307. Testard, V., L. Berthier, and W. Kob, *Intermittent dynamics and logarithmic domain growth during the spinodal decomposition of a glass-forming liquid.* The Journal of Chemical Physics, 2014. 140(16): p. 164502.
308. Demus, D., et al., *Handbook of Liquid Crystals, Four Volume Set*. 1998: Wiley.
309. Wu, J., W. Pisula, and K. Müllen, *Graphenes as Potential Material for Electronics.* Chemical Reviews, 2007. 107(3): p. 718-747.

310. Fischbach, I., et al., *Structure and Dynamics in Columnar Discotic Materials: A Combined X-ray and Solid-State NMR Study of Hexabenzocoronene Derivatives.* The Journal of Physical Chemistry B, 2002. 106(25): p. 6408-6418.
311. Ochsenfeld, C., et al., *Structure Assignment in the Solid State by the Coupling of Quantum Chemical Calculations with NMR Experiments: A Columnar Hexabenzocoronene Derivative.* Journal of the American Chemical Society, 2001. 123(11): p. 2597-2606.
312. Tasios, N., et al., *Self-Assembly, Dynamics, and Phase Transformation Kinetics of Donor–Acceptor Substituted Perylene Derivatives.* Journal of the American Chemical Society, 2010. 132(21): p. 7478-7487.
313. Glüsen, B., et al., *On the character of the glass transition in columnar discotics.* Journal of Non-Crystalline Solids, 1998. 241(2–3): p. 113-120.
314. Möller, M., et al., *The nature of the glass transition in a columnar hexagonal ordered phase.* Journal of Non-Crystalline Solids, 1994. 170(3): p. 295-299.
315. Grigoriadis, C., et al., *Negative thermal expansion in discotic liquid crystals of nanographenes.* Advanced Materials, 2010. 22(12): p. 1403-1406.
316. Leisen, J., et al., *Molecular dynamics at the glass transition: One dimensional and two dimensional nuclear magnetic resonance studies of a glass-forming discotic liquid crystal.* The Journal of Chemical Physics, 1992. 97(5): p. 3749-3759.
317. Vallerien, S., et al., *Molecular dynamics and the glass transition in a columnar liquid crystal formed by a chiral discotic mesogen.* Liquid crystals, 1990. 8(6): p. 889-893.
318. Elmahdy, M., et al., *Molecular dynamics of branched hexaalkyl hexa-peri-hexabenzocoronenes.* Journal of Physics: Condensed Matter, 2008. 20(24): p. 244105.
319. Elmahdy, M., et al., *Origin of the complex molecular dynamics in functionalized discotic liquid crystals.* Physical review letters, 2008. 100(10): p. 107801.
320. Elmahdy, M.M., et al., *Self-assembly, molecular dynamics, and kinetics of structure formation in dipole-functionalized discotic liquid crystals.* Journal of the American Chemical Society, 2008. 130(15): p. 5311-5319.
321. Feng, X., et al., *Towards high charge-carrier mobilities by rational design of the shape and periphery of discotics.* Nature materials, 2009. 8(5): p. 421-426.
322. van de Craats, A.M., et al., *Record Charge Carrier Mobility in a Room-Temperature Discotic Liquid-Crystalline Derivative of Hexabenzocoronene.* Advanced Materials, 1999. 11(17): p. 1469-1472.
323. Haase, N., et al., *Effect of Dipole Functionalization on the Thermodynamics and Dynamics of Discotic Liquid Crystals.* The Journal of Physical Chemistry B, 2011. 115(19): p. 5807-5814.
324. Elmahdy, M.M., et al., *Slow kinetics of phase transformation in a dipole-functionalized discotic liquid crystal.* The Journal of Chemical Physics, 2009. 131(11): p. 114704.
325. Papadopoulos, P., et al., *Dynamics of Structure Formation in a Discotic Liquid Crystal by Infrared Spectroscopy and Related Techniques.* The Journal of Physical Chemistry B, 2011. 115(50): p. 14919-14927.

Appendix A

In vivo studies of hydrogels

The two different polymers are consisted of synthetic amphiphilic pentablock terpolypeptide hydrogel (PTH) where the polymeric material is of the type poly(L-lysine)-*b*-poly(L-histidine-*co*-*γ*-benzyl-L-glutamate)-poly(L-lysine)-*b*-poly(L-histidine-*co*-*γ*-benzyl-L-glutamate)-*b*-poly(L-lysine) (PLys-*b*-(PHis-*co*-PBLG)-PLys'-*b*-(PHis-*co*-PBLG)-*b*-PLys) or pentablock quarterpolymer hydrogel (PQH) where the polymeric material is of the type poly(L-lysine)-*b*-poly(L-histidine-*co*-*γ*-benzyl-L-glutamate)-poly(ethylene oxide)-*b*-poly(L-histidine-*co*-*γ*-benzyl-L-glutamate)-*b*-poly(L-lysine). PTH as well as PQH can be reproducibly and easily produced in high purity and large quantities, and the chemicals employed during their synthesis can be completely removed. In addition, the samples are free of pyrogens or biological contaminants. By fine tuning of the pH and the polymer concentration of the hydrogels their strength can be increased to the desired levels, therefore it is possible to control the period of time of the targeted drug delivery.

Amphiphilic Pentablock Terpolypeptide Hydrogels

Amphiphilic pentablock terpolypeptide hydrogels (PTH) are synthetic materials that are formed by using polymeric material of the type poly(L-lysine)-*b*-poly(L-histidine-*co*-*γ*-benzyl-L-glutamate)-*b*-poly(L-lysine)-*b*-poly(L-histidine-*co*-*γ*-benzyl-L-glutamate)-*b*-poly(L-lysine). Their properties can be varied by altering the relative PBLG/PHIS molar ratio. In order to determine the influence of the PBLG composition on the properties of the hydrogel, we synthesized a series of pentablock terpolypeptides where the poly(L-lysine) blocks were always the same while the molar ratios of PBLG/PHIS+PBLG was varied at the values 70, 50, 30 and 0. It was found that the 50% molar ratio gave the best

results concerning the strong pH and responsiveness along with low polymer concentration to achieve the desired hydrogel strength.

The hydrogels with and without gemcitabine were prepared by dissolving freeze dried polymeric samples in MiliQ water. Specifically, the hydrogels loaded with gemcitabine were prepared by dissolving first the appropriate amount of gemcitabine in pyrogen free MilliQ water, adjusting the pH=7.4 or any other pH with the required amount of NaOH solution of 0.1 N in pyrogen free MilliQ water, and the adding the solution of gemcitabine in the polymer. The formulation (hydrogel+gemcitabine named hydrogem) was left for 2-3 hours and dissolution was enhanced through vortex mixing. The rheological properties were not affected by the agitation; identical mechanical properties were obtained by letting the terpolypeptide dissolving to form the hydrogel after three days without agitation. The molecular characteristics of the PTH terpolypeptide are given in Table A.1.

Segments	M_n x 10^3 g/mol
$PLys'_{200}$	25.6
$PHis_{20}$-*co*-$PBLG_{20}$	7.1
$PLys_{60}$	7.7
Total Molecular Weight	55.2

Table A.1. *Molecular Characteristics of the Pentablock Terpolypeptide* $PLys_{60}$-*b*-($PHis_{20}$-*co*-$PBLG_{20}$)-$PLys'_{200}$-*b*-($PHis_{20}$-*co*-$PBLG_{20}$)-*b*-$PLys_{60}$.

Amphiphilic Pentablock Quarterpolymer Hydrogels

Amphiphilic pentablock hybrid quarterpolymer hydrogels (PQH) are synthetic materials that are formed by using polymeric material of the type poly(L-lysine)-*b*-poly(L-histidine-*co*-*γ*-benzyl-L-glutamate)-poly(ethylene oxide)-*b*-poly(L-histidine-*co*-*γ*-benzyl-L-glutamate)-*b*-poly(L-lysine). The properties of the PQH can be varied in the same way as described in the paragraph regarding the PTH. It was found that the middle hydrophilic block of poly(ethylene oxide) should have a high molecular weight in order to

form strong hydrogels at concentrations as low as 4% (w/w) in water. The molecular weight of the PEO middle block was varied from 6.0×10^3, 10.0×10^3 and 20.0×10^3 g/mol, while the poly(L-lysine) and poly(L-histidine-*co*-*γ*-benzyl-L-glutamate) blocks remained stable. The molecular weight of the poly(L-lysine) block had a molecular weight of 7.7×10^3 g/mol while the poly(L-histidine-*co*-*γ*-benzyl-L-glutamate) block had a molecular weight of 7.1×10^3 g/mol. It was found that the 50% molar ratio of PHIS in the responsive polypeptidic block gave the best results concerning the strong pH and temperature responsiveness along with low polymer concentration to achieve the desired strength of the hydrogel. The molecular characteristics are given in Table A.2.

Segments	M_n x 10^3 g/mol
PEO	20.0
$PHis_{20}$-*co*-$PBLG_{20}$	7.1
$PLys_{60}$	7.7
Total	49.6

Table A.2. *Molecular Characteristics of the Pentablock Terpolypeptide $PLys_{60}$-b-($PHis_{20}$-co-$PBLG_{20}$)-PEO-b-($PHis_{20}$-co-$PBLG_{20}$)-b-$PLys_{60}$.*

In vivo studies

Furthermore, in *vivo* studies were conducted on the empty PTH hydrogel as well as on the hydrogem formed by the PTH loaded with gemcitabine. The amount of gemcitabine that was loaded was 1:1 compared to the weight of the PTH, as the samples tested in rheology. In *vivo* studies were conducted on mice as human pancreatic cancer xenograft models. Human pancreatic cancer cell line AsPC1 was used. 1x106 cancer cells were inoculated subcutaneously at the rear axilla flank of the recipient mice. Each mouse received one injection of cancer cells. 35 NOD/SCID male mice were used for this study. Mice were observed after the inoculation of the cells for the appearance of tumors. Upon

appearance, tumors were measured twice weekly using a caliper. The two diameters were measured and recorded. Using these diameters and the formula (axb2/2) where a=the longest and b=the shortest diameter the volume of each tumor was calculated.

Using the volumes of the tumors a curve vs the time (in days post cells' inoculation) was plotted to observe the growth of the tumors. When the tumors reached a size of about 200mm^3 (advanced stage model) the mice were arbitrary divided into 5 groups, each groups consisting of 7 mice (7 tumors/group). One group received nothing serving as a control. A second and a third group received gemcitabine either ip or sc at close vicinity with the tumors (peritumoral, pt, administration) serving as positive controls, a fourth group received unloaded hydrogel serving as a negative control while the fifth group received the hydrogem peritumoraly. The gemcitabine groups received two injections of the chemotherapeutic drug at a week interval and at a dose of 100mg/kg/injection/mouse. The hydrogem group received only a single injection with 83μl of the hydrogem corresponding to the same dose (100mg/kg) of gemcitabine while the hydrogel group received 83μl of unloaded hydrogel. The growth of the tumors and the survival of the animals was measured and recorded. When the tumor exceeded the 10% of the mouse weight mice were euthanized using ether and the experiment terminated when all the animals were euthanized. As a sign of toxicity the weights of the animals were also measured and record twice weekly. Animals were also observed twice weekly for any other signs that could indicate toxicity.

The in vivo results of the PTH hydrogem showed that the material is very effective in the delaying of the development of human pancreatic cancer, since by using only 40% of the drug compared to the set of animals that 100% of the drug was delivered subcutaneously close to the cancer tissue, the delay through the hydrogem was comparable and even better. This shows that the polymeric material directs the delivery of the drug targeted towards the cancer tissue rather than the healthy tissue.

The subsequent efficacy study suggested that the combination of hydrogel with gemcitabine was superior to the administration of the drug alone as compared to both routes of administration (ip or pt) under the experimental condition tested. Indeed 40% of the dose of gemcitabine when administered loaded in the form of hydrogem could delay at the same level the growth of the tumors as was shown by the growth curves of the tumors (FIG. A.1). Apart from the control of the tumor size, another parameter was reperted, i.e. the %DT/DC parameter. This one is defined as the ratio $(T - D_0) \,/\, (C - D_0)$, where D_0 is the average value of tumor at the beginning of the study and T, C are the calculated tumor values at the measuring time. Hydrogem demonstrated comparable and even better %DT/DC parameter as compared to free gemcitabine (ip or pt) and increased the doubling time of the tumors at the same level as the two doses of peritumoral free gemcitabine (100% of gemcitabine).

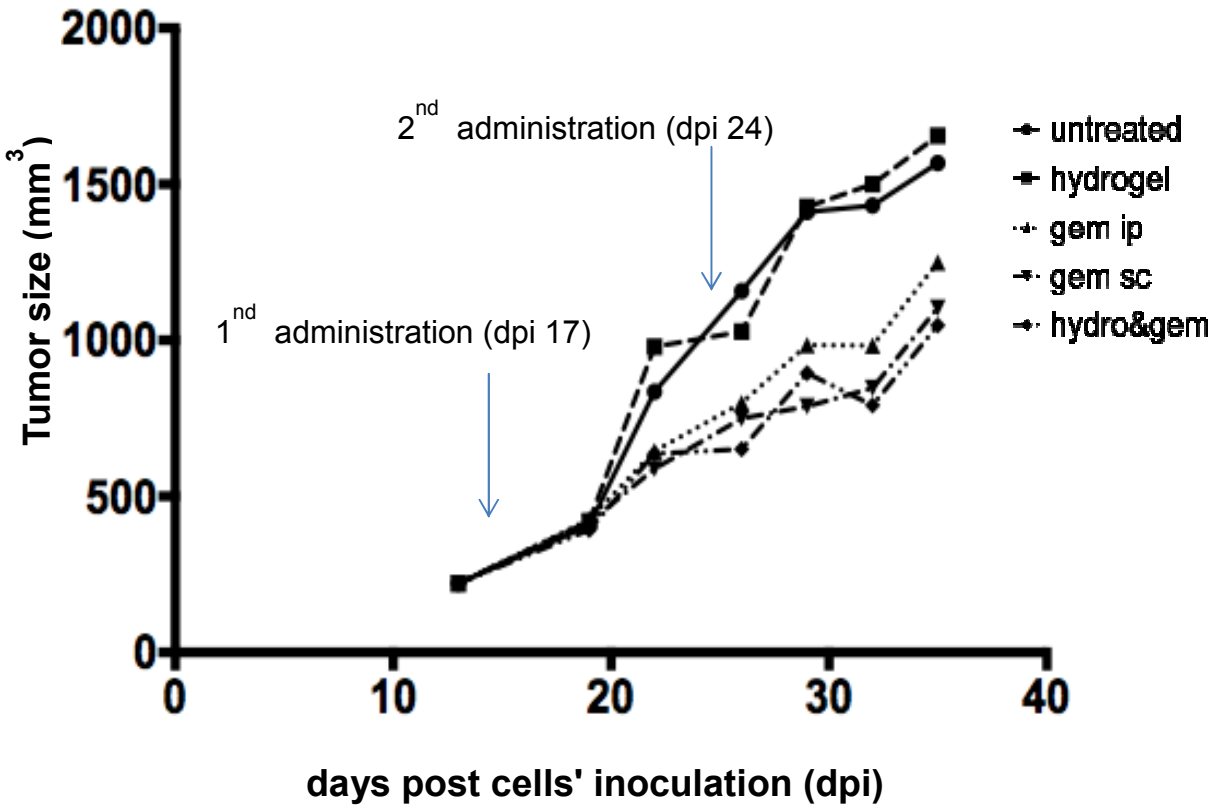

Figure A.1. *Tumor size as a function of time for different sets of injection on human pancreatic cancer mice models. Squares, circles, up triangles, down triangles and rhombi represent the untreated mice, pure hydrogel, intraperitoneal injection of pure gemcitabine, subcutaneous injection of pure gemcitabine, injection of hydrogem.*

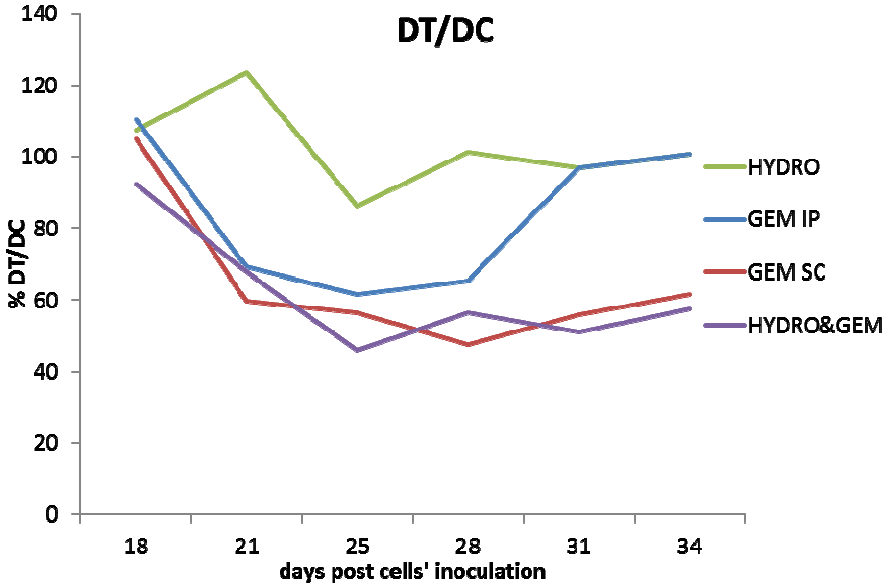

Figure A.2. *The %DT/DC at different ways of administration as a function of time.*

Finally the Kaplan-Meier survival curve showed that hydrogem was more effective compared to free gemcitabine as it increased the life span of the recipient mice more than the free drug did (FIG. A.3).

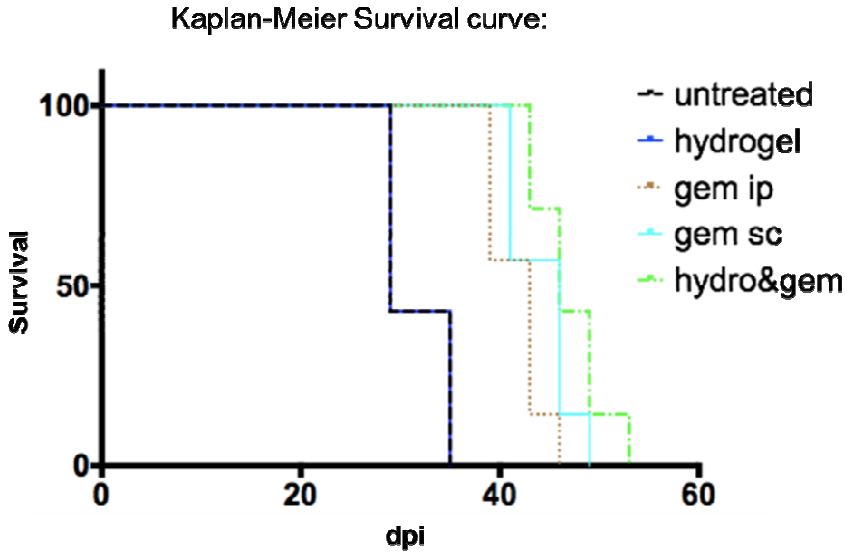

Figure A.3. *Kaplan-Meier survival curves of the different injection schemes on human pancreatic cancer mice models.*

Appendix B

Theoretical analysis and simulations in star mixtures

The theoretical analysis of the star polymers and colloidal additives mixtures properties was based on the assumption that the colloids are smaller than the polymers. Star polymers are macromolecular colloidal species consisting of a number f of homopolymers grafted on a central core. They can be regarded as soft spherical colloids with a gyration radius $R_S^{(g)}$ scaling as $R_S^{(g)} \sim f^{1/5} N^{\nu}$ under good solvency conditions [108], where N is the degree of polymerization per arm, f the arm number (functionality) and $\nu = 0.588 \simeq 3/5$ the self-avoiding Flory exponent. The second component of the mixtures are colloids, i.e., hard spherical nanoparticles with radius R_H. Each species is rendered as a spherical object (soft and hard, respectively) and coarse-grained through its center. Accordingly, we introduce effective potentials $V_{ij}(r)(i,j = S,H)$ acting between the sphere centers at distance r.

The effective interaction potential $V_{SH}(r)$ between star polymers and hard colloids in good solvent conditions depends on f and on the size ratio q, defined as:

$$q \equiv R_S^{(g)}/R_H \tag{B.1}$$

whereby we focus here exclusively on the case q > 1. The coarse-graining procedure allows the extraction of the effective force between the star polymer and the colloid by integrating the osmotic pressure $\Pi(s)$ exerted by the star polymer on the surface of the colloid [280, 293]. In this way, the effective force $F_{SH}(z)$ between the anchor point of the star and the surface of the colloid can be evaluated as:

$$F_{SH}(z) = \frac{R_H}{(z+R_H)^2} \int_z^{s_{max}} ds[z^2 + 2R_H z + s^2]\,[\Pi(s) - \Pi(s+t)] \tag{B.2}$$

where $z = r - R_H > 0$ is the distance from the center of the star to the surface of the colloid, $s_{max} = \sqrt{z(z + 2R_H)}$ and $t(s) = (z(2R_H + z) - s^2) \,/\, s$. The functional form of the osmotic pressure $\Pi(s)$can be found in Refs. [280, 293]; for the numerical coefficient $\Lambda(f)$ appearing there, the high- f -limit $\Lambda(f)$ = 5/36 has been employed in this work for all $f \geq 200$. We note that the results for the structure of the mixtures are rather insensitive to the precise value of $\Lambda(f)$, even within a factor of 2 to 3. The effective force can be readily integrated to yield the theoretical prediction for the effective potential $V_{SH}(r = R_H + z)$, the validity of which was firmly corroborated via extensive, full-monomer Monte-Carlo simulations [280].

Within the coarse-grained representation the colloid-colloid interaction, $V_{HH}(r)$, is represented by the hard sphere potential for particles with diameter $\sigma_H = 2R_H$,

$$\beta V_{HH}(r) = \begin{cases} \infty & r < \sigma_H; \\ 0 & r \geq \sigma_H. \end{cases} \tag{B.3}$$

Finally, for the star-star effective interaction, $V_{SS}(r)$, the effective potential derived in Ref. [167] was employed. The latter features a crossover from a Yukawa-like tail to a logarithmic behavior as the star-star separation diminishes. More explicitly, the effective interaction between two star-polymers whose centers are held at distance r apart reads as:

$$\beta V_{SS}(r) = \frac{5}{18} f^{3/2} \begin{cases} -\ln\left(\frac{r}{\sigma_s}\right) + \frac{1}{1 + \sqrt{f}/2} & r < \sigma_S; \\ \frac{1}{1 + \sqrt{f}/2} \left(\frac{\sigma_S}{r}\right) exp\left[-\frac{\sqrt{f}}{2\sigma_S}(r - \sigma_S)\right] & r \geq \sigma_S. \end{cases} \tag{B.4}$$

where $\sigma_S \simeq (4/3) R_S^{(g)}$ is the corona diameter of the stars and $\beta = (k_B \mathrm{T})^{-1}$, k_B being the Boltzmann constant and T the absolute temperature. All the effective potentials used in this work are fully repulsive and arise in systems whose only microscopic interactions are excluded volume effects. The set of effective interactions given by Eqs. (B.2-B.4) was employed to investigate the structural and dynamic features of mixtures characterized by high functionalities $f = 214, 250, 300$ and size ratios $2 \leq q \leq 8$. We will be mostly

working in concentration regimes in which there is no osmotic shrinkage of the stars due to either other stars or the colloids [163]; therefore the interaction parameter σ_S as well as the size ratio will be treated as concentration-independent constants.

In Fig. B.1, some examples of the effective interactions are shown for different f and two size ratios q. Since the colloids are considered as hard spheres, the star-colloid interaction $V_{SH}(r)$ diverges at $r = R_H$ and, as expected, it also diverges at smaller distances for larger q, since smaller colloids can penetrate the stars more easily than larger ones. For a given q, the stars become less penetrable by the colloids as the functionality of the star increases. In this way, this reliably determined set of effective potentials provides full and realistic coarse-graining of the complex mixture. We used two-component Ornstein-Zernike equation [297] with the Rogers-Young closure (OZ-RY) [298] to calculate the partial structure factors for mixtures characterized by partial number densities $\rho_i = {}^{N_i}/_{V}$ $(i, j = S, H)$. Their validity was confirmed by the excellent agreement with Monte Carlo simulations for the coarse-grained mixtures at selected points. The Rogers-Young closure was chosen, as it is known to give thermodynamically consistent results for mixtures of star polymers and hard colloidal particles [299].

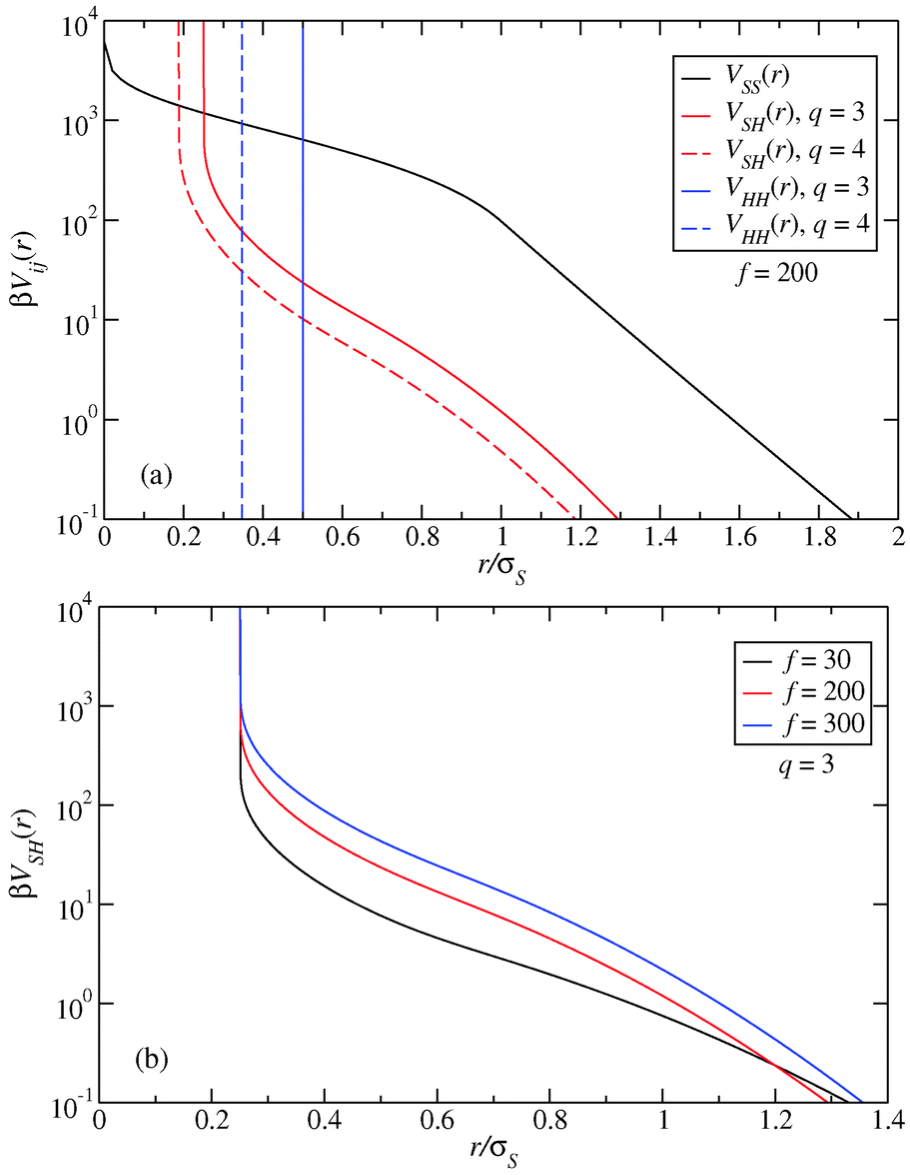

Figure B.1. *(a) The effective interactions between star-star, $V_{SS}(r)$, star-colloid, $V_{SH}(r)$, and colloid-colloid, $V_{HH}(r)$, for star functionality f=200 and size ratios q=3 (solid lines) and q=4 (dashed lines). The colloid-colloid interactions are of the hard-sphere type and are thus represented here by vertical lines. (b) The cross-interaction $V_{SH}(r)$ for fixed size ratio q=3 and varying functionality f of the star.*

Representative results are shown in Fig. B.2. The left panel of Fig. B.2 shows the dependence of the partial structure factors for $f = 30$, $q = 3$ and $\rho_S\sigma_S^3 = 0.3$ on the density of the colloidal additives. As the colloidal density ρ_H increases, the main peak of $S_{SS}(Q)$ diminishes in height and its location shifts to larger wavenumbers; increasing the colloidal density thus reduces the star-star nearest-neighbor distance, while at the same time it also “loosens" the correlations between the stars. Due to the presence of the

colloids, the stars overlap more frequently, they penetrate deeper into each other, i.e., they are “pushed together" by the colloids. This is a typical depletion effect, present for all functionalities. In fact, the colloid-induced depletion can drive the system to a demixing instability, as implied by the structural data for $f = 250$ in the right panel of Fig. B.2. We can see that even for a small amount of additives, $\rho_H\sigma_S^3 = 0.1$, the colloid-colloid structure factor $S_{HH}(Q)$ develops a high peak for long wavelengths ($Q \to 0$) signaling that the system is approaching the spinodal line, and therefore, phase separation would take place for further increase of ρ_H. The possible existence of a demixing region can be accounted for by the well-known fact that in the neighborhood of a spinodal line, iterative schemes as OZ-RY fail to converge [300]. In this way, an estimate of the phase-separated region can be obtained by locating the convergence line, above which the homogeneous mixture is expected to become unstable with respect to a demixing transition into colloid-rich and star-rich fluid phases, as will be made clearer below. At this point, Fig. B.2 indicate that increasing the functionality of the star results in a stiffer particle, which is less penetrable for the colloidal additive and yields demixing at lower concentration of the latter, as can be concluded by comparing the values of $S_{HH}(Q \to 0)$ for $\rho_H\sigma_S^3 = 0.1$.

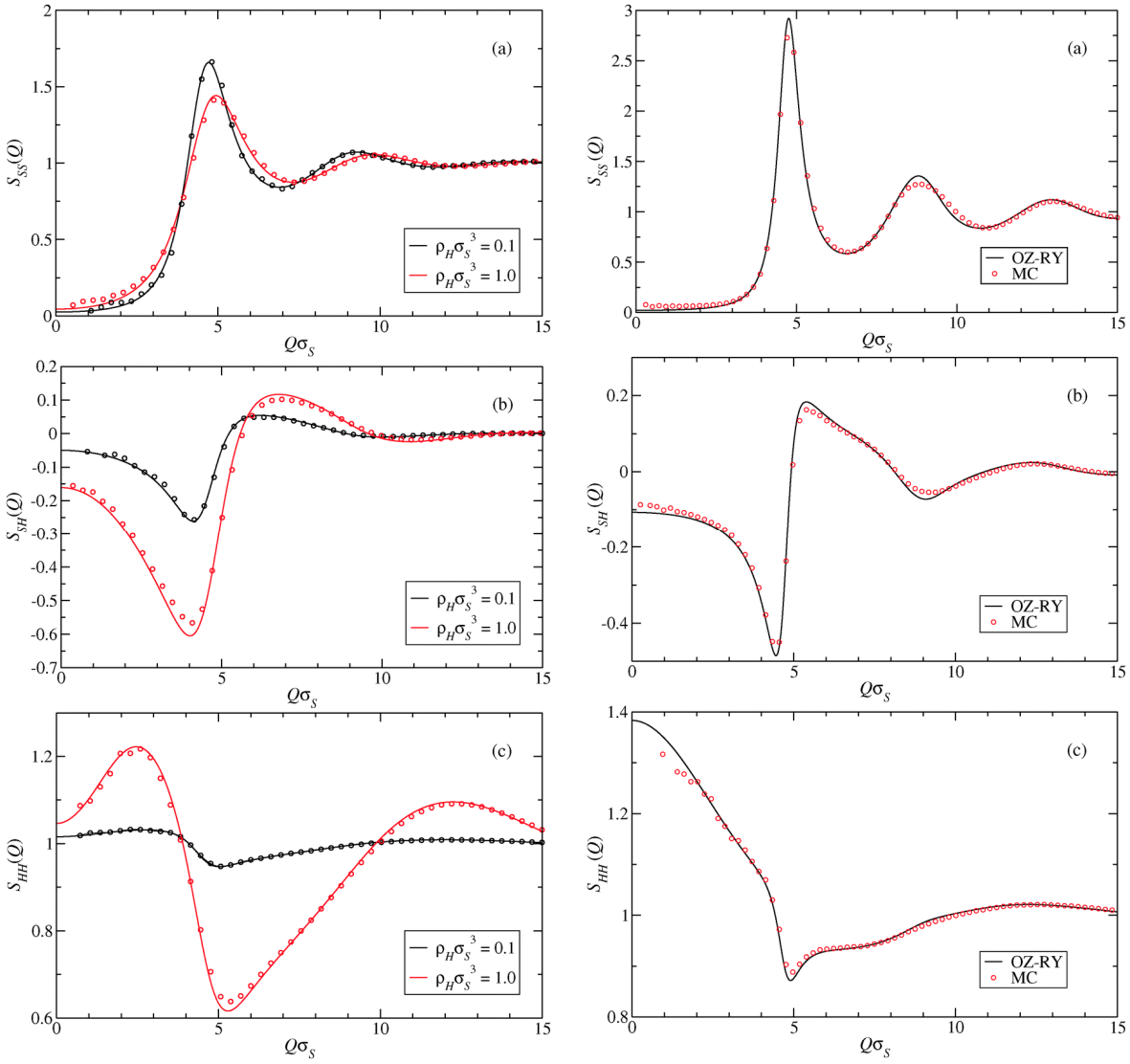

Figure B.2. *Left Panel: Partial structure factors obtained from the solution of the OZ-RY equation (lines) and Monte-Carlo simulations (symbols) for* $f = 30$, $q = 3$, $\rho_S\sigma_S^3 = 0.3$, *and two different colloidal densities,* $\rho_H\sigma_S^3 = 0.1$ *and* $\rho_H\sigma_S^3 = 1.0$ *as indicated in the legends. Right Panel: Partial structure factors obtained from the solution of the OZ-RY equation and Monte-Carlo (MC) simulations for* $f = 250, q = 3$, $\rho_S\sigma_S^3 = 0.3$, *and* $\rho_H\sigma_S^3 = 0.1$.

Moreover, following the Hansen Verlet criterion, mentioning that when the main peak of $S_{SS}(Q)$ reaches values higher than 2.8 (Top Right in Fig. B.2), the pure star polymer fluid would crystallize, someone would expect a fluid to solid transition at high star concentrations. However, many experimental works have shown that a disordered kinetically arrested state is more favorable [91, 301, 302]. To study the effect of the colloidal addition in our soft star system, we focused on the non-ergodicity factor $\phi(Q)$ of

the stars, which is defined as the long-time limit of the star-star density autocorrelation function. The latter vanishes for all values of the wavenumber Q in an ergodic liquid and it is nonzero in the glass.

Given the structural data obtained by the OZ-RY approach, the calculation of the non-ergodicity factor is readily achieved within the framework of the Mode Coupling Theory (MCT) by employing the one-component version [107, 303]. Inherent in this approach is the assumption that within the glassy state of the stars, the small colloidal particles remain ergodic; were this not to be the case, then the full, two-component version of the MCT [276, 303] should be employed. This assumption has been fully confirmed by our Molecular Dynamics simulations.

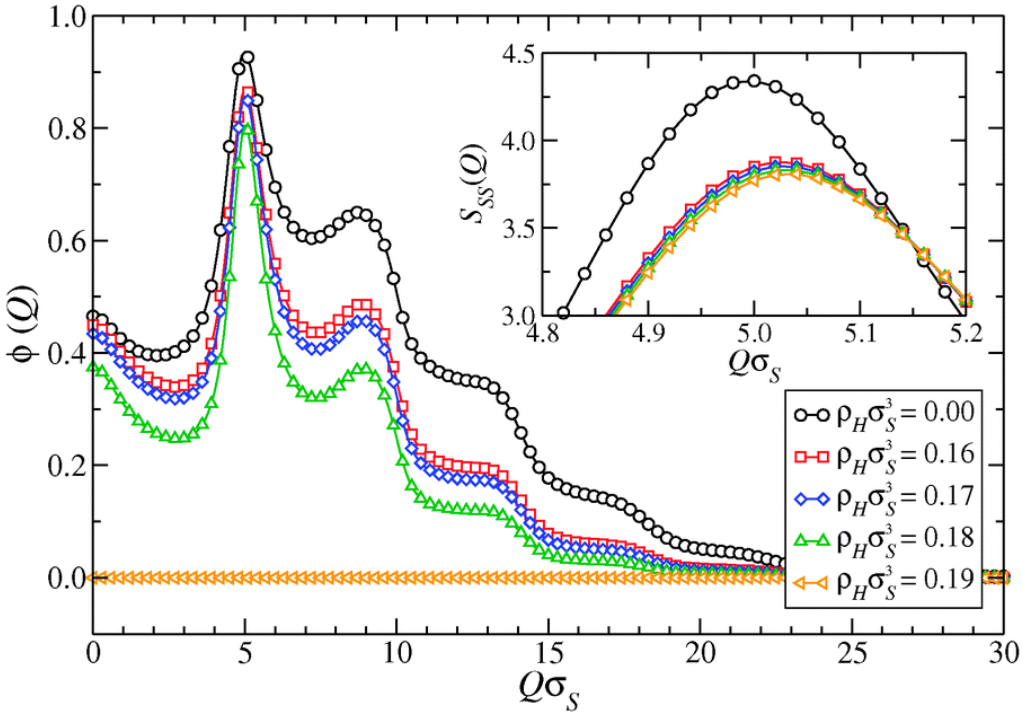

Figure B.3. *Dependence of the non-ergodicity factor on the density of added colloids for* $f = 214, q = 3, and\ \rho_S\sigma_S^3 = 0.36$. *Inset: Close-up to the main peak of the corresponding star-star factors.*

A representative result of the dependence of the non-ergodicity factor of the stars on the colloidal additive is shown in Fig. B.3, for the experimentally relevant combination $f = 214$, $q = 3$, $\rho_S\sigma_S^3 = 0.36$ and increasing colloidal density. Upon the addition of the

colloids, the star-star structure weakens and for $\rho_H \sigma_S^3 \geq 0.18$ the glass melts and ergodicity is restored. As more hard colloids penetrate the stars, the cages of the repulsive star glass are perturbated and finally broken leading to melting of the system. The physical mechanism responsible for this transition lies in the fact that the small colloids act as depletants to the big stars – a situation specular to the usual, colloid/polymer case, in which the small polymers deplete the big colloids [268-271, 277]. Upon further addition of colloids, net attractions between the stars appear, which drive the system towards a demixing phase separation into a star- and a colloid-rich phase, as already predicted in Ref. [280]. This is manifested in the integral equation approach by the fact that all structure factors develop increasingly high peaks at $Q = 0$ and convergence cannot be achieved any more. The locus of points for which the solution is lost, which can be loosely identified with the demixing line of the system, is denoted in Fig. 6.6b with a dashed line. This figure presents a compilation of the MCT-results and it should be directly compared to its experimental counterpart, Fig. 6.6a.

The experimental results on phase separation were supported theoretically by resorting to an effective one-component depletion picture, in which the colloids are canonically traced out, resulting in modified star-star interactions. Carrying out a further coarse graining procedure, the mixture is effectively considered as one-component system, in which the stars interact through a modified effective potential $V_{SS}^{(mod)}(r)$, for which the degrees of freedom of the hard particles have been traced out. The colloid-modified, effective star-star interaction can be determined in the limit of vanishing ρ_S as:

$$\beta V_{SS}^{(mod)}(r;\rho_H) = -\ln[g_{SS}(r;f,q,\rho_S \to 0,\rho_H)] \qquad \text{(B.5)}$$

where the pair correlation function $g_{SS}(r)$ can be evaluated by solving the OZ-RY iteration, for the two-component mixture. By construction, this colloid-modified

interaction potential leaves the correlation functions $g_{SS}(r)$ and $S_{SS}(Q)$ between the stars invariant [304, 305].

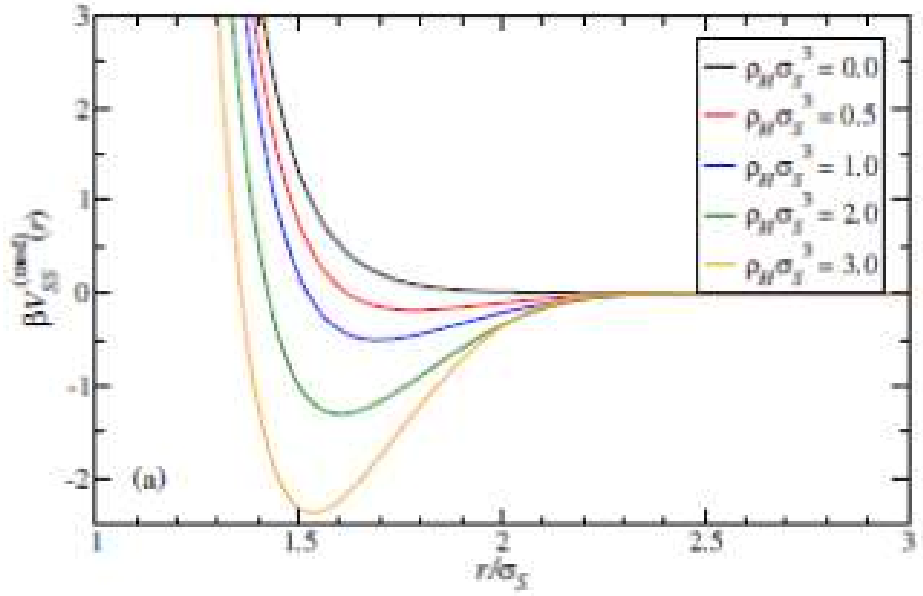

Figure B.4. *Effective star-star interaction in the presence of colloids for* $f = 300$ *and* $q = 3$*. The colloid densities are indicated in the legends.*

Figure B.4 show representative results for the colloid modified, effective star-star interaction and for the depletion interaction for different values of $\rho_H\sigma_S^3$. As the colloidal density increases the location of $V_{SS}^{(mod)}$ minimum tends to $r \simeq 1.5\sigma_S \simeq 2R_S^{(g)}$. For shorter distances, the repulsive contribution coming from the overlap of the outer Daoud-Cotton blobs of the stars [108] rapidly counteracts the effect of the excess osmotic pressure due to the colloids, and dominates the effective interaction. Upon addition of the colloids, we thus have first a reduction in the repulsive interaction, leading to glass melting and subsequently, at higher colloid concentrations, to the development of effective, depletion-induced attractions between the stars that bring about the demixing, binodal line. The glass- and binodal lines meet, leading to the arrested phase separation [271, 306, 307].

For systems with finite ρ_S, Eq. (B.5) can still be employed to map the binary mixture onto an effective one-component system. However in this case the potential should be

determined at fixed chemical potential μ_H of the colloidal additive [305], meaning that the colloid density in the system, ρ_H, has to be replaced by the colloid density of a reservoir ρ_H^r, which is such that μ_H in the reservoir and in the system coincide. In this way, the effective one-component description allows the determination of the phase behavior of the binary mixture in contact with a colloid reservoir, i.e., the calculation of the binodal demixing line in the (ρ_S, ρ_H^r) plane. The results are displayed in Fig. 6.12, where the binodal lines were calculated at fixed density of stars ρ_S and the chemical potential of colloids μ_H, quoting the reservoir colloidal density ρ_H^r as an equivalent way of fixing the former.

Figures B.5-B.7 demonstrate the elastic representations of different strain amplitude for three regimes. In general three strains were used: a) in the linear regime, b) on the moduli crossover in the strain sweep (yield point) and c) in nonlinear regime. An interesting feature in the double glass regime is that the stress of the viscous regimes decreases in high nonlinear strain amplitudes. Strain amplitudes higher than 100% lead the particles to flow easier, therefore exhibiting lower stresses in the viscous regimes of LB plots.

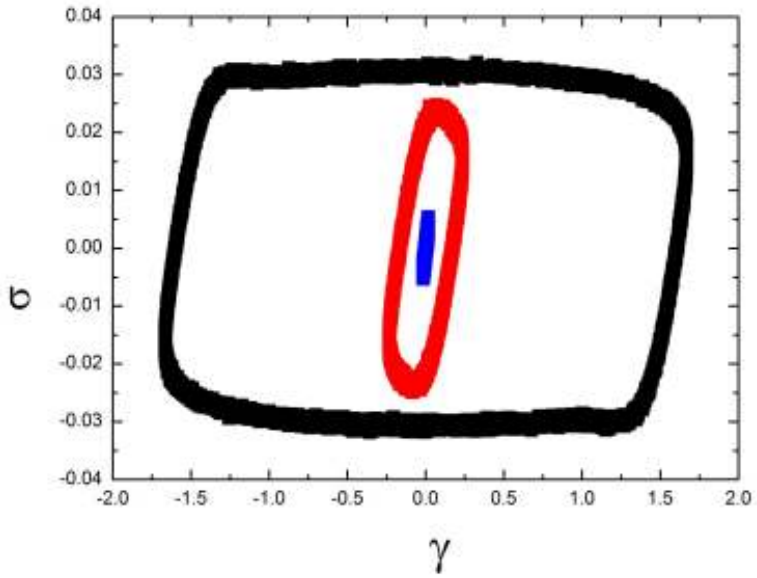

Figure B.5. *Lissajou plot (Elastic stress vs Strain) of three strain amplitudes in repulsive glass regime ($\rho_H\sigma_S^3 = 0.023$). The plotted data are extracted from time sweeps at 1%, 14%, 100%*

strain amplitudes and are shown with blue, red and black colors, respectively. The angular frequency of the experiments was 1 rad/s.

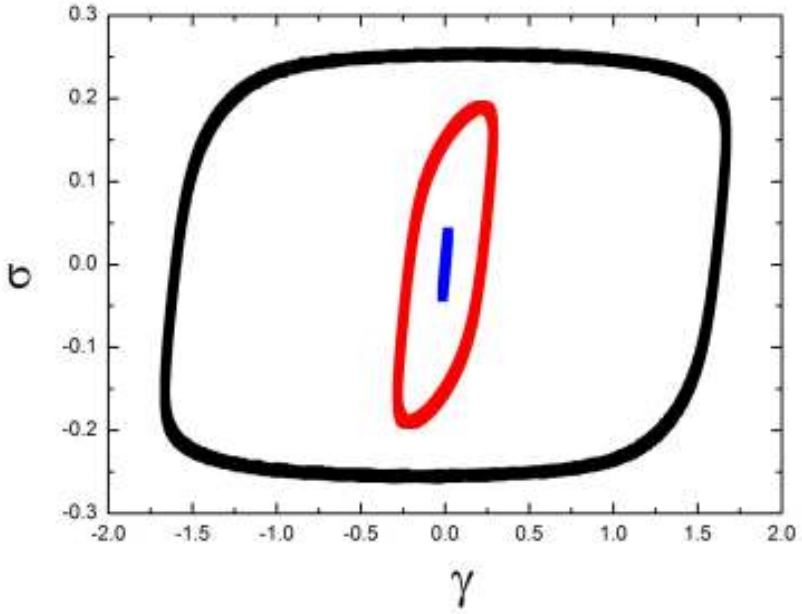

Figure B.6. *Lissajou plot (Elastic stress vs Strain) of three strain amplitudes in arrested phase separation regime ($\rho_H\sigma_S^3 = 3.094$). The plotted data are extracted from time sweeps at 1%, 17%, 100% strain amplitudes and are shown with blue, red and black colors , respectively. The angular frequency of the experiments was 1 rad/s.*

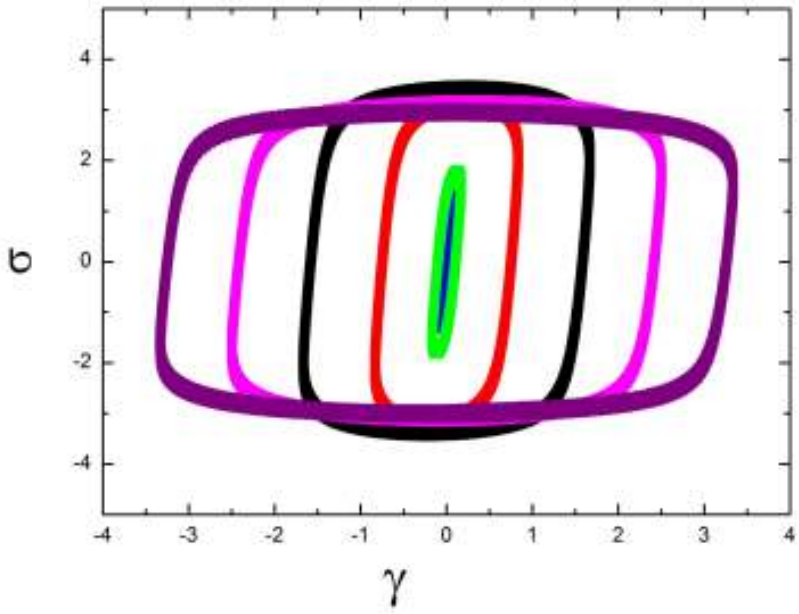

Figure B.7. *Lissajou plot (Elastic stress vs Strain) of three strain amplitudes in double glass regime ($\rho_H\sigma_S^3 = 15.026$). The plotted data are extracted from time sweeps at 1%, 5%, 10%, 20%, 50%, 100%, 150%, 200% strain amplitudes and are shown with blue, green, red, black, magenta and purple colors , respectively. The angular frequency of the experiments was 1 rad/s.*

Additional Fourier transform analysis has been applied for measurements in the double glass regime (Fig. B.8-B.9). In fig. B.8 and B.9 we observe that the anharmonicity of the system (I_n/I_1) increases as we go further into the non linear regime. However, in Fig. B.8 the anharmonicity seems to reach a plateau since the (I_n/I_1) does not change with the strain amplitude increase. This is not observed in Fig. B.9, manifesting that the strain to reach that plateau is even higher.

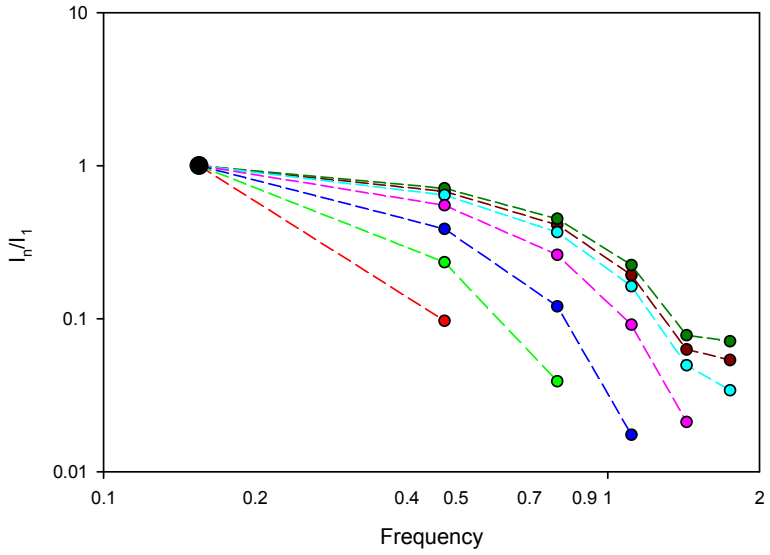

Figure B.8 *Normalized amplitudes of higher harmonics in the double glass regime ($\rho_H\sigma_S^3 = 15.026$) for different strain amplitude . Strain amplitudes of 1%,5%,10%, 20%, 50%, 100%,150% and 200% are represented with black, red, green, blue, magenta, cyan, wine and olive colors, respectively.*

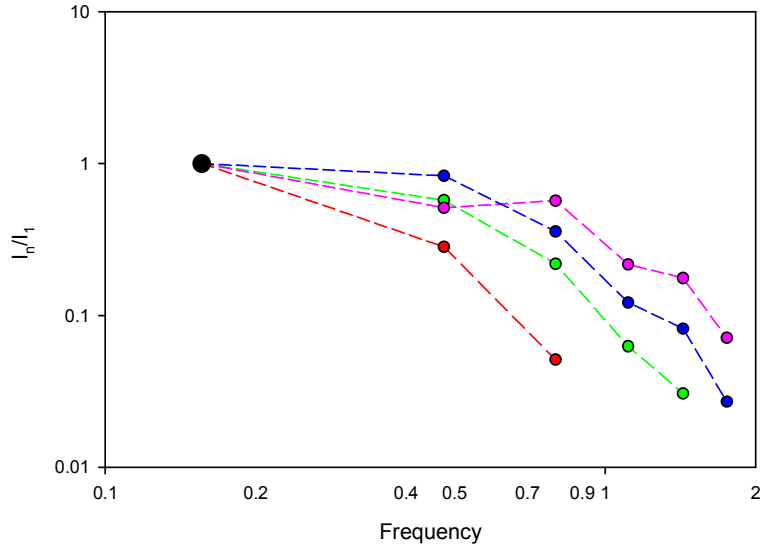

Figure B.9 *Normalized amplitudes of higher harmonics in the double glass regime ($\rho_H\sigma_S^3 = 18.085$) for different strain amplitude . Strain amplitudes of 1% ,10%, 50%, 100%, and 200% are represented with black, red, green, blue and magenta colors, respectively.*

Appendix C

Star - Linear mixtures

In chapter 6, we described the effects of hard particle additions in a soft glassy solution. The hard particles induced multiple transitions in the soft colloid glass; melting of the initial repulsive glass system, a reentrant glassy state with phase separation and eventually a double glass where the stars have shrunk due to the osmotic pressure from the high colloidal concentrations. The same phenomenon has been observed in similar works in which the depletion is caused by linear chains. A recent work has shown similar structural transitions in a soft glassy solution upon the addition of linear chains [296]. We tried to explore different size ratios than the one ($\delta = 0.05$) described in that publication. We employed multi-arm 1,4-polybutadiene (PBD) stars with a weight-average functionality, $f_S \equiv f = 364$ arms and a weight-average arm molar mass $M_a = 23\ kg/mol$, whose synthesis is described elsewhere [106, 170]. The linear 1,4-polybutadiene chains (L) used, were obtained from Polymer Source (Canada) and had a weight-average molar mass $M_w = 992000\ g/mol$.

The polymers were dissolved in squalene, a nearly athermal and nonvolatile solvent. The hydrodynamic radii were determined from dynamic light scattering (DLS) measurements in dilute solution at 20°C and found to be $R_h^S = 39nm$ and $R_h^L = 41nm$. Their respective overlap concentrations were $c_S^* = 56\ mg/ml$ and $c_L^* = 5.7\ mg/ml$. We studied several star polymer solutions by adding linear chains which were prepared at apparent volume fractions (based on single star size) $\Phi_S = c_S/c_S^* = 0.5\ to$ 4.0. When preparing mixtures with linear chains, the same fraction (number density) of star polymers was maintained in the samples. This means practically that the added linear chains replaced the squalene solvent.

To investigate the state of the star/linear mixtures, we used rheological measurements, which were carried out with a sensitive strain-controlled rheometer (ARES-HR 100FRTN1 from TA USA, formerly Rheometric Scientific). Due to the very limited amount of samples available, a home-made cone-and-plate geometry (stainless steel cone of 8mm diameter and 0.166 rad cone angle) was used. The temperature was set at 20.00°C and controlled by a Peltier plate with a recirculating water/ethylene glycol bath. During an experimental run, the sample was loaded on the rheometer, and a well-defined preshear protocol (described in Chapter 2.3) was applied.

Figure C.1. demonstrates the shifting of the moduli crossover as a function of linear concentration. The increase of the linear chains in the system creates a larger number of entanglements driving it to higher relaxation times. The right panel of figure C.2 shows the extracted relaxation times from different star and linear densities. At the low star densities, below the overlap concentration, the rheological behavior of the mixtures seems to govern by the linear response. This phenomenon is also supported by the evolution of the plateau modulus as a function of the chain concentration, shown in Figure C.1. Below the star overlap concentration, all the mixtures manifest the same increase as pure linear solutions in good solvent.

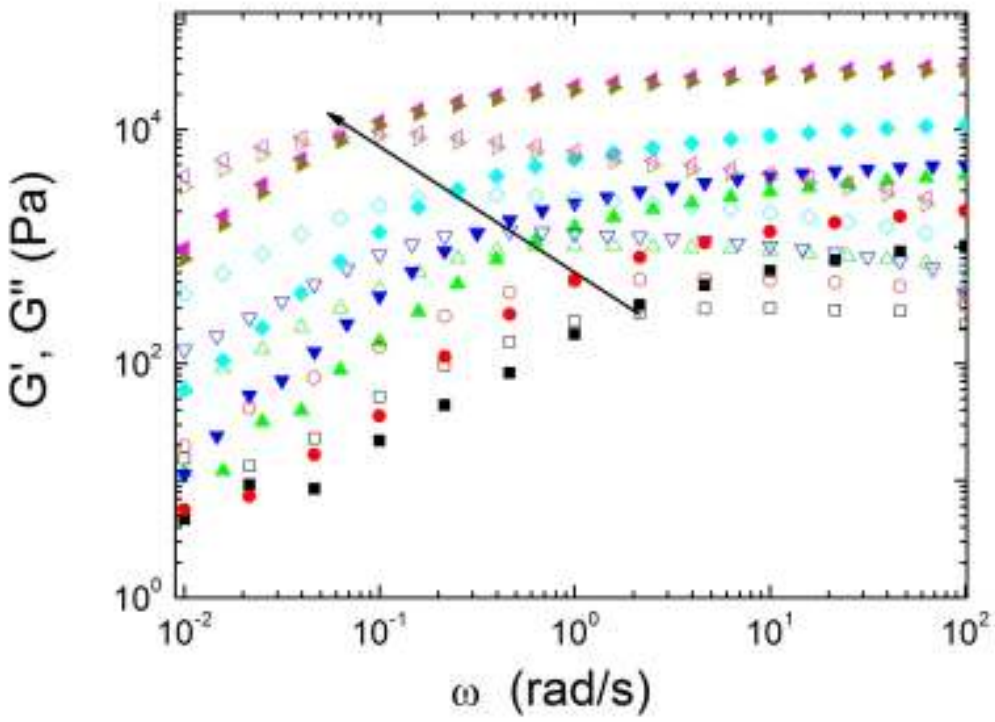

Figure C.1. *Linear viscoelastic spectra for star-linear mixtures at* $\phi_S = 0.5$. G' *and* G'' *are shown with full and empty symbols respectively. Linear concentrations of* $\phi_L = 0.034, 0.06, 0.08, 0.10, 0.15, 0.30$ *and* 0.35 *are represented with black squares, red circles, green up triangles, blue down triangles, cyan rhombi, magenta left triangles and dark yellow right triangles, respectively. The black arrow shows the shifting of the moduli crossover.*

In low linear concentrations, the two higher star densities, show strong deviations from the rest studied mixtures. Both modulus and characteristic times, extracted from the maximum of the loss modulus, display a weak dependence on the linear concentration, meaning that the response of the mixture is ruled by the stars. The relaxation time does not seem to change since the linear polymers do not understand the presence of the other linear chains. However, as the chain densities in the mixtures increase, they seem to take over the behavior of the solutions. It is really interesting that all the points, regardless the star density, coincide in the same line which falls together with the pure linear polymer behavior. We believe that, the reason for this change of system behavior is the shrinkage of the stars due to osmotic pressure caused by the linear chains. The stars collapse and thus the interparticle distance of the linear chains becomes smaller than the respective one

of the stars. As a consequence their response rules the mixture behavior and coincides with pure linear solutions.

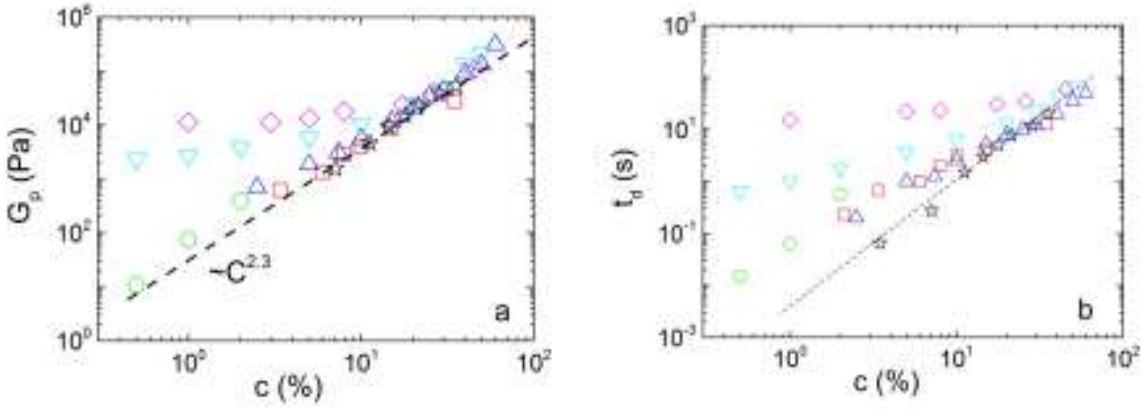

Figure C.2. *Left Panel: The dependence of the plateau modulus as a function of linear concentration. Star densities are demonstrated with different symbols and colors. 0.5c*, 0.7c*, 0.9c*, 2c* and 4c* are represented with red squares, green circles, blue up triangles, cyan down triangles and magenta rhombi, respectively. The black stars represent data acquired from pure linear solutions. Right Panel: The dependence of the characteristic time of the mixtures as function of the linear concentration. The different colors and symbols represent the same data sets as in left panel.*

Appendix D

Large amplitude oscillatory shear in Discotic Liquid Crystals

Discotic liquid crystals (DLC), consisting of rigid disk-shaped aromatic cores and disordered alkyl substituents self-assemble into columnar supramolecular structures [217, 308, 309]. Their self-assembly is driven by non-covalent intermolecular interactions favoring the π-stacking of aromatic cores and the unfavorable interactions between the cores and the alkyl chains leading to nanophase separation [310, 311].

Recently the controlled synthesis of DLC bearing large aromatic cores, such as hexa peri-hexabenzocoronenes (HBC), allowed extensive investigations of their self-assembly [217, 309-312], thermodynamics [313-315], dynamics [312, 316-320] and electronic [321, 322] properties. Investigations with X-ray scattering revealed two main columnar structures in HBCs: a hexagonal liquid crystalline phase (Col_h) and a crystalline phase (C_r) at higher and lower temperatures, respectively.

Of particular interest, with respect to the high charge carrier mobility along the columnar axis (i.e., molecular wires), is the crystalline phase composed of columns of tilted disks giving rise to the well-known herringbone structure. Recent efforts through the application of pressure [319, 320, 323] aided in constructing the complete phase diagrams for two dipolesubstituted HBCs. They reveal that the crystalline phase can be effectively stabilized at elevated pressures (Fig. D.2). In parallel with the phase diagrams, there have been efforts [320, 324] to probe the pathways of the phase transformation from the Col_h to the C_r phase in some HBCs. These experiments aimed at identifying the exact mechanism of phase transformation including metastable [324] or coexisting states, possible nucleation sites, and structural defects. A relevant question is the interplay of flow and dynamics. In the following, we will describe some rheological experiments manifesting phase transformations through metastable states.

D.1. Synthesis

The synthesis of the monobromo hexa-perihexabenzocoronene (HBC) has been reported earlier [323]. After preparing the 1-(4-bromo)-2,3,4,5,6-pentakis-(4-dodecylphenyl) hexa-phenylbenzene 1 (Br-HPB) via a Diels_Alder cycloaddition, the desired Br-HBC-derivative can be subsequently obtained through an intramolecular Scholl reaction in good yields (80%). The molecular structure is shown in Figure D.1.

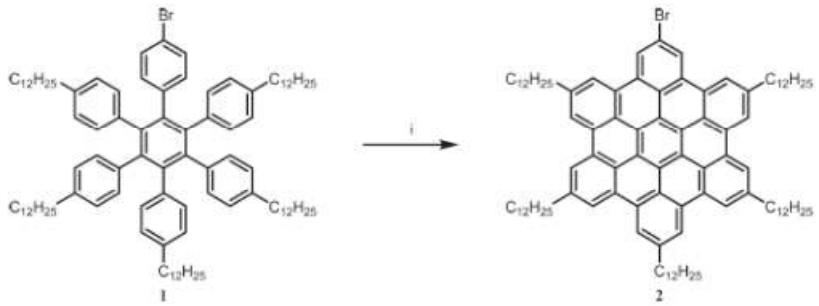

Figure D.1. *Preparation of Br-HBC (i) 18 equiv. FeCl3, DCM, 1 h, 80%. Taken from [325].*

Selective probing of the vibration modes corresponding to the aromatic core and the alkyl chains, allowed investigation of their role in the phase transformation dynamics over an extraordinarily broad time window (1-10^5 s). Identical kinetics were found suggesting that both the core and the alkyl chains simultaneously drive the system from the undercooled liquid crystalline to the crystalline phase with the herringbone structure Fig. D.2 [325].

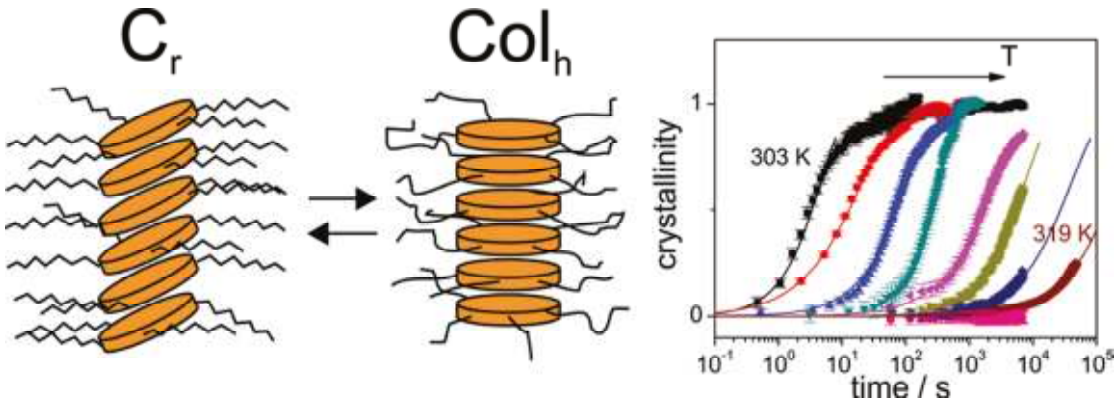

Figure D.2. *Schematic representation of the crystalline phase (C_r) and the undercooled crystalline phase (Col_h). Taken from [325].*

D.2. Rheology

The dynamic mechanical properties of the HBC-Br were studied using strain controlled rheology. Shear rheometry probes the linear and nonlinear viscoelastic response of a sample in rheometric simple shear flows. Rheological measurements were performed with a sensitive strain-controlled ARES 2k FRTN1 rheometer (Rheometric Scientific, USA) used in the oscillatory mode for recording the viscoelastic properties of the HBC-Br. The sample was prepared on the lower stainless steel plate of the 8 mm diameter parallel plate geometry setup and heated under a nitrogen atmosphere until it could flow. The environmental temperature was controlled with the use of a homemade oven with nitrogen circulation. Subsequently, the upper plate was brought into contact, the gap thickness was adjusted to 1 mm, and the atmosphere was slowly adjusted to the desired starting temperature. The storage (G') and loss (G'') shear moduli were monitored in different types of experiments.

D.3. Results and Discussion

First, we explored the transitions between the crystalline and the liquid phases through several temperature sweeps with a rate of 2°C/min. Figure D.3 displays a characteristic example of these transitions. At 40°C the system crystallizes, manifested by a absent increase in both moduli. However, it exhibits a hysteresis though heating process since it melts at temperatures close to 70°C. The crystal structure at low temperatures is also shown in Fig. D.4, where the storage modulus increases by one decade.

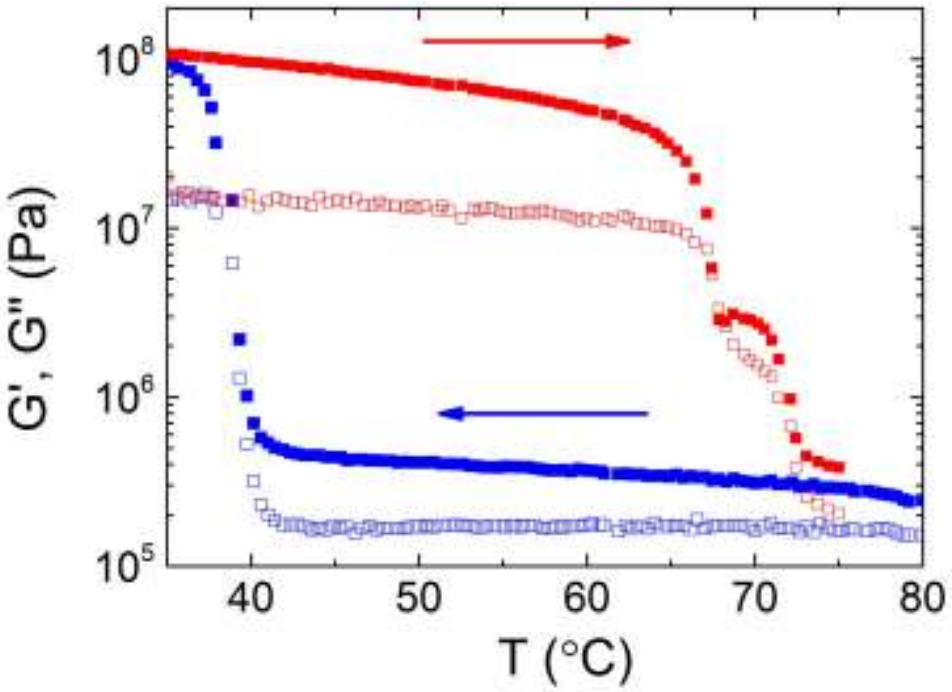

Figure D.3. *Dynamic Temperature ramp of HBC-Br obtained at 0.1rad/s with 0.1% strain amplitude. Full and empty squares denote the storage (G') and the loss (G'') moduli, respectively. The arrows show the initial cooling (blue) and the following heating (red) ramps.*

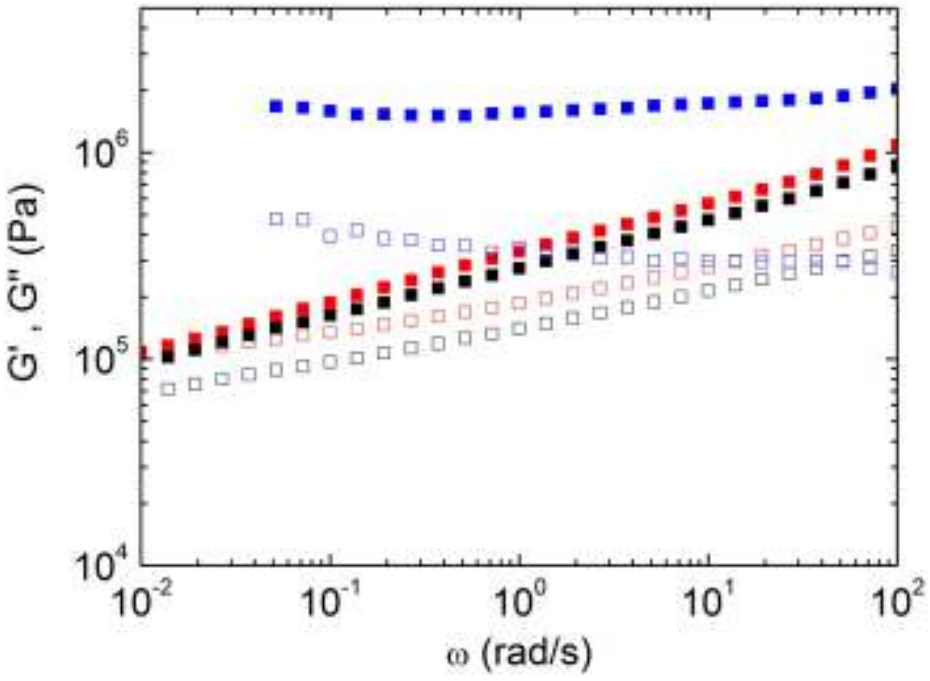

Figure D.4. *Frequency dependence of the storage (G′) and loss (G′′) moduli of HBC-Br obtained at 0.1% strain amplitude at three different temperatures. Red, black and blue symbols represent data for 80°C, 60°C and 40°C, respectively. Full and empty squares stand for storage and loss moduli, respectively.*

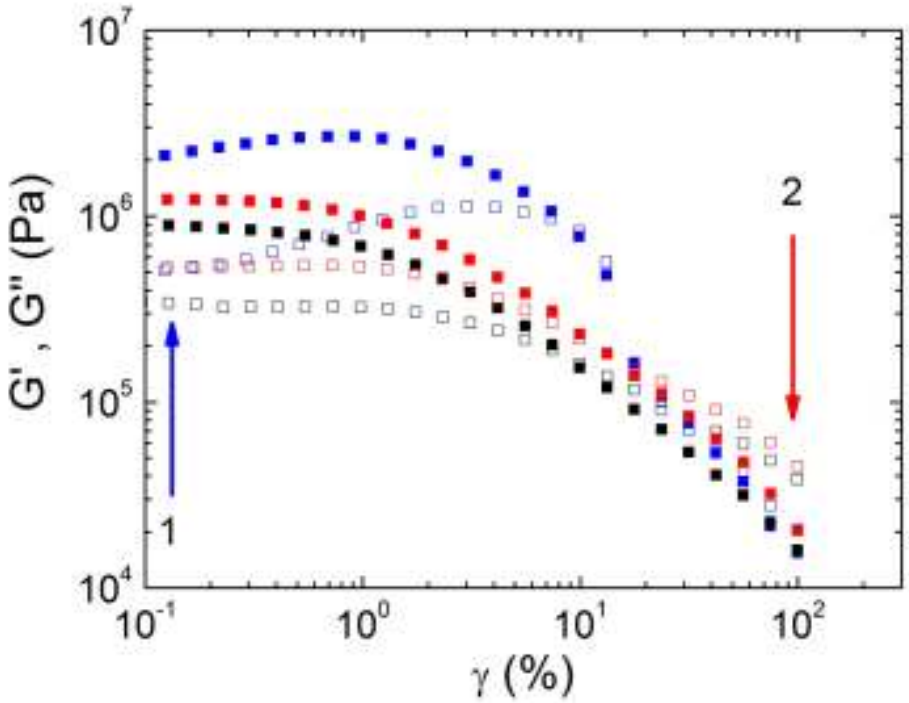

Figure D.5. *Strain amplitude dependence of the storage (G′) and loss (G″) moduli of HBC-Br obtained at 1rad/s frequency at three different temperatures. Red, black and blue symbols represent data for 80°C, 60°C and 40°C, respectively. Full and empty squares stand for storage and loss moduli, respectively. The arrows show the states of the time sweeps. State1 (blue arrow) stand for the oscillations in the linear regime while state 2 (red arrow) depicts the state of large strain amplitude.*

We, also, examined the effect of large amplitude (close to the yield strain) oscillatory deformation on the system's structure. To accomplish this, we applied the following protocol: a) Dynamic time sweep at low frequency (usually 1rad/s) for easier processing due to lower modulus and a low strain amplitude (0.1%) in the linear regime, with duration long enough ($2 \cdot 10^4$ s) to ensure that steady state is reached. b) Dynamic frequency sweep in order to probe the viscoelastic relaxation spectrum at this initial equilibrium state. c) Dynamic time sweep at low frequency (usually 1rad/s) and a large strain amplitude (100%), with duration long enough to ensure that steady state is reached. d) Dynamic frequency sweep in order to probe the viscoelastic relaxation spectrum immediately after the cessation of shear e) Dynamic time sweep at low frequency (usually 1rad/s) and a low strain amplitude (0.1%), with duration long enough to ensure that steady

state is reached f) Dynamic frequency sweep in order to compare the viscoelastic spectra before and after the large oscillatory shear.

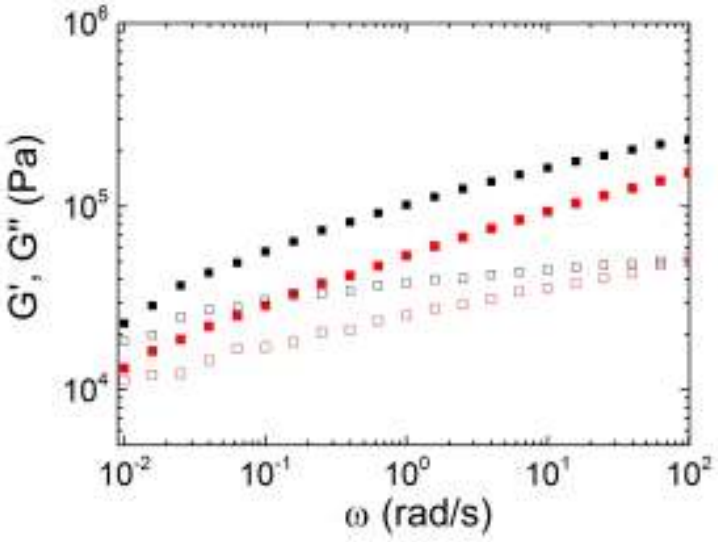

Figure D.6. *Frequency dependence of the storage and loss moduli of HBC-Br obtained at 0.1% strain amplitude before and after LAOS, at 80°C. The black symbols denote the initial state while the red stand for the state after LAOS. Full and empty squares stand for storage and loss moduli, respectively.*

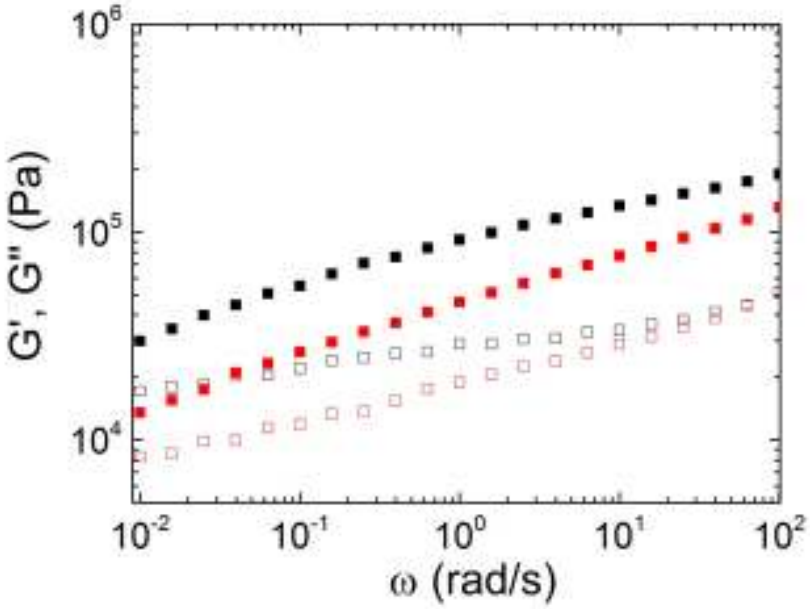

Figure D.7. *Frequency dependence of the storage and loss moduli of HBC-Br obtained at 0.1% strain amplitude before and after LAOS, at 60°C. The black symbols denote the initial state while the red stand for the state after LAOS. Full and empty squares stand for storage and loss moduli, respectively.*

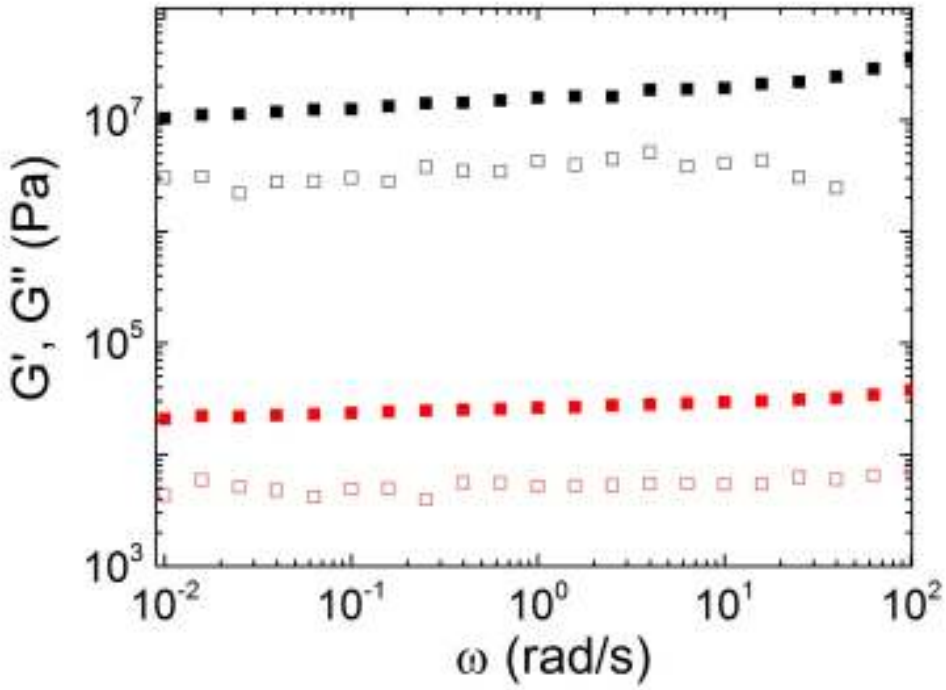

Figure D.8. *Frequency dependence of the storage and loss moduli of HBC-Br obtained at 0.1% strain amplitude before and after LAOS, at 35°C. The black symbols denote the initial state while the red stand for the state after LAOS. Full and empty squares stand for storage and loss moduli, respectively.*

Figures D.6-D.8 manifest the effect of the large oscillatory shear on the systems structure. We observe that at all temperatures examined, the moduli recorded from the frequency sweeps before and after LAOS show discrepancies, which are only quantitative. In the melted state ($T > 40°C$), the deviations are not so strong, with both moduli decreasing after LAOS by a factor of two compared to the initial measurement (Figures D.6 and D.7). On the other hand, in the crystalline state (Fig. D.8) the moduli decrease by almost three decades. This suggests that the moduli probe different structures in the system with the kinetics of structural changes not being accounted for.

In summary, the large amplitude oscillatory shear induces changes in the internal structure of our system. These variations are more pronounced at the crystalline regime, demonstrating that it is another metastable state. Also, rheology proves to be a valuable tool for probing transitions between metastable states and a strong ally in our path to deeper understanding of metastability roots.